

UNIVERSITÀ DEGLI STUDI DI UDINE  
DIPARTIMENTO POLITECNICO DI INGEGNERIA E ARCHITETTURA  
PHD IN INDUSTRIAL AND INFORMATION ENGINEERING



BROADBAND VIBRATION CONTROL  
THROUGH PERIODIC ARRAYS OF  
LOCALLY RESONANT INCLUSIONS

AUTHOR:  
Michał Zientek

SUPERVISOR:  
Prof. Paolo Gardonio

ACADEMIC YEAR 2017-2018

*Dedicated to the memory*

*of my father and*

*To my mother*

*with love and appreciation*

---

## ABSTRACT

---

This dissertation presents theoretical and experimental investigations concerning the control of flexural vibrations in beams and plates equipped with dense arrays of periodic inclusions. The thesis first considers a simplified model problem, which is composed of an infinite beam structure with a one-dimensional grid of inclusions, that is: discrete masses, tunable vibration absorbers and shunted piezoelectric patch transducers. A finite element model is introduced to derive the flexural propagation constants, which are used to illustrate and characterize the physics of the wave attenuation mechanism also known as the stop band phenomenon. In the next part of the thesis, two-dimensional regular arrays of inclusions are employed to control wave propagation in an infinite plate. Also in this case, the finite element method is used to characterize the performance of point masses, spring-mass vibration absorbers and shunted piezoelectric patch transducers. More importantly, a novel mathematical formulation of multi-resonant shunt circuits connected to piezoelectric patches is introduced. It allows to overcome the conventional issue of the nonlinear eigenvalue problem and to obtain dispersion properties of the two-dimensional structures characterised by multiple locally resonant effects. Based on this approach, the band diagram of a 2D metamaterial with periodic arrays of piezoelectric patch transducers connected to double-resonance shunts is calculated. The results show, that indeed the resonances of the shunting network split the dispersion curves by forming two distinct resonance band gaps. Further on in the thesis, mobility-impedance based and fully coupled modal models are introduced to investigate the responses of finite plate with periodic arrays of point masses, tunable vibration absorbers and shunted piezoelectric patch transducers. In this framework, besides the analyses of mid to high-frequency band gaps, a new method of low-frequency flexural vibration suppression is investigated. The proposed approach utilises piezoelectric patch transducers connected to multi-resonant electrical shunts in such a way as they reduce the resonant effects of flexural vibrations of the hosting structure over a wide low-frequency band. The shunts are formed by multiple resistance-inductance-capacitance (RLC) branches connected in parallel. The proposed method sequentially tunes the RL elements of the branches in each shunt in such a way as to maximise the vibration energy absorption from a progressively larger number of resonant flexural modes of the hosting structure. In practice the vibration energy absorption is estimated from the measured electric power absorbed by each shunt so

that the on-line tuning algorithm can be conveniently implemented locally. To prove the validity of the proposed algorithm, simulation and experimental studies are presented considering the flexural response of a thin plate, which is equipped with piezoelectric patches connected to multi-resonant shunts. The study shows that the proposed approach allows the on-line tuning of the RLC branches in each shunt to control the resonant response of low order flexural modes so that the flexural response of the plate is effectively reduced over a wide frequency band in the low to mid-frequency range. The proposed algorithm can be implemented in real time such that the tuning of the RLC branches can track changes in the dynamic response of the hosting structure due to operation conditions. The validity of the proposed self-tuning algorithm has been verified experimentally on a thin rectangular aluminium plate equipped with five piezoelectric patches connected to multi-resonant shunts. The shunts are tuned in a dSPACE digital platform with the proposed algorithm, that maximises the flexural vibration power absorption of the target resonant modes by maximising the correspondent electrical power absorption by each shunt.



---

## ACKNOWLEDGEMENTS

---

I would like to express my sincere gratitude and thanks to my supervisor Prof. Paolo Gardonio for his invaluable support of my study, for his patience, motivation and his willingness to share his immense knowledge.

I would like also to thank my colleagues from the office Dr. Daniel Casagrande, Dr. Emanuele Turco, Dr. Federica Arrigoni, Aleksander Kras and Loris Dal Bo. It was a great pleasure working with all of you, I appreciate your valuable advices, help and continuous good humour during my stay at University of Udine.

The work presented in this dissertation was founded by the European Commission through the MSC ITN ANTARES program and it is gratefully acknowledged.

On a personal level my deepest appreciation belongs to my beloved girlfriend Dr. Karina Wilgan for her endless patience, everlasting love and all the support I have got over the course of PhD studies.



---

# CONTENTS

---

ABSTRACT iii

ACKNOWLEDGEMENTS vi

LIST OF FIGURES xii

LIST OF TABLES xxii

NOMENCLATURE xxiv

## 1. INTRODUCTION 1

1.1 Means of vibration treatment 2

1.1.1 *Passive vibration control* 2

1.1.2 *Active vibration control* 3

1.1.3 *Semi-active vibration control* 4

1.2 Shunted piezoelectric transducers 4

1.2.1 *Multi-resonating shunts* 5

1.3 Modern Periodic structures 7

1.3.1 *Mechanical structures with shunted arrays of piezoelectric patch transducers* 9

1.4 Objective of the thesis 10

1.5 Contributions of the thesis 10

1.6 Structure of the thesis 11

## 2. INFINITE BEAM WITH PERIODIC INCLUSIONS 12

2.1 Introduction 12

2.2 Model formulation 13

2.2.1 *FEM discretization* 13

2.2.2 *Piezoelectric transducer* 15

2.2.3 *Hamilton's principle* 17

2.2.4 *Variation indicator* 19

2.3 Wave propagation in one-dimensional periodic beam 22

2.3.1 *Infinite beam with no inclusions* 23

2.3.2 *Infinite beam with regular grid of point masses* 28

2.3.3 *Infinite beam with regular grid of spring-mass vibration absorbers* 31

2.3.4 *Infinite beam with regular grid of vibration absorbers equipped with base masses* 37

2.3.5 *Infinite beam with regular grid of piezoelectric patch transducers connected to inductive shunts* 39

2.3.6 *Infinite beam with regular grid of piezoelectric patch transducers connected to resistive-inductive shunts* 42

2.3.7 *Infinite beam with regular grid of piezoelectric patch transducers connected to multi-resonant shunt circuits* 45

2.4 Concluding remarks 49

### 3 INFINITE PLATE WITH PERIODIC INCLUSIONS 51

3.1 Introduction 51

3.2 Model formulation 52

3.2.1 *FEM discretization* 52

3.2.2 *Piezoelectric effects on plate* 56

3.2.3 *Hamilton's principle* 59

3.2.4 *Variation indicator* 60

3.3 Dispersion properties 63

3.3.1 *Infinite plate with no inclusions* 64

3.3.2 *Infinite plate with regular array of point masses* 69

3.3.3 *Infinite plate with regular array of spring-mass vibration absorbers* 72

3.3.4 *Infinite plate with regular array of vibration absorbers equipped with base masses* 77

3.3.5 *Infinite plate with regular array of piezoelectric patch transducers connected to inductive shunts* 80

3.3.6 *Infinite plate with regular array of piezoelectric patch transducers connected to multi-resonant shunt circuits* 85

3.4 Concluding remarks 88

## 4. FINITE PLATE WITH PERIODIC INCLUSIONS 90

### 4.1 Description of the system 91

### 4.2 Stop band phenomena in finite plates 92

4.2.1 *Finite plate with regular array of point masses / spring-mass vibration absorbers* 92

4.2.2 *Finite plate with regular array of piezoelectric patch transducers connected to resistive-inductive shunts* 99

4.2.3 *Finite plate with arrays of shunted piezoelectric patch transducers connected to multi-resonating shunts* 105

### 4.3 Concluding remarks 106

## 5. FINITE PLATE WITH ARRAYS OF SHUNTED PIEZOELECTRIC PATCHES FOR LOW FREQUENCIES VIBRATION CONTROL 108

### 5.1 Introduction 109

### 5.2 Description of the system 109

### 5.3 Mathematical model 111

5.3.1 *Mechanical and electrical equations* 112

5.3.2 *Multi-resonant shunt equations* 113

5.3.3 *State-space formulation* 115

5.3.4 *Time averaged energy functions* 116

5.3.5 *Power spectral density of the time average energy functions* 117

### 5.4 Tuning of multi-resonant shunts 120

5.4.1 *Effects produced by RL and RLC single branches* 120

5.4.2 *Incremental effect produced by multiple RLC branches* 124

5.4.3 *Tuning algorithm based on the maximisation of electric power absorbed by a multi resonant shunt* 129

5.5 Smart plate equipped with increasingly denser arrays of piezoelectric patches connected to multi-resonant shunts tuned to maximise power absorption 133

5.6 Experimental validation of the proposed tuning method of multi resonant shunts 135

5.7 Experimental setup 136

5.8 Kinetic energy and power absorption measurements 139

5.9 Concluding remarks 143

CONCLUSIONS 144

LIST OF PUBLICATIONS 150

BIBLIOGRAPHY 151

---

## LIST OF FIGURES

---

- Figure 1.1 Multi-resonant, current flowing shunt circuit
- Figure 2.1 (a) Representation of an infinite Euler-Bernoulli beam, comprised by aluminum and piezoelectric ceramic. (b) An exemplary single finite element.
- Figure 2.2 (a) Depiction of an infinite, uniform Euler-Bernoulli beam. (b) An exemplary meshed unit cell.
- Figure 2.3 Dispersion curves for an infinite Euler-Bernoulli beam. Plots (a) and (b) positive and negative going evanescent waves. Plots (c) and (d) positive and negative going flexural waves. Black lines -real parts, blue lines - imaginary parts of propagation constants.
- Figure 2.4 (a) Depiction of an infinite Euler-Bernoulli beam with discrete masses spaced by a distance  $L_{cell}$ . (b) An exemplary meshed unit cell.
- Figure 2.5 Dispersion curves for an infinite Euler-Bernoulli beam with periodic point masses equal to 20% of the unit cell mass. Plots (a) and (b) positive and negative going evanescent waves. Plots (c) and (d) positive and negative going flexural waves. Black lines -real parts, blue lines - imaginary parts of propagation constants.
- Figure 2.6 (a) The evolution of the attenuation constant of positive going flexural waves in an infinite Euler-Bernoulli beam with periodic point masses against dimensionless weight of point masses. Attenuation constants of flexural waves associated with (b)  $\gamma = 1$ , (c)  $\gamma = 0.5$  and (d)  $\gamma = 0.25$ .
- Figure 2.7 (a) Depiction of an infinite Euler-Bernoulli beam with tunable vibration absorbers spaced by a distance  $L_{cell}$ . (b) An exemplary meshed unit cell.
- Figure 2.8 Dispersion curves for an infinite Euler-Bernoulli beam with periodic point tunable vibration absorbers whose masses are equal to 20% of the unit cell mass. Plots (a) and (b) positive and negative going evanescent waves. Plots (c) and (d) positive and negative going flexural waves. Black lines -real parts, blue lines - imaginary parts of propagation constants.

- Figure 2.9 (a) The evolution of the attenuation constant of positive going flexural waves in an infinite Euler-Bernoulli beam with periodic TVAs whose masses are equal to 20% of the unit cell mass against the dimensionless frequency of the absorbers Attenuation constants of flexural waves associated with resonance frequency of the absorbers (b)  $\Omega_0 = 1.1$ , (c)  $\Omega_0 = 0.9$  and (d)  $\Omega_0 = 0.8$ .
- Figure 2.10 (a) The evolution of the attenuation constant of positive going flexural waves in an infinite Euler-Bernoulli beam with periodic TVAs tuned to  $\Omega_0 = 0.5$  against the dimensionless weight of proof masses. Attenuation constants of flexural waves associated to dimensionless weight of proof masses (b)  $\gamma = 1$ , (c)  $\gamma = 0.5$  and (d)  $\gamma = 0.25$ .
- Figure 2.11 (a) The evolution of the attenuation constant of positive going flexural waves in an infinite Euler-Bernoulli beam with damped, periodic TVAs whose masses are equal to 20% of the unit cell mass, against the dimensionless frequency of the absorbers Attenuation constants of flexural waves associated with resonance frequency of the absorbers (b)  $\Omega_0 = 1.1$ , (c)  $\Omega_0 = 0.9$  and (d)  $\Omega_0 = 0.8$ . Black lines – undamped TVAs, blue lines – TVAs with 3% of damping ratio.
- Figure 2.12 (a) The evolution of the attenuation constant of positive going flexural waves in an infinite Euler-Bernoulli beam with periodic TVAs tuned to  $\Omega_0 = 0.5$  and whose proof masses are equal to 20% of the unit cell mass, against damping ratio of the TVAs. Attenuation constants of flexural waves associated to TVAs damping ratios (b)  $\zeta = 0.1$ , (c)  $\zeta = 0.05$  and (d)  $\zeta = 0.015$ .
- Figure 2.13 (a) The evolution of the attenuation constant of positive going flexural waves in an infinite Euler-Bernoulli beam with damped, periodic TVAs with base masses equal to 40% and proof masses to 20% of the unit cell mass, against the dimensionless frequency of the absorbers Attenuation constants of flexural waves associated with resonance frequency of the absorbers (b)  $\Omega_0 = 1.5$ , (c)  $\Omega_0 = 0.9$  and (d)  $\Omega_0 = 0.5$ . Black lines – undamped TVAs, blue lines – TVAs with 3% of damping ratio.

- Figure 2.14 (a) The evolution of the attenuation constant of positive going flexural waves in an infinite Euler-Bernoulli beam with damped, periodic TVAs with base masses equal to 40% and proof masses to 20% of the unit cell mass, against the dimensionless frequency of the absorbers Attenuation constants of flexural waves associated with resonance frequency of the absorbers (b)  $\Omega_0 = 1.5$ , (c)  $\Omega_0 = 0.9$  and (d)  $\Omega_0 = 0.5$ . Black lines – undamped TVAs, blue lines – TVAs with 3% of damping ratio.
- Figure 2.15 (a) Depiction of an infinite Euler-Bernoulli beam with piezoelectric patch transducers spaced by a distance  $L_{cell}$ . (b) An exemplary mesh of the unit cell.
- Figure 2.16 The evolution of the attenuation constant of positive going flexural waves in an infinite Euler-Bernoulli beam with piezoelectric patch transducers connected to inductive shunts, against the dimensionless resonance frequency of the shunts. Attenuation constants of flexural waves associated with resonance frequency of the shunts (b)  $\Omega_0 = 1.5$ , (c)  $\Omega_0 = 0.9$  and (d)  $\Omega_0 = 0.5$ .
- Figure 2.17 The evolution of the attenuation constant of positive going flexural waves in an infinite Euler-Bernoulli beam with piezoelectric patch transducers connected to series RL shunts, against the dimensionless resonance frequency of the shunts. Attenuation constants of flexural waves associated with resonance frequency of the shunts (b)  $\Omega_0 = 1.5$ , (c)  $\Omega_0 = 0.9$  and (d)  $\Omega_0 = 0.5$ . Black lines - inductive shunt, blue lines – series RL shunt.
- Figure 2.18 The evolution of the attenuation constant of positive going flexural waves in an infinite Euler-Bernoulli beam with piezoelectric patch transducers connected to series RL shunts and tuned to  $\Omega_0 = 0.5$ , against the quality factor of the shunts. Attenuation constants of flexural waves associated with quality factors of the of the shunt (b)  $Q = 90$ , (c)  $Q = 45$  and (d)  $Q = 10$ .
- Figure 2.19 Attenuation constants of flexural waves associated with resonance frequencies 0.5, 0.8 (a) and 0.65, 1.3 (b). Black lines – multi-resonating, inductive shunts, blue lines – multi-resonating RL shunts. Whose resistances were set to  $5\Omega$  and  $7k\Omega$ .
- Figure 3.1 FEM element.

- Figure 3.2 (a) Depiction of a unit cell comprising FEM mesh (b) Reciprocal space with irreducible Brillouin zone indicated by blue color.
- Figure 3.3 (a) Dispersion curves for a uniform infinite plate; (b) Depiction of the unit cell.
- Figure 3.4 Displacement patterns for 9 unit cells of a uniform, infinite plate. The visualized displacement patterns: (b), (c), (d), (e), (f) correspond to the points indicated with black dots on dispersion diagram in plot (a).
- Figure 3.5 Dispersion curves for an infinite plate with periodic point mass equal to 20% (b) and 70% (b) of the mass of the unit cell. (c) Depiction of the unit cell.
- Figure 3.6 Relation between added discrete mass and distribution of the stop band effect.
- Figure 3.7 Displacement patterns for 9 unit cells of an infinite plate with periodic point masses equal to 20% of the mass of the unit cells. The visualized displacement patterns: (b), (c), (d), (e), (f) correspond to the points indicated with black dots on dispersion diagram in plot (a).
- Figure 3.8 Dispersion curves for an infinite plate with periodic vibration absorbers tuned to dimensionless frequency  $\Omega_0 = 0.5$  (a) and  $\Omega_0 = 1$  (b) and whose mass is equal to 20% of the unit cell mass. (c) Depiction of a unit cell.
- Figure 3.9 Relations between resonance frequency of the absorbers and distributions of the stop band effects for the absorbers equipped with suspended mass equal to 20% (a) and 40% (b) of the unit cell mass. (c) Relation between suspended mass of the absorbers and distribution of the stop band effect for the arbitrarily chosen resonance frequency 0.5.
- Figure 3.10 Displacement patterns for 9 unit cells of an infinite plate with periodic spring-mass vibration absorbers tuned to dimensionless frequency 0.5 and whose masses are equal to 20% of the mass of the unit cell. The visualized displacement patterns: (b), (c), (d), (e), (f) correspond to the points indicated with black dots on dispersion diagram in plot (a).
- Figure 3.11 (a) Dispersion curves for an infinite plate with periodic vibration absorbers equipped with base masses and tuned to dimensionless frequency 0.5. The base masses are equal to 70% and proof masses to 20% of the unit cell mass. (b) Depiction of a unit cell.

- Figure 3.12 Relations between resonance frequency of the absorbers and distributions of the stop band effects for the absorbers equipped with base masses equal to 40% (a) and 70% (b) of the unit cell mass. In both cases the proof masses are equal to 20% of the unit cell mass
- Figure 3.13 Displacement patterns for 9 unit cells of an infinite plate with periodic spring-mass vibration absorbers tuned to dimensionless frequency 0.5 and whose proof masses are equal to 20% and base masses to 70% of the mass of the unit cell. The visualized displacement patterns: (b), (c), (d), (e), (f) corresponds to the points indicated with black dots on dispersion diagram in plot (a).
- Figure 3.14 (a) Dispersion curves of an infinite plate with periodic piezoelectric patch transducers whose electrical terminals are open. (b) Depiction of a unit cell.
- Figure 3.15 Displacement patterns for 9 unit cells of an infinite plate with piezoelectric patch transducers whose electrical terminals are open. The visualized displacement patterns: (b), (c), (d), (e), (f) correspond to the points indicated with black dots on dispersion diagram in plot (a).
- Figure 3.16 (a) Dispersion curves of an infinite plate with periodic piezoelectric patch transducers connected to single inductors tuned to dimensionless frequency 0.5 (b) Depiction of a unit cell. (c) Shunting inductor.
- Figure 3.17 (a) Relation between resonance frequency of the piezoelectric patches connected to single inductors and distribution of the stop band effects. (b) Magnified part of the relation indicated in plot (a).
- Figure 3.18 Displacement patterns for 9 unit cells of an infinite plate with piezoelectric patch transducers connected to single inductors and tuned to dimensionless frequency 0.5. The visualized displacement patterns: (b), (c), (d), (e), (f) correspond to the points indicated with black dots on dispersion diagram in (a).
- Figure 3.19 (a) Dispersion curves of an infinite plate with periodic piezoelectric patch transducers connected to multi-resonating shunt circuits and tuned to dimensionless frequencies 0.5 and 1. (b) Depiction of a unit cell. (c) Multi-resonating shunt circuit. (d) Simplification of the multi-resonating circuit.

- Figure 4.1 Finite plate material equipped with  $5 \times 5$  array of inclusions and excited by the rain-on-the-roof stochastic process, modelled as  $4 \times 4$  matrix of uncorrelated point forces. Four types of inclusions used in this framework point mass (b), vibration absorber (c), vibration absorber with base mass (d), piezoelectric patch transducer (e).
- Figure 4.2 (a) Evolution of the flexural kinetic energy of the finite plate equipped with periodic masses against their dimensionless ratio. Power spectral density functions of the kinetic energy when dimensionless mass is equal to 0.5 (d), 1 (c) and 1.5 (b).
- Figure 4.3 (a) Evolution of flexural kinetic energy of the finite plate equipped with a  $5 \times 5$  array of vibration absorbers whose masses are equal to 20% of the plate mass with respect to their resonance frequency (A). Power spectral density functions of the kinetic energy when absorbers are tuned to 1300 Hz (b), 900 Hz (c) and 460 Hz (d).
- Figure 4.4 (a) Evolution of the flexural kinetic energy of the finite plate equipped with a  $5 \times 5$  array of vibration absorbers whose masses are equal to 40% of the plate mass with respect to their resonance frequency. Power spectral density functions of the kinetic energy when absorbers are tuned to 1300 Hz (b), 900 Hz (c) and 460 Hz (d).
- Figure 4.5 (a) Evolution of the flexural kinetic energy of the finite plate equipped with a  $5 \times 5$  array of vibration absorbers tuned to 650 Hz against the dimensionless mass ratio of the absorbers. The power spectral density functions of the kinetic energy when the mass ratios are equal to 0.2 (b), 1 (c) and 0.5 (d).
- Figure 4.6 (a) Evolution of flexural kinetic energy of the finite plate equipped with a  $5 \times 5$  array of vibration absorbers with base masses equal to 0.7 and proof masses to 0.2 of the plates mass, with reference to resonance frequency of the absorbers. Power spectral density functions of the kinetic energy when absorbers are tuned to 460 Hz (d), 900 Hz (c) and 1350 Hz (b).
- Figure 4.7 (a) Evolution of flexural kinetic energy of the finite plate equipped with a  $5 \times 5$  array of piezoelectric patch transducers connected to series RL shunts. Power spectral density function of the kinetic energy when the shunts are tuned to 400 Hz (b), 900 Hz (c) and 1600 Hz (d).

- Figure 4.1 Finite plate material equipped with  $5 \times 5$  array of inclusions and excited by the rain-on-the-roof stochastic process, modelled as  $4 \times 4$  matrix of uncorrelated point forces. Four types of inclusions used in this framework point mass (b), vibration absorber (c), vibration absorber with base mass (d), piezoelectric patch transducer (e).
- Figure 4.2 (a) Evolution of the flexural kinetic energy of the finite plate equipped with periodic masses against their dimensionless ratio. Power spectral density functions of the kinetic energy when dimensionless mass is equal to 0.5 (d), 1 (c) and 1.5 (b).
- Figure 4.3 (a) Evolution of flexural kinetic energy of the finite plate equipped with a  $5 \times 5$  array of vibration absorbers whose masses are equal to 20% of the plate mass with respect to their resonance frequency (A). Power spectral density functions of the kinetic energy when absorbers are tuned to 1300 Hz (b), 900 Hz (c) and 460 Hz (d).
- Figure 4.4 (a) Evolution of the flexural kinetic energy of the finite plate equipped with a  $5 \times 5$  array of vibration absorbers whose masses are equal to 40% of the plate mass with respect to their resonance frequency. Power spectral density functions of the kinetic energy when absorbers are tuned to 1300 Hz (b), 900 Hz (c) and 460 Hz (d).
- Figure 4.5 (a) Evolution of the flexural kinetic energy of the finite plate equipped with a  $5 \times 5$  array of vibration absorbers tuned to 650 Hz against the dimensionless mass ratio of the absorbers. The power spectral density functions of the kinetic energy when the mass ratios are equal to 0.2 (b), 1 (c) and 0.5 (d).
- Figure 4.6 (a) Evolution of flexural kinetic energy of the finite plate equipped with a  $5 \times 5$  array of vibration absorbers with base masses equal to 0.7 and proof masses to 0.2 of the plates mass, with reference to resonance frequency of the absorbers. Power spectral density functions of the kinetic energy when absorbers are tuned to 460 Hz (d), 900 Hz (c) and 1350 Hz (b).
- Figure 4.7 (a) Evolution of flexural kinetic energy of the finite plate equipped with a  $5 \times 5$  array of piezoelectric patch transducers connected to series RL shunts. Power spectral density function of the kinetic energy when the shunts are tuned to 400 Hz (b), 900 Hz (c) and 1600 Hz (d).

- Figure 4.8 (a) Power spectral density function of the kinetic energy of the plate with a  $5 \times 5$  array of piezoelectric patches connected to multi-resonating shunts in open circuit configuration (blue line) and tuned to  $f_1 = 780\text{Hz}$  and  $f_1 = 1200\text{Hz}$  (red line). (b) Spatial configuration of piezoelectric patches. (c) Depiction of the multi-resonating shunt circuit.
- Figure 5.1 (a) Plate equipped with two piezoelectric patches subject to a rain on the roof excitation modelled as a  $4 \times 4$  array of uncorrelated point forces. (b) Electrical model of a piezoelectric patch connected to the current-flowing shunt composed of multiple RLC branches. (c) Simplified electrical model of the shunt.
- Figure 5.2 Time averaged total flexural kinetic energy of the smart plate structure (a) and time averaged electrical power absorbed (b) by the RL shunt circuit connected to the piezoelectric patch N.1 (c).
- Figure 5.3 Figure 5.3 Time averaged total flexural kinetic energy of the smart plate structure (a) and time averaged electrical power absorbed (b) by the RLC shunt circuits connected to the piezoelectric patch N.1 (c) having  $C_{f11} = 10C_{pe1}$  (first row),  $C_{f11} = C_{pe1}$  (second row),  $C_{f11} = 0.1C_{pe1}$  (third row).
- Figure 5.4 (a) Time averaged total flexural kinetic energy of the smart plate structure, (b) time averaged electrical power absorbed and (c) PSD of the plate flexural kinetic energy (solid blue line no shunt; dashed red line with shunt) and electric power absorbed by the shunt (dotted black line) by the RLC multi-resonant shunt circuits connected to the piezoelectric patch N.1 (d) while the piezoelectric patch N.2 is in open circuit.
- Figure 5.5 (a) Time averaged total flexural kinetic energy of the smart plate structure, (b) time averaged electrical power absorbed and (c) PSD of the plate flexural kinetic energy (solid blue line no shunt; dashed red line with shunt) and electric power absorbed by the shunt (dotted black line) by the RLC multi-resonant shunt circuits connected to the piezoelectric patch N.2 (d) while the piezoelectric patch N.1 implements a four branches multi-resonant shunt.
- Figure 5.6 (c) Time averaged electrical power absorbed by the shunt circuit shown in (d). Plots (a) and (b) present slices of the surface plot (c) cut along a constant resistance  $R_{s11} = 200 \Omega$  (a) and constant inductance  $L_{b11} = 21.1 \text{ H}$  (b), that is a plate and shunt resonance frequency  $f_{b11} = 184.5\text{Hz}$ .

- Figure 5.7 First stage coarse (a, b, c) and fine (d, e, f) inductance (frequency) tuning based on the maximisation of the electrical power absorbed by the shunt branches. (a, d) Amplitude, (b, e) first derivative, (c, f) second derivatives of the absorbed power with respect to the inductances implemented in the four branches. Thick vertical bands indicate the inductances (frequencies) where the fine frequency tuning is performed as shown in plots (d, e, f).
- Figure 5.8 Second stage fine (a, b, c) resistance tuning based on the maximisation of the electrical power absorbed by the shunt branches. (a) Amplitude, (b) first derivative, (c) second derivative of the absorbed electric power with respect to the resistances implemented in the four branches.
- Figure 5.9 Power spectral densities of the total flexural kinetic energy of the plate equipped with 1, 6, 12, 20, 35, 48 piezoelectric patches in open loop (solid blue lines) and connected to shunts with respectively 4, 7, 8, 8, 8, 8 branches (dashed red lines) whose RL elements are set in such a way as to maximize the electric power absorbed by the shunts (dotted black lines).
- Figure 5.10 Power spectral densities of the total flexural kinetic energy of the plate equipped with 48 piezoelectric patches in open loop (solid blue lines) and connected to shunts with 12 branches (dashed red lines) whose RL elements are set in such a way as to maximize the electric power absorbed by the shunts (dotted black lines).
- Figure 5.11 (a) Experimental setup. (b) Perspex box showing the five patches. (c) Hexagonal piezoelectric patch.
- Figure 5.12 (a) Electrical implementation of the synthetic shunt impedances in dSPACE platform. (b) An equivalent electrical circuit.
- Figure 5.13 Multi-resonant, current flowing shunt circuit
- Figure 5.14 (a) The flexural kinetic energy per unit force of the smart plate structure. (b) The electrical power absorbed by five identical shunts illustrated in plot (c).
- Figure 5.15 (a) The flexural kinetic energy per unit force (solid blue line - shunts in open loop; solid red line - optimal shunts) and power absorbed per unit force by five optimal shunts (dotted black line). (b) Configurations of the optimal multi-resonant shunt circuits.



---

## LIST OF TABLES

---

- |           |   |
|-----------|---|
| Table 2.1 | Physical and geometrical parameters of the beam and piezoelectric patches.  |
| Table 3.1 | Physical and geometrical parameters of the plate and piezoelectric patches. |
| Table 4.1 | Physical and geometrical parameters of the plate.                           |
| Table 5.1 | Physical and geometrical parameters of the plate.                           |
| Table 5.2 | Dimensions and physical properties of the panel and piezoelectric patches.  |



---

## NOMENCLATURE

---

### LIST OF ACRONYMS

RL	Resistive-inductive
RLC	Resistive-inductive-capacitive
PC	Phononic crystal
LR	Locally resonant
LRPC	Locally resonant phononic crystal
AM	Acoustic metamaterial
TVA	Tunable vibration absorber
PWE	Plane wave expansion
FEM	Finite element method
TM	Transfer matrix method
PSD	Power spectral density

### LIST OF SYMBOLS

$L_b$	Length of the finite beam element	[m]
$\rho_b$	Density of the beam material	[kg/m <sup>3</sup> ]
$\rho_p$	Density of the plate material	[kg/m <sup>3</sup> ]
$\rho_{pe}$	Density of the piezoelectric patch material	[kg/m <sup>3</sup> ]
$Y_b$	Young's modulus of the beam material	[N/m <sup>2</sup> ]
$Y_p$	Young's modulus of the plate material	[N/m <sup>2</sup> ]
$Y_{pe}$	Young's modulus of the piezoelectric material	[N/m <sup>2</sup> ]
$\nu_b$	Poisson's ratio for the beam material	—
$\nu_p$	Poisson's ratio for the plate material	—
$\nu_{pe}$	Poisson's ratio for the piezoelectric material	—
$\mathbf{D}, D_{ij}$	Electric displacement vector and coefficients	[C/m <sup>2</sup> ]
$\mathbf{E}, E_{ij}$	Electric field vector and coefficients	[V/m]
$\mathbf{T}, T_{ij}$	Stress vector and coefficients	[N/m <sup>2</sup> ]
$\mathbf{S}, S_{ij}$	Strain vector and coefficients	—
$C_{pe}$	Capacitance of the piezoelectric patch	[F]
$\mathbf{s}_{pe}, s_{pe\ ij}$	Compliance matrix and coefficients	[m <sup>2</sup> /N]

$d_{peij}$	Piezoelectric strain constants	$[m/V]$ $[C/N]$
$e_{peij}$	Piezoelectric stress constants	$[N/Vm]$ $[C/m^2]$
$t$	Time	$[s]$
$\omega$	Angular frequency	$[rad/s]$
$f$	Frequency	$[Hz]$

Symbol	Chapters 2-3	Chapters 4-5	Unit
$h_p$	Thickness of the finite plate element	Thickness of the plate	$[m]$
$h_{pe}$	Thickness of the finite piezoelectric patch element	Thickness of the piezoelectric patch	$[m]$
$A_p$	Area of the finite plate element	Area of the plate	$[m^2]$
$A_{pe}$	Area of finite piezoelectric patch element	Area of the piezoelectric patch	$[m^2]$
$V_p$	Volume of the finite plate element	Volume of the plate	$[m^3]$
$V_{pe}$	Volume of finite piezoelectric patch element	Volume of the piezoelectric patch	$[m^3]$



---

## INTRODUCTION

---

Mechanical vibrations arise from the dynamic response of mechanical systems subjected to impulsive, harmonic and stochastic excitations. Often, mechanical vibrations lead to undesired effects both, for the vibrating mechanical system itself as well as for people and the environment. In the worst case, excessive mechanical vibrations can cause fatigue phenomena that can damage or destroy a mechanical system or structure. Also, in few cases they can bring a direct danger to human life and to the environment. In general, vibrations of distributed flexible structures are effectively connected into sound or unwanted noise. In fact, a prolonged exposure to high levels of noise may have far-reaching consequences for human health [1]. Starting from annoyance and insomnia through cognitive impairment to permanent tinnitus and cardiovascular diseases. The sphere of human life is not the only one affected by the negative effects of mechanical vibrations and noise radiation. They are also present in many other fields, and in various branches of industry and technology, not excluding the most advanced sectors such as aerospace, space and semiconductor, where problems related to mechanical vibrations and noise have a specific economic dimension. For example, noise of the rocket boosters generates high level of mechanical vibrations in the fairing part, which can damage or even destroy the payload. In the semiconductor industry, the mapping of transistors and other electronic elements on the surface of a silicon wafer covered by photoresist takes place through a high precision lithography process, which can be jeopardised by vibrations of the base structure, the current resolution of this technology, the so-called half-pitch, or in other words half distance between two identical details reproduced on the surface of the photoresist, reaches about  $7 \cdot 10m^{-9}$ . With this in mind, it is not difficult to realize how even the smallest mechanical vibrations can be a serious problem in practical applications. Therefore, vibrations can have a direct impact on productivity, and thus affect share capital. Examples being closer to our everyday lives are mainly related to household goods, electro-mechanical tools or cars, where a consumer discomfort may result in a loss of the market share [1-3]. Finally, many countries have

legislated on the permissible vibration standards that workers in the industrial sectors may be subjected to. For example, in the European Union regulations on noise and vibrations are the Noise at Work Directive 2003/10/EC and the Human Vibration Directive 2002/44/EC, establishing a limit of 87 dB as a daily averaged dose of noise, and  $2.5 \frac{m}{s^2}$  of vibration magnitude for single action hand for maximum 8 hours daily, or  $5 \frac{m}{s^2}$  for whole body for no more than 8 hours daily.

All of these are just few examples of the problems which brought scientists to study and develop vibration and noise control systems and treatments.

## 1.1 MEANS OF VIBRATION TREATMENT

Over the years many techniques have been developed to control vibration of mechanical structures. Most often they are divided into three main categories depending on the use of an external power source, such as passive vibration control, active vibration control and an intermediate category, called semi-active vibration control.

### 1.1.1 *Passive vibration control*

Passive vibration control is based on modification of the physical parameters of a mechanical structure such as mass, stiffness or damping to improve its vibro-acoustic properties, i.e. making it less responsive to unwanted excitations [3]. These modifications can be provided in many ways, for example by adding to the structure elements in the form of masses and dynamic absorbers, which placed in the right locations, can effectively reduce vibrations. Also, batches of highly damped material can be used to reduce resonant response of structures. Finally, design optimization of the mechanical system itself may improve the response of a system by, for example, shifting the resonance frequencies away from excitation harmonies.

In general, passive vibration control performs very well at high frequencies but presents poor efficiency at low frequencies. The reason for this is that obtaining effective control of vibrations at low frequencies would require, bulky mass, stiffness and damping treatments that would considerably increase the structure mass or volume, making the whole solution impractical.

### *1.1.2 Active vibration control*

In contrast to passive solutions, active vibration control is most often well suited for low frequencies. In general, these systems are formed by vibration sensors and actuators connected via a single or multi-channel controller that implements either a feed forward or a feedback control architecture. Several types of actuators are used, such as electromechanical, electromagnetic or electro-pneumatic, whose task is to create a vibration that will cancel out those caused by external excitations. Active systems are composed of sensors that measure the vibration level of the structure, as well as the electronic system that processes information from the sensors and provides the appropriate control signal, which drives the actuator. Active systems are usually divided into two categories, namely feedforward and feedback systems. The first type relies on advance knowledge of the controlled disturbance, both when the disturbance is deterministic (i.e. tonal), or stochastic (i.e. stationary random noise) when there is a reference signal strongly correlated with the disturbance [4]. Based on this a-priori knowledge, feed-forward systems can deliver a secondary vibration control field with a similar amplitude but opposite phase to the primary one, to obtain a strong destructive interference effect. Active systems of this kind are also capable of adapting to changing conditions, if combined with an adaptive filter. In this case, an external signal is measured and sent to the adaptive filter.

Feedback vibration control is most often implemented when the excitation of the structure is not deterministic or cannot be directly observed. In general, in situations where there is no advance information on the primary disturbance, feedback control could be effectively implemented. Feedback vibration control systems are most often used to control structures whose frequency response is characterised by well separated resonance peaks of low order natural modes.

Beside numerous advantages, active vibration control also has its limitations, that include an additional power source, and therefore the ability to supply energy to a controlled system, which by itself may lead to instability or the so called spillover effect which is a phenomenon of strengthening of vibration levels at certain frequencies.

### 1.1.3 *Semi-active vibration control*

The third important approach for vibration treatment is the so called semi-active vibration control, which includes solutions at the interface between active and passive category. Semi-active control systems expand a small amount of energy to change system parameters, such as damping and stiffness to update or adapt to changes in working and environmental conditions that may affect the properties of the controlled structure. A spectacular example of systems comprised within this category are piezoelectric transducers connected to electrical shunting circuits, where electrical components of the circuit can be varied to obtain the desired effects of vibration control [5].

## 1.2 SHUNTED PIEZOELECTRIC TRANSDUCERS

The use of shunted piezoelectric patches has nowadays become a practical option for the reduction of vibrations in mechanical thin structures. Since their inception by Forward [7], many works have been carried out on this technology, investigating not only the underlying physics of piezoelectric shunts, but also exploring a variety of passive and active shunt circuits that would enhance the vibration absorption effects. Some of these works can be found in references [8-15]; but the initial concept of a tuned vibration absorber composed of a piezoelectric patch transducer connected to a resistance-inductance (RL) shunt is contained in the work by Hagood and von Flotow [5]. The operating principle of an RL shunted piezoelectric patch is like the one that characterise tuned spring-mass-damper vibration absorber [16]. In fact, the combination of the piezoelectric patch capacitance and shunt circuit resistance-inductance elements produce an equivalent of the tuned spring-mass-damper vibration absorption effect on the hosting structure via the piezoelectric transducer [17]. Therefore, Hagood and von Flotow [5] could employ the classical approach proposed by Den Hartog for tunable mechanical vibration absorbers [16] to optimally tune the resistance and inductance of the shunt circuit to reduce the resonant vibration of a mechanical system excited by a broad band disturbance. As can be found in Refs. [17-22], over the years several criteria have been proposed to tune the RL components of such a resonant shunt. In general, to effectively reduce the broad band vibration of the structure where the shunted piezoelectric patch is bonded, the inductance should be tuned in such a way as the shunt resonates at a frequency close to the resonance frequency of the target flexural mode of the hosting structure and

the resistance should then be fixed in such a way as to minimise the broad band vibration response of the hosting structure. Also, the smaller is the capacitance of the piezoelectric patch, the higher is the vibration absorption effect. Parallel and series RL networks are currently the most commonly used shunts to form piezoelectric vibration absorbers [5,15,23], although their performances are often enhanced by adding a synthetic negative capacitance to form a resistance-inductance-capacitance (RLC) shunt [17,24-42]. Indeed, a negative capacitance can be added to the RL elements to reduce the inherent capacitance of the piezoelectric patch and thus enhance the vibration absorption effect of the shunted piezoelectric patch [17]. In practice, this can only be accomplished with active electronic circuits and thus care must be taken in the parameters design to avoid instability problems.

### 1.2.1 Multi-resonating shunts

Research efforts have also been focused on the development of multi-resonant shunts [43-50], such that the shunted piezoelectric patch can effectively absorb flexural vibrations in correspondence of several resonance frequencies of the structure where it is bonded. Particularly noteworthy is the idea proposed by Behrens et al. [43], who, starting from the work of Hollkamp [44], developed the so called “current-flowing” shunt as a mean for simplifying the implementation of high order multi-resonant circuits. Indeed, in comparison to other configurations, this circuit is much simpler to implement since it requires a relatively smaller number of electrical components.



Figure 1.1 (a) Multi-resonant, current flowing shunt circuit. (b) Simplified current flowing shunt circuit.

Figure 1.1 shows the current flowing shunt circuit introduced by Behrens *et al.* [43], which is formed by  $N$ -RLC branches, where, each branch can be tuned in such a way as to absorb flexural vibrations of the structure at several frequencies. Considering the

shunt connected to the piezoelectric patch, the  $i$ -th branch is characterised by the series inductance  $L_{fi}$  and capacitance  $C_{fi}$  that create the so called current-flowing effect. These two components are tuned in such a way as to approximate a short circuit at the target resonance frequency of the flexural mode to be controlled by the branch and an open circuit at the resonance frequencies where the other branches of the shunt are tuned. In other words, the branch acts as a narrow band pass filter centred at the resonance frequency of the target flexural mode. The classical RL shunt vibration absorption effect from the target resonating flexural mode is then obtained by setting the additional inductance  $L_{si}$  and resistance  $R_{si}$  in such a way as to maximise the vibration energy absorption from the target resonant flexural mode of the hosting structure via the piezoelectric patch transducer. Therefore, assuming the capacitances  $C_{f1}, \dots, C_{fN}$  are fixed a priori, to obtain the narrow band filtering effects the inductances  $L_{f1}, \dots, L_{fN}$  are set equal to  $L_{f1} = \frac{1}{\omega_{r1}^2 C_{f1}}, L_{f2j} = \frac{1}{\omega_{r1}^2 C_{f2}}, \dots, L_{fNj} = \frac{1}{\omega_{rN}^2 C_{fN}}$ , where  $\omega_{r1}, \omega_{r2}, \dots, \omega_{rN}$  are the resonance frequencies of the target flexural modes of the hosting structure. Moreover, for the given capacitance  $C_{pe}$  of the piezoelectric patch, to obtain the tuned vibration absorption effects, the inductances  $L_{s1}, \dots, L_{sN}$  are set equal to:  $L_{s1} = \frac{1}{\omega_{r1}^2 C_{pe}}, L_{s2} = \frac{1}{\omega_{r2}^2 C_{pe}}, \dots, L_{sNj} = \frac{1}{\omega_{rN}^2 C_{pe}}$  whereas the resistances  $R_{s1}, \dots, R_{sN}$  can be tuned in such a way as to maximise the vibration energy absorption of the target flexural mode of the hosting structure. Since the two inductances in each branch are connected in series, as schematically shown in Figure 1.1 (b), they can be combined into a single inductance  $L_{bij}$ , which is given by:

$$L_{bij} = L_{fi} + L_{si} = \frac{1}{\omega_{ri}^2 C_{fi}} + \frac{1}{\omega_{ri}^2 C_{pe}} = \frac{C_{fi} + C_{pe}}{\omega_{ri}^2 C_{fi} C_{pe}}, \quad (1.1)$$

and can be used as an approximate inductance tuning formula for inductive elements of the branches. This is especially important because most of multi-resonant shunt circuits do not possess an analytical tuning formula. Due to this fact and to the simplicity of the circuit, which requires only two components to form a resonating branch, the current flowing shunt has been chosen to be exploited in this work.

### 1.3 MODERN PERIODIC STRUCTURES

Periodic structures can be described as assemblies of identical components (micro or macroscopic), also called unit cells, which are connected to each other with their ends or walls to form a whole structure. Rayleigh was the first to consider continuous periodic structures at the end of the nineteenth century, but the mathematical techniques needed to analyse wave propagation in periodic media became available during the first few decades of the twentieth century. During that time, Brillouin who was working on the propagation of electron waves in the crystal lattice, suggested that there should be frequency ranges over which the wave propagation is stopped [51]. These frequency ranges, called stop bands or band gaps, have been later confirmed experimentally and the concept was adopted in photonics. Photonic structures in the form of multiple layers of alternating materials with varying refractive index [52] became extensively used to manipulate light waves, and quickly inspired many inventions present in light emitting diodes and lasers, optical fiber tractions as well as in many sophisticated quantum devices [53].

In the next decades, following the pioneering work by Liu [54], the concepts developed for electromagnetism began to be strongly explored in the field of acoustic and elastic waves under a common name of phononic crystals (PC). Stop band phenomenon in both photonic and phononic crystals arise from the same oscillation interference mechanism called Bragg scattering, which occur due to the destructive interference between transmitted and reflected waves traveling through the periodic medium. In case of non-periodic and uniform structures, it is expected that the waves will propagate unaffected until they reach the boundary. However, when the medium possesses discontinuities, as for example in the form of density changes (phononic crystals) or interfaces between materials characterised by different refractive indexes (photonic crystals), the wave will be partially transmitted and partially reflected. Interactions between incident and reflected waves produce constructive and destructive interferences. Thus, periodically engineered discontinuities can indeed generate frequency bands in which the free wave propagation is stopped. These kinds of band gaps are generally known as Bragg gaps (BG) or interference stop bands, and the frequencies of their occurrence are linked to the length of the periodicity by the following relation:

$$f = n(v/2a) \quad \text{for } n = (1,2,3, \dots), \quad (1.2)$$

where  $v$  is the elastic velocity of the material structure and  $a$  is the periodicity length or the so-called lattice constant. The relationship between the Bragg gap frequency and the lattice constant makes stop bands of this kind difficult to obtain at low frequencies due to overall size of the structures.

A locally resonant (LR) mechanism is a way to overcome these difficulties. Resonant stop band effects can be obtained at frequencies two orders of magnitude lower than those limited by the Bragg scattering [55]. Solutions based on the local resonance effect are often called locally resonant phononic crystals (LRPC), or acoustic metamaterials (AM). These types of materials are often characterised by a periodic structure at a sub-wavelength scale, where each cell either contains or acts as a localised resonator [55]. Normally, this can be accomplished by a set of tunable vibration absorbers (TVAs) regularly distributed on a mechanical structure such as rods, beams or plates. It is known, that coupled systems of this kind can exhibit Fano scattering phenomenon, which manifests into asymmetric amplitudes of the coupled resonators responses [56]. The phenomenon itself was first described by Ugo Fano during his work on inelastic scattering of helium electrons [57], however due to the general wave nature of the phenomenon, is observed in many areas of physics. Fano's effect is a resonant scattering phenomenon that occurs through interference between the scattering effect of a hosting structure with the resonant scattering of the localised resonator. In classical vibro-acoustic applications coupled systems composed of a mechanical structure connected with spring-mass vibration absorbers can be employed to produce Fano's scattering. In this case, when the resonance frequency of the TVA corresponds to a resonance frequency of the hosting structure, the resonance peak of the hosting structure is modified into a pair of peaks of about the same amplitude that characterize the frequency response of the coupled system. The amplitude of the two peaks can then be lowered by the introduction of damping into the TVA.

Concepts of this type have been revised for many simple mechanical structures such as wires, beams, cylinders or plates [58-62] and can be further extended by using arrays of shunted piezoelectric patch vibration absorbers.

### *1.3.1 Mechanical structures with shunted arrays of piezoelectric patch transducers*

The regular arrays of piezoelectric patches mounted on structures and connected to electrical shunting circuits allow implementations of the wave propagation control strategies whose spatial periods significantly exceed the dimensions of the patches. The approach was first proposed by Thorp et al [98]. who used periodic array of RL shunted piezo-patches as the mean to create resonance band gaps at frequencies corresponding to resonance frequencies of the shunt circuits. Due to its tunable character, the concept became attractive and was quickly adopted to more complex mechanical structures such as fluid-loaded shells [99] and plates [80,100]. In these investigations, the authors showed how to utilise piezoelectric resonance shunts to affect the equivalent mechanical properties of hosting structures. This allowed for better understanding of the stop band generation at frequencies not associated with the Bragg scattering and classified structures with shunted piezoelectric arrays as one of potential forms of acoustic metamaterials. That is the vibro-acoustic materials whose properties resulting mainly from the properties of resonant compositional cells rather than the inherent material properties. Despite the periodic organization, which is often characteristic for these materials, the stop bands are no longer conditioned through the Bragg's law. Therefore, they provide an attractive opportunity for practical implementations of low-frequency wave attenuation, which is immensely important in the field of noise transmission and vibration control. For this reason, many theoretical and experimental works have been carried out in this field. Noteworthy are in particular the works of Casadei et al [80,100-102] as closely related to this dissertation, in which the authors conducted both, theoretical and experimental studies on the implementation of shunted piezoelectric arrays on plates. In these investigations, the finite element method was employed to build up a coupled (plate/piezoelectric patch/shunt circuit) mathematical model to predict the attenuation bands, which were then confirmed experimentally. Despite the good performance, systems of this kind are still facing some limitations. The required inductance of the shunts needed to produce the vibration absorption effect is very large [21,103]. Furthermore, the narrow bandwidth of the resonance effect allows to control only one mode in a low frequency range. For this purpose multi-resonant shunts were introduced but suffered by the lack of closed form tuning solutions and large number of components required for dense arrays [44, 104]. To overcome some of these difficulties the synthetic, multi-resonant, current flowing shunts are used in this work.

#### 1.4 OBJECTIVE OF THE THESIS

The main purpose of this dissertation is to investigate the low, mid and high-frequency control effects produced in one and two-dimensional structures equipped with periodic arrays of discrete masses, discrete vibration absorbers and shunted piezoelectric patch vibration absorbers.

#### 1.5 CONTRIBUTIONS OF THE THESIS

The principal contributions of the dissertation are the following

- Development of a fully coupled, finite element model of the metamaterial comprised by the Euler-Bernulli beam with one-dimensional grid of piezoelectric patch vibration absorbers connected to multi-resonant shunts for mid to high frequency wave propagation control.
- Development of a fully coupled, finite element model of the metamaterial plate with two-dimensional array of piezoelectric patch vibration absorbers connected to multi-resonant shunts for mid to high frequency wave propagation control.
- Analysis and characterisation of the stop band phenomena derived from the finite element models of the beam and plate with periodic arrays of piezoelectric patch vibration absorbers connected to the classical RL and multi-resonant shunt circuits.
- Extension of the studies of the stop-band phenomena to finite metamaterial plates equipped with shunted piezoelectric patch vibration absorbers.
- Development of a novel approach for the tuning of multi-resonant shunts connected to arrays of piezoelectric patches bonded on flexible structures, which is based on maximisation of the vibration absorption by each shunted patch through the measured electric power absorbed by each shunt.
- Experimental implementation of the proposed tuning approach, with a rig composed of a plate equipped with five piezoelectric patches, connected via an interface circuit to a dSPACE digital platform where the tuning algorithms of the multi-resonant shunts are implemented.

## 1.6 STRUCTURE OF THE THESIS

The first part of the thesis contained in Chapters 2 and 3 is focused on mid to high-frequency wave propagation control in beams and plates. Chapter 2 considers simplified model problems for the analysis of flexural wave propagation in an infinite Euler-Bernoulli beam. In particular, it devotes the characterisation of stop band phenomena produced by the one-dimensional grids of inclusions through scattering and locally resonant processes. Chapter 3 continues from the previous one, considering the more complex problem of wave propagation in an infinite plate. Also in this case, the investigation is focused on the analysis of stop band phenomena produced by the two-dimensional arrays of inclusions. Both chapters contain derivations of the fully coupled finite element models which allow to obtain dispersion properties of the considered periodic structures.

Chapter 4 supplements the simulation studies with the analysis of stop band phenomena in finite plates. It begins with the introduction of mobility-impedance and fully coupled modal models, which are then utilised to investigate the effects of periodic inclusions on vibration properties of finite plates.

In the second part of the thesis, summarised in Chapter 5, the study focuses on low-frequencies vibration control of a finite plate through regular arrays of RLC shunted piezoelectric patch transducers. In particular, a novel approach for the broadband flexural vibration control in a thin panel equipped with piezoelectric patch transducers connected to multi-resonant RLC shunts is proposed and investigated. A practical algorithm for the on-line tuning of the multi-resonant shunt circuit components is also presented. In the following sections Chapter 5 presents both simulation and experimental studies carried out to demonstrate the feasibility of the proposed tuning approach of multi-resonant shunts connected to piezoelectric patches, which are bonded on a thin rectangular plate.

The last chapter is a general summary of the conducted studies, where suggestions about the further work are also made.

---

## INFINITE BEAM WITH PERIODIC INCLUSIONS

---

This chapter presents the theoretical study on the wave propagation in one-dimensional infinite beam with the periodic cells delimited by the following inclusions: point masses, vibration absorbers and piezoelectric patch transducers connected to shunting circuits. The finite element method has been used to model the flexural wave propagation, whereas the governing equation of the beam cell composed of a number of beam segments were derived from Hamilton's principle for electro-mechanical systems. Finally, Bloch's theorem and the transfer matrix technique were employed to obtain the wave propagation constants and characterize stop band phenomena produced by the inclusions. The first section contains the derivation of the mathematical model for the flexural wave propagation in unit cell, while the second section presents implementations of inclusions and parametric studies on the stop band effects.

### 2.1 INTRODUCTION

The wave propagation in an infinite periodic structure can be regarded by the analysis of the response of a single unit cell [63-66]. A properly defined unit cell contains all the information needed to analyse wave propagation in the entire structure. Many methods can be applied to model a unit cell, among others the Plane Wave Expansion (PWE) and combination of the Finite Element Method (FE, FEM) and the Transfer Matrix method (TM) are often used in engineering. Most works on flexural vibration in beams, on longitudinal vibration in rods and wave propagation in one-dimensional solids reported in literature use one of these methods to obtain the wave propagation properties of the structures [63-70].

In the PWE method the material constants of an infinitely periodic unit cell are expanded as Fourier series. Given the propagation vector (i.e. wave direction and spatial period), the PWE method can be used calculate all natural of the periodic structure. In case of a high discrepancy between the physical properties of materials

contained in a unit cell, the method becomes inaccurate unless many Fourier components is employed to model the transition [71].

For the majority of practical systems, the partial differential equations describing the physical system cannot be solved with analytical methods. Instead discretized equations can be derived and solved. For instance, in the FE method a unit cell is discretized into a number of smaller, continuous structural elements, called finite elements. The elements are connected to each other at intersecting points known as nodes. When the compatibility of displacements is maintained at these points, the structure behaves as a single entity. In such framework the TM method can be conveniently applied to model wave propagation in structures composed of a number of identical unit cells. The TM method relies on the continuity of displacements and the force equilibrium across boundaries of sequential unit cells. With the knowledge of the displacement field at the beginning of a unit cell the TM technique allows to compute the field at the end of the unit cell from a simple matrix expression.

Due to the flexibility and ease of operation, the finite element method and the transfer matrix technique were selected for the studies presented in this chapter.

## 2.2 MODEL FORMULATION

In this section the finite element model is derived for a unit cell composed of a beam structure with a piezoelectric patch on top.

### 2.2.1 FEM discretization

The finite element discretization has been performed according to Ref. [72]. For the beam discretization, i.e. transformation of the infinite dimensional partial differential equation into an ordinary differential equation, the beam has been split into finite length elements as illustrated in Figure 2.1. Each beam element has two vertices with degrees of freedom on each side. Between these vertices, the displacement is interpolated by Hermite shape functions.

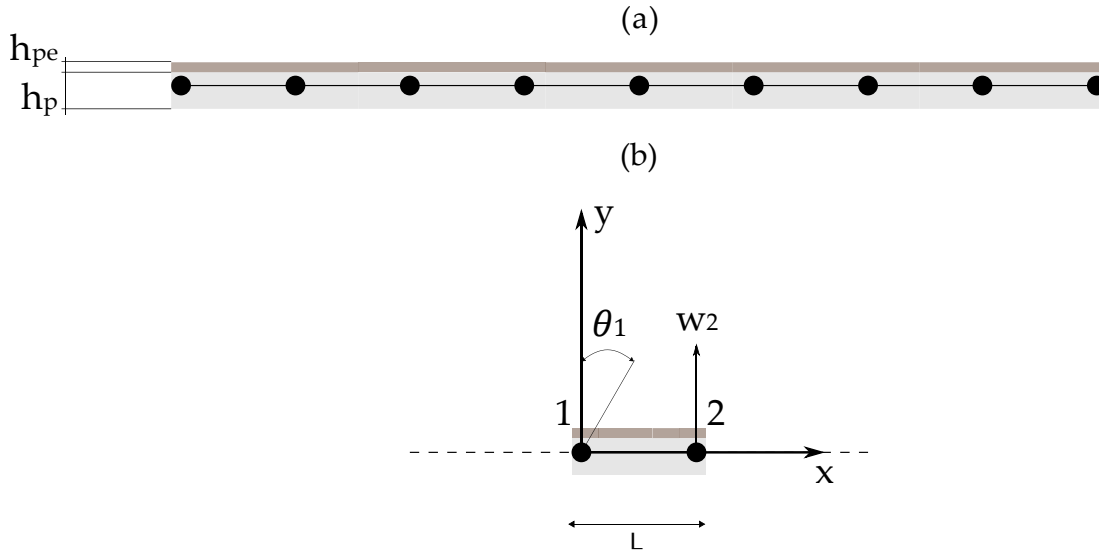


Figure 2.1 (a) Representation of an infinite Euler-Bernoulli beam, comprised by aluminum and piezoelectric ceramic. (b) An exemplary single finite element.

Considering the effect of flexural vibrations only, the transverse and axial displacements of a section of the beam are given by

$$w(x, y) = w(x), \quad (2.1)$$

$$u(x, y) = -y\theta = -y \frac{\partial w(x)}{\partial x}. \quad (2.2)$$

Where,  $w$  accounts for the displacements (also called deflections) perpendicular to the beam and  $u$  for the displacements in  $x$  direction.

The bending strain relation is given by

$$S = \frac{\partial u(x, y)}{\partial x} = -y \frac{\partial^2 w(x)}{\partial x^2}. \quad (2.3)$$

Since the beam is not excited in the  $y$  and  $z$  directions, the bending stress is given by

$$T = Y_b S. \quad (2.4)$$

Where  $Y_b$  is the Young's modulus of the beam material.

Every beam element has two nodes with two degrees of freedom at each node: displacement in perpendicular direction to the beam normal and rotation (i.e. cross section rotation), thus the following nodal displacement vector can be defined

$$\mathbf{d}_i = \begin{bmatrix} w_i \\ \theta_i \end{bmatrix}, \quad (2.5)$$

where  $i = 1, 2$ .

A nodal displacement can then be defined for the two nodes of the element

$$\mathbf{d}_e = \begin{bmatrix} \mathbf{d}_1 \\ \mathbf{d}_2 \end{bmatrix} = \begin{bmatrix} w_1 \\ \theta_1 \\ w_2 \\ \theta_2 \end{bmatrix} \quad (2.6)$$

The Hermite shape functions can be used to define the element displacement with reference to the nodal displacements:

$$w = \mathbf{N}\mathbf{d}_e, \quad (2.7)$$

where  $\mathbf{N}$  contains the shape functions

$$\mathbf{N} = \begin{bmatrix} \frac{1}{L_b^3}(2x^3 - 3L_b x^2 + L_b^3) \\ \frac{1}{L_b^2}(x^3 - 2L_b x^2 + L_b^2 x) \\ \frac{1}{L_b^3}(-2x^3 + 3L_b x^2) \\ \frac{1}{L_b^2}(x^3 - L_b x^2) \end{bmatrix}^T \quad (2.8)$$

Substitution of Eq. (2.7) into Eq. (1.1) gives the following strain-displacement relation

$$S = -y \frac{\partial^2}{\partial x^2} \mathbf{N}\mathbf{d}_e, \quad (2.9)$$

which can be written as

$$S = -\frac{y}{L_b^3} \mathbf{B}_K \mathbf{d}_e, \quad (2.10)$$

where

$$\mathbf{B}_K = [12x - 6L_b \quad 6L_b x - 4L_b^2 \quad -12x + 6L_b \quad 6L_b x - 2L_b^2]. \quad (2.11)$$

Substituting Eq. (2.10) to Eq. (2.4) yields

$$T = Y_b \frac{y}{L_b^3} \mathbf{B}_K \mathbf{d}_e. \quad (2.12)$$

### 2.2.2 Piezoelectric transducer

Piezoelectric phenomena are characterised by the following linear constitutive relations:

$$T = -e_{pe} E_{pe} + c_{pe}^E S, \quad (2.13)$$

$$D_{pe} = \epsilon_{pe}^S E_{pe} + e_{pe}^T S. \quad (2.14)$$

Here,  $E_{pe} = E_3$  and  $D_{pe} = D_3$  are the electric field and electric displacement components in the direction 3, respectively. Also,  $e_{pe}$  is the stress / charge constants defined as

$$e_{pe} = e_{31} . \quad (2.15)$$

Moreover, the elastic constant of the piezoelectric material under constant electric field ( $E = 0$ ) is given by

$$c_{pe}^E = Y_{pe}^E , \quad (2.16)$$

where,  $Y_{pe}^E$  denotes the Young's modulus of the piezoelectric material measured at constant field intensity. Finally,  $\varepsilon_{pe}^S = \varepsilon_{33}^S$  is the piezoelectric material permittivity in transverse direction under constant strain ( $S = 0$ ).

Note, that normally parameters  $e_{31}$  and  $\varepsilon_{33}^S$  are not available in commercial datasheets of piezoelectric transducers, thus they need to be derived from the governing equations expressed in the following form:

$$S = d_{pe}E_{pe} + s_{pe}^E T , \quad (2.17)$$

$$D_{pe} = \varepsilon_{pe}^T E_{pe} + d_{pe} T . \quad (2.18)$$

Here  $d_{pe}$  is the piezoelectric strain / charge constant

$$d_{pe} = d_{31} , \quad (2.19)$$

and  $s_{pe}^E$  is the compliance constant for the piezoelectric material

$$s_{pe}^E = \frac{1}{Y_{pe}^E} . \quad (2.20)$$

Finally,  $\varepsilon_{pe}^T$  is the permittivity of piezoelectric material in transverse direction under constant stress ( $T = 0$ ).

The value of the piezoelectric material permittivity under constant strain  $\varepsilon_{pe}^S$  and the value of  $e_{pe}$  can be now obtain by setting the stress  $T$  to zero in Eqs. (2.13), (2.14), (2.17) and (2.18).

$$0 = -e_{pe}E_{pe} + c_{pe}^E S , \quad (2.21)$$

$$D_{pe} = \varepsilon_{pe}^S E_{pe} + e_{pe} S , \quad (2.22)$$

$$S = d_{pe}E_{pe} , \quad (2.23)$$

$$D_{pe} = \varepsilon_{pe}^T E_{pe} . \quad (2.24)$$

Substituting Eq. (2.23) to (2.21) yields

$$e_{pe} = c_{pe}^E d_{pe} , \quad (2.25)$$

also substituting Eqs. (2.23), (2.24) and (2.25) to Eq. (2.22) gives

$$\varepsilon_{pe}^S = \varepsilon_{pe}^T (1 - k^2) , \quad (2.26)$$

where,  $k$  denotes the electromechanical coupling coefficient [15,73] of the piezoelectric material and can be defined as

$$k^2 = \frac{e_{pe} c_{pe}^E d_{pe}}{\varepsilon_{pe}^T} . \quad (2.27)$$

Application of a potential difference to the electrodes forces the piezoelectric material to expand such that the upper layer of the beam contracts. This results in a curvature of the beam. The inverse effect will generate a charge across the electrodes, which is collected through the surface of the electrodes as a voltage. Considering a transverse poling direction, the applied or induced voltage through the piezoelectric transducer is given by the following relation [74].

$$v_{pey} = \frac{\left(y - \frac{h_b}{2}\right)}{h_{pe}} v_{pe} , \quad (2.28)$$

where  $h_b$  and  $h_{pe}$  are thicknesses of the beam and piezoelectric patch respectively and  $v_{pe}$  is the maximum electric potential at the external surfaces of the piezoelectric layer, while  $y$  is defined as

$$\frac{h_b}{2} \leq y \leq \frac{h_b}{2} + h_{pe} . \quad (2.29)$$

Assuming the electric field to be constant through the piezoelectric transducer, the following relation can be written

$$E_{pe} = -\frac{\partial v_{pey}}{\partial y} = -\frac{v_{pe}}{h_{pe}} . \quad (2.30)$$

### 2.2.3 Hamilton's principle

Hamilton's principle is employed here to derive the governing equations of a beam element [73, 88, 89]. The Lagrangian for electro-mechanical system is defined as

$$L = T^* - V + W_e^* , \quad (2.31)$$

where  $T^*$  is the kinetic co-energy,  $V$  is the elastic potential energy and  $W_e^*$  is the work done by electrical forces.

Hamilton's principle states that

$$\int_{t_1}^{t_2} [\delta L + \delta W_{nc}] dt = 0 . \quad (2.32)$$

Where  $\delta$  is the variation operator and  $\delta W_{nc}$  stands for the work done by non-conservative forces.

The kinetic energy due to transverse motion in the of the beam is given by

$$T^* = \frac{1}{2} \int_{V_b} \rho_b \dot{w}^2 dV_b + \frac{1}{2} \int_{V_{pe}} \rho_{pe} \dot{w}^2 dV_{pe} . \quad (2.33)$$

Here,

$$dV_b = \int_0^{h_p} \int_0^b \int_0^{L_b} dx dy dz , \quad (2.34)$$

$$dV_{pe} = \int_{h_p}^{h_p+h_{pe}} \int_0^b \int_0^{L_{pe}} dx dy dz , \quad (2.35)$$

Only thin beams are considered in this study; thus, the rotatory inertia is neglected.

The strain energy of the beam due to bending is given by

$$V = \frac{1}{2} \int_{V_b} ST dV_b + \frac{1}{2} \int_{V_{pe}} ST dV_{pe} . \quad (2.36)$$

The work done by electrical forces and the work done by non-conservative forces is defined as

$$W_e^* = \frac{1}{2} \int_{V_{pe}} E_{pe} D_{pe} dV_{pe} , \quad (2.37)$$

$$W_{nc} = \int_0^{L_b} w \mathbf{f}_x dx - \int_{A_{pe}} \sigma v_{pe} A_{pe} . \quad (2.38)$$

Here,  $\mathbf{f}_x$  is uncorrelated transverse force excitation per unit length,  $\sigma$  is the surface charge density at the electrodes of the piezoelectric transducer.

Substituting Eq. (2.4) and (2.14) into Eq. (2.36) results in

$$V = \frac{1}{2} \int_{V_b} S^2 Y_b dV_b + \frac{1}{2} \int_{V_{pe}} S^2 Y_{pe}^E dV_{pe} - \frac{1}{2} \int_{V_{pe}} S e_{pe} E_{pe} dV_{pe} . \quad (2.39)$$

Then, substituting into Eqs. (2.13) and (2.14) to Eq. (2.37) yields

$$W_e^* = \frac{1}{2} \int_{V_{pe}} E_{pe} \epsilon_{pe}^S E_{pe} dV_{pe} + \frac{1}{2} \int_{V_{pe}} E_{pe} e_{pe} S dV_{pe} \quad (2.40)$$

#### 2.2.4 Variation indicator

The variations of the Lagrangian and the work done by the non-conservative forces can be calculated by using exact differentiation summarised in the following expressions for the functions used in Hamilton's principle.

$$\delta L = \frac{\partial L}{\partial \dot{w}} \delta \dot{w} + \frac{\partial L}{\partial S} \delta S + \frac{\partial L}{\partial E_{pe}} \delta E_{pe} , \quad (2.41)$$

$$\delta W_{nc} = \frac{\partial W_{nc}}{\partial w} \delta w + \frac{\partial W_{nc}}{\partial v_{pe}} \delta v_{pe} . \quad (2.42)$$

$$\delta T^* = \frac{\partial T^*}{\partial \dot{w}} \delta \dot{w} + \frac{\partial T^*}{\partial S} \delta S + \frac{\partial T^*}{\partial E_{pe}} \delta E_{pe} , \quad (2.43)$$

$$\delta V = \frac{\partial V}{\partial \dot{w}} \delta \dot{w} + \frac{\partial V}{\partial S} \delta S + \frac{\partial V}{\partial E_{pe}} \delta E_{pe} , \quad (2.44)$$

$$\delta W_e^* = \frac{\partial W_e^*}{\partial \dot{w}} \delta \dot{w} + \frac{\partial W_e^*}{\partial S} \delta S + \frac{\partial W_e^*}{\partial E_{pe}} \delta E_{pe} , \quad (2.45)$$

After some mathematical manipulations Eqs. (2.42)-(2.45) give the following expressions:

$$\frac{\partial W_{nc}}{\partial w} \delta w = \int_0^{L_b} \delta w f_x dx , \quad (2.46)$$

$$\frac{\partial W_{nc}}{\partial v_{pe}} \delta v_{pe} = - \int_{A_{pe}} \sigma \delta v_{pe} A_{pe} , \quad (2.47)$$

$$\frac{\partial T^*}{\partial \dot{w}} \delta \dot{w} = \int_{V_b} \rho_p \delta \dot{w} \dot{w} dV_b + \int_{V_{pe}} \rho_{pe} \delta \dot{w} \dot{w} dV_{pe} , \quad (2.48)$$

$$\frac{\partial T^*}{\partial S} \delta S = 0 , \quad (2.49)$$

$$\frac{\partial T^*}{\partial E_{pe}} \delta E_{pe} = 0 , \quad (2.50)$$

$$\frac{\partial V}{\partial \dot{w}} \delta \dot{w} = 0 , \quad (2.51)$$

$$\frac{\partial V}{\partial S} \delta S = \int_{V_b} \delta S Y_b S dV_b + \int_{V_{pe}} \delta S Y_{pe}^E S dV_{pe} - \frac{1}{2} \int_{V_{pe}} \delta S e_{pe} E_{pe} dV_{pe} , \quad (2.52)$$

$$\frac{\partial V}{\partial E_{pe}} \delta E_{pe} = -\frac{1}{2} \int_{V_{pe}} S e_{pe} \delta E_{pe} dV_{pe} , \quad (2.53)$$

$$\frac{\partial W_e^*}{\partial \dot{w}} \delta \dot{w} = 0 , \quad (2.54)$$

$$\frac{\partial W_e^*}{\partial S} \delta S = \frac{1}{2} \int_{V_{pe}} E_{pe} e_{pe} \delta S dV_{pe} , \quad (2.55)$$

$$\frac{\partial W_e^*}{\partial E_{pe}} \delta E_{pe} = \int_{V_{pe}} \delta E_{pe} \varepsilon_{pe}^S E_{pe} dV_{pe} + \frac{1}{2} \int_{V_{pe}} \delta E_{pe} e_{pe} S dV_{pe} . \quad (2.56)$$

Variation of the Lagrangian is the sum of all terms from Eq. (2.46) to (2.56):

$$\begin{aligned} & \int_{t_1}^{t_2} \left[ \int_{V_b} \rho_p \delta \dot{w} \dot{w} dV_b + \int_{V_{pe}} \rho_{pe} \delta \dot{w} \dot{w} dV_{pe} - \int_{V_b} \delta SY_b S dV_b - \right. \\ & - \int_{V_{pe}} \delta SY_{pe}^E S dV_{pe} + \frac{1}{2} \int_{V_{pe}} \delta S e_{pe} E_{pe} dV_{pe} + \frac{1}{2} \int_{V_{pe}} S e_{pe} \delta E_{pe} dV_{pe} + \\ & + \frac{1}{2} \int_{V_{pe}} E_{pe} e_{pe}^T \delta S dV_{pe} + \int_{V_{pe}} \delta E_{pe} \varepsilon_{pe}^S E_{pe} dV_{pe} + \frac{1}{2} \int_{V_{pe}} \delta E_{pe} e_{pe}^T S dV_{pe} + \\ & \left. + \int_0^{L_b} \delta w \mathbf{f}_x dx - \int_{A_{pe}} \sigma \delta v_{pe} dA_{pe} \right] dt = 0 . \end{aligned} \quad (2.57)$$

The integral equation can be simplified as follow

$$\begin{aligned} & \int_{t_1}^{t_2} \left[ \int_{V_b} \rho_p \delta \dot{w} \dot{w} dV_b + \int_{V_{pe}} \rho_{pe} \delta \dot{w} \dot{w} dV_{pe} - \int_{V_b} \delta SY_b S dV_b + \right. \\ & + \int_{V_{pe}} (\delta S e_{pe} E_{pe} - \delta SY_{pe}^E S + \delta E_{pe} \varepsilon_{pe}^S E_{pe} + \delta E_{pe} e_{pe} S) dV_{pe} + \\ & \left. + \int_0^{L_b} \delta w \mathbf{f} dx - \int_{A_{pe}} \sigma \delta v_{pe} dA_{pe} \right] dt = 0 . \end{aligned} \quad (2.58)$$

Then, integration by parts of the first two terms yields

$$\begin{aligned} & \int_{t_1}^{t_2} \left[ - \int_{V_b} \rho_b \delta w \ddot{w} dV_b - \int_{V_{pe}} \rho_{pe} \delta w \ddot{w} dV_{pe} - \int_{V_b} \delta SY_b S dV_b + \right. \\ & + \int_{V_{pe}} (\delta S e_{pe} E_{pe} - \delta SY_{pe}^E S + \delta E_{pe} \varepsilon_{pe}^S E_{pe} + \delta E_{pe} e_{pe}^T S) dV_{pe} + \\ & \left. + \int_0^{L_b} \delta w \mathbf{f}_x dx - \int_{A_{pe}} \sigma \delta v_{pe} dA_{pe} \right] dt = 0 , \end{aligned} \quad (2.59)$$

and

$$\begin{aligned} & \int_{t_1}^{t_2} \left[ - \int_{V_b} (\rho_b \delta w \ddot{w} + \delta SY_b S) dV_b + \int_{V_{pe}} (\delta S e_{pe} E_{pe} - \delta SY_{pe}^E S + \right. \\ & + \delta E_{pe} \varepsilon_{pe}^S E_{pe} + \delta E_{pe} e_{pe}^T S - \rho_{pe} \delta w \ddot{w}) dV_{pe} + \\ & \left. + \int_0^{L_b} \delta w \mathbf{f}_x dx - \int_{A_{pe}} \sigma \delta v_{pe} dA_{pe} \right] dt = 0 . \end{aligned} \quad (2.60)$$

Substituting Eqs.(2.7), (2.10), (2.12) to Eq. (2.59)

$$\int_{t_1}^{t_2} \left[ - \int_{V_b} \delta \mathbf{d}_e^T \left( \rho_b \mathbf{N}^T \mathbf{N} \dot{\mathbf{d}}_e + \mathbf{B}_K^T \frac{\gamma^2}{L_b^6} Y_b \mathbf{B}_K \mathbf{d}_e \right) dV_b + \right. \quad (2.61)$$

$$\begin{aligned}
& + \int_{V_{pe}} \delta \mathbf{d}_e^T \left( \mathbf{B}_K^T \frac{y}{h_{pe} L_b^3} \mathbf{e}_{pe} v_{pe} - \mathbf{B}_K^T \frac{y^2}{L_b^6} Y_{pe}^E \mathbf{B}_K \mathbf{d}_e - \mathbf{N}^T \mathbf{N} \ddot{\mathbf{d}}_e \right) dV_{pe} + \\
& + \int_{V_{pe}} \delta v_{pe} \left( \frac{y}{h_{pe} L_b^3} \mathbf{e}_{pe}^T \mathbf{B}_K \mathbf{d}_e + \frac{1}{h_{pe}^2} \varepsilon_{pe}^S v_{pe} \right) dV_{pe} - \\
& - \int_{A_{pe}} \delta v_{pe} \sigma dA_{pe} \int_0^{L_b} \delta \mathbf{d}_e^T \mathbf{f}_x dx \Big] dt = 0
\end{aligned}$$

Expression (2.32) can be now rewritten as

$$\begin{aligned}
& \int_{t_1}^{t_2} \{ \delta \mathbf{d}_k^T [ (\mathbf{M}_b + \mathbf{M}_{pe}) \ddot{\mathbf{d}}_k + (\mathbf{K}_b + \mathbf{K}_{pe}) \mathbf{d}_k + \boldsymbol{\theta}_{pe} v_{pe} - \mathbf{f} ] + \\
& + \delta v_{pe} [ \boldsymbol{\theta}_{pe}^T \mathbf{d}_k + C_{pe} v_{pe} + q ] \} dt = 0 ,
\end{aligned} \tag{2.62}$$

where,

$$\mathbf{M}_b = \rho_p \int_{V_b} \mathbf{N}^T \mathbf{N} dV_b \tag{2.63}$$

$$\mathbf{M}_{pe} = \rho_{pe} \int_{V_{pe}} \mathbf{N}^T \mathbf{N} dV_{pe} , \tag{2.64}$$

$$\mathbf{K}_b = \int_{V_b} \mathbf{B}_K^T \frac{y^2}{L_b^6} Y_b \mathbf{B}_K dV_b , \tag{2.65}$$

$$\mathbf{K}_{pe} = \int_{V_{pe}} \mathbf{B}_K^T \frac{y^2}{L_b^6} Y_{pe}^E \mathbf{B}_K dV_{pe} , \tag{2.66}$$

$$\boldsymbol{\theta}_{pe} = - \int_{V_{pe}} \mathbf{B}_K^T \frac{y}{L_b^3} \mathbf{e}_{pe} dV_{pe} , \tag{2.67}$$

$$C_{pe} = \int_{V_{pe}} \frac{1}{h_{pe}^2} \varepsilon_{pe}^S dV_{pe} , \tag{2.68}$$

$$q = \int_{A_{pe}} \sigma A_{pe} . \tag{2.69}$$

$$\mathbf{f} = \int_0^{L_b} \mathbf{f}_x dx . \tag{2.70}$$

Breaking volume integrals into products of integrals over length and area gives:

$$\mathbf{M}_p = \rho_p A_b \int_0^{L_b} \mathbf{N}^T \mathbf{N} dV_b , \tag{2.71}$$

$$\mathbf{M}_{pe} = \rho_{pe} A_{pe} \int_0^{L_b} \mathbf{N}^T \mathbf{N} dV_{pe} , \tag{2.72}$$

$$\mathbf{K}_p = \frac{I_b}{L_b^6} Y_b \int_0^{L_b} \mathbf{B}_K^T \mathbf{B}_K dV_b , \tag{2.73}$$

$$\mathbf{K}_{pe} = \frac{I_b}{L_b^6} Y_{pe}^E \int_0^{L_b} \mathbf{B}_K^T \mathbf{B}_K dV_{pe} , \tag{2.74}$$

$$\boldsymbol{\theta}_{pe} = -\frac{h_p+h_{pe}}{2L_b^3} b_{pe} \int_{V_{pe}} \mathbf{B}_K^T \mathbf{e}_{pe} dV_{pe} , \quad (2.75)$$

$$C_{pe} = \int_{V_{pe}} \frac{1}{h_{pe}^2} \varepsilon_{pe}^S dV_{pe} = \frac{A_{pe} \varepsilon_{pe}^S}{h_{pe}} , \quad (2.76)$$

$$q = \int_{A_{pe}} \sigma A_{pe} , \quad (2.77)$$

$$\mathbf{f} = \int_0^{L_b} \mathbf{f}_x dx . \quad (2.78)$$

Allowing arbitrary variations of  $\mathbf{d}_e$  and  $v_{pe}$ , governing matrix equations can be written for  $k$ -th element as follows:

$$(\mathbf{M}_b + \mathbf{M}_{pe}) \ddot{\mathbf{d}}_k + (\mathbf{K}_b + \mathbf{K}_{pe}) \mathbf{d}_k + \boldsymbol{\theta}_{pe} v_{pe} = \mathbf{f} , \quad (2.79)$$

$$\boldsymbol{\theta}_{pe}^T \mathbf{d}_k + C_{pe} v_{pe} = q . \quad (2.80)$$

### 2.3 WAVE PROPAGATION IN ONE-DIMENSIONAL PERIODIC BEAM

The most suitable way to characterize wave propagation in one-dimensional periodic media is through the so-called propagation constant:

$$\mu = \delta + i\epsilon , \quad (2.81)$$

which is a measure of wave attenuation and phase delay across a unit cell length. In general, the propagation constant  $\mu$  is a complex term, where the real part, also known as attenuation constant  $\delta$ , represents the attenuation of the wave amplitude through a unit cell, while the imaginary part  $\epsilon$ , also called phase constant, represents the phase delay the propagating wave builds up through a cell.

The transfer matrix technique can be conveniently employed to obtain complex propagation constants for one-dimensional media. To implement this method, a matrix relation between forces and displacements at both ends of a unit cell is required. Since the neighbouring cells are connected in sequence, the resulting total transfer matrix through a structure is a product of the single transfer matrix through a unit cell. In periodic structures a unit cell repeats unchanged indefinitely, thus the study of a unit cell transfer matrix is enough to describe the behaviour of a whole structure. An eigenvalue problem can then be defined and solved to obtain complex propagation constants [63-66] and that characterize the wave propagation.

The material and geometrical properties of the beam used for the investigations contained in this chapter are summarized in Table 2.1.

Table 2.1. Physical and geometrical parameters of the beam and piezoelectric patches.

Parameter	Plate	Piezoelectric patch
thickness	$h_p = 1 \text{ mm}$	$h_{pe} = 1 \text{ mm}$
length	$L_b = 10 \text{ cm}$	$L_{pe} = 3.33 \text{ cm}$
density	$\rho_b = 2700 \text{ kg/m}^3$	$\rho_{pe} = 7600 \text{ kg/m}^3$
Young's modulus	$Y_p = 7 \times 10^{10} \text{ N/m}^2$	$Y_{pe} = 2.7 \times 10^{10} \text{ N/m}^2$
Poisson's ratio	$\nu_p = 0.33$	$\nu_{pe} = 0.275$
strain / charge constants		$d_{31}^0 = 150 \times 10^{-12} \text{ m/V}$ $d_{32}^0 = 150 \times 10^{-12} \text{ m/V}$ $d_{36}^0 = 0$
permittivity		$\epsilon_{pe} = 84 \times 10^{-9} \text{ F/m}$
capacitance		$C_{pe} = 3.167 \times 10^{-9} \text{ F}$
lattice constant	$L_{cell} = 10 \text{ cm}$	

### 2.3.1 Infinite beam with no inclusions

To start with, since the structure is uniform and possesses no inclusions, the elementary unit cell can be defined by an arbitrarily chosen section of the beam, comprising a finite number of finite elements as depicted in Figure 2.2.

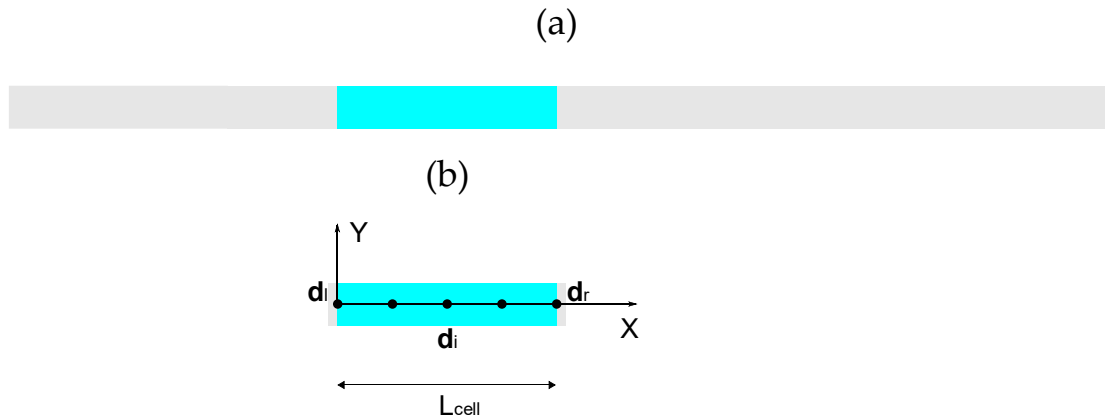


Figure 2.2 (a) Depiction of an infinite, uniform Euler-Bernoulli beam. (b) An exemplary meshed unit cell.

The equation of motion of the unit cell of a one-dimensional infinite beam composed of  $n$  finite elements is given by

$$\mathbf{M}_b \ddot{\mathbf{d}} + \mathbf{K}_b \mathbf{d} = \mathbf{f}, \quad (2.82)$$

where  $\mathbf{M}_b$  and  $\mathbf{K}_b$  are the global mass and the global stiffness matrices of the unit cell. They are assembled from the stiffness and mass matrices of the beam elements obtained by the finite element method,  $\mathbf{d} = [\mathbf{d}_i \ \mathbf{d}_l \ \mathbf{d}_r]^T$  is the vector of the all nodal degrees of freedom, and  $\mathbf{f} = [\mathbf{f}_i \ \mathbf{f}_l \ \mathbf{f}_r]^T$  is the vector of the cell nodal forces, indexes  $i, l$  and  $r$  indicate the inner, the left and the right nodes of the unit cell. Assuming harmonic motion at frequency  $\omega$  Eq. (2.82) can be rewritten as

$$(\mathbf{K}_b - \omega^2 \mathbf{M}_b) \mathbf{d} = \mathbf{f}, \quad (2.83)$$

where  $(\mathbf{K}_b - \omega^2 \mathbf{M}_b)$  is the dynamic stiffness matrix of the unit cell assembled in the following manner

$$\mathbf{D} = \begin{bmatrix} \mathbf{D}_{ii} & \mathbf{D}_{il} & \mathbf{D}_{ir} \\ \mathbf{D}_{li} & \mathbf{D}_{ll} & \mathbf{D}_{lr} \\ \mathbf{D}_{ri} & \mathbf{D}_{rl} & \mathbf{D}_{rr} \end{bmatrix}. \quad (2.84)$$

Expressing the matrix equation of motion in term of dynamic stiffness yields

$$\begin{bmatrix} \mathbf{D}_{ii} & \mathbf{D}_{il} & \mathbf{D}_{ir} \\ \mathbf{D}_{li} & \mathbf{D}_{ll} & \mathbf{D}_{lr} \\ \mathbf{D}_{ri} & \mathbf{D}_{rl} & \mathbf{D}_{rr} \end{bmatrix} \begin{bmatrix} \mathbf{d}_i \\ \mathbf{d}_l \\ \mathbf{d}_r \end{bmatrix} = \begin{bmatrix} \mathbf{f}_i \\ \mathbf{f}_l \\ \mathbf{f}_r \end{bmatrix}. \quad (2.85)$$

Assuming no external forces are exerted at internal nodes  $\mathbf{f}_i = 0$ , the inner degrees of freedom can be eliminated through the first row of Eq. (2.85)

$$\mathbf{d}_i = \mathbf{D}_{ii}^{-1} (\mathbf{D}_{il} \mathbf{d}_l + \mathbf{D}_{ir} \mathbf{d}_r). \quad (2.86)$$

Substitution of Eq. (2.86) back to Eq. (2.85) yields

$$\begin{bmatrix} \boldsymbol{\alpha}_{ll} & \boldsymbol{\alpha}_{lr} \\ \boldsymbol{\alpha}_{rl} & \boldsymbol{\alpha}_{rr} \end{bmatrix} \begin{bmatrix} \mathbf{d}_l \\ \mathbf{d}_r \end{bmatrix} = \begin{bmatrix} \mathbf{f}_l \\ \mathbf{f}_r \end{bmatrix}, \quad (2.87)$$

where matrices  $\boldsymbol{\alpha}$  are can be calculated from

$$\boldsymbol{\alpha}_{ll} = \mathbf{D}_{ll} - \mathbf{D}_{li} \mathbf{D}_{ii}^{-1} \mathbf{D}_{il}, \quad (2.88)$$

$$\boldsymbol{\alpha}_{lr} = \mathbf{D}_{rl} - \mathbf{D}_{ri} \mathbf{D}_{ii}^{-1} \mathbf{D}_{il}, \quad (2.89)$$

$$\boldsymbol{\alpha}_{rl} = \mathbf{D}_{lr} - \mathbf{D}_{li} \mathbf{D}_{ii}^{-1} \mathbf{D}_{ir}, \quad (2.90)$$

$$\boldsymbol{\alpha}_{rr} = \mathbf{D}_{rr} - \mathbf{D}_{ri} \mathbf{D}_{ii}^{-1} \mathbf{D}_{ir}. \quad (2.91)$$

The continuity of displacements and force equilibrium at the boundaries of the unit cells are defined by the following relations

$$\mathbf{d}_l(n+1) = \mathbf{d}_r(n), \quad (2.92)$$

$$\mathbf{f}_l(n+1) = -\mathbf{f}_r(n). \quad (2.93)$$

The state vectors composed of degrees of freedom and forces on the left-hand side of adjacent unit cells can be now introduced

$$\mathbf{u}_l(n) = \begin{bmatrix} \mathbf{d}_l(n) \\ \mathbf{f}_l(n) \end{bmatrix}, \quad (2.94)$$

$$\mathbf{u}_l(n+1) = \begin{bmatrix} \mathbf{d}_l(n+1) \\ \mathbf{f}_l(n+1) \end{bmatrix}. \quad (2.95)$$

By considering the boundary conditions from Eqs. (2.92), (2.93), Eq. (2.97) turns into

$$\mathbf{u}_l(n+1) = \begin{bmatrix} \mathbf{d}_r(n) \\ -\mathbf{f}_r(n) \end{bmatrix}. \quad (2.96)$$

Eq. (2.87) can be now reformulated in terms of the state vectors  $\mathbf{u}_l$  as

$$\begin{bmatrix} \mathbf{d}_r(n) \\ -\mathbf{f}_r(n) \end{bmatrix} = \mathbf{T} \begin{bmatrix} \mathbf{d}_l(n) \\ \mathbf{f}_l(n) \end{bmatrix}, \quad (2.97)$$

where the transfer matrix  $\mathbf{T}$  is given by

$$\mathbf{T} = \begin{bmatrix} -\alpha_{lr}^{-1} \alpha_{ll} & \alpha_{lr}^{-1} \\ -\alpha_{rl} + \alpha_{rr} \alpha_{lr}^{-1} \alpha_{ll} & -\alpha_{rr} \alpha_{lr}^{-1} \end{bmatrix}. \quad (2.98)$$

Application of the Bloch's theorem implies

$$\mathbf{u}_l(n+1) = e^{\mu} \mathbf{u}_l(n), \quad (2.99)$$

where  $\mu$  is the propagation constant? Substituting Eq. (2.97) to Eq. (2.99) leads to linear eigenvalue problem of the form

$$\mathbf{T} \begin{bmatrix} \mathbf{d}_l(n) \\ \mathbf{f}_l(n) \end{bmatrix} = e^{\mu} \begin{bmatrix} \mathbf{d}_l(n) \\ \mathbf{f}_l(n) \end{bmatrix}. \quad (2.100)$$

The general eigenvalue problem can be therefore expressed as

$$\mathbf{T} \begin{bmatrix} \mathbf{d}_l \\ \mathbf{f}_l \end{bmatrix} = e^{\mu} \begin{bmatrix} \mathbf{d}_l \\ \mathbf{f}_l \end{bmatrix}. \quad (2.101)$$

It has been noticed by Zhong and Williams [75], that direct solution of the eigenvalue problem given in Eq. (2.101) can lead to numerical ill-conditioning since the state vectors are partitioned into displacement and force components whose values may

diverge significantly. To overcome this difficulty a homogenization of the eigenvalue problem has been proposed, where

$$\begin{bmatrix} \mathbf{d}_l \\ \mathbf{f}_l \end{bmatrix} = \mathbf{L} \begin{bmatrix} \mathbf{d}_l \\ \mathbf{d}_r \end{bmatrix}, \quad \begin{bmatrix} \mathbf{d}_r \\ -\mathbf{f}_r \end{bmatrix} = \mathbf{N} \begin{bmatrix} \mathbf{d}_l \\ \mathbf{d}_r \end{bmatrix}, \quad (2.102-2.103)$$

and matrices are

$$\mathbf{L} = \begin{bmatrix} \mathbf{I} & \mathbf{0} \\ \boldsymbol{\alpha}_{ll} & \boldsymbol{\alpha}_{lr} \end{bmatrix}, \quad \mathbf{N} = \begin{bmatrix} \mathbf{0} & \mathbf{I} \\ -\boldsymbol{\alpha}_{rl} & -\boldsymbol{\alpha}_{rr} \end{bmatrix}. \quad (2.104-2.105)$$

This leads to the following expression of the eigenvalue problem:

$$(\mathbf{N} - e^{\mu} \mathbf{L}) \begin{bmatrix} \mathbf{d}_l \\ \mathbf{d}_r \end{bmatrix} = \mathbf{0} \quad (2.106)$$

Solving the eigenvalue problem and calculating the propagation constant for a given frequency range delivers important information about both attenuation and phase delay that waves build up while traveling through a unit cell. In the following studies the propagation constants are presented as functions of normalised frequency  $\Omega$ , which is a ratio of the frequency and the frequency at which the wavelength is equal to twice the unit cell length i.e. the phase shift across the cell is equal to  $\pi$

$$\Omega = \frac{\omega}{\omega_B}. \quad (2.107)$$

Here,  $\omega_B$  is the Bragg frequency, which in case of the one-dimensional, infinite Euler-Bernulli beam without inclusions is given by

$$\omega_B = \frac{\pi^2}{L_{cell}^2} \sqrt{\frac{Y_b I_b}{\rho_b A_b}}. \quad (2.108)$$

Expressing the propagation constants in this way makes the result independent upon the lattice constant i.e. unit cell length  $L_{cell}$ .

The plots in Figure 2.3 present the propagation constants for a normalized frequency range 0 to 2.5. The results indicate that propagation in beams is characterised by two wave types. The first type illustrated in plots (a) and (b) of Figure 2.3 corresponds to spatially decaying waves in both, positive and negative directions, also known as evanescent waves or near-field. The decay rate of these attenuated waves is represented by the frequency dependent attenuation constant  $\text{Re}\{\mu\}$ .

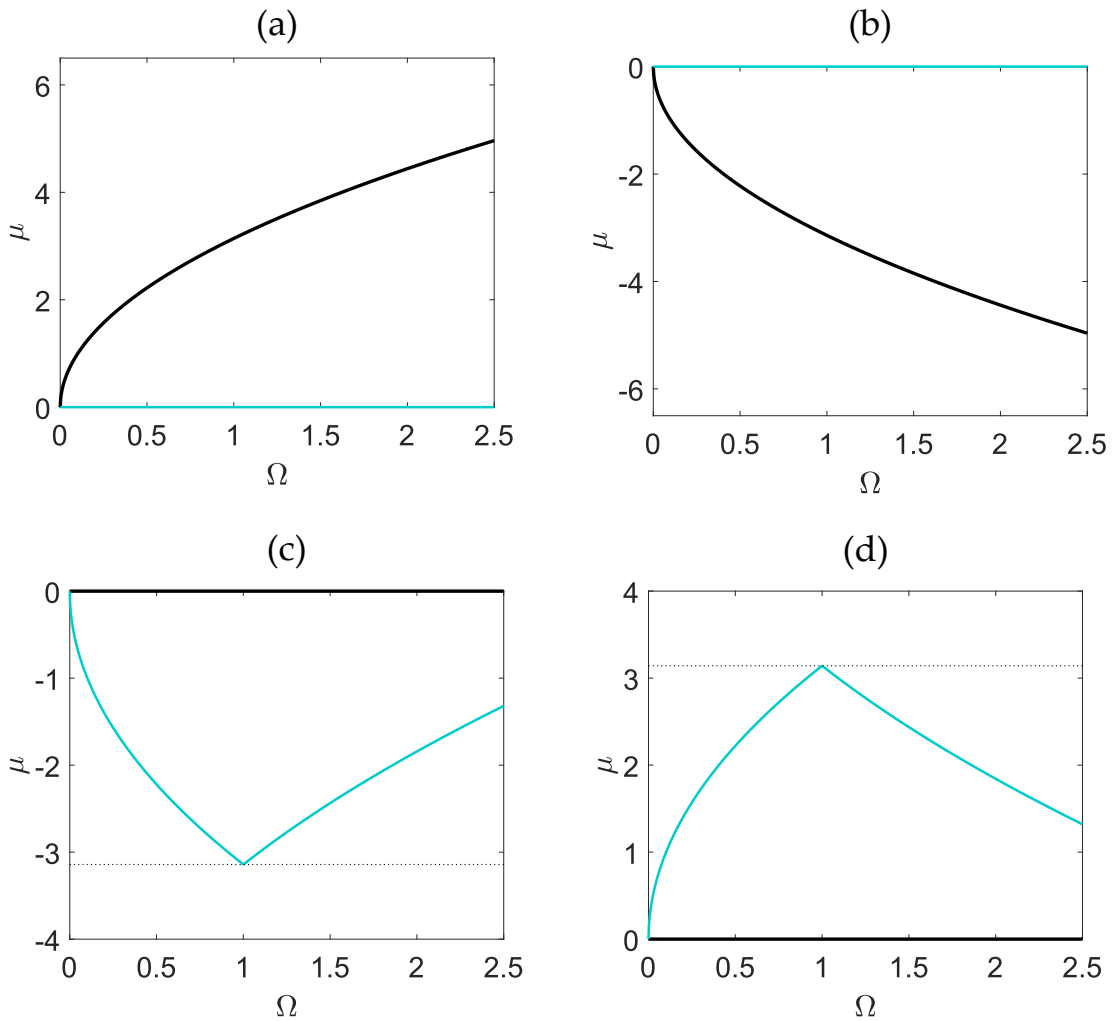


Figure 2.3 Dispersion curves for an infinite Euler-Bernoulli beam. Plots (a) and (b) positive and negative going evanescent waves. Plots (c) and (d) positive and negative going flexural waves. Black lines -real parts, blue lines - imaginary parts of propagation constants.

The second wave type shown in plots (c) and (d) of Figure 2.3 is characterised by attenuation constant  $\text{Re}\{\mu\} = 0$  in both directions, which indicates freely traveling waves. That is propagating without distortions and whose phase constant  $\text{Im}\{\mu\}$  varies with frequency. Since the second wave type can propagate freely at any given frequency, the uniform one-dimensional beam cannot possess wave filtering capabilities.

### 2.3.2 Infinite beam with regular grid of point masses

This paragraph considers the wave propagation in an infinite beam with a regular grid of point masses. Application of a discrete point mass to the unit cell of a beam is straight forward and requires only addition of a mass value to the associated node in the global mass matrix of the unit cell. It is known that point masses can produce the flexural wave scattering effects. The scattering occurs due to the impedance mismatch between the uniform beam segments and the point masses, that leads to traveling waves being partially reflected and partially transmitted to neighbouring cells. At certain frequencies the interactions between reflected and transmitted waves give rise to destructive interference effects, which results in frequency bands where the free wave propagation is stopped. Due to the interference nature of the phenomenon, the stop band frequency is directly linked to the spatial organization of a unit cell, namely the lattice constant  $L_{cell}$ . The frequency at which the structural wavelength is equal twice the unit cell and thus the phase delay is equal to  $\pi$  across the single cell, makes destructive interference possible.

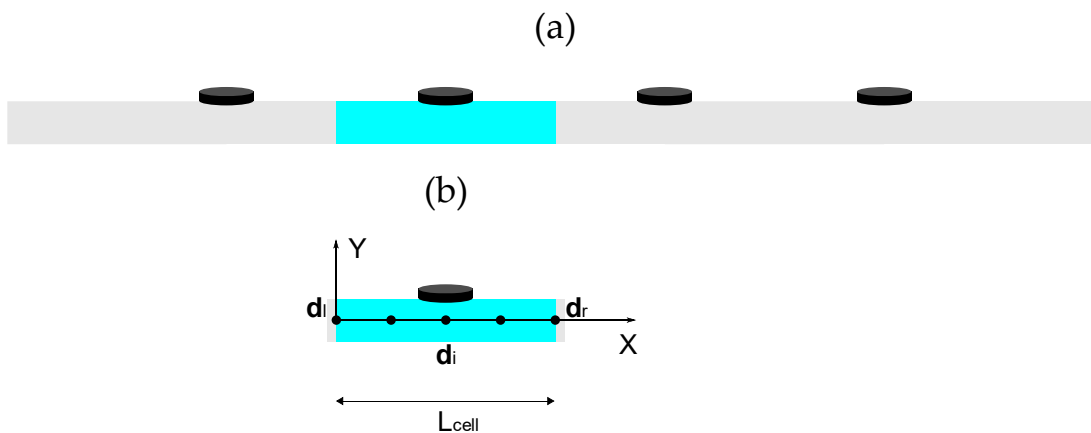


Figure 2.4 (a) Depiction of an infinite Euler-Bernoulli beam with discrete masses spaced by a distance  $L_{cell}$ . (b) An exemplary meshed unit cell.

The plots in Figure 2.5 presents dispersion curves for the unit cell with point mass equal to 20% of the unit cell mass. Again, two types of waves are found, plots (a) and (b) in Figure 2.5 show the propagation constants of the rapidly decaying near field, which do not differ from those calculated for the uniform beam. Plots (c) and (d) present dispersion curves for flexural waves, which are propagating freely in positive and negative directions, with increasing phase delay ranging from dimensionless

frequency 0 to about 0.8. At around 0.8 the phase shift across the unit cell length reaches  $\pi$  and becomes constant making negative interference possible up to dimensionless frequency 1.

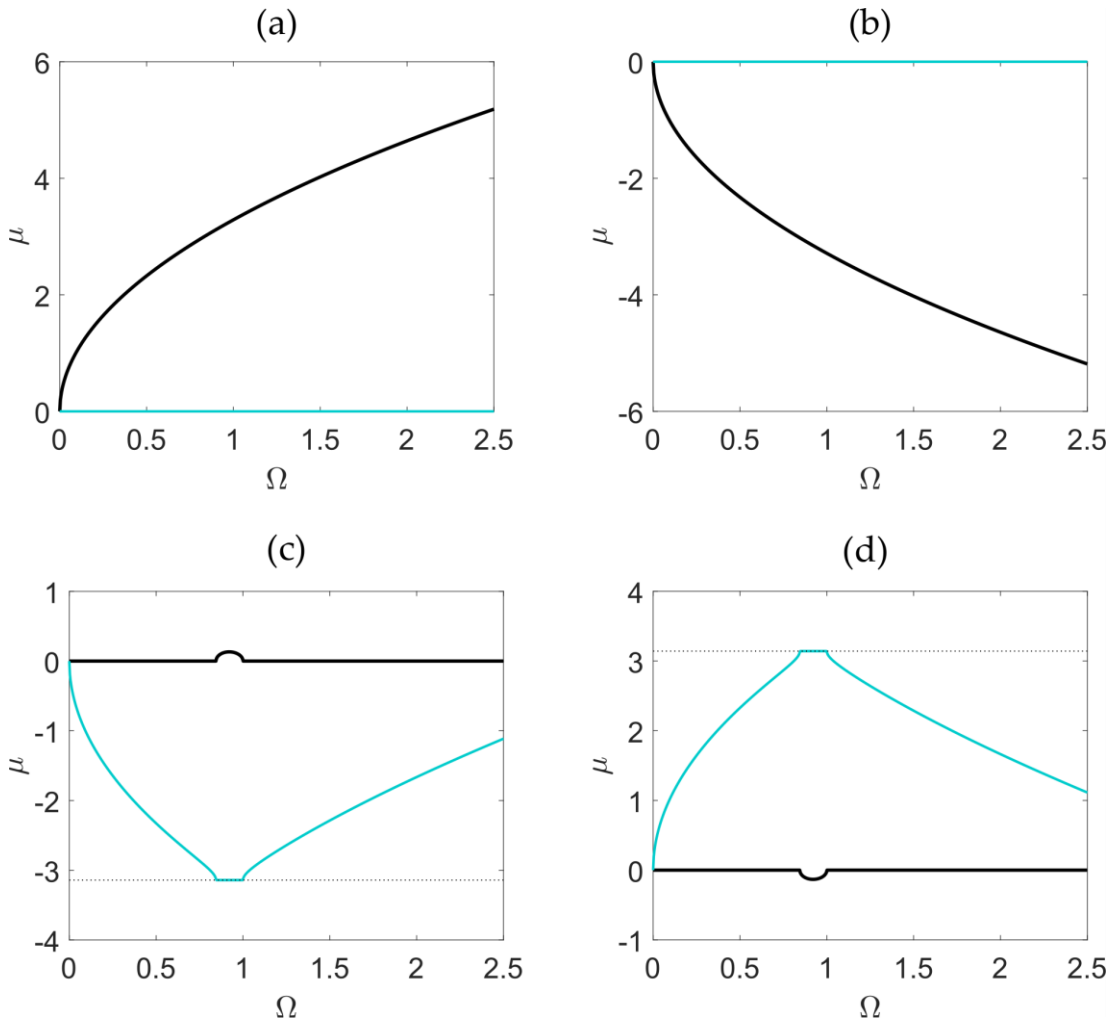


Figure 2.5 Dispersion curves for an infinite Euler-Bernoulli beam with periodic point masses equal to 20% of the unit cell mass. Plots (a) and (b) positive and negative going evanescent waves. Plots (c) and (d) positive and negative going flexural waves. Black lines -real parts, blue lines - imaginary parts of propagation constants.

Considering now the attenuation constant, it is noted that, although no energy dissipation effects are considered, the attenuation constant is non-zero over the frequency region from 0.8 to 1. This frequency band is called interference stop band, since the wave attenuation effect depends on the wave circulations inside the cells rather than on material dissipation effects. In other words, it is the result of a wave

interference effects produced by the point masses. This phenomenon, also called the Bragg scattering, has been investigated in several studies for different types of physical systems [76].

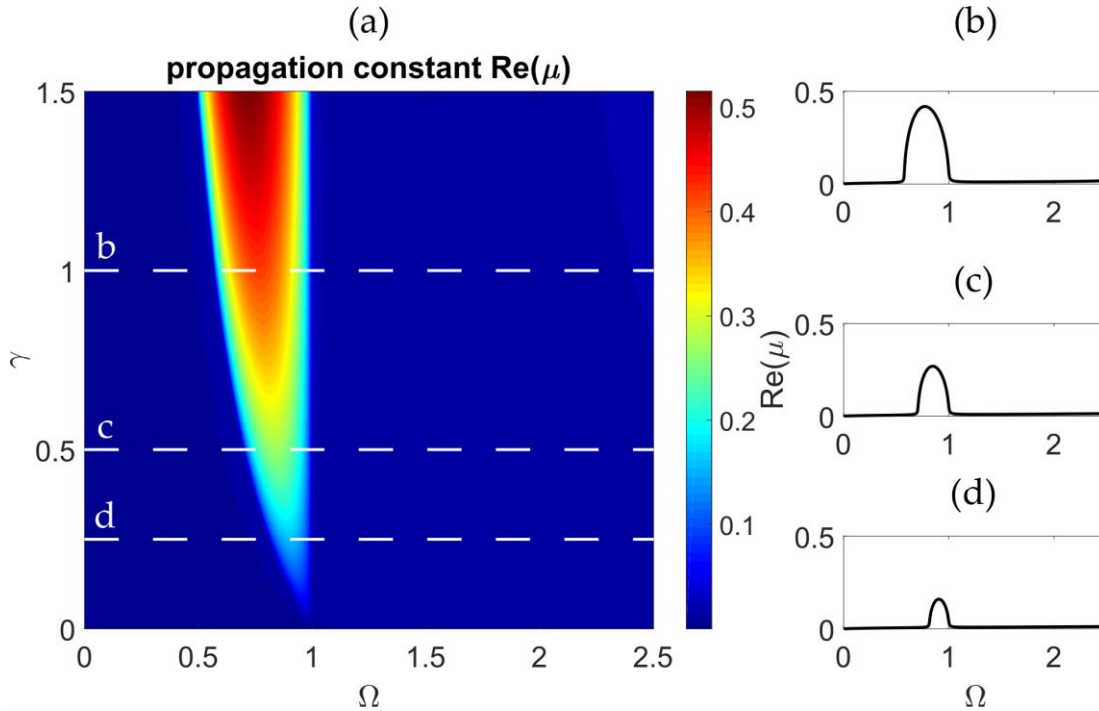


Figure 2.6 (a) The evolution of the attenuation constant of positive going flexural waves in an infinite Euler-Bernoulli beam with periodic point masses against dimensionless weight of point masses. Attenuation constants of flexural waves associated with (b)  $\gamma = 1$ , (c)  $\gamma = 0.5$  and (d)  $\gamma = 0.25$ .

Figure 2.6(a) presents the evolution of the interference stop band distribution with reference to dimensionless mass, defined as the ratio of the point mass relative to the mass of the unit cell  $\gamma = \frac{m_p}{m_{cell}}$ .

In general, when the mass ratio increases the stop band distribution expands towards lower frequencies but maintains the upper bound limit at normalised frequency equal to 1. As depicted in Figure 2.6 (a) and (b) the interference stop band effect can cover an impressive bandwidth, however to achieve such effect, a significant mass addition is required. Considering vibration treatment this is rather undesired, since the increase in total mass of a structure should be minimal. Thus, the generation of stop

bands in this way seems to be impractical and suitable only to large and heavy structures i.e. bridges.

### 2.3.3 Infinite beam with regular grid of spring-mass vibration absorbers

As proposed by Liu [54], stop bands can also be produced by periodic cells with resonating elements. For example, in this study the behaviour of the cell with a tunable vibration absorber (TVA), modelled as the single degree of freedom translational spring-mass system is considered.

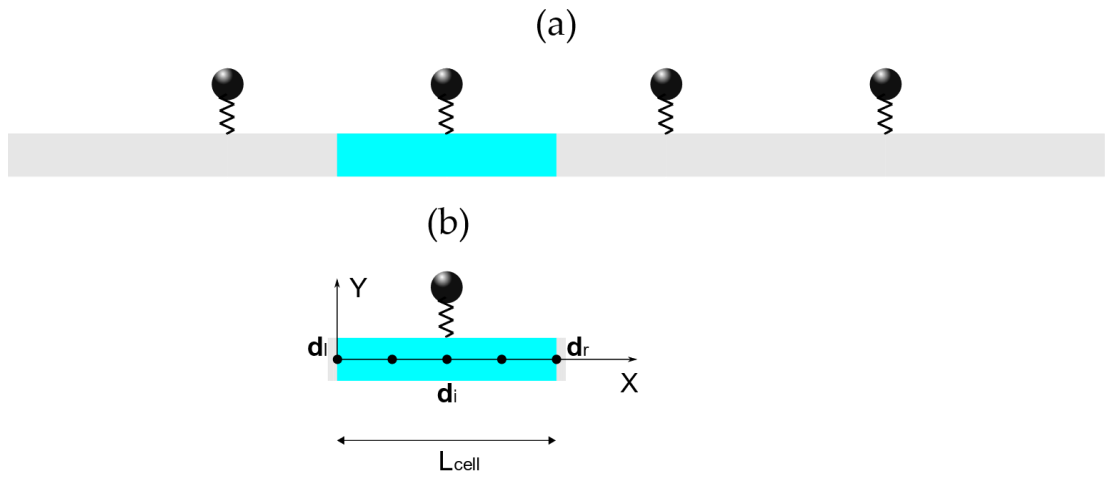


Figure 2.7 (a) Depiction of an infinite Euler-Bernoulli beam with tunable vibration absorbers spaced by a distance  $L_{cell}$ . (b) An exemplary meshed unit cell.

The same formulation introduced above for the beam with cells equipped with point masses is used here considering the dynamic stiffness of the absorber. Addition of the TVA into the system requires an additional degree of freedom associated with the absorber. Therefore, equation of motion is given by

$$\begin{Bmatrix} 0 & 0 \\ 0 & \mathbf{D} \end{Bmatrix} + \mathbf{D}_{tva} \begin{bmatrix} d_{tva} \\ \mathbf{d} \end{bmatrix} = \begin{bmatrix} f_{tva} \\ \mathbf{f} \end{bmatrix}, \quad (2.109)$$

where,  $\mathbf{D}$  is the dynamic stiffness matrix given by Eq. (2.84), the vectors containing degrees of freedom and forces related to the unit cell are arranged in the following way  $\mathbf{d} = [d_l \ d_i \ d_r]^T$ ,  $\mathbf{f} = [f_l \ f_i \ f_r]^T$ .  $\mathbf{D}_{tva}$  is the dynamic stiffness matrix of the vibration absorber composed of stiffness and mass matrices and assembled as the global matrix

$$\mathbf{D}_{tva} = \mathbf{K}_{tva} - \omega^2 \mathbf{M}_{tva}, \quad (2.110)$$

with non-zero elements distributed in accordance to degrees of freedom associated with the inter-connection node (i.e. central inner node). The degree of freedom associated to the vibration absorber can be treated as the  $i$ -th inner degree of freedom and thus the total stiffness matrix can be rewritten in the form of

$$\mathbf{D} = \begin{bmatrix} \tilde{\mathbf{D}}_{ii} & \tilde{\mathbf{D}}_{il} & \tilde{\mathbf{D}}_{ir} \\ \tilde{\mathbf{D}}_{li} & \tilde{\mathbf{D}}_{ll} & \tilde{\mathbf{D}}_{lr} \\ \tilde{\mathbf{D}}_{ri} & \tilde{\mathbf{D}}_{rl} & \tilde{\mathbf{D}}_{rr} \end{bmatrix}. \quad (2.111)$$

Assuming no external forces are exerted on the internal nodes, the internal degrees of freedom can be eliminated, such that equation of motion can be written in terms of left-hand side and right-hand side degrees of freedom and forces of the unit cell. The procedure to obtain the propagation constants is the same as already described in previous subsection. To be consistent with the previous analysis, reference is made to dimensionless frequency of the absorbers

$$\Omega_0 = \frac{\omega_0}{\omega_B}, \quad (2.112)$$

where,  $\omega_0 = \sqrt{\frac{k}{m_s}}$  is the resonance frequency of the absorbers. In this study, the spring  $k$  was chosen so that the dimensionless resonance frequency of the absorbers is given by  $\Omega_0 = 0.5$  and the suspended masses equal to 20% of the unit cell mass. The calculated band structures of the propagation constants for the infinite beam with periodically added vibration absorbers are presented in Figure 2.8.

Considering first the diagrams of the phase constants given by the blue lines, it is noted that they are characterised by similar shapes to those found for the beam with cells containing point mass, except for a new sharp peak in correspondence to the absorber resonance frequency, i.e.  $\Omega = 0.5$ . Similar conclusions can be drawn also for the attenuation constants, which, as depicted by black lines, is in this case characterised by rather high and sharp peak for  $\Omega = 0.5$  and then one tiny peak centred at  $\Omega = 1.1$ . The former is classified as a resonance stop band effect while the latter is classified as an interference stop band, which in this case, is due to wave scattering effect produced by absorber itself. The resonance stop band is instead due to the well-known property of vibration absorbers, which effectively absorb energy from the flexural vibration of the hosting structure where they are mounted at frequencies close to their fundamental resonance frequency i.e.  $\omega = \omega_0$ . The attenuation constant produced by the absorber at  $\Omega = 0.5$  reaches a peak value of about 2, which is well above 0.5 produced by point masses.

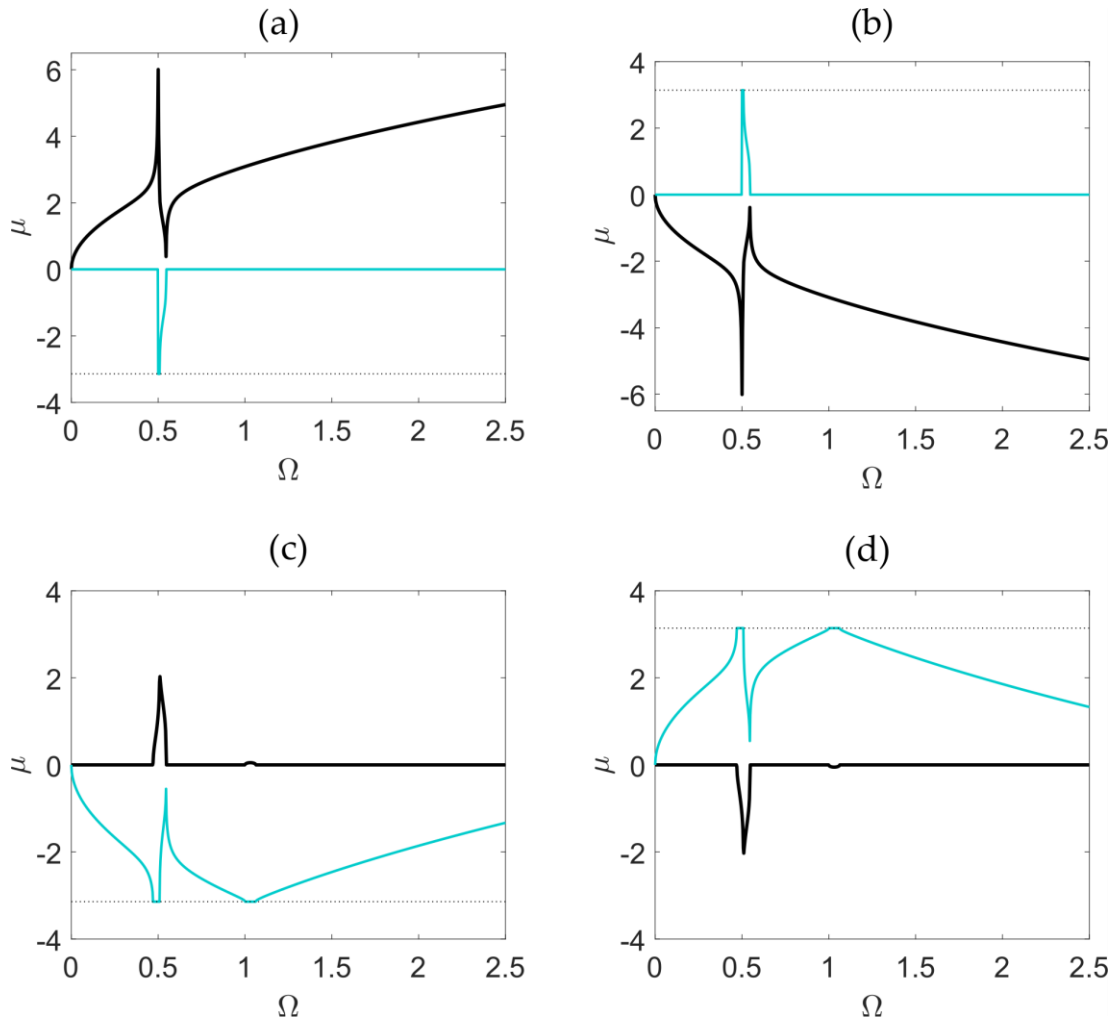


Figure 2.8 Dispersion curves for an infinite Euler-Bernoulli beam with periodic point tunable vibration absorbers whose masses are equal to 20% of the unit cell mass. Plots (a) and (b) positive and negative going, evanescent waves. Plots (c) and (d) positive and negative going flexural waves. Black lines -real parts, blue lines - imaginary parts of propagation constants.

Due to its nature, the resonance stop band is not dependent on the unit cell geometry and can be tuned to any given frequency by varying the physical properties of the absorbers (mass or stiffness). Figure 2.9 (a) shows the evolution of the attenuation factor associated with the flexural waves with reference to the dimensionless frequency of the absorbers  $\Omega_0$  assuming the proof mass of the tunable vibration absorbers is 20% of the unit cell beam mass. This figure shows the presence of both resonance and interference stop band branches, which couples when the absorber

resonance frequency is tuned such that  $\Omega_0 \approx 1$ . When the plot is sliced in correspondence to  $\Omega_0 \approx 1$ , the resonance and interference stop bands merge into significantly wider and higher attenuation band gaps. The nature of the coupling gap formation mechanism in one-dimensional system can be explained mathematically by the band edge frequency dependences, which can be derived from the trigonometric form of the propagation constant by using a combination of the spectral element method and Bloch theorem [77].

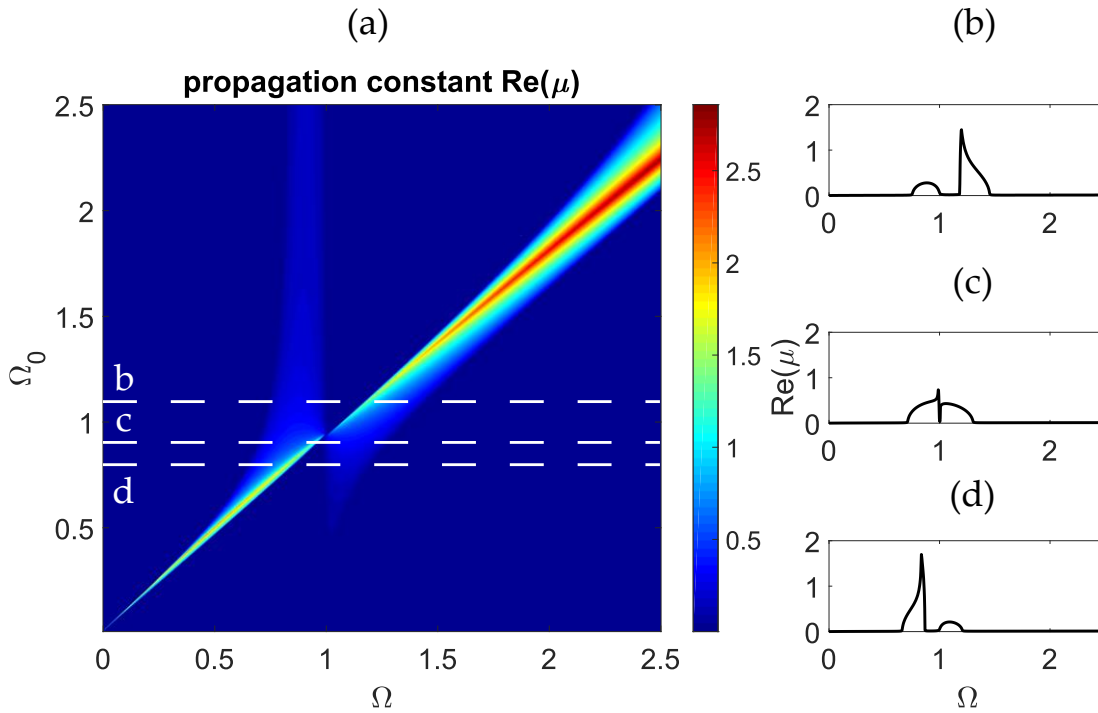


Figure 2.9 (a) The evolution of the attenuation constant of positive going flexural waves in an infinite Euler-Bernoulli beam with periodic TVAs whose masses are equal to 20% of the unit cell mass against the dimensionless frequency of the absorbers Attenuation constants of flexural waves associated with resonance frequency of the absorbers (b)  $\Omega_0 = 1.1$ , (c)  $\Omega_0 = 0.9$  and (d)  $\Omega_0 = 0.8$ .

The effect of changing the proof mass while keeping the resonance frequency of the absorbers constant is now considered. Figure 2.10 (a) shows the evolution of the attenuation factor associated with the flexural wave with reference to the mass ratio:  $\gamma = \frac{m_s}{m_{cell}}$ . The plot considers absorbers tuned to the dimensionless resonance frequency 0.5. Thus, in this case the stiffness of the TVAs is continuously adjusted to maintain constant resonance frequency.

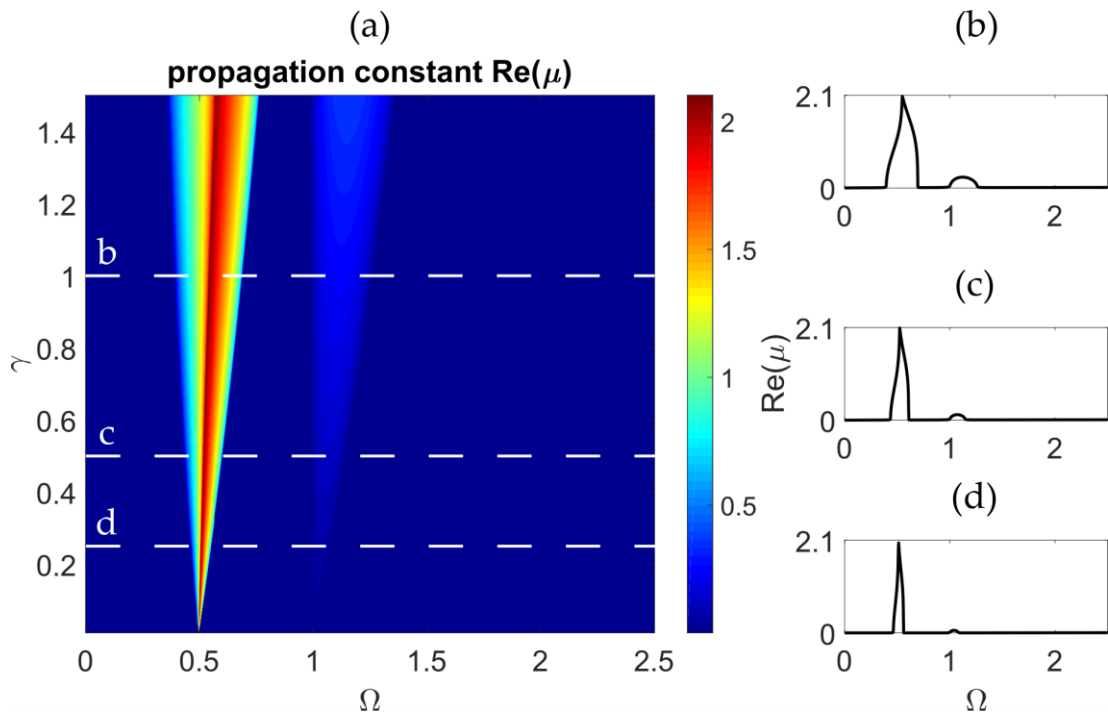


Figure 2.10 (a) The evolution of the attenuation constant of positive going flexural waves in an infinite Euler-Bernoulli beam with periodic TVAs tuned to  $\Omega_0 = 0.5$  against the dimensionless weight of proof masses. Attenuation constants of flexural waves associated to dimensionless weight of proof masses (b)  $\gamma = 1$ , (c)  $\gamma = 0.5$  and (d)  $\gamma = 0.25$ .

As depicted in Figure 2.10, increasing the proof mass of the absorber leads to wider stop band distributions, both for the resonance and the interference stop bands. The resonance stop band is concentrated around  $\Omega = 0.5$  and expands towards lower and higher frequencies as the proof mass is increased. Apart from that, at dimensionless frequency 1 the interference effect arises as the result of wave scattering from the proof mass of the absorber which is moving out of phase with respect to the beam. The bandwidth distribution associated with this effect is left hand limited by the edge frequency 1 and expands with added proof mass only towards higher frequencies.

So far, no consideration was made about damping. Adding a dashpot in parallel to the spring allows to investigate the effect of damped vibration absorbers on the distribution of the stop bands. Damping elements can be useful and effective in terms of increasing the width of the band gaps. In this case the dynamic stiffness matrix from Eq. (2.110) becomes

$$\mathbf{D}_{tva} = \mathbf{K}_{tva} - \omega^2 \mathbf{M}_{tva} + j\omega \mathbf{C}_{tva}, \quad (2.113)$$

Where  $\mathbf{C}_{tva}$  contains non-zero damping coefficients associated with degrees of freedom of the absorber and inter-connecting node.

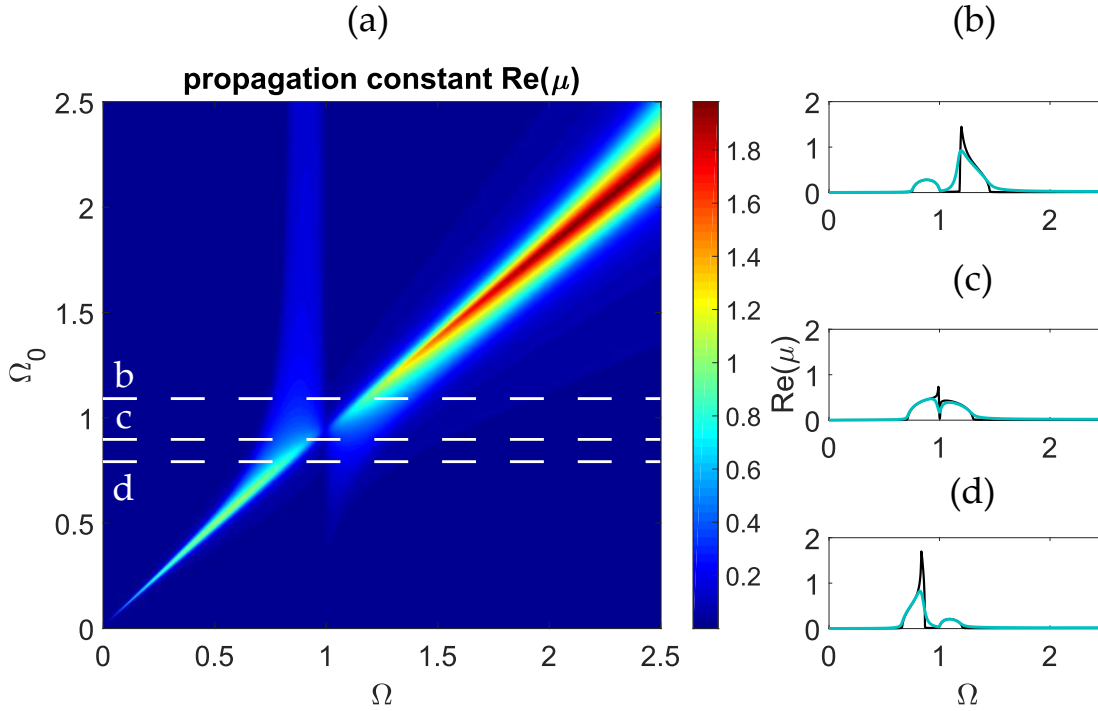


Figure 2.11(a) The evolution of the attenuation constant of positive going flexural waves in an infinite Euler-Bernoulli beam with damped, periodic TVAs whose masses are equal to 20% of the unit cell mass, against the dimensionless frequency of the absorbers Attenuation constants of flexural waves associated with resonance frequency of the absorbers (b)  $\Omega_0 = 1.1$ , (c)  $\Omega_0 = 0.9$  and (d)  $\Omega_0 = 0.8$ . Black lines – undamped TVAs, blue lines – TVAs with 3% of damping ratio.

Figure 2.11 (a) presents the evolution of the propagation constant of the flexural wave, when vibration absorbers are equipped with dashpot with 3% of damping ratio. As one can expect the sharp contours indicating boundaries of the stop band phenomenon when dashpot is not present, become smoother and the overall effect within investigated dimensionless frequency range is weaker but has wider frequency range. This is particularly visible in plots (b), (c) and (d) of Figure 2.11, where dispersion curves are shown for an infinite beam containing absorbers with and without dashpots.

The influence of damping of the vibration absorbers on the distribution of the attenuation band is also depicted in Figure 2.12. This figure illustrates the evolution of the resonance stop band effect generated by the absorbers at  $\Omega = 0.5$  with respect to added damping 0-0.3. As shown in subsequent plots (b), (c) and (d), a gradual increase of damping decreases the response amplitudes of the absorbers but makes their distributions wider in frequency.

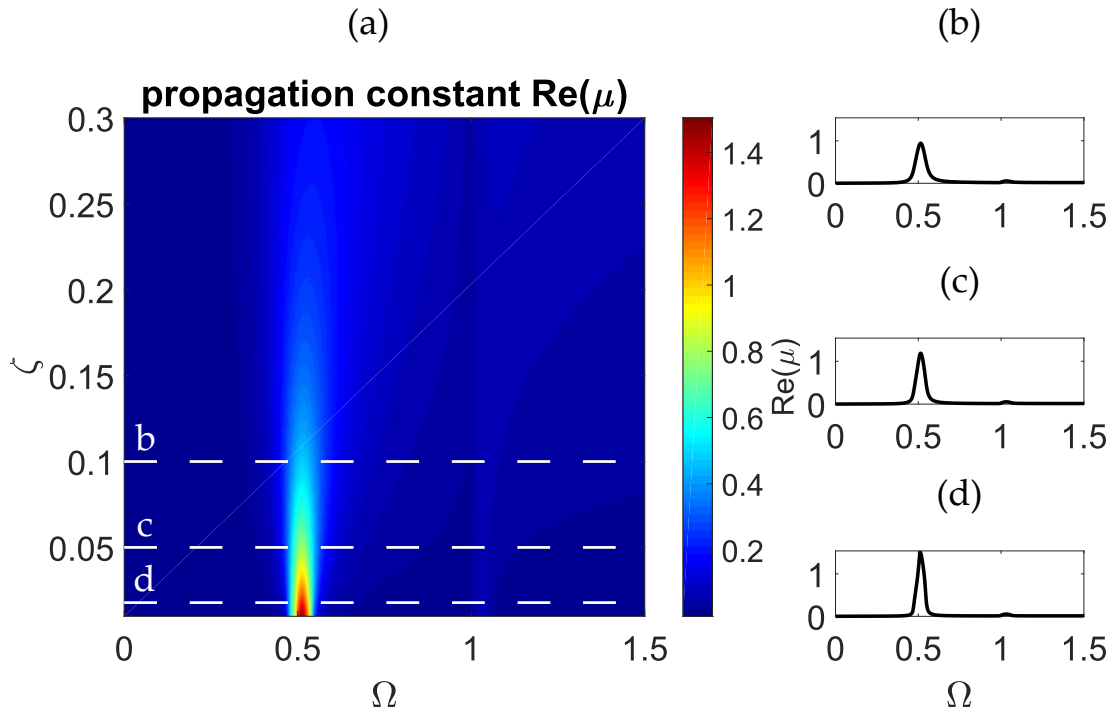


Figure 2.12 (a) The evolution of the attenuation constant of positive going flexural waves in an infinite Euler-Bernoulli beam with periodic TVAs tuned to  $\Omega_0 = 0.5$  and whose proof masses are equal to 20% of the unit cell mass, against damping ratio of the TVAs. Attenuation constants of flexural waves associated to TVAs damping ratios (b)  $\zeta = 0.1$ , (c)  $\zeta = 0.05$  and (d)  $\zeta = 0.015$ .

#### 2.3.4 Infinite beam with regular grid of vibration absorbers equipped with base masses

In the next step, the evolution of the stop band effects of vibration absorbers equipped with base masses is examined.

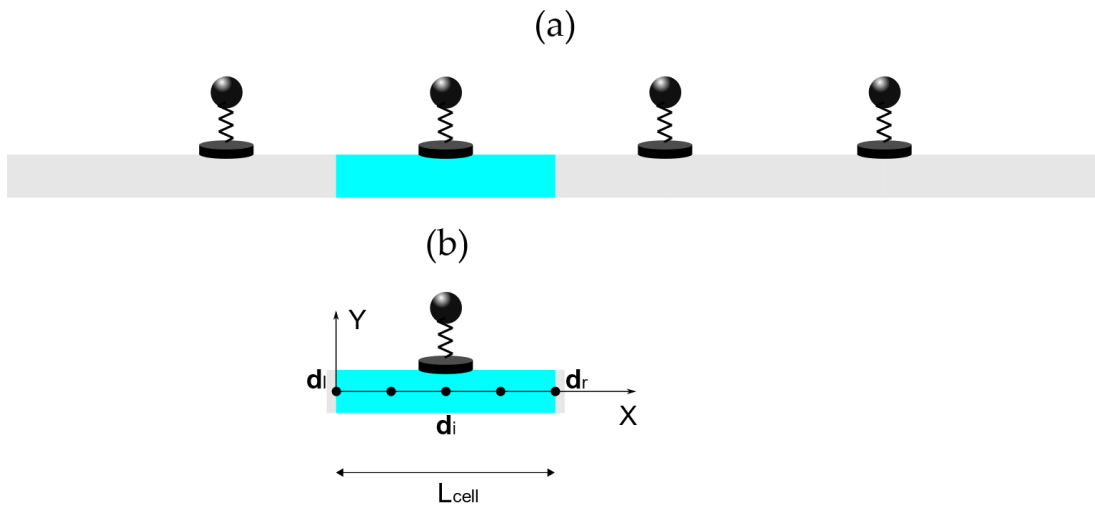


Figure 2.13 (a) Depiction of an infinite Euler-Bernoulli beam with tunable vibration absorbers equipped with base masses and spaced by a distance  $L_{cell}$ . (b) An exemplary mesh of the unit cell.

The base masses introduce additional wave scattering effects, that can produce stop bands at frequencies near to the edge frequency given by the Bragg's condition. Due to the interference nature of this phenomenon, the effect is right-hand side limited by the dimensionless frequency 1 linked to the lattice constant. Thus, the bandwidth of the effect can only be extended towards lower frequencies, by increasing the weight of base masses. When weight of base masses is significant with respect to the unit cell, an interesting feature of this system is its ability to produce resonance and interference bands simultaneously. As shown in Figure 2.14 (a), the resonance stop band evolves in the same manner as the one produced by spring-mass vibration absorbers by delivering noticeable effect and allowing for an arbitrary tuning across considered frequency range. However, due to the presence of the base masses the additional stop band is present near dimensional frequency 1, this effect maintains its bandwidth, along with the increase of dimensionless resonance frequency up to  $\Omega_0 = 0.6$ . As a result, two distinct stop band effects can be produced also at frequencies below the strong coupling regime of the resonance and interference effects, as presented in plot (d) of Figure 2.14.

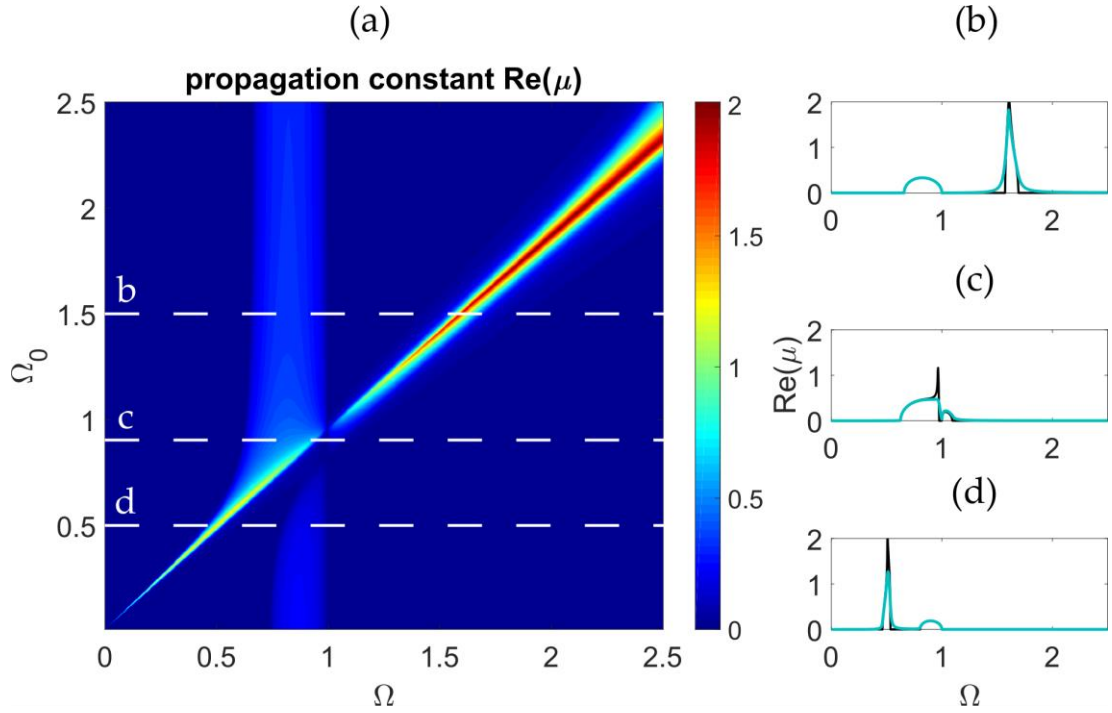


Figure 2.14 (a) The evolution of the attenuation constant of positive going flexural waves in an infinite Euler-Bernoulli beam with damped, periodic TVAs with base masses equal to 40% and proof masses to 20% of the unit cell mass, against the dimensionless frequency of the absorbers Attenuation constants of flexural waves associated with resonance frequency of the absorbers (b)  $\Omega_0 = 1.5$ , (c)  $\Omega_0 = 0.9$  and (d)  $\Omega_0 = 0.5$ . Black lines – undamped TVAs, blue lines – TVAs with 3% of damping ratio.

### 2.3.5 Infinite beam with regular grid of piezoelectric patch transducers connected to inductive shunts

Periodically spaced piezoelectric patch transducers connected to electrical shunts can also produce resonance stop band effects. In this section it is assumed the piezoelectric patches are connected to identical shunts formed only by inductive elements. The resistive component is for the time being neglected. In each shunt the inductance is connected in parallel with the internal capacitance of the piezoelectric patch to form a resonating electrical circuit whose resonance frequency can be derived from the following relation

$$L = \frac{1}{\omega_0^2 c_{pe}}, \quad (2.114)$$

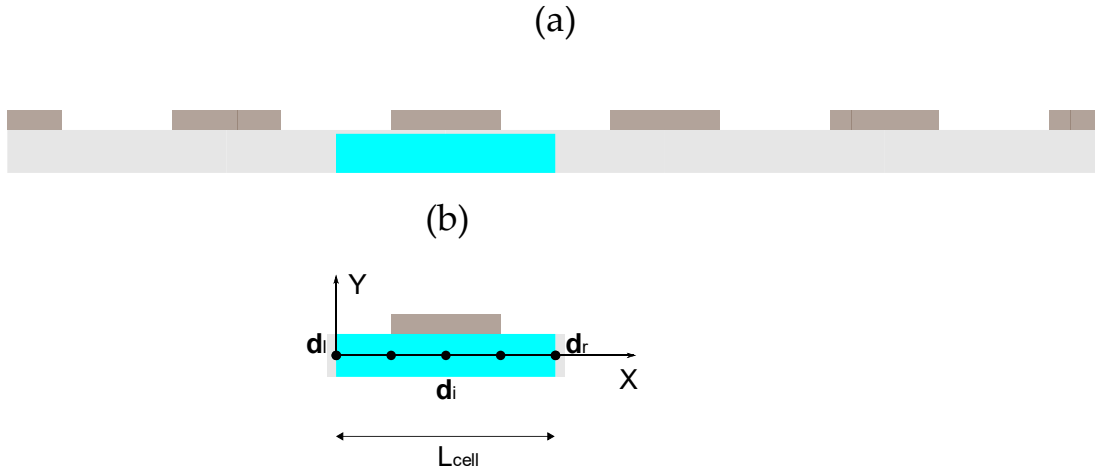


Figure 2.15 (a) Depiction of an infinite Euler-Bernoulli beam with piezoelectric patch transducers spaced by a distance  $L_{cell}$ . (b) An exemplary mesh of the unit cell.

Recalling the systems governing equations from Eqs. (2.79), (2.80)

$$(\mathbf{M}_b + \mathbf{M}_{pe})\ddot{\mathbf{d}}_k + (\mathbf{K}_b + \mathbf{K}_{pe})\mathbf{d}_k + \boldsymbol{\theta}_{pe}v_{pe} = \mathbf{f}, \quad (2.115)$$

$$\boldsymbol{\theta}_{pe}^T \mathbf{d}_k + C_{pe}v_{pe} = q, \quad (2.116)$$

and if piezoelectric patch is connected only to the electrical inductance  $L$ , the voltage across the patch is given by

$$v_{pe} = \ddot{q}L. \quad (2.117)$$

Substituting Eq. (2.117) into Eqs. (2.115) and (2.116) yields

$$\mathbf{M}_t \ddot{\mathbf{d}}_k + \mathbf{K}_t \mathbf{d}_k + \boldsymbol{\theta}_{pe}L\ddot{q} = \mathbf{f}, \quad (2.118)$$

$$\boldsymbol{\theta}_{pe}^T \mathbf{d}_k + C_{pe}L\ddot{q} = q. \quad (2.119)$$

These equations can now be reformulated in terms of state vectors in the following way

$$\mathbf{M}\ddot{\mathbf{u}} + \mathbf{K}\mathbf{u} = \mathbf{F}, \quad (2.120)$$

where the vectors are defined in the following way  $\mathbf{u} = [q \ \mathbf{d}_i \ \mathbf{d}_l \ \mathbf{d}_r]^T$ ,  $\mathbf{F} = [0 \ \mathbf{f}_i \ \mathbf{f}_l \ \mathbf{f}_r]^T$ . Also, the global matrices are assembled as follows:

$$\mathbf{M} = \begin{bmatrix} \boldsymbol{\theta}_{pe}L & \mathbf{M}_t \\ C_{pe}L & \mathbf{0} \end{bmatrix}, \quad (2.121)$$

$$\mathbf{K} = \begin{bmatrix} \mathbf{0} & \mathbf{K}_t \\ -1 & \boldsymbol{\theta}_{pe}^T \end{bmatrix}. \quad (2.122)$$

The dynamic stiffness matrix can then be derived from the following equation

$$\mathbf{D} = \mathbf{K} - \omega^2 \mathbf{M} \quad (2.123)$$

By treating charge as an inner degree of freedom, the dynamic stiffness matrix can be arranged in the same form as that presented above

$$\mathbf{D} = \begin{bmatrix} \mathbf{D}_{ii} & \mathbf{D}_{il} & \mathbf{D}_{ir} \\ \mathbf{D}_{li} & \mathbf{D}_{ll} & \mathbf{D}_{lr} \\ \mathbf{D}_{ri} & \mathbf{D}_{rl} & \mathbf{D}_{rr} \end{bmatrix}. \quad (2.124)$$

As described previously, assuming no forces act on internal nodes, the inner degrees of freedom can be eliminated, and the equation of motion can be expressed in the following way

$$\begin{bmatrix} \boldsymbol{\alpha}_{ll} & \boldsymbol{\alpha}_{lr} \\ \boldsymbol{\alpha}_{rl} & \boldsymbol{\alpha}_{rr} \end{bmatrix} \begin{bmatrix} \mathbf{d}_l \\ \mathbf{d}_r \end{bmatrix} = \begin{bmatrix} \mathbf{f}_l \\ \mathbf{f}_r \end{bmatrix}. \quad (2.125)$$

From this point the derivation of propagation constants proceeds in the same way as already described in the previous subsections.

The effects produced by an array of shunted piezoelectric patch transducers are now examined. The stop band distribution pattern shown in Figure 2.16 is very similar to the one illustrated in Figure 2.14 for spring-mass vibration absorbers equipped with base masses. The only difference is that the entire distribution pattern is shifted towards lower frequencies with respect to the one from Figure 2.14. For example, one can notice that the right-hand side edge frequency associated with the interference stop band effects is lowered to about 0.75. This occurrence is related to the spatial distribution of the mass of piezoelectric transducers, which is not concentrated in a point as it was in the case of vibration absorbers equipped with base masses. As a result, the obtained spectrum is characterised by the edge frequency which deviates from the approximate frequency given by the Bragg's condition for an infinite Euler-Bernoulli beam.

In practice, point masses are bound to occupy a certain length of the beam cell. Therefore, the results presented above consider an idealised system which could be representative for rather small masses.

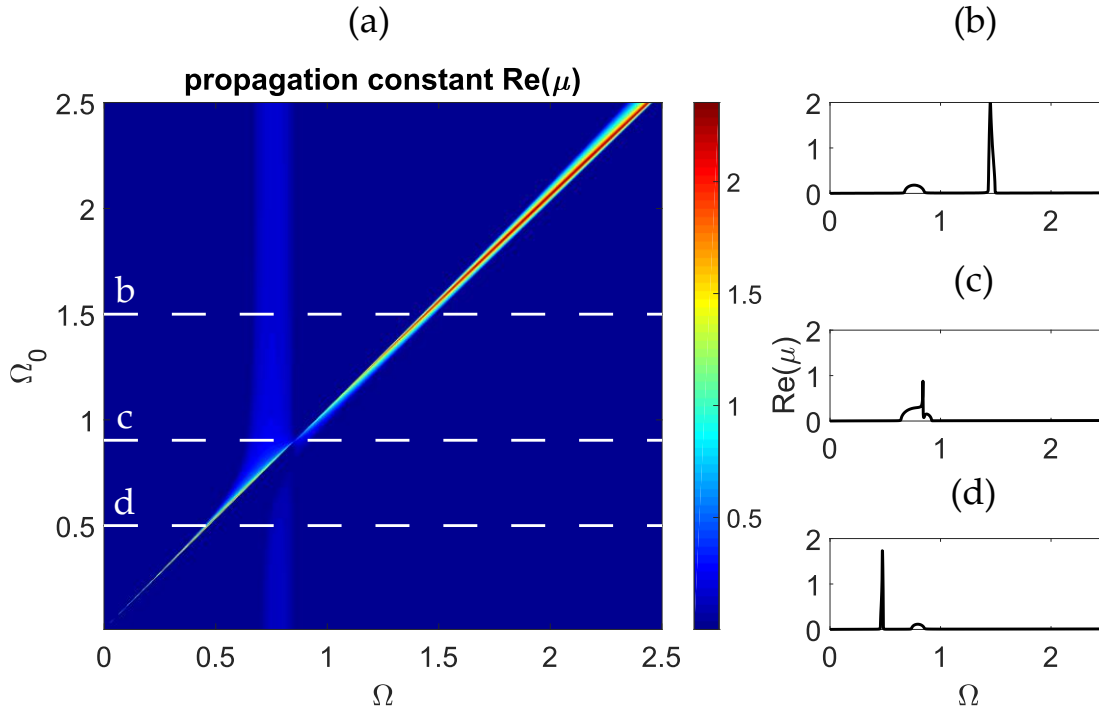


Figure 2.16 The evolution of the attenuation constant of positive going flexural waves in an infinite Euler-Bernoulli beam with piezoelectric patch transducers connected to inductive shunts, against the dimensionless resonance frequency of the shunts. Attenuation constants of flexural waves associated with resonance frequency of the shunts (b)  $\Omega_0 = 1.5$ , (c)  $\Omega_0 = 0.9$  and (d)  $\Omega_0 = 0.5$ .

### 2.3.6 Infinite beam with regular grid of piezoelectric patch transducers connected to resistive-inductive shunts

When a resistance is introduced in the shunt circuits, the distribution of local resonance effects is broadened. A resistance in the shunt circuit produces a comparable effect to that of a dashpot in a tunable vibration absorber. Thus, it produces energy dissipation effect. In the following part of this analysis, the quality factor is introduced as a dimensionless measure of energy dissipation produced by the resistor in the resonating RLC circuit of the shunted piezoelectric patch, given by:

$$Q_{RL} \approx \frac{\omega_0 L}{R_s}. \quad (2.126)$$

Here  $L$  and  $R_s$  are respectively the inductance and the resistance of the shunt. The implementation of the resistance in the shunt circuit is relatively easy but requires some mathematical manipulations in the formulation of the state matrices.

Recalling the systems governing equations from Eqs. (2.79), (2.80)

$$(\mathbf{M}_b + \mathbf{M}_{pe})\ddot{\mathbf{d}}_k + (\mathbf{K}_b + \mathbf{K}_{pe})\mathbf{d}_k + \boldsymbol{\theta}_{pe}v_{pe} = \mathbf{f}, \quad (2.127)$$

$$\boldsymbol{\theta}_{pe}^T \mathbf{d}_k + C_{pe}v_{pe} = q. \quad (2.128)$$

If piezoelectric patch is connected only to the series RL shunt, the voltage across the patch is given by

$$v_{pe} = \ddot{q}L + \dot{q}R_s. \quad (2.129)$$

Substituting Eq. (2.117) into Eqs. (2.115) and (2.116) yields

$$\mathbf{M}_t \ddot{\mathbf{d}}_k + \mathbf{K}_t \mathbf{d}_k + \boldsymbol{\theta}_{pe}L\ddot{q} + \boldsymbol{\theta}_{pe}\dot{q} = \mathbf{f}, \quad (2.130)$$

$$\boldsymbol{\theta}_{pe}^T \mathbf{d}_k + C_{pe}L\ddot{q} + C_{pe}R\dot{q} - q = 0. \quad (2.131)$$

These equations can now be reformulated in terms of state vectors in the following way

$$\mathbf{M}\ddot{\mathbf{u}} + \mathbf{K}\mathbf{u} = \mathbf{F}. \quad (2.132)$$

Where the vectors are arranged as  $\mathbf{u} = [q \ \mathbf{d}_i \ \mathbf{d}_l \ \mathbf{d}_r]^T$ ,  $\mathbf{F} = [0 \ \mathbf{f}_i \ \mathbf{f}_l \ \mathbf{f}_r]^T$ .

And the matrices given by

$$\mathbf{M} = \begin{bmatrix} \boldsymbol{\theta}_{pe}L & \mathbf{M}_t \\ C_{pe}L & \mathbf{0} \end{bmatrix}, \quad (2.133)$$

$$\mathbf{C} = \begin{bmatrix} \boldsymbol{\theta}_{pe}R & \mathbf{0} \\ C_{pe}R & \mathbf{0} \end{bmatrix}, \quad (2.134)$$

$$\mathbf{K} = \begin{bmatrix} \mathbf{0} & \mathbf{K}_t \\ -1 & \boldsymbol{\theta}_{pe}^T \end{bmatrix}. \quad (2.135)$$

The dynamic stiffness matrix is in this case given by the following expression:

$$\mathbf{D} = \mathbf{K} - \omega^2\mathbf{M} + j\omega\mathbf{C} \quad (2.136)$$

Treating electrical charge as an inner degree of freedom, the dynamic stiffness matrix can be arranged in the already well-known form

$$\mathbf{D} = \begin{bmatrix} \mathbf{D}_{ii} & \mathbf{D}_{il} & \mathbf{D}_{ir} \\ \mathbf{D}_{li} & \mathbf{D}_{ll} & \mathbf{D}_{lr} \\ \mathbf{D}_{ri} & \mathbf{D}_{rl} & \mathbf{D}_{rr} \end{bmatrix}. \quad (2.137)$$

As described previously, by assuming no forces are exerted on internal nodes, the inner degrees of freedom can be eliminated, and the equation of motion can be expressed in the following way

$$\begin{bmatrix} \alpha_{ll} & \alpha_{lr} \\ \alpha_{rl} & \alpha_{rr} \end{bmatrix} \begin{bmatrix} \mathbf{d}_l \\ \mathbf{d}_r \end{bmatrix} = \begin{bmatrix} \mathbf{f}_l \\ \mathbf{f}_r \end{bmatrix}. \quad (2.138)$$

From this point onwards, the derivation of propagation constants proceeds in the same way as already described in the previous subsections.

The evolution of the attenuation constant with respect to the dimensionless resonance frequency of the shunt for the beam with the array of piezoelectric patches connected to series RL shunts is depicted in Figure 2.17 (a). The quality factor was arbitrarily chosen as  $Q_{RL} = 25$  and kept constant by adopting the resistance with reference to resonance frequency. As one would expect, due to the presence of dissipative elements, a blue shadow surrounding the edge frequencies of the stop band phenomena is now visible, which indicates that the width of the stop band effect is widened although the effect is also lowered.

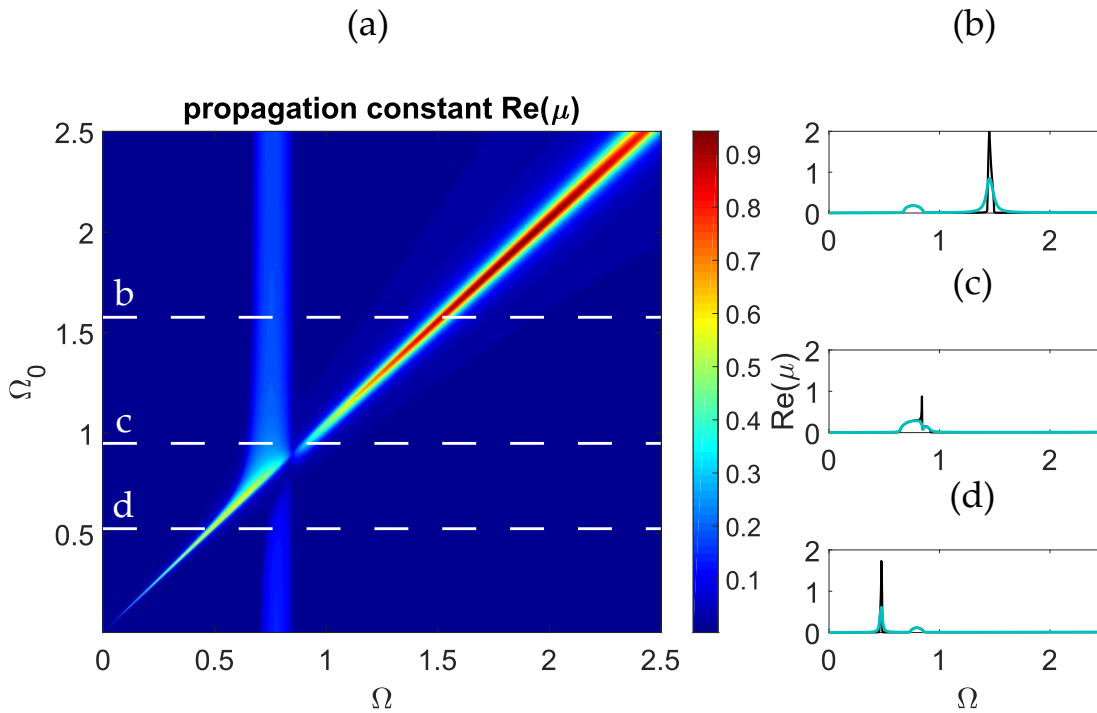


Figure 2.17 The evolution of the attenuation constant of positive going flexural waves in an infinite Euler-Bernoulli beam with piezoelectric patch transducers connected to series RL shunts, against the dimensionless resonance frequency of the shunts. Attenuation constants of flexural waves associated with resonance frequency of the shunts (b)  $\Omega_0 = 1.5$ , (c)  $\Omega_0 = 0.9$  and (d)  $\Omega_0 = 0.5$ . Black lines - inductive shunt, blue lines – series RL shunt.

To illustrate the influence of the electrical energy dissipation on the distribution of the resonance stop band effect, the resonance frequency of the shunts was kept at dimensionless frequency  $\Omega_0 = 0.5$ , while the resistances was varied in such a way as to gradually increase the quality factor from 1 to 100. Figure 2.18 (a) illustrate changes in the stop distribution and in the attenuation rate with reference to quality factor that characterizes the losses produced by the resistors in the electrical shunts. The set of plots (b), (c) and (d) in Figure 2.18 shows how the locally resonant effect generated by the shunted transducers becomes weaker, due to the lower quality factors.

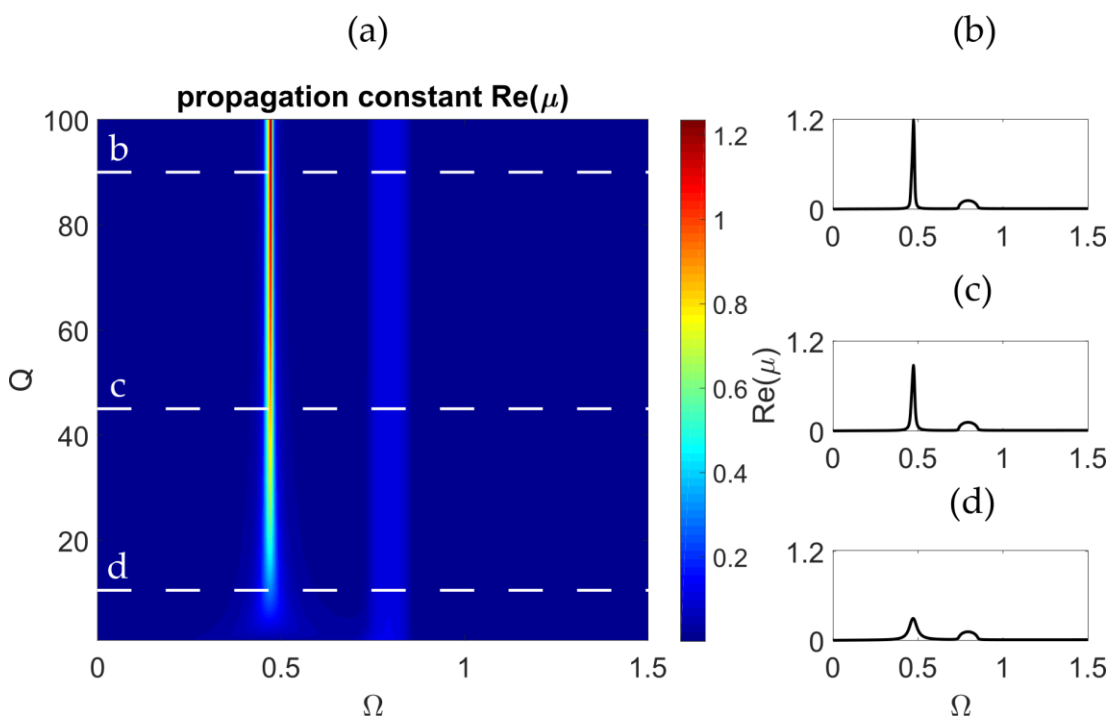


Figure 2.18 The evolution of the attenuation constant of positive going flexural waves in an infinite Euler-Bernoulli beam with piezoelectric patch transducers connected to series RL shunts and tuned to  $\Omega_0 = 0.5$ , against the quality factor of the shunts. Attenuation constants of flexural waves associated with quality factors of the of the shunt (b)  $Q = 90$ , (c)  $Q = 45$  and (d)  $Q = 10$ .

### 2.3.7 Infinite beam with regular grid of piezoelectric patch transducers connected to multi-resonant shunt circuits

In this section, the effects produced by multi-resonant shunt circuits introduced by Behrens [43] are considered. Assuming the electrical functions are time-harmonic and

given in the form  $f(t) = f(\omega)\exp(j\omega t)$ , where  $f(\omega)$  is the complex amplitude,  $\omega$  is the circular frequency, the ratio of charge and potential difference across of the current flowing shunt circuit can be expressed as the sum of two second order terms:

$$\frac{q}{v_{pe}} = \frac{\frac{1}{L_{b1}}}{-\omega^2 + j\omega\frac{R_{s1}}{L_{b1}} + \frac{1}{C_{f1}L_{b1}}} + \frac{\frac{1}{L_{b2}}}{-\omega^2 + j\omega\frac{R_{s2}}{L_{b2}} + \frac{1}{C_{f2}L_{b2}}} . \quad (2.139)$$

Each second order term in Eq. (2.139) can be envisaged as the ratio between a generalized charge and a voltage across piezoelectric patch. Thus, the charge can be expressed with the following matrix equation

$$q = \Psi \Lambda , \quad (2.140)$$

where,  $\Psi = \left[ \frac{1}{\sqrt{L_{b1}}} \quad \frac{1}{\sqrt{L_{b2}}} \right]$ . and  $\Lambda = [\Lambda_1 \quad \Lambda_2]^T$  is the vectors with generalized charges, which can be given by the following matrix relation

$$\Lambda = \mathbf{G}\Psi^T v_{pe} , \quad (2.141)$$

that is

$$\begin{bmatrix} \Lambda_1 \\ \Lambda_2 \end{bmatrix} = \begin{bmatrix} \frac{1}{-\omega^2 + j\omega\frac{R_{s1}}{L_{b1}} + \frac{1}{C_{f1}L_{b1}}} & \\ & \frac{1}{-\omega^2 + j\omega\frac{R_{s2}}{L_{b2}} + \frac{1}{C_{f2}L_{b2}}} \end{bmatrix} \begin{bmatrix} \frac{1}{\sqrt{L_{b1}}} \\ \frac{1}{\sqrt{L_{b2}}} \end{bmatrix} v_{pe} . \quad (2.142)$$

Considering the expanded form of Eq. (2.142)

$$\mathbf{I}\ddot{\Lambda} + \Delta\dot{\Lambda} + \Omega\Lambda = \Psi^T v_{pe} , \quad (2.143)$$

where the matrices are defined

$$\mathbf{I} = \begin{bmatrix} 1 & \\ & 1 \end{bmatrix} , \quad (2.144)$$

$$\Delta = \begin{bmatrix} \frac{R_{s1}}{L_{b1}} & \\ & \frac{R_{s2}}{L_{b2}} \end{bmatrix} , \quad (2.145)$$

$$\Omega = \begin{bmatrix} \frac{1}{C_{f1}L_{b1}} & \\ & \frac{1}{C_{f2}L_{b2}} \end{bmatrix} . \quad (2.146)$$

Starting from Eqs. (2.140)-(2.143) it is possible to express the governing system of Eqs. (2.127), (2.128) in terms of the vectors:  $\ddot{\mathbf{d}}$ ,  $\dot{\mathbf{d}}$ ,  $\mathbf{d}$  and  $\ddot{\boldsymbol{\Lambda}}$ ,  $\dot{\boldsymbol{\Lambda}}$ ,  $\boldsymbol{\Lambda}$ . First, substituting Eq. (2.140) to Eq. (2.128) yields

$$\boldsymbol{\theta}_{pe}^T \mathbf{d} + C_{pe} v_{pe} = \boldsymbol{\Psi} \boldsymbol{\Lambda}, \quad (2.147)$$

so that potential difference can be written as

$$v_{pe} = C_{pe}^{-1} \boldsymbol{\Psi} \boldsymbol{\Lambda} - C_{pe}^{-1} \boldsymbol{\theta}_{pe}^T \mathbf{d}. \quad (2.148)$$

This expression can then be substituted to Eq. (2.127) to obtain the first set of governing equations in terms of  $\ddot{\mathbf{d}}$ ,  $\mathbf{d}$  and  $\boldsymbol{\Lambda}$ .

$$\mathbf{M}_t \ddot{\mathbf{d}} + (\mathbf{K}_t - \boldsymbol{\theta}_{pe} C_{pe}^{-1} \boldsymbol{\theta}_{pe}^T) \mathbf{d} + \boldsymbol{\theta}_{pe} C_{pe}^{-1} \boldsymbol{\Psi} \boldsymbol{\Lambda} = \mathbf{f}. \quad (2.149)$$

The second set of governing equations is then obtained by pre-multiplication of Eq. (2.148) by  $\boldsymbol{\Psi}^T$

$$\boldsymbol{\Psi}^T v_{pe} = \boldsymbol{\Psi}^T C_{pe}^{-1} \boldsymbol{\Psi} \boldsymbol{\Lambda} - \boldsymbol{\Psi}^T C_{pe}^{-1} \boldsymbol{\theta}_{pe}^T \mathbf{d}, \quad (2.150)$$

and substitution of Eq. (2.150) into Eq. (2.143).

$$\mathbf{I} \ddot{\boldsymbol{\Lambda}} + \Delta \dot{\boldsymbol{\Lambda}} + \boldsymbol{\Omega} \boldsymbol{\Lambda} = \boldsymbol{\Psi}^T C_{pe}^{-1} \boldsymbol{\Psi} \boldsymbol{\Lambda} - \boldsymbol{\Psi}^T C_{pe}^{-1} \boldsymbol{\theta}_{pe}^T \mathbf{d}. \quad (2.151)$$

In this way the governing system equations are reformulated to account for multi-resonating shunt circuit, composed of two RLC branches.

$$\mathbf{M}_t \ddot{\mathbf{d}} + (\mathbf{K}_t - \boldsymbol{\theta}_{pe} C_{pe}^{-1} \boldsymbol{\theta}_{pe}^T) \mathbf{d} + \boldsymbol{\theta}_{pe} C_{pe}^{-1} \boldsymbol{\Psi} \boldsymbol{\Lambda} = \mathbf{f}, \quad (2.152)$$

$$\mathbf{I} \ddot{\boldsymbol{\Lambda}} + \Delta \dot{\boldsymbol{\Lambda}} + \boldsymbol{\Psi}^T C_{pe}^{-1} \boldsymbol{\theta}_{pe}^T \mathbf{d} + (\boldsymbol{\Omega} - \boldsymbol{\Psi}^T C_{pe}^{-1} \boldsymbol{\Psi}) \boldsymbol{\Lambda} = \mathbf{0}. \quad (2.153)$$

The governing equations can be now casted in the canonical matrix form

$$\mathbf{M} \ddot{\mathbf{u}} + \mathbf{C} \dot{\mathbf{u}} + \mathbf{K} \mathbf{u} = \mathbf{F}, \quad (2.154)$$

where,  $\mathbf{M}$  and  $\mathbf{K}$  matrices are organized as

$$\mathbf{M} = \begin{bmatrix} \mathbf{I} & \mathbf{0} \\ \mathbf{0} & \mathbf{M}_t \end{bmatrix}, \quad (2.155)$$

$$\mathbf{C} = \begin{bmatrix} \Delta & \mathbf{0} \\ \mathbf{0} & \mathbf{0} \end{bmatrix}, \quad (2.156)$$

$$\mathbf{K} = \begin{bmatrix} \boldsymbol{\Omega} - \boldsymbol{\Psi}^T C_{pe}^{-1} \boldsymbol{\Psi} & \boldsymbol{\Psi}^T C_{pe}^{-1} \boldsymbol{\theta}_{pe}^T \\ \boldsymbol{\theta}_{pe} C_{pe}^{-1} \boldsymbol{\Psi} & \mathbf{K}_t - \boldsymbol{\theta}_{pe} C_{pe}^{-1} \boldsymbol{\theta}_{pe}^T \end{bmatrix}. \quad (2.157)$$

and vectors are arranged according to the Figure 2.15  $\mathbf{u} = [\Lambda_1 \Lambda_2 \mathbf{d}_i \mathbf{d}_l \mathbf{d}_r]^T$ ,  $\mathbf{F} = [0 \ 0 \ \mathbf{f}_i \ \mathbf{f}_l \ \mathbf{f}_r]^T$ .

The dynamic stiffness matrix can be formulated as

$$\mathbf{D} = j\omega\mathbf{C} + \mathbf{K} - \omega^2\mathbf{M} \quad (2.158)$$

Considering the generalised charges as the inner degrees of freedom, the dynamic stiffness matrix can be arranged in the familiar form

$$\mathbf{D} = \begin{bmatrix} \mathbf{D}_{ii} & \mathbf{D}_{il} & \mathbf{D}_{ir} \\ \mathbf{D}_{li} & \mathbf{D}_{ll} & \mathbf{D}_{lr} \\ \mathbf{D}_{ri} & \mathbf{D}_{rl} & \mathbf{D}_{rr} \end{bmatrix}. \quad (2.159)$$

Assuming no external forces are exerted on internal nodes, the inner degrees of freedom can be eliminated, and the equation of motion can be expressed as follows

$$\begin{bmatrix} \boldsymbol{\alpha}_{ll} & \boldsymbol{\alpha}_{lr} \\ \boldsymbol{\alpha}_{rl} & \boldsymbol{\alpha}_{rr} \end{bmatrix} \begin{bmatrix} \mathbf{d}_l \\ \mathbf{d}_r \end{bmatrix} = \begin{bmatrix} \mathbf{f}_l \\ \mathbf{f}_r \end{bmatrix}. \quad (2.160)$$

From this point onwards, the derivation of propagation constants proceeds in the same way as already described in the previous subsections.

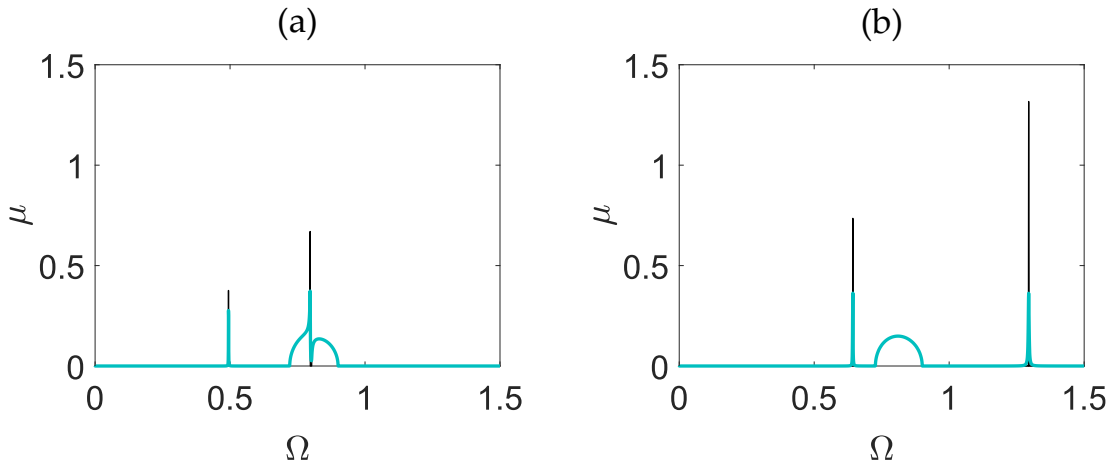


Figure 2.19 Attenuation constants of flexural waves associated with resonance frequencies 0.5, 0.8 (a) and 0.65, 1.3 (b). Black lines – multi-resonating, inductive shunts, blue lines – multi-resonating RL shunts. Whose resistances were set to  $5\Omega$  and  $7k\Omega$ .

Figure 2.19 shows the propagation constants for an infinite beam equipped with periodic piezoelectric patch transducers combined with a two-resonances electrical shunt. As can be noticed, both resonance effects are characterised by a relatively high attenuation constant and a narrow bandwidth, which can be slightly increased by adding resistance components into the shunt topology, as indicated by the blue lines.

## 2.4 CONCLUDING REMARKS

The study presented in this chapter has shown that, both interference and resonance stop bands can be produced in a beam structure with periodic grids of considered inclusions. The results indicate that the interference effects are characterised by rather weak attenuation in relatively wide frequency band. In line with the Bragg's condition the study showed, that the stop bands generated by the wave scattering from the periodic masses are limited at dimensionless frequency 1. Although the effects can still be extended towards lower frequencies by increasing the mass of the inclusions, the noticeable extensions require significant mass addition relative to unit cell mass. Weighty inclusions can also improve the attenuation properties of the structure by limiting the wave amplitude transmission from one unit cell to the other. In contrary to the interference stop bands, the effects produced by the resonant inclusions are characterised by rather strong attenuation within narrow frequency band. As shown in this chapter, these types of structures are mostly driven by the unit cell resonance frequency and can generate stop band effects despite the unit cell spatial organisation. This is a doubtless practical advantage over the interference-based solutions, since the effects can be conveniently tuned to the target frequency by adjusting the physical properties of the resonant inclusions. The obtained results also indicated that bandwidths of the resonance effects widen as the resonance frequency of the inclusions increase towards the Bragg's frequency. This phenomenon is most likely a manifestation of the increasing coupling between the resonance and interference effects that proceeds until both effects are fully coupled and create very wide attenuation phenomena. The bandwidth extends also when damping of the inclusions is considered. This is also true for the shunted piezoelectric patch vibration absorbers when resistance is present in a circuit. Although, addition of the energy loss mechanism allows for a slight extension of the frequency band it also reduces the attenuation amplitude.

Finally, the studies demonstrated that periodic piezoelectric patches connected to multi-resonant shunts can be utilised to produce multiple locally resonant stop band

effects in one-dimensional beam. Thus, validating that the original modal formulation of the shunt equations can be regarded as an effective way to model the effects of periodic piezoelectric patch transducers connected to complex shunting circuits on wave propagation and vibration properties of the one-dimensional mechanical structure.

The analysis of stop band effects is continued for an infinite two-dimensional plate in the next chapter.

---

## INFINITE PLATE WITH PERIODIC INCLUSIONS

---

This chapter is a natural extension of the previous one and considers the wave propagation in an infinite plate equipped with two-dimensional regular arrays of inclusions. It focuses on the characterisation of stop band phenomena, resulting from the implementation of several types of inclusions, that is discrete masses, spring-mass vibration absorbers and piezoelectric patch transducers connected to single and multi-resonant shunts that produce single or multiple resonance effects. A novel mathematical formulation of the modal electrical response of the multi-resonant shunt circuit is introduced to characterize electrical branches of the shunts as additional degrees of freedom and to overcome the conventional issue of the nonlinear eigenvalue problem. In this chapter the finite element method is utilised as a framework to model the dynamic response of the unit cell, whereas the governing equations of the unit cell were derived from Hamilton's principle for electro-mechanical systems. The Bloch's theorem is then applied in the so-called inverse approach to obtain the band diagrams of the analysed two-dimensional periodic structures.

### 3.1 INTRODUCTION

In this chapter the inverse approach is used to calculate the band structures of an infinite plate with two-dimensional regular arrays of inclusions. As pointed out by Spadoni [80], dynamic stiffness matrices of two-dimensional structures are given by complicated functions of frequency and thus, the direct approach utilised in Chapter 2 cannot calculate the dispersion properties of waves propagating in arbitrary directions. In the same work, the authors generalized the direct transfer matrix technique and showed that the dispersion properties can only be obtained for waves propagating in some specific directions. To overcome this problem the inverse approach was developed as a mean of modelling to predict the dispersion properties in an arbitrary direction. In contrary to the direct approach, where the propagation constants are calculated directly, the inverse method consists in finding all

frequencies at which free wave propagation is possible. The frequency ranges for which no free wave propagation is found are the stop bands. To implement this approach, the electro-mechanical model should not account for energy loss effects (i.e. damping matrix is equal to zero-matrix) and should only consider free wave propagation [63,78,79]. For waves propagating in infinite two-dimensional periodic structures the complex propagation vector  $\boldsymbol{\mu}$  can be defined as a measure of the amplitude attenuation and the phase delay across the lengths of an elementary unit cell along x and y axes as

$$\boldsymbol{\mu} = [\mu_x, \mu_y] = [\delta_x + j\epsilon_x, \delta_y + j\epsilon_y]. \quad (3.1)$$

Here,  $\mu_x$  and  $\mu_y$  are complex terms, whose real parts:  $\delta_x, \delta_y$  represents the attenuation of the wave amplitude through a cell along x and y axes, while the imaginary parts:  $\epsilon_x, \epsilon_y$  represents the spatial periods across the unit cell along x and y axes. Since the waves are meant to propagate without distortions, this chapter considers only purely imaginary propagation vectors:  $\delta_x = 0$  and  $\delta_y = 0$ .

### 3.2 MODEL FORMULATION

The finite element formulation considered in this chapter is based on the works of de Abreu and Szilard [72, 81]. For the finite element discretization, the plate has been split into 4 nodes, 12 degrees of freedom, square elements based on Kirchhoff plate theory. The transverse displacement of the plate element is interpolated with polynomial shape functions.

#### 3.2.1 FEM discretization

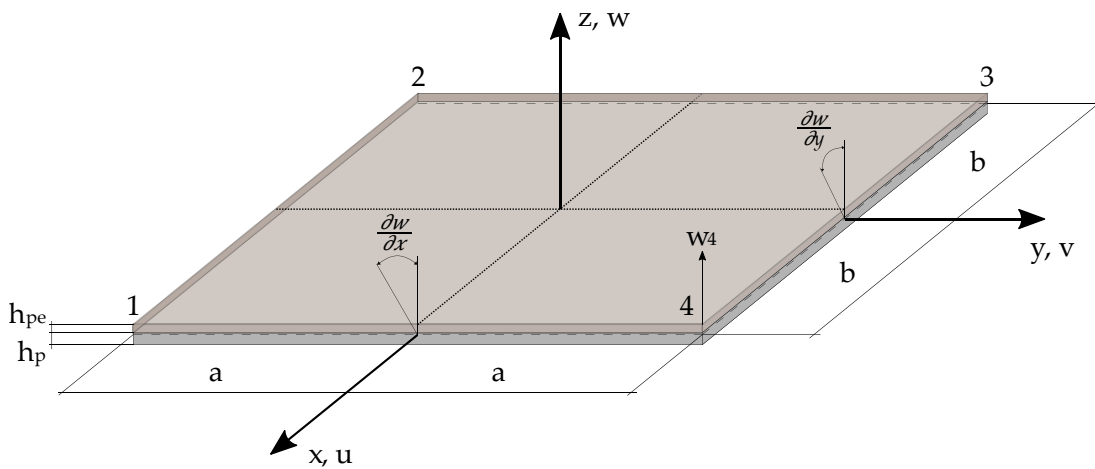


Figure 3.1 FEM element.

According to Kirchhoff hypotheses, the in-plane:  $u$ ,  $v$  and out-of-plane:  $w$  displacements (Figure 3.1) can be expressed by the following linear relationships [85]:

$$u(x, y, z) = -z \frac{\partial w(x, y)}{\partial x}, \quad (3.2)$$

$$v(x, y, z) = -z \frac{\partial w(x, y)}{\partial y}, \quad (3.3)$$

$$w(x, y, z) = w(x, y), \quad (3.4)$$

where  $x$  and  $y$  are the in-plane axes and  $z$  is the axis along the plate thickness direction,  $u$  and  $v$  are displacements in  $x$  and  $y$ -axes, whereas  $w$  is transverse displacement along the  $z$ -axis. The Kirchhoff hypothesis assumes a plane strain state, which leads to strain components:  $S_3$ ,  $S_4$  and  $S_5$  being equal to zero.

Assuming shear strains  $S_4$  and  $S_5$  to be zero for isotropic materials turns shear stresses  $T_4$  and  $T_5$  also to zero. Then, the out-of-plane stress is assumed to be significantly small compared to the in-plane normal stresses, which leads to  $T_3$  also equal to zero.

$$\mathbf{T} = \begin{bmatrix} T_1 \\ T_2 \\ T_6 \end{bmatrix}, \quad \mathbf{S} = \begin{bmatrix} S_1 \\ S_2 \\ S_6 \end{bmatrix}, \quad (3.5-3.6)$$

Linear strain-displacement relation is given by:

$$S_1 = \frac{\partial u}{\partial x}, \quad (3.7)$$

$$S_2 = \frac{\partial v}{\partial y}, \quad (3.8)$$

$$S_6 = \frac{\partial u}{\partial y} + \frac{\partial v}{\partial x}. \quad (3.9)$$

Substituting displacements from Eqs. (3.2)-(3.4) leads to the following strain-displacement relations:

$$S_1 = -z \frac{\partial^2 w}{\partial x^2}, \quad (3.10)$$

$$S_2 = -z \frac{\partial^2 w}{\partial y^2}, \quad (3.11)$$

$$S_6 = \frac{\partial u}{\partial y} + \frac{\partial v}{\partial x} = -2z \frac{\partial^2 w}{\partial x \partial y}. \quad (3.12)$$

Considering only out-of-plane displacement, the strain vector can be expressed as

$$\mathbf{S} = -z \begin{bmatrix} \frac{\partial^2 w}{\partial x^2} \\ \frac{\partial^2 w}{\partial y^2} \\ 2 \frac{\partial^2 w}{\partial x \partial y} \end{bmatrix}. \quad (3.13)$$

For isotropic material, the relation between plane stress and strain can be expressed by the following matrix relation

$$\mathbf{T} = \mathbf{c}_p \mathbf{S}, \quad (3.14)$$

where  $\mathbf{c}_p$  is the matrix containing elastic constants of the plate material given by

$$\mathbf{c}_p = \begin{bmatrix} \frac{Y_p}{1-\nu_p^2} & \frac{\nu_p Y_p}{1-\nu_p^2} & 0 \\ \frac{\nu_p Y_p}{1-\nu_p^2} & \frac{Y_p}{1-\nu_p^2} & 0 \\ 0 & 0 & \frac{Y_p}{2(1+\nu_p)} \end{bmatrix}. \quad (3.15)$$

Here,  $\nu_p$  is the Poisson ratio and  $Y_p$  denotes the Young's modulus of the plate. Considering a four-node plate element illustrated in Figure 3.1, where each node possesses three degrees of freedom: a displacement in  $z$  direction and two rotations about  $x$  and  $y$  axis, the nodal displacement vector can be defined

$$\mathbf{d}_i = \begin{bmatrix} w_i \\ \theta_{x_i} \\ \theta_{y_i} \end{bmatrix}, \quad (3.16)$$

with  $i = 1, 2, 3, 4$ . The polynomial expression to define the transversal displacement field of the rectangular element can be computed from

$$w(x, y) = \alpha_1 + \alpha_2 x + \alpha_3 y + \alpha_4 x^2 + \alpha_5 xy + \alpha_6 y^3 + \alpha_7 x^3 + \alpha_8 x^2 y + \alpha_9 xy^2 + \alpha_{10} y^3 + \alpha_{11} x^3 y + \alpha_{12} xy^3, \quad (3.17)$$

and re-written as

$$w(x, y) = \mathbf{w}^T \boldsymbol{\alpha}, \quad (3.18)$$

where  $\boldsymbol{\alpha} = [\alpha_1 \dots \alpha_{12}]^T$  is the coefficient vector and

$$\mathbf{w} = [1 \ x \ y \ x^2 \ xy \ y^2 \ x^3 \ x^2 y \ xy^2 \ y^3 \ x^3 y \ xy^3]^T. \quad (3.19)$$

The rotations about  $x$  axis of nodal points are obtained from

$$\theta_{x_i} = \frac{\partial w_i}{\partial y} = \alpha_3 + \alpha_5 x + 2\alpha_6 y + \alpha_8 x^2 + 2\alpha_9 xy + 3\alpha_{10} y^2 + \alpha_{11} x^3 + 3\alpha_{12} xy^2, \quad (3.20)$$

whereas the rotations of nodal points about y axis from

$$\theta_{y_i} = -\frac{\partial w_i}{\partial x} = -\alpha_2 - 2\alpha_4 x - \alpha_5 y - 3\alpha_7 x^2 - 2\alpha_8 xy - \alpha_9 y^2 + 3\alpha_{11} x^2 y - \alpha_{12} y^3, \quad (3.21)$$

In order to determine unknown vector of parameters  $\alpha$  we substitute the nodal point coordinates  $x_i$  and  $y_i$  are substituted into equations (3.17), (3.20) and (3.21).

$$\mathbf{d}_e = \begin{bmatrix} \mathbf{d}_1 \\ \mathbf{d}_2 \\ \mathbf{d}_3 \\ \mathbf{d}_4 \end{bmatrix} = \begin{bmatrix} w_1 \\ \theta_{x_1} \\ \theta_{y_1} \\ \vdots \\ w_4 \\ \theta_{x_4} \\ \theta_{y_4} \end{bmatrix} = \mathbf{A} \begin{bmatrix} \alpha_1 \\ \vdots \\ \alpha_{12} \end{bmatrix}. \quad (3.22)$$

Here the vector  $\mathbf{d}_e$  contains nodal displacement field in the element, and the explicit form of matrix A is given by

$$\mathbf{A} = \begin{bmatrix} 1 & x_1 & y_1 & x_1^2 & x_1 y_1 & y_1^2 & x_1^3 & x_1^2 y_1 & x_1 y_1^2 & y_1^3 & x_1^3 y_1 & x_1 y_1^3 \\ 0 & 0 & 1 & 0 & x_1 & 2y_1 & 0 & x_1^2 & 2x_1 y_1 & 3y_1^2 & x_1^3 & 3x_1 y_1^2 \\ 0 & -1 & 0 & -2x_1 & -y_1 & 0 & -3x_1^2 & 2x_1 y_1 & -y_1^2 & 0 & -3x_1^2 y_1 & -y_1^3 \\ 1 & x_2 & y_2 & x_2^2 & x_2 y_2 & y_2^2 & x_2^3 & x_2^2 y_2 & x_2 y_2^2 & y_2^3 & x_2^3 y_2 & x_2 y_2^3 \\ 0 & 0 & 1 & 0 & x_2 & 2y_2 & 0 & x_2^2 & 2x_2 y_2 & 3y_2^2 & x_2^3 & 3x_2 y_2^2 \\ 0 & -1 & 0 & -2x_2 & -y_2 & 0 & -3x_2^2 & 2x_2 y_2 & -y_2^2 & 0 & -3x_2^2 y_2 & -y_2^3 \\ 1 & x_3 & y_3 & x_3^2 & x_3 y_3 & y_3^2 & x_3^3 & x_3^2 y_3 & x_3 y_3^2 & y_3^3 & x_3^3 y_3 & x_3 y_3^3 \\ 0 & 0 & 1 & 0 & x_3 & 2y_3 & 0 & x_3^2 & 2x_3 y_3 & 3y_3^2 & x_3^3 & 3x_3 y_3^2 \\ 0 & -1 & 0 & -2x_3 & -y_3 & 0 & -3x_3^2 & 2x_3 y_3 & -y_3^2 & 0 & -3x_3^2 y_3 & -y_3^3 \\ 1 & x_4 & y_4 & x_4^2 & x_4 y_4 & y_4^2 & x_4^3 & x_4^2 y_4 & x_4 y_4^2 & y_4^3 & x_4^3 y_4 & x_4 y_4^3 \\ 0 & 0 & 1 & 0 & x_4 & 2y_4 & 0 & x_4^2 & 2x_4 y_4 & 3y_4^2 & x_4^3 & 3x_4 y_4^2 \\ 0 & -1 & 0 & -2x_4 & -y_4 & 0 & -3x_4^2 & 2x_4 y_4 & -y_4^2 & 0 & -3x_4^2 y_4 & -y_4^3 \end{bmatrix}. \quad (3.23)$$

Thus, coefficient vector  $\alpha$  can be obtained from

$$\alpha = \mathbf{A}^{-1} \mathbf{d}_e. \quad (3.24)$$

By substituting Eq. (3.25) into Eq. (3.18)

$$w(x, y) = \mathbf{N} \mathbf{d}_e, \quad (3.25)$$

where  $\mathbf{N}$  is the shape functions matrix given by

$$\mathbf{N} = \mathbf{w}^T \mathbf{A}^{-1}. \quad (3.26)$$

Now, substituting Eq. (3.25) into Eq. (3.13) the following strain expression is obtained

$$\mathbf{S} = -z \begin{bmatrix} \frac{\partial^2 w}{\partial x^2} \\ \frac{\partial^2 w}{\partial y^2} \\ 2 \frac{\partial^2 w}{\partial x \partial y} \end{bmatrix} \mathbf{A}^{-1} \mathbf{d}_e, \quad (3.27)$$

which, after manipulations results in

$$\mathbf{S} = -z \mathbf{B}_K \mathbf{A}^{-1} \mathbf{d}_e, \quad (3.28)$$

where

$$\mathbf{B}_K = \begin{bmatrix} 0 & 0 & 0 & 2 & 0 & 0 & 6x & 2y & 0 & 0 & 6xy & 0 \\ 0 & 0 & 0 & 0 & 0 & 2 & 0 & 0 & 2x & 6y & 0 & 6xy \\ 0 & 0 & 0 & 0 & 2 & 0 & 0 & 4x & 4y & 0 & 6x^2 & 6y^2 \end{bmatrix}. \quad (3.29)$$

The displacement field  $(u, v, w)$  is now cast into the following vector

$$\mathbf{d} = \begin{bmatrix} w \\ u \\ v \end{bmatrix} = \begin{bmatrix} w \\ -z \frac{\partial w}{\partial x} \\ -z \frac{\partial w}{\partial y} \end{bmatrix}. \quad (3.30)$$

Substituting Eq. (3.54) into (3.30) yields

$$\mathbf{d} = \mathbf{H} \mathbf{B}_M \mathbf{A}^{-1} \mathbf{d}_e, \quad (3.31)$$

where

$$\mathbf{B}_M = \begin{bmatrix} 1 & x & y & x^2 & xy & y^2 & x^3 & x^2y & xy^2 & y^3 & x^3y & xy^3 \\ 0 & 1 & 0 & 2x & y & 0 & 3x^2 & 2xy & y^2 & 0 & 3yx^2 & y^3 \\ 0 & 0 & 1 & 0 & x & 2y & 0 & x^2 & 2xy & 3y^2 & x^3 & 3xy^2 \end{bmatrix}, \quad (3.32)$$

and

$$\mathbf{H} = \begin{bmatrix} 1 & 0 & 0 \\ 0 & -z & 0 \\ 0 & 0 & -z \end{bmatrix}. \quad (3.33)$$

### 3.2.2 Piezoelectric effects on plate

The formulation for the piezoelectric effects on plates is based on the following linear constitutive relations for piezoelectric material

$$\mathbf{T} = -\mathbf{e}_{pe} E_{pe} + \mathbf{c}_{pe}^E \mathbf{S}, \quad (3.34)$$

$$D_{pe} = \varepsilon_{pe}^S E_{pe} + \mathbf{e}_{pe}^T \mathbf{S}, \quad (3.35)$$

where,  $E_{pe} = E_3$  and  $D_{pe} = D_3$  are the electric field and electric displacement components in the direction 3, respectively. Since the electric field generated by the potential difference at the piezoelectric material electrodes is characterised by the same direction as the polarization vector, the vectoral notation of electric field and electric displacement given by

$$\mathbf{E} = \begin{bmatrix} E_1 \\ E_2 \\ E_3 \end{bmatrix} = \begin{bmatrix} 0 \\ 0 \\ E_3 \end{bmatrix}, \quad \mathbf{D} = \begin{bmatrix} D_1 \\ D_2 \\ D_3 \end{bmatrix} = \begin{bmatrix} 0 \\ 0 \\ D_3 \end{bmatrix}, \quad (3.36-3.37)$$

can be replaced by scalars  $E_{pe}$ , and  $D_{pe}$ . Also,  $\mathbf{e}_{pe}$  is the vector with stress / charge constants defined as

$$\mathbf{e}_{pe} = \begin{bmatrix} e_{31} \\ e_{32} \\ 0 \end{bmatrix}, \quad (3.38)$$

and the matrix  $\mathbf{c}_{pe}^E$  contains elastic constants of the piezoelectric material under constant electric field ( $\mathbf{E} = 0$ )

$$\mathbf{c}_{pe}^E = \begin{bmatrix} \frac{Y_{pe}^E}{1-\nu_{pe}^E} & \frac{\nu_{pe}^E Y_{pe}^E}{1-\nu_{pe}^E} & 0 \\ \frac{\nu_{pe}^E Y_{pe}^E}{1-\nu_{pe}^E} & \frac{Y_{pe}^E}{1-\nu_{pe}^E} & 0 \\ 0 & 0 & \frac{Y_{pe}^E}{2(1+\nu_{pe}^E)} \end{bmatrix}. \quad (3.39)$$

Here,  $\nu_{pe}^E$  is the Poisson ratio and  $Y_{pe}^E$  denotes the Young's modulus of the piezoelectric material measured at constant field intensity. Finally,  $\varepsilon_{pe}^S = \varepsilon_{33}^S$  is the piezoelectric material permittivity in transverse direction under constant strain ( $\mathbf{S} = 0$ ).

Since the parameters  $e_{31}$ ,  $e_{32}$ , as well as  $\varepsilon_{33}^S$  are normally not available in commercial datasheets of the piezoelectric ceramics, they must be derived by using the following form of the governing equations

$$\mathbf{S} = \mathbf{d}_{pe} E_{pe} + \mathbf{s}_{pe}^E \mathbf{T}, \quad (3.40)$$

$$D_{pe} = \varepsilon_{pe}^T E_{pe} + \mathbf{d}_{pe}^T \mathbf{T}, \quad (3.41)$$

where  $\mathbf{d}_{pe}$  is the vector with piezoelectric strain / charge constants

$$\mathbf{d}_{pe} = \begin{bmatrix} d_{31} \\ d_{32} \\ 0 \end{bmatrix}, \quad (3.42)$$

and  $\mathbf{s}_{pe}^E$  gives the compliance constants for the piezoelectric material

$$\mathbf{s}_{pe}^E = \begin{bmatrix} \frac{1}{Y_{pe}^E} & -\frac{\nu_{pe}^E}{Y_{pe}^E} & 0 \\ -\frac{\nu_{pe}^E}{Y_{pe}^E} & \frac{1}{Y_{pe}^E} & 0 \\ 0 & 0 & \frac{2(1+\nu_{pe}^E)}{Y_{pe}^E} \end{bmatrix}. \quad (3.43)$$

Finally,  $\varepsilon_{pe}^T$  is the permittivity of piezoelectric material in transverse direction under constant stress ( $\mathbf{T} = 0$ ).

The values of the piezoelectric material permittivity under constant strain  $\varepsilon_{pe}^S$  and the values contained in the vector  $\mathbf{e}_{pe}$  can now be obtain by setting stress vector  $\mathbf{T}$  to zero in Eqs. (2.13), (2.14), (2.17) and (2.18):

$$0 = -\mathbf{e}_{pe} E_{pe} + \mathbf{c}_{pe}^E \mathbf{S}, \quad (3.44)$$

$$D_{pe} = \varepsilon_{pe}^S E_{pe} + \mathbf{e}_{pe}^T \mathbf{S}, \quad (3.45)$$

$$\mathbf{S} = \mathbf{d}_{pe} E_{pe}, \quad (3.46)$$

$$D_{pe} = \varepsilon_{pe}^T E_{pe}. \quad (3.47)$$

Substituting Eq. (2.23) into (2.21) yields

$$\mathbf{e}_{pe} = \mathbf{c}_{pe}^E \mathbf{d}_{pe}. \quad (3.48)$$

Also substituting Eqs. (2.23), (2.24) and (2.25) to Eq. (2.22) gives

$$\varepsilon_{pe}^S = \varepsilon_{pe}^T (1 - k^2), \quad (3.49)$$

where,  $k$  denotes the electromechanical coupling coefficient [15,73] of the piezoelectric material and can be defined as

$$k^2 = \frac{\mathbf{e}_{pe}^T \mathbf{c}_{pe}^E \mathbf{d}_{pe}}{\varepsilon_{pe}^T}. \quad (3.50)$$

Application of a potential difference to piezoelectric materials electrodes forces the plate lower layer to expand and upper layer to contract, resulting in a curvature. The inverse effect will generate a charge across the electrodes, which is collected through the surface as a voltage.

Considering only the poling direction, the applied or induced voltage through the piezoelectric transducer is given by the following relation [74].

$$v_{pe_z} = \frac{\left(z - \frac{h_p}{2}\right)}{h_{pe}} v_{pe} , \quad (3.51)$$

where  $h_p$  and  $h_{pe}$  are thicknesses of the plate and piezoelectric patch and  $v_{pe}$  is the maximum electric potential at the external surfaces of the piezoelectric layer, while  $z$  is defined as

$$\frac{h_p}{2} \leq z \leq \frac{h_p}{2} + h_{pe} . \quad (3.52)$$

Assuming the electric field to be constant through the piezoelectric layer, the following relation can be written

$$E_{pe} = -\frac{\partial v_{pe_z}}{\partial z} = -\frac{v_{pe}}{h_{pe}} . \quad (3.53)$$

### 3.2.3 Hamilton's principle

Hamilton's principle is used here to derive the set of equations governing the finite plate element with a piezoelectric transducer layer [73, 88, 89]. In this case the functional of the Lagrangian can be written as follows

$$\delta S = \int_{t_1}^{t_2} [\delta(T^* - V + W_e^*) + \delta W_{nc}] dt = 0 , \quad (3.54)$$

where  $\delta$  is the variation operator,  $T^*$  is the kinetic co-energy  $V$  is the elastic potential energy and  $\delta W_{nc}$  stands for the virtual work done by non-conservative forces:

$$T^* = \frac{1}{2} \int_{V_p} \rho_p \mathbf{d}^T \mathbf{d} dV_p + \frac{1}{2} \int_{V_{pe}} \rho_{pe} \mathbf{d}^T \mathbf{d} dV_{pe} , \quad (3.55)$$

$$V = \frac{1}{2} \int_{V_p} \mathbf{S}^T \mathbf{T} dV_p + \frac{1}{2} \int_{V_{pe}} \mathbf{S}^T \mathbf{T} dV_{pe} , \quad (3.56)$$

$$W_e^* = \frac{1}{2} \int_{V_{pe}} E_{pe} D_{pe} dV_{pe} , \quad (3.57)$$

$$W_{nc} = \int_{A_p} \mathbf{d}^T \mathbf{f}_s A_p + \int_{V_p} \mathbf{d}^T \mathbf{f}_b V_p - \int_{A_{pe}} \sigma v_{pe} A_{pe} , \quad (3.58)$$

where,  $dV_p$  and  $dV_{pe}$  are given by

$$dV_p = \int_{-h_p/2}^{h_p/2} \int_{-a}^a \int_{-b}^b dx dy dz , \quad (3.59)$$

$$dV_{pe} = \int_{h_p/2}^{h_p/2+h_{pe}} \int_{-a}^a \int_{-b}^b dx dy dz , \quad (3.60)$$

Substituting Eqs. (3.14) and (2.13) into Eq. (3.56) results in

$$V = \frac{1}{2} \int_{V_p} \mathbf{S}^T \mathbf{c}_p \mathbf{S} dV_p + \frac{1}{2} \int_{V_{pe}} \mathbf{S}^T \mathbf{c}_{pe}^E \mathbf{S} dV_{pe} - \frac{1}{2} \int_{V_{pe}} \mathbf{S}^T \mathbf{e}_{pe} E_{pe} dV_{pe} , \quad (3.61)$$

Finally, by substituting Eq. (2.14) into (3.57) gives:

$$W_e^* = \frac{1}{2} \int_{V_{pe}} E_{pe} \varepsilon_{pe}^S E_{pe} dV_{pe} + \frac{1}{2} \int_{V_{pe}} E_{pe} \mathbf{e}_{pe}^T \mathbf{S} dV_{pe} . \quad (3.62)$$

### 3.2.4 Variation indicator

The variations of the Lagrangian and the work done by the non-conservative forces can be calculated with the following exact differentiations:

$$\delta L = \frac{\partial L}{\partial \mathbf{d}} \delta \mathbf{d} + \frac{\partial L}{\partial \mathbf{S}} \delta \mathbf{S} + \frac{\partial L}{\partial E_{pe}} \delta E_{pe} , \quad (3.63)$$

$$\delta W_{nc} = \frac{\partial W_{nc}}{\partial \mathbf{d}} \delta \mathbf{d} + \frac{\partial W_{nc}}{\partial v_{pe}} \delta v_{pe} . \quad (3.64)$$

$$\delta T^* = \frac{\partial T^*}{\partial \mathbf{d}} \delta \mathbf{d} + \frac{\partial T^*}{\partial \mathbf{S}} \delta \mathbf{S} + \frac{\partial T^*}{\partial E_{pe}} \delta E_{pe} , \quad (3.65)$$

$$\delta V = \frac{\partial V}{\partial \mathbf{d}} \delta \mathbf{d} + \frac{\partial V}{\partial \mathbf{S}} \delta \mathbf{S} + \frac{\partial V}{\partial E_{pe}} \delta E_{pe} , \quad (3.66)$$

$$\delta W_e^* = \frac{\partial W_e^*}{\partial \mathbf{d}} \delta \mathbf{d} + \frac{\partial W_e^*}{\partial \mathbf{S}} \delta \mathbf{S} + \frac{\partial W_e^*}{\partial E_{pe}} \delta E_{pe} . \quad (3.67)$$

Solving Eqs. (3.64)-(3.67) results in

$$\frac{\partial W_{nc}}{\partial \mathbf{d}} \delta \mathbf{d} = \int_{A_p} \delta \mathbf{d}^T \mathbf{f}_s A_p + \int_{V_p} \delta \mathbf{d}^T \mathbf{f}_b V_p , \quad (3.68)$$

$$\frac{\partial W_{nc}}{\partial v_{pe}} \delta v_{pe} = - \int_{A_{pe}} \sigma \delta v_{pe} A_{pe} , \quad (3.69)$$

$$\frac{\partial T^*}{\partial \mathbf{d}} \delta \mathbf{d} = \int_{V_p} \rho_p \delta \mathbf{d}^T \mathbf{d} dV_p + \int_{V_{pe}} \rho_{pe} \delta \mathbf{d}^T \mathbf{d} dV_{pe} , \quad (3.70)$$

$$\frac{\partial T^*}{\partial \mathbf{S}} \delta \mathbf{S} = 0 , \quad (3.71)$$

$$\frac{\partial T^*}{\partial E_{pe}} \delta E_{pe} = 0 , \quad (3.72)$$

$$\frac{\partial V}{\partial \mathbf{d}} \delta \mathbf{d} = 0 , \quad (3.73)$$

$$\frac{\partial V}{\partial \mathbf{S}} \delta \mathbf{S} = \int_{V_p} \delta \mathbf{S}^T \mathbf{c}_p \mathbf{S} dV_p + \int_{V_{pe}} \delta \mathbf{S}^T \mathbf{c}_{pe}^E \mathbf{S} dV_{pe} - \frac{1}{2} \int_{V_{pe}} \delta \mathbf{S}^T \mathbf{e}_{pe} E_{pe} dV_{pe} , \quad (3.74)$$

$$\frac{\partial V}{\partial E_{pe}} \delta E_{pe} = -\frac{1}{2} \int_{V_{pe}} \mathbf{S}^T \mathbf{e}_{pe} \delta E_{pe} dV_{pe} , \quad (3.75)$$

$$\frac{\partial W_e^*}{\partial \mathbf{d}} \delta \mathbf{d} = 0 , \quad (3.76)$$

$$\frac{\partial W_e^*}{\partial \mathbf{S}} \delta \mathbf{S} = +\frac{1}{2} \int_{V_{pe}} E_{pe} \mathbf{e}_{pe}^T \delta \mathbf{S} dV_{pe} , \quad (3.77)$$

$$\frac{\partial W_e^*}{\partial E_{pe}} \delta E_{pe} = \int_{V_{pe}} \delta E_{pe} \varepsilon_{pe}^S E_{pe} dV_{pe} + \frac{1}{2} \int_{V_{pe}} \delta E_{pe} \mathbf{e}_{pe}^T \mathbf{S} dV_{pe} . \quad (3.78)$$

The Lagrangian variation is then given by the sum of all terms in Eqs. (3.68) to (3.78):

$$\begin{aligned} & \int_{t_1}^{t_2} \left[ \int_{V_p} \rho_p \delta \mathbf{d}^T \dot{\mathbf{d}} dV_p + \int_{V_{pe}} \rho_{pe} \delta \mathbf{d}^T \dot{\mathbf{d}} dV_{pe} - \int_{V_p} \delta \mathbf{S}^T \mathbf{c}_p \mathbf{S} dV_p \right. \\ & \quad - \int_{V_{pe}} \delta \mathbf{S}^T \mathbf{c}_{pe}^E \mathbf{S} dV_{pe} + \frac{1}{2} \int_{V_{pe}} \delta \mathbf{S}^T \mathbf{e}_{pe} E_{pe} dV_{pe} + \\ & \quad + \frac{1}{2} \int_{V_{pe}} \mathbf{S}^T \mathbf{e}_{pe} \delta E_{pe} dV_{pe} + \frac{1}{2} \int_{V_{pe}} E_{pe} \mathbf{e}_{pe}^T \delta \mathbf{S} dV_{pe} + \\ & \quad + \int_{V_{pe}} \delta E_{pe} \varepsilon_{pe}^S E_{pe} dV_{pe} + \frac{1}{2} \int_{V_{pe}} \delta E_{pe} \mathbf{e}_{pe}^T \mathbf{S} dV_{pe} + \\ & \quad \left. + \int_{A_p} \delta \mathbf{d}^T \mathbf{f}_s A_p + \int_{V_p} \delta \mathbf{d}^T \mathbf{f}_b V_p - \int_{A_{pe}} \sigma \delta v_{pe} A_{pe} \right] dt = 0 . \end{aligned} \quad (3.79)$$

Since  $\mathbf{S}$  and  $\mathbf{e}_{pe}$  are vectors, Eq. (3.79) can be simplified

$$\begin{aligned} & \int_{t_1}^{t_2} \left[ \int_{V_p} \rho_p \delta \mathbf{d}^T \dot{\mathbf{d}} dV_p + \int_{V_{pe}} \rho_{pe} \delta \mathbf{d}^T \dot{\mathbf{d}} dV_{pe} - \int_{V_p} \delta \mathbf{S}^T \mathbf{c}_p \mathbf{S} dV_p + \right. \\ & \quad \left. + \int_{V_{pe}} (\delta \mathbf{S}^T \mathbf{e}_{pe} E_{pe} - \delta \mathbf{S}^T \mathbf{c}_{pe}^E \mathbf{S} + \delta E_{pe} \varepsilon_{pe}^S E_{pe} + \delta E_{pe} \mathbf{e}_{pe}^T \mathbf{S}) dV_{pe} + \right. \\ & \quad \left. + \int_{A_p} \delta \mathbf{d}^T \mathbf{f}_s A_p + \int_{V_p} \delta \mathbf{d}^T \mathbf{f}_b V_p - \int_{A_{pe}} \sigma \delta v_{pe} A_{pe} \right] dt = 0 . \end{aligned} \quad (3.80)$$

Variation and differentiation operators are commutative; therefore, integration by parts of the first two terms yields

$$\begin{aligned} & \int_{t_1}^{t_2} \left[ - \int_{V_p} \rho_p \delta \mathbf{d}^T \ddot{\mathbf{d}} dV_p - \int_{V_{pe}} \rho_{pe} \delta \mathbf{d}^T \ddot{\mathbf{d}} dV_{pe} - \int_{V_p} \delta \mathbf{S}^T \mathbf{c}_p \mathbf{S} dV_p + \right. \\ & \quad \left. + \int_{V_{pe}} (\delta \mathbf{S}^T \mathbf{e}_{pe} E_{pe} - \delta \mathbf{S}^T \mathbf{c}_{pe}^E \mathbf{S} + \delta E_{pe} \varepsilon_{pe}^S E_{pe} + \delta E_{pe} \mathbf{e}_{pe}^T \mathbf{S}) dV_{pe} + \right. \\ & \quad \left. + \int_{A_p} \delta \mathbf{d}^T \mathbf{f}_s A_p + \int_{V_p} \delta \mathbf{d}^T \mathbf{f}_b V_p - \int_{A_{pe}} \sigma \delta v_{pe} A_{pe} \right] dt = 0 . \end{aligned} \quad (3.81)$$

Note that  $\delta \mathbf{d}^T = 0$ , for  $t = t_1$  and  $t = t_2$ . Now, substitution of Eqs. (3.28) (3.31) and (2.30) leads to

$$\int_{t_1}^{t_2} \{ \delta \mathbf{d}_k^T [ (\mathbf{M}_p + \mathbf{M}_{pe}) \ddot{\mathbf{d}}_k + (\mathbf{K}_p + \mathbf{K}_{pe}) \mathbf{d}_k + \boldsymbol{\theta}_{pe} v_{pe} - \mathbf{f} ] + \delta v_{pe} [ \boldsymbol{\theta}_{pe}^T \mathbf{d}_k + C_{pe} v_{pe} + q ] \} dt = 0 . \quad (3.82)$$

Here,

$$\mathbf{M}_p = \rho_p \int_{V_p} \mathbf{A}^{-T} \mathbf{B}_M^T \mathbf{H}^T \mathbf{H} \mathbf{B}_M \mathbf{A}^{-1} dV_p \quad (3.83)$$

$$\mathbf{M}_{pe} = \rho_{pe} \int_{V_{pe}} \mathbf{A}^{-T} \mathbf{B}_M^T \mathbf{H}^T \mathbf{H} \mathbf{B}_M \mathbf{A}^{-1} dV_{pe} , \quad (3.84)$$

$$\mathbf{K}_p = \mathbf{A}^{-T} \int_{V_p} z^2 \mathbf{B}_K^T \mathbf{c}_p \mathbf{B}_K \mathbf{A}^{-1} dV_p , \quad (3.85)$$

$$\mathbf{K}_{pe} = \mathbf{A}^{-T} \int_{V_{pe}} z^2 \mathbf{B}_K^T \mathbf{c}_{pe}^E \mathbf{B}_K \mathbf{A}^{-1} dV_{pe} , \quad (3.86)$$

$$\boldsymbol{\theta}_{pe} = - \int_{V_{pe}} \frac{1}{h_{pe}} z \mathbf{e}_{pe}^T \mathbf{B}_K \mathbf{A}^{-1} dV_{pe} , \quad (3.87)$$

$$C_{pe} = \int_{V_{pe}} \frac{1}{h_{pe}^2} \varepsilon_{pe}^S dV_{pe} , \quad (3.88)$$

$$q = \int_{A_{pe}} \sigma A_{pe} . \quad (3.89)$$

$$\mathbf{f} = \int_{A_{pe}} \mathbf{f}_s dA_p + \int_{V_{pe}} \mathbf{f}_b dV_p , \quad (3.90)$$

Breaking the volume integrals from Eqs. (3.85) and (3.86) into products of area and thickness integrals and solving those thickness integrals gives the following expressions for the stiffness matrices

$$\mathbf{K}_p = h_1 \mathbf{A}^{-T} \int_{A_p} \mathbf{B}_K^T \mathbf{c}_p \mathbf{B}_K \mathbf{A}^{-1} dV_p , \quad (3.91)$$

$$\mathbf{K}_{pe} = h_2 \mathbf{A}^{-T} \int_{A_{pe}} \mathbf{B}_K^T \mathbf{c}_{pe}^E \mathbf{B}_K \mathbf{A}^{-1} dA_{pe} , \quad (3.92)$$

where

$$h_1 = \int_{-\frac{1}{2}h_p}^{\frac{1}{2}h_p} z^2 dz = \frac{h_p^3}{12} , \quad (3.93)$$

$$h_2 = \int_{\frac{1}{2}h_p}^{\frac{1}{2}h_p + h_{pe}} z^2 dz = h_{pe} \left( \frac{h_p}{2} + \frac{h_{pe}}{2} \right)^2 + \frac{h_{pe}^3}{12} . \quad (3.94)$$

Similarly, integration in the  $z$  direction, Eqs. (3.84) and (3.85) results in the mass matrix expressions

$$\mathbf{M}_p = \rho_p \int_{A_p} \mathbf{A}^{-T} \mathbf{B}_M^T \mathbf{H}_p \mathbf{B}_M \mathbf{A}^{-1} dA_p, \quad (3.95)$$

$$\mathbf{M}_{pe} = \rho_{pe} \int_{A_{pe}} \mathbf{A}^{-T} \mathbf{B}_M^T \mathbf{H}_{pe} \mathbf{B}_M \mathbf{A}^{-1} dA_{pe}, \quad (3.96)$$

where matrices  $\mathbf{H}_p$  and  $\mathbf{H}_{pe}$  are given by

$$\mathbf{H}_p = \begin{bmatrix} h_p & & \\ & h_1 & \\ & & h_1 \end{bmatrix}, \quad \mathbf{H}_{pe} = \begin{bmatrix} h_{pe} & & \\ & h_2 & \\ & & h_2 \end{bmatrix}. \quad (3.97- 3.98)$$

Now, integration in the  $z$  direction Eq. (3.87) gives

$$\boldsymbol{\theta}_{pe} = -\frac{1}{2}(h_p + h_{pe}) \int_{A_{pe}} \mathbf{e}_{pe}^T \mathbf{B}_K \mathbf{A}^{-1} dA_{pe}. \quad (3.99)$$

Finally integrating Eq. (3.88) over the volume of piezoelectric element results in

$$C_{pe} = \frac{4ab\epsilon_{pe}^S}{h_{pe}}. \quad (3.100)$$

Allowing arbitrary variations of  $\mathbf{d}_k(t)$  and  $v_{pe}(t)$ , such that  $\mathbf{d}_k = 0$  for  $t = t_1, t = t_2$ , Eq. (3.82) leads to the following two matrix equations:

$$(\mathbf{M}_p + \mathbf{M}_{pe})\ddot{\mathbf{d}}_k + (\mathbf{K}_p + \mathbf{K}_{pe})\mathbf{d}_k + \boldsymbol{\theta}_{pe}v_{pe} - \mathbf{f} = \mathbf{0}, \quad (3.101)$$

$$\boldsymbol{\theta}_{pe}^T \mathbf{d}_k + C_{pe}v_{pe} + q = 0. \quad (3.102)$$

### 3.3 DISPERSION PROPERTIES

In this section an infinite, two-dimensional periodic material is considered, which consists of a thin aluminium substrate with arrays of periodic inclusions. Inclusions were chosen to be point masses, spring-mass vibration absorbers and shunted piezoelectric patch transducers. The dispersion relations for an infinite plate with periodic arrays of inclusions are calculated considering a free wave propagation. In periodic media, a free wave propagation can be conveniently investigated by analysing the dynamics of a single unit cell. For this purpose, real parts of the propagation vectors are always set to zero, i.e.

$$\boldsymbol{\mu} = [\mu_x, \mu_y] = [0 + j\epsilon_x, 0 + j\epsilon_y]. \quad (3.103)$$

where,  $\epsilon_x = k_x L$  and  $\epsilon_y = k_y L$  are equal to the wavenumber component in propagation direction multiplied by the spatial period of the unit cell. Purely imaginary propagation vectors correspond to waves which are propagating freely,

without amplitude attenuation as elastic waves propagate from one cell to the other. In this respect, the finite element method has been used to model the dynamics of the unit cells composed of  $10 \times 10$ , 4-nodes, 12-degrees of freedom Kirchhoff plate elements. The material and geometrical properties used for these studies are summarized in Table 3.1.

Table 3.1. Physical and geometrical parameters of the plate and piezoelectric patches.

Parameter	Plate	Piezoelectric patch
Thickness	$h_p = 1 \text{ mm}$	$h_{pe} = 1 \text{ mm}$
Area	$A_p = 10 \text{ cm} \times 10 \text{ cm}$	$A_{pe} = 4 \text{ cm} \times 4 \text{ cm}$
Density	$\rho_p = 2700 \text{ kg/m}^3$	$\rho_{pe} = 7600 \text{ kg/m}^3$
Young's modulus	$Y_p = 7 \times 10^{10} \text{ N/m}^2$	$Y_{pe} = 2.7 \times 10^{10} \text{ N/m}^2$
Poisson's ratio	$\nu_p = 0.33$	$\nu_{pe} = 0.275$
strain/charge constants		$d_{31}^0 = 150 \times 10^{-12} \text{ m/V}$ $d_{32}^0 = 150 \times 10^{-12} \text{ m/V}$ $d_{36}^0 = 0$
permittivity		$\epsilon_{pe} = 84 \times 10^{-9} \text{ F/m}$
capacitance		$C_{pe} = 3.167 \times 10^{-9} \text{ F}$
Lattice constant	10 cm	

### 3.3.1 Infinite plate with no inclusions

The governing equation for the undamped plate unit is given by the following relation

$$\mathbf{M}_p \ddot{\mathbf{d}} + \mathbf{K}_p \mathbf{d} = \mathbf{f}. \quad (3.104)$$

Here,  $\mathbf{d} = [\mathbf{d}_i \ \mathbf{d}_b \ \mathbf{d}_t \ \mathbf{d}_l \ \mathbf{d}_r \ \mathbf{d}_{lb} \ \mathbf{d}_{rb} \ \mathbf{d}_{lt} \ \mathbf{d}_{rt}]^T$  is the vector of nodal displacements, partitioned according to the nodal positions illustrated in Figure 3.2 (a). Also,  $\mathbf{f} = [\mathbf{f}_i \ \mathbf{f}_b \ \mathbf{f}_t \ \mathbf{f}_l \ \mathbf{f}_r \ \mathbf{f}_{lb} \ \mathbf{f}_{rb} \ \mathbf{f}_{lt} \ \mathbf{f}_{rt}]^T$  is the corresponding vector of nodal forces. Structural mass and stiffness matrices are defined in Eq. (3.91) and (3.95).

Assuming harmonic motion at frequency  $\omega$  Eq. (3.104) turns into

$$(\mathbf{K}_{uu} - \omega^2 \mathbf{M}_{uu}) \mathbf{d} = \mathbf{f}. \quad (3.105)$$

Application of the Bloch theorem yields

$$\mathbf{d}_t = \mathbf{I} e^{jk_y L} \mathbf{d}_b, \quad (3.106)$$

$$\mathbf{d}_r = \mathbf{I}e^{jk_x L} \mathbf{d}_l, \quad (3.107)$$

$$\mathbf{d}_{lt} = \mathbf{I}e^{jk_y L} \mathbf{d}_{lb}, \quad (3.108)$$

$$\mathbf{d}_{rb} = \mathbf{I}e^{jk_x L} \mathbf{d}_{lb}, \quad (3.109)$$

$$\mathbf{d}_{rt} = \mathbf{I}e^{j(k_x+k_y)L} \mathbf{d}_{lb}, \quad (3.110)$$

and

$$\mathbf{f}_b + e^{-jk_y L} \mathbf{f}_t = \mathbf{0}, \quad (3.111)$$

$$\mathbf{f}_l + e^{-jk_x L} \mathbf{f}_r = \mathbf{0}, \quad (3.112)$$

$$\mathbf{f}_{lb} + e^{-jk_x L} \mathbf{f}_{rb} + e^{-jk_y L} \mathbf{f}_{lt} + e^{-j(k_x+k_y)L} \mathbf{f}_{rt}, \quad (3.113)$$

where  $k_x L$  and  $k_y L$  are the propagation wave vector components in x and y directions and  $L$  is the length of a unit cell. Note that, since a free wave propagation is considered only purely imaginary propagation vectors are utilized.

Using the relations (3.106)-(3.113) the following transfer matrix can be defined

$$\mathbf{T} = \begin{bmatrix} \mathbf{I} & \mathbf{0} \\ \mathbf{0} & \mathbf{I} & \mathbf{I}e^{jk_y L} & \mathbf{0} & \mathbf{0} & \mathbf{0} & \mathbf{0} & \mathbf{0} & \mathbf{0} \\ \mathbf{0} & \mathbf{0} & \mathbf{0} & \mathbf{I} & \mathbf{I}e^{jk_x L} & \mathbf{0} & \mathbf{0} & \mathbf{0} & \mathbf{0} \\ \mathbf{0} & \mathbf{0} & \mathbf{0} & \mathbf{0} & \mathbf{0} & \mathbf{I} & \mathbf{I}e^{jk_x L} & \mathbf{I}e^{jk_y L} & \mathbf{I}e^{j(k_x+k_y)L} \end{bmatrix}^T, \quad (3.114)$$

for the displacement vector transformation

$$\mathbf{d} = \mathbf{T} \mathbf{d}_{re}, \quad (3.115)$$

Where  $\mathbf{d}_{re} = [\mathbf{d}_i \ \mathbf{d}_b \ \mathbf{d}_l \ \mathbf{d}_{lb}]^T$  is the reduced displacement vector. Substituting Eq. (3.114) into Eq. (3.105) yields

$$(\mathbf{K}_p \mathbf{T} - \omega^2 \mathbf{M}_p \mathbf{T}) \mathbf{d}_{re} = \mathbf{f}. \quad (3.116)$$

Pre-multiplying the above equation by  $\mathbf{T}^H$  imposes force equilibrium condition at the boundaries between the unit cells and leads to

$$(\mathbf{T}^H \mathbf{K}_p \mathbf{T} - \omega^2 \mathbf{T}^H \mathbf{M}_p \mathbf{T}) \mathbf{d}_{re} = \mathbf{T}^H \mathbf{f}. \quad (3.117)$$

Here,  $\mathbf{K}_e = \mathbf{T}^H \mathbf{K}_p \mathbf{T}$  and  $\mathbf{M}_{re} = \mathbf{T}^H \mathbf{M}_p \mathbf{T}$  are reduced stiffness and mass matrices and  $\mathbf{f}_{re} = \mathbf{T}^H \mathbf{f}$  is the reduced force vector. Superscript  $^H$  denotes the Hermitian transpose.

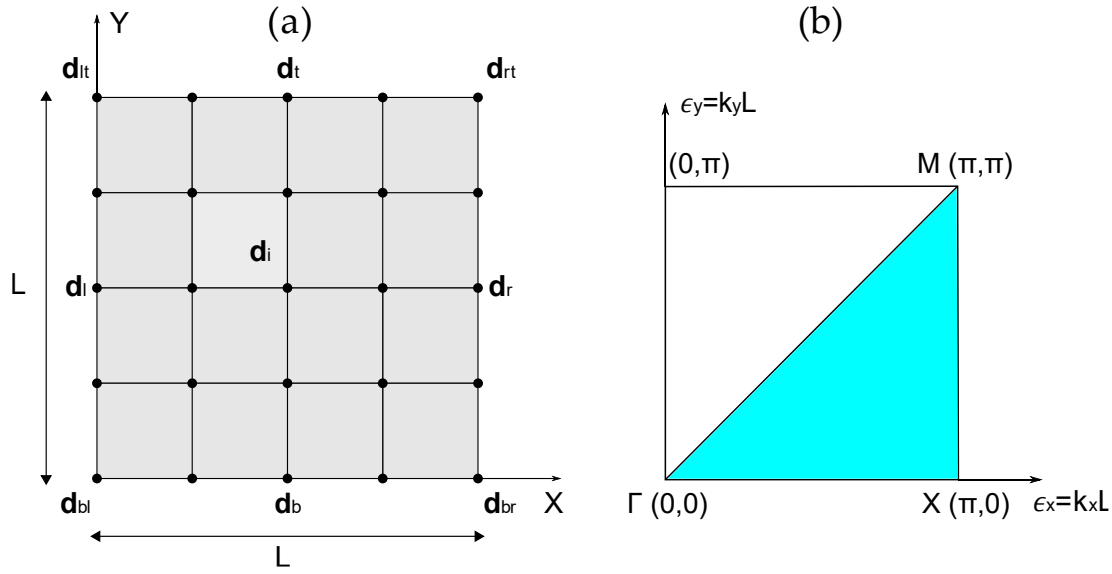


Figure 3.2 (a) Depiction of a unit cell comprising FEM mesh (b) Reciprocal space with irreducible Brillouin zone indicated by blue color.

Under the assumption of no external forces applied on the internal nodes  $\mathbf{f}_{re} = \mathbf{0}$ , Eq. (3.119) becomes the linear eigenvalue problem of the form

$$(\mathbf{K}_{re} - \omega^2 \mathbf{M}_{re}) \mathbf{d}_{re} = \mathbf{0} . \quad (3.118)$$

Eq. (3.118) can be solved to obtain dispersion relations for given propagation direction  $\epsilon = [\epsilon_x \ \epsilon_y]$ , where  $\epsilon_x = k_x L$  and  $\epsilon_y = k_y L$ . To ensure completeness of the band structure of the two-dimensional lattice, it is necessary to solve the eigenvalue problem for all  $\epsilon$  belonging to the irreducible Brillouin zone indicated by blue colour in Figure 3.2 (b) [83,84]. However, in this case, due to axial symmetries and angular symmetry of the unit cell it is sufficient to solve only for vectors belonging to irreducible Brillouin contour:  $\Gamma(0,0) \rightarrow X(0,\pi) \rightarrow M(\pi,\pi) \rightarrow \Gamma(0,0)$  [84]. Solving eigenvalue problems for the vectors comprised in the irreducible Brillouin contour, the frequency zones of free wave propagation are acquired. Frequency bands that are not the solutions to the eigenvalue problem are the frequencies at which waves cannot propagate without attenuation and thus belong to the stop band effects.

Figure 3.3 (a) shows the dispersion curves obtained for an infinite uniform plate with reference to the vectors belonging to irreducible Brillouin contour and frequency ratio

$$\Omega = \frac{\omega}{\omega_B} , \quad (3.119)$$

where  $\omega_B$  is the so-called Bragg frequency and defines the frequency at which the flexural wavelength on the plate equals the separation distance between the centres of two consecutive unit cells.

$$\omega_B = \frac{2\pi^2}{2L_{cell}^2} \sqrt{\frac{h_p^2 Y_p}{12\rho_p(1-\nu_p^2)}} \quad (3.120)$$

Expressing the frequencies as ratios, makes the result independent from the unit cell length.

As can be seen from Figure 3.3 (a) every dimensionless frequency can be associated with the wave vector belonging to irreducible Brillouin contour, thus the stop band phenomenon does not occur in this structure. The visualisations of the displacement patterns related to particular points (propagation vectors) on the dispersion diagram are depicted in Figure 3.4. Here, plot (b) depicts no propagation, since both propagation vector components are equal to zero. Plot (c) depicts propagation in x direction with a spatial periodicity equal to  $\frac{\pi}{2}$  per unit cell length. Plot d illustrates the propagation along the x axis when the spatial period reaches  $\pi$  over a unit cell length. In contrast to the previous ones, plots e and f illustrate wave propagation in both directions, with spatial periods across the unit cell equal to  $[\frac{\pi}{2}, \pi]$  and  $[\pi, \pi]$ , respectively.

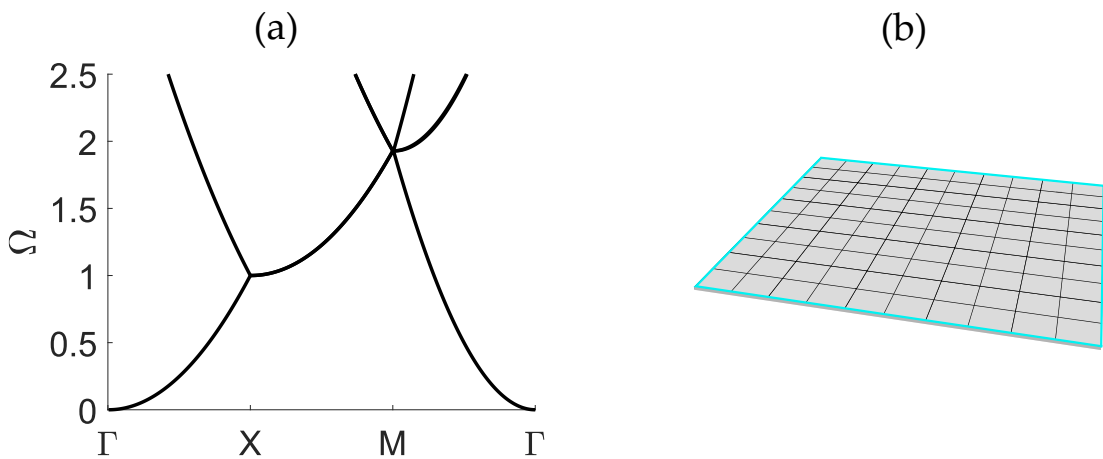


Figure 3.3 (a) Dispersion curves for a uniform infinite plate; (b) Depiction of the unit cell.

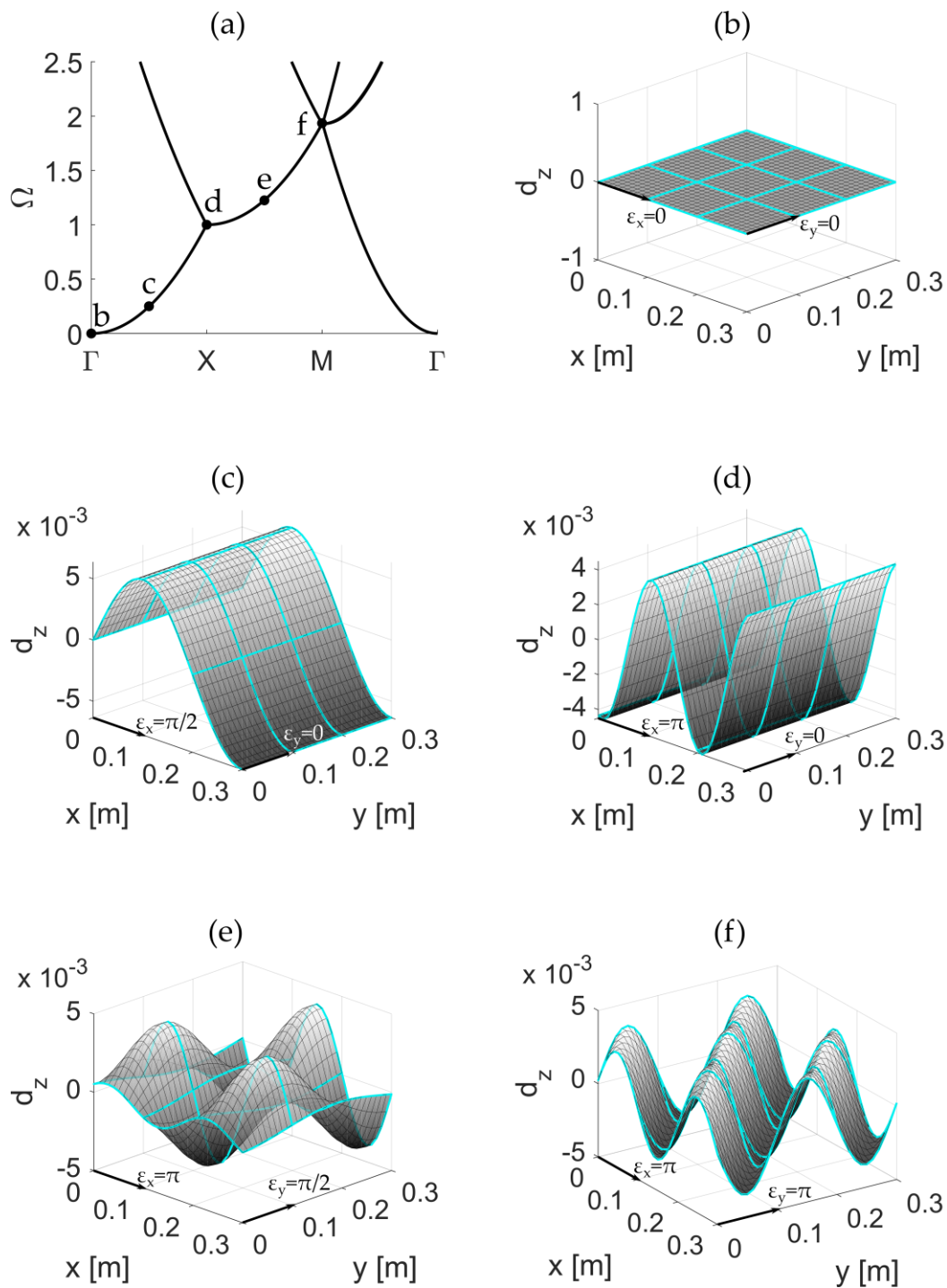


Figure 3.4 Displacement patterns for 9 unit cells of a uniform, infinite plate. The visualized displacement patterns: (b), (c), (d), (e), (f) correspond to the points indicated with black dots on dispersion diagram in plot (a).

### 3.3.2 Infinite plate with regular array of point masses

Addition of periodic point masses to a plate structure creates impedance mismatch zones and give foundations for the interference stop band effect.

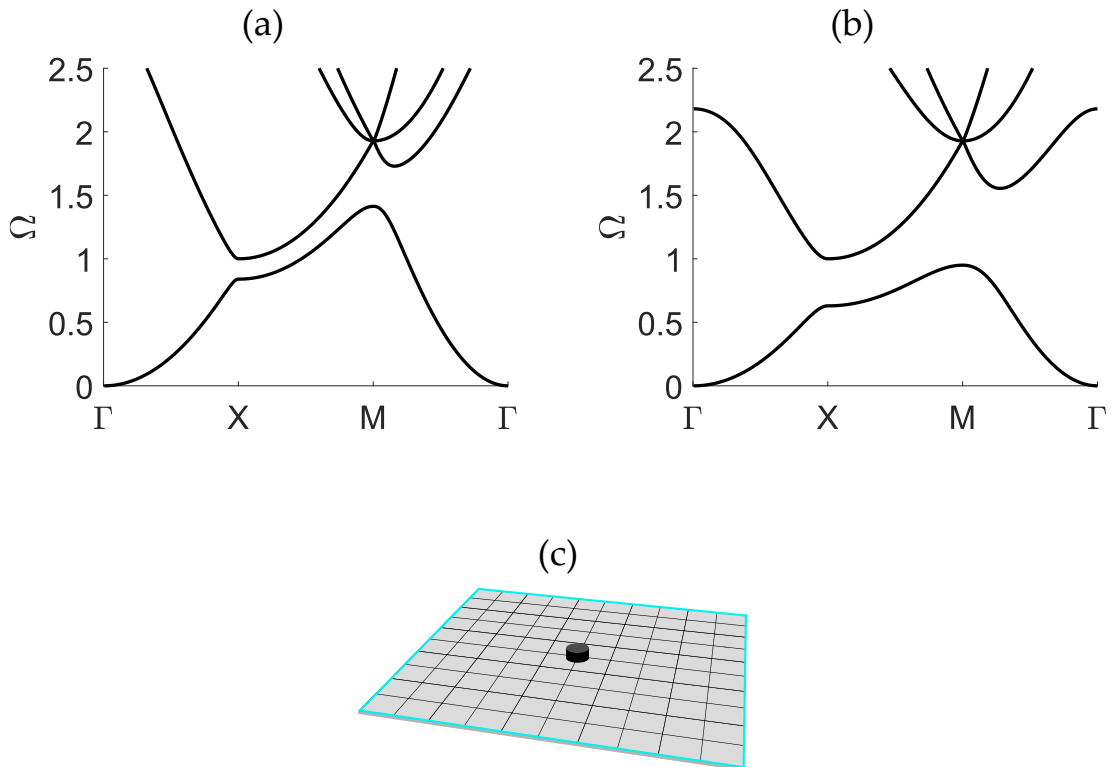


Figure 3.5 Dispersion curves for an infinite plate with periodic point mass equal to 20% (a) and 70% (b) of the mass of the unit cell. (c) Depiction of the unit cell.

Figure 3.5 (a) and (b), presents dispersion curves for an infinite plate equipped with periodic point masses equal to 20% and 70% of the unit cell mass. As can be noticed from plot (a), the addition of point mass creates an opening for dimensionless frequencies from about 0.8 to 1 for point  $X(0, \pi)$  of irreducible Brillouin contour, indicating a frequency zone for which the free wave propagation in  $\Gamma \rightarrow X$  direction is stopped. A similar effect is visible for point  $M(\pi, \pi)$  for dimensionless frequencies of 1.4 to 1.8, leading to the conclusion that a free wave propagation in certain directions is prohibited, but not in all directions due to the significant mismatch between frequency zones in which the openings occur for X and M.

Increasing the point mass to 70% of the unit cell mass creates wider openings at points  $X(0, \pi)$  and  $M(\pi, \pi)$ , and the frequency zones associated with openings partially overlap allowing the stop band effect to develop within dimensionless frequency between 0.9 and 1. Due to rather significant mass required to achieve this effect, generation of stop bands in this way appears to be rather impractical.

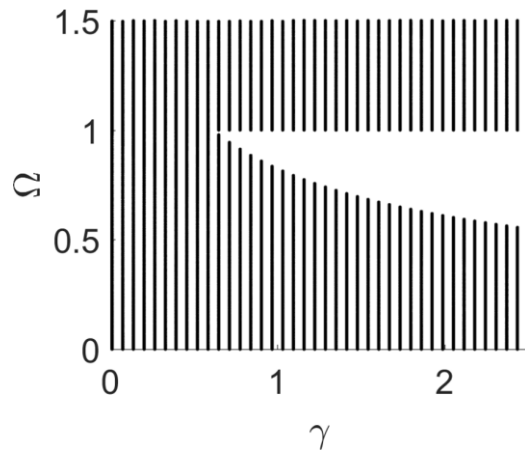


Figure 3.6 Relation between added discrete mass and distribution of the stop band effect.

Figure 3.6 shows the relationship between dimensionless mass defined as the ratio of discrete mass and mass of the unit cell

$$\gamma = \frac{m_d}{m_{cell}}, \quad (3.121)$$

and the frequency distribution of the stop band effect. According to Figure 3.6 waves can propagate in the frequency ranges associated with black vertical lines, while the white opening refers to the frequencies at which propagation in every direction is stopped.

It is easy to notice that the upper frequency of the stop band effect ( $\Omega = 1$ ) does not vary despite of the increasing mass, which can be explained by the scatterers being in nodal positions [63, 78]. Thus, at frequencies higher than 1 waves can propagate without interactions with discrete masses as depicted in plots (c), (e) and (f) of Figure 3.7.

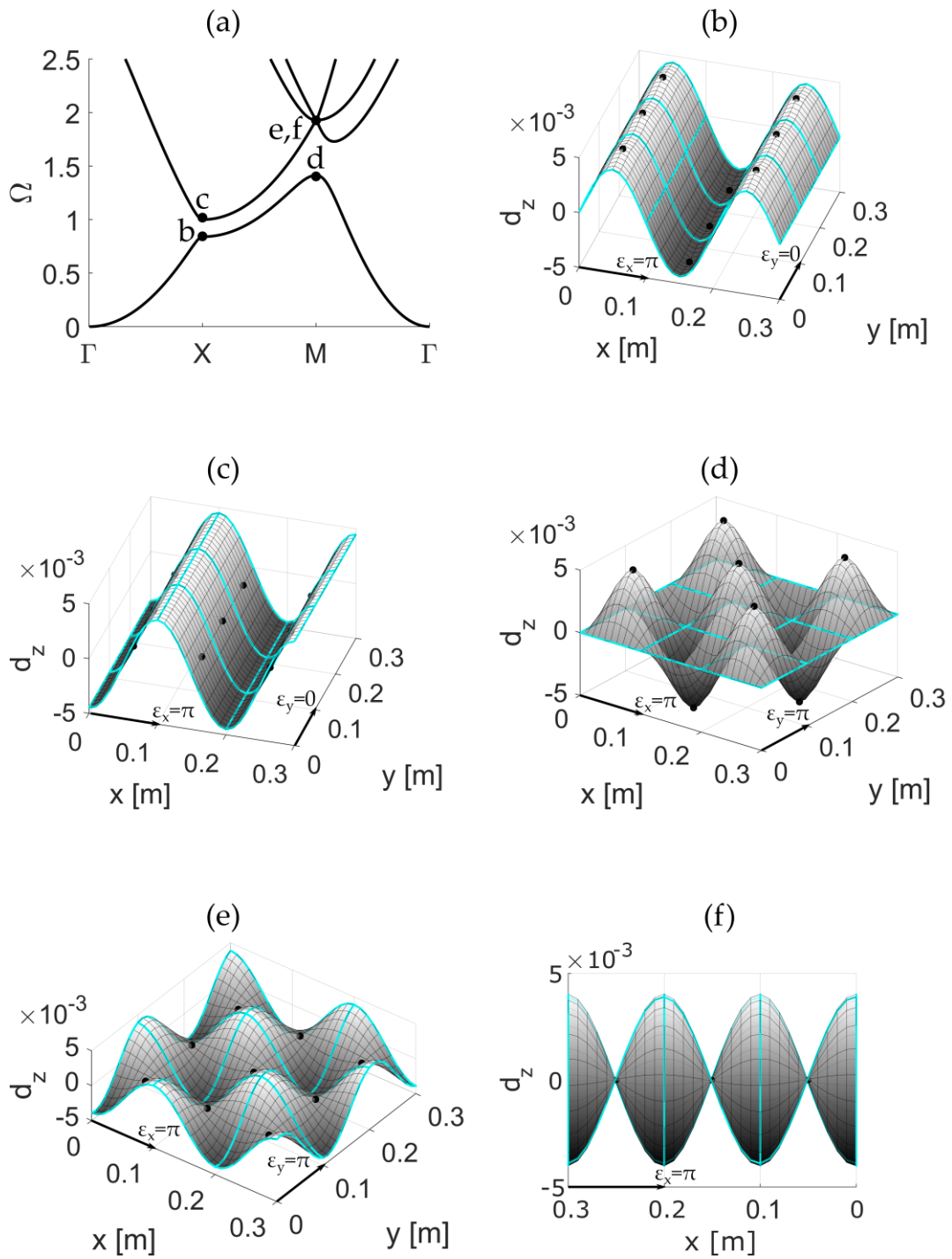


Figure 3.7 Displacement patterns for 9 unit cells of an infinite plate with periodic point masses equal to 20% of the mass of the unit cells. The visualized displacement patterns: (b), (c), (d), (e), (f) correspond to the points indicated with black dots on dispersion diagram in plot (a).

### 3.3.3 Infinite plate with regular array of spring-mass vibration absorbers

Another type of stop band effect can be generated through locally resonant inclusions i.e. spring-mass vibration absorbers (TVAs). Application of the vibration absorber to a cell structure is simple but requires an additional degree of freedom associated with the TVA. Thus, the displacement and force vectors become  $\tilde{\mathbf{d}} = [d_{tva} \mathbf{d}^T]^T$ ,  $\tilde{\mathbf{f}} = [f_{tva} \mathbf{f}^T]^T$  as well as the transfer matrix

$$\tilde{\mathbf{T}} = \begin{bmatrix} 1 & 0 \\ 0 & \mathbf{T}^T \end{bmatrix}^T, \quad (3.122)$$

where matrix  $\mathbf{T}$  is given by Eq. (3.114).

Mass and stiffness matrices of a unit cell also need to be expanded by one row and one column

$$\tilde{\mathbf{M}}_p = \begin{bmatrix} 0 & 0 \\ 0 & \mathbf{M}_p \end{bmatrix}, \quad (3.123)$$

$$\tilde{\mathbf{K}}_p = \begin{bmatrix} 0 & 0 \\ 0 & \mathbf{K}_p \end{bmatrix}, \quad (3.124)$$

and sum with corresponding mass and stiffness matrices of the TVA, whose matrices are given by

$$\mathbf{M}_{tva} = \begin{bmatrix} m_s & 0 \\ 0 & 0 \end{bmatrix}, \quad (3.125)$$

$$\mathbf{K}_{tva} = \begin{bmatrix} k_{tva} & -k_{tva} \\ -k_{tva} & k_{tva} \end{bmatrix}. \quad (3.126)$$

Note that  $\mathbf{K}_{tva}$  and  $\mathbf{M}_{tva}$  need to be first assembled into global system matrices compatible with matrices of a unit cell.

In the following example, the vibration absorber is attached to the inner node of a unit cell, thus  $\mathbf{K}_{tva}$  turns into  $N \times N$   $\tilde{\mathbf{K}}_{tva}$  matrix with four non-zero elements

$$\tilde{\mathbf{K}}_{tva}(1,1) = k_{tva}, \quad \tilde{\mathbf{K}}_{tva}(1,i) = -k_{tva}, \quad (3.127-3.128)$$

$$\tilde{\mathbf{K}}_{tva}(i,1) = -k_{tva}, \quad \tilde{\mathbf{K}}_{tva}(i,i) = k_{tva}, \quad (3.129-3.130)$$

while  $\mathbf{M}_{tva}$  is formed into a  $N \times N$   $\tilde{\mathbf{M}}_{tva}$  matrix, with one non-zero element

$$\tilde{\mathbf{M}}_{tva}(1,1) = m_s. \quad (3.131)$$

In above equations,  $k_{tva}$  is the stiffness of the spring and  $m_s$  is the suspended mass, and  $N$  stands for the total number of degrees of freedom in the unit cell. From this

point onwards, the procedure of obtaining dispersion relations is the same as that already described for point masses.

In this case, the normalised frequency is defined with the following formula

$$\Omega_0 = \frac{\omega_{tva}}{\omega_B} = \frac{\sqrt{k_{tva}}}{m_s} / \omega_B, \quad (3.132)$$

Where, Figure 3.8 presents dispersion curves for an infinite plate equipped with periodic vibration absorbers tuned to  $\Omega_0 = 0.5$  and whose suspended masses are equal to 20% of the unit cell mass.

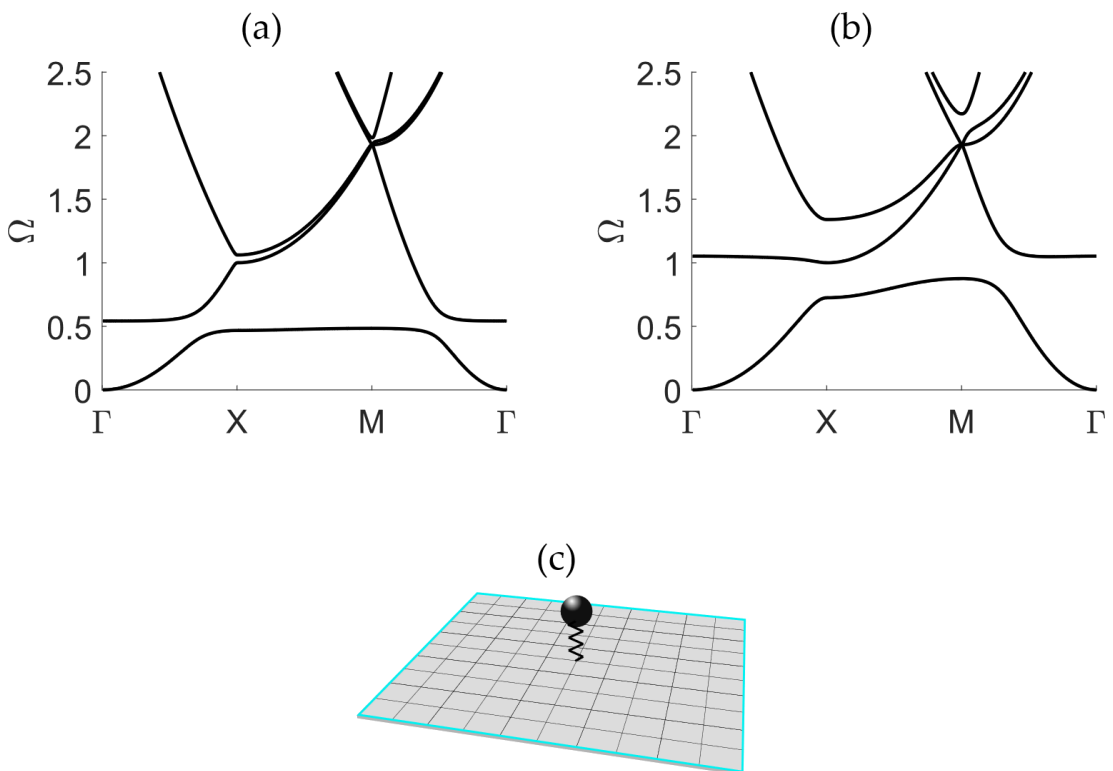


Figure 3.8 Dispersion curves for an infinite plate with periodic vibration absorbers tuned to dimensionless frequency  $\Omega_0 = 0.5$  (a) and  $\Omega_0 = 1$  (b) and whose mass is equal to 20% of the unit cell mass. (c) Depiction of a unit cell.

Due to resonance effects of vibration absorbers, the resonance stop band phenomenon develops from dimensionless frequency of about 0.48 to 0.51. One can notice that this effect differs from the one developed for the point masses. The differences relate to the way how the bottom curve is being held down by the resonance effect and the presence of additional curve above resonance frequency of the TVAs. The top and bottom curves illustrate the classic effect of phase change of the motion of the

oscillating spring mass system when crossing its resonance frequency. Where the bottom curve is associated with in-phase, and top curve with out of phase motion of the plate and TVAs masses [63,78].

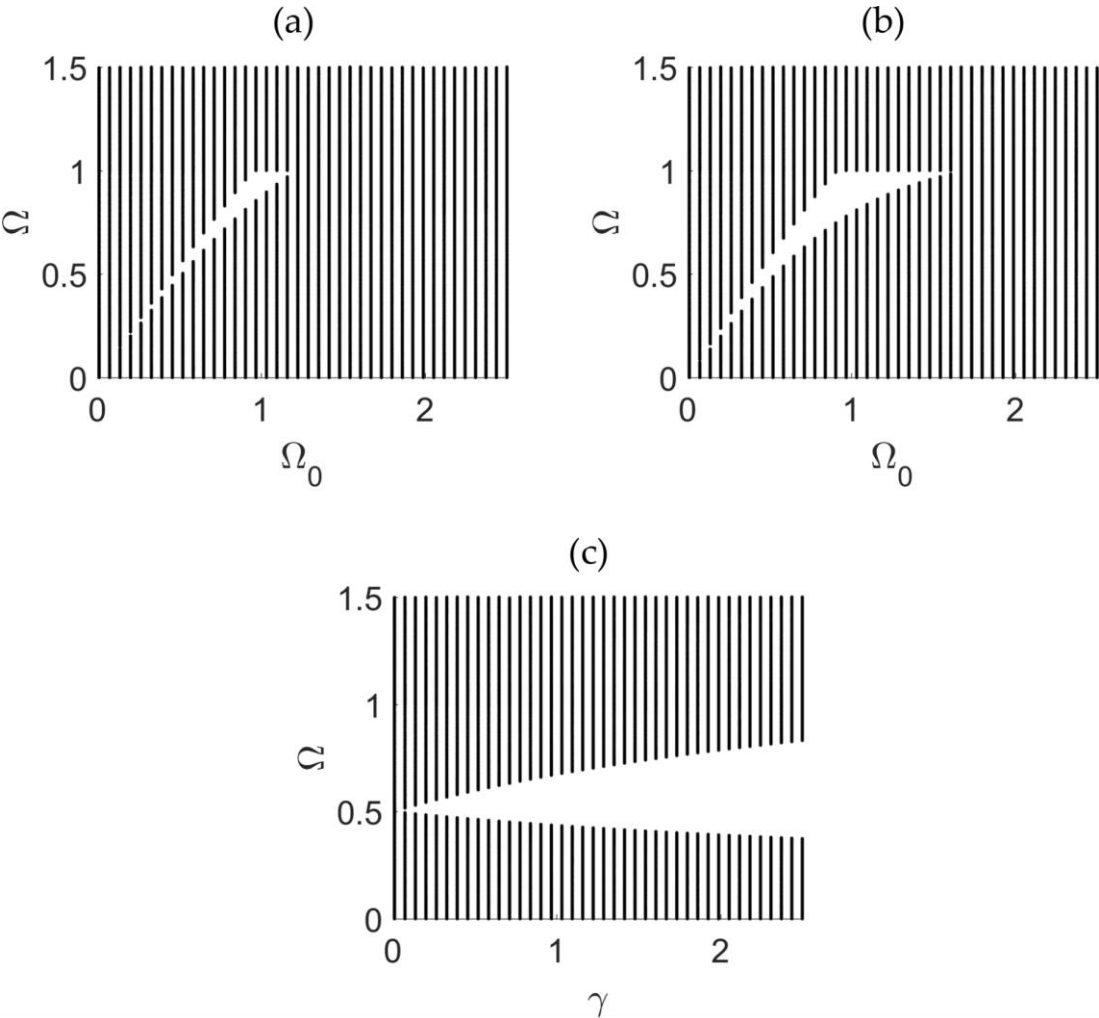


Figure 3.9 Relations between resonance frequency of the absorbers and distributions of the stop band effects for the absorbers equipped with suspended mass equal to 20% (a) and 40% (b) of the unit cell mass. (c) Relation between suspended mass of the absorbers and distribution of the stop band effect for the arbitrarily chosen resonance frequency 0.5.

A wider resonance stop band effect is depicted in plot (b) of Figure 3.8, which is generated by setting the resonance frequency of vibration absorbers to dimensionless frequency 1, which is in fact the upper frequency limit for the TVAs. This can be confirmed by plots (a) and (b) of Figure 3.9, where the frequency distribution of the

stop band effect is shown in relation to the resonance frequency of vibration absorbers equipped with mass equal to 20% and 40% of the unit cell, respectively. Plots (a) and (b) indicate that the resonance stop band effect does not appear above dimensionless frequency 1, despite of vibration absorbers being tuned to dimensionless frequency higher than one. This is because TVAs are either in nodal positions or if the spatial wavelengths are short enough to create displacement pattern that avoids interactions with the periodic grid of resonators. Another interesting phenomenon can also be seen from plots a and b in Figure 3.9. Namely, the tendency of broadening of the resonance stop band effect when resonance frequency of the vibration absorbers become close to dimensionless frequency 1. In this case of the resonance stop band effect couples with the interference stop band effect generated by the waves scattered from the suspended masses and as a result, a wider broadband attenuation phenomenon is obtained. Figure 3.9 (c) shows the relation between stop band distribution and the suspended mass of the absorbers. The resonance frequency was arbitrarily chosen to be 0.5 and the stiffness of the absorbers was varied to maintain the resonance frequency while increasing the suspended mass ratio. Increasing the mass results in broadening the resonance stop band phenomenon, although a significant mass is required to achieve low frequency broad band effects. Finally, Figure 3.10 illustrates the displacement patterns for the edge frequencies of the resonance stop band effect associated with two propagation vectors  $[\pi, 0]$  and  $[\pi, \pi]$ .

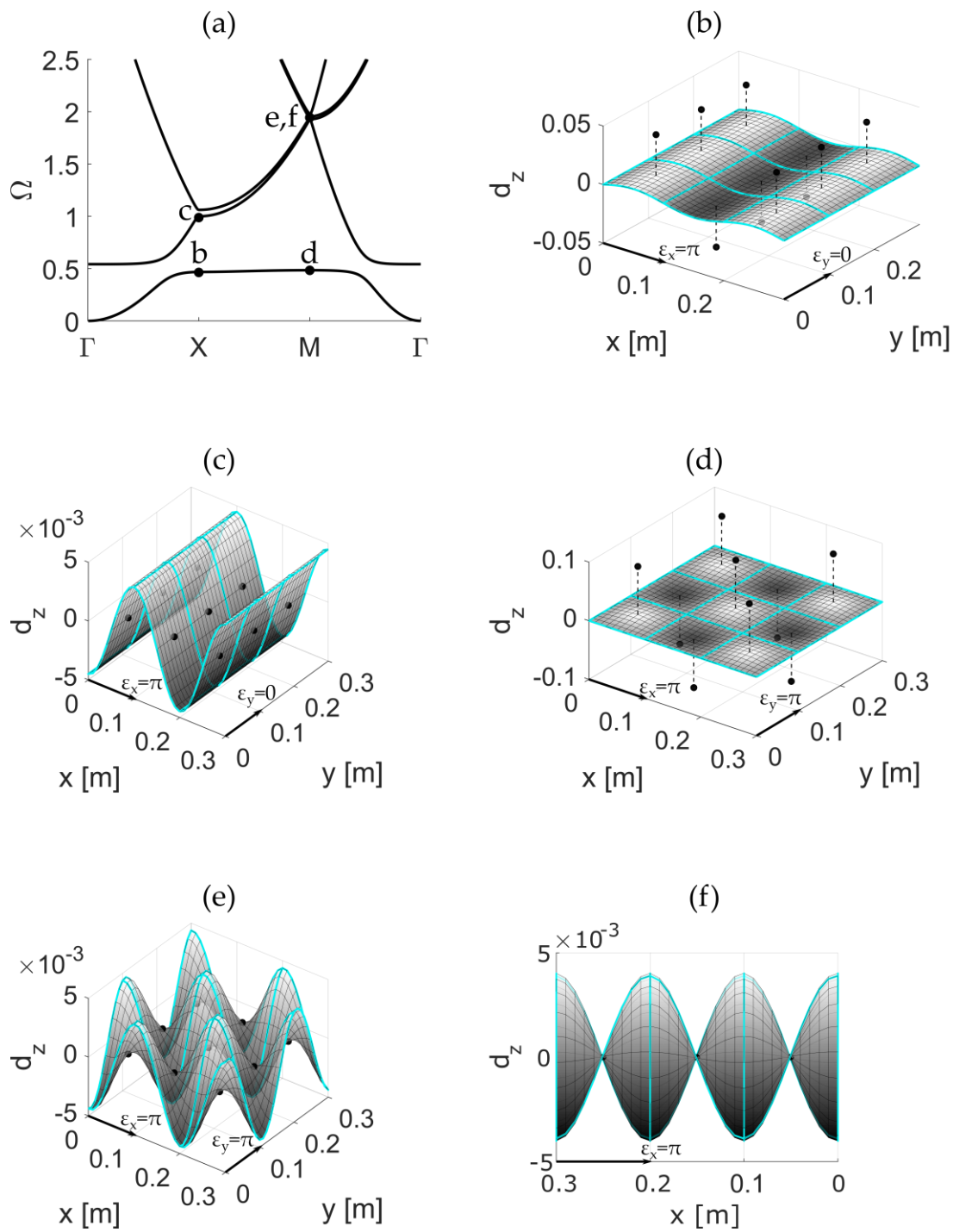


Figure 3.10 Displacement patterns for 9 unit cells of an infinite plate with periodic spring-mass vibration absorbers tuned to dimensionless frequency 0.5 and whose masses are equal to 20% of the mass of the unit cell. The visualized displacement patterns: (b), (c), (d), (e), (f) correspond to the points indicated with black dots on dispersion diagram in plot (a).

### 3.3.4 Infinite plate with regular array of vibration absorbers equipped with base masses

In this section the effect produced by arrays of vibration absorbers with base point mass is analysed. As seen in Section 3.3.2 the point base mass should introduce an interference stop band effect alongside with the resonance stop bane effect of the TVA. Casting the base mass  $m_b$  in vibration absorber is simple and limited to addition of a single nonzero element into  $\mathbf{M}_{tva}$  matrix, so that

$$\mathbf{M}_{tva} = \begin{bmatrix} m_s & 0 \\ 0 & m_b \end{bmatrix}, \quad (3.133)$$

which after turning into  $N \times N$  global matrix is characterised by two non-zero elements:

$$\tilde{\mathbf{M}}_{tva}(1,1) = m_s, \quad \tilde{\mathbf{M}}_{tva}(i,i) = m_b. \quad (3.134-3.135)$$

From this point onwards, the derivation of the band structure does not differ from the one already described.

Figure 3.11 (a) depicts the band structure obtained for infinite plate equipped with periodic grid of tunable vibration absorbers, whose base mass is equal to 70% and suspended mass to 20% of the unit cell mass. As anticipated above, Figure 3.11 (a) shows coexistence of two kinds of stop band phenomena. The first stop band effect occurs around resonance frequency of the oscillating vibration absorbers and has pure resonance character, while the second, around dimensionless frequency 1 and relates to the interference effects of the scattering waves from the base masses. The relation between the distributions of those stop band effects and the resonance frequency of the vibration absorbers is summarised in plots (a) and (b) of Figure 3.12, where plot (a) accounts for the vibration absorbers whose base masses are equal to 40% of the unit cell mass, while plot (b) for the base masses equal to 70% of the unit cell mass. In both cases suspended mass was at 20% of the unit cell mass.

As can be seen from both plots of Figure 3.12 the resonance stop band becomes wider with the resonance frequency  $\Omega_0$  due to stronger coupling with interference effect generated by the suspended mass until it reaches its maximum width at around  $\Omega_0 = 1$ . Further, increasing the resonance frequency of vibration absorbers does not generate stop band effect above dimensionless frequency 1 and has no impact on the distribution of the existing stop band. This leads to the conclusion, that the remaining effect is mostly driven by the interference, due to the base mass. Moreover, as depicted in plot (b) if the suspended mass is significant, an additional interference

stop band coexists with the resonance stop band up to the resonance frequencies close to dimensionless frequency 1. At these frequencies distribution of the interference stop band effect becomes narrow, until it vanishes at around  $\Omega_0 = 0.8$ . Figure 3.13 illustrates the displacement patterns for the edge frequencies of the resonance and interference stop band effects associated with two propagation vectors  $[\pi, 0]$  and  $[\pi, \pi]$ .

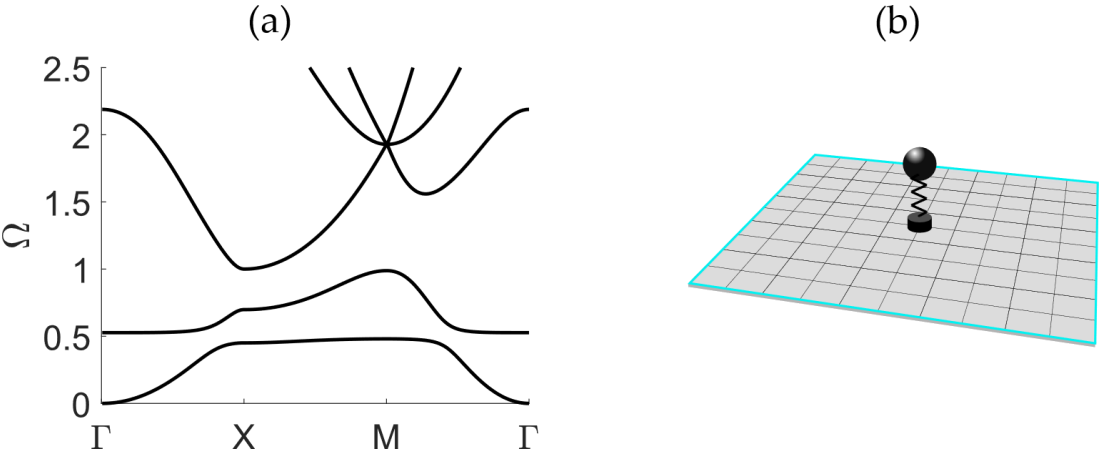


Figure 3.11 (a) Dispersion curves for an infinite plate with periodic vibration absorbers equipped with base masses and tuned to dimensionless frequency 0.5. The base masses are equal to 70% and proof masses to 20% of the unit cell mass. (b) Depiction of a unit cell.

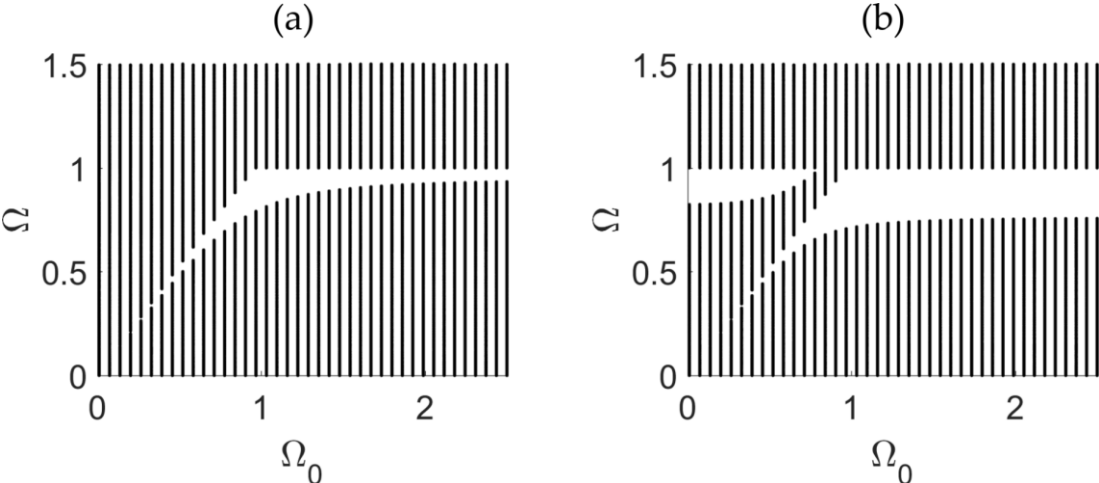


Figure 3.12 Relations between resonance frequency of the absorbers and distributions of the stop band effects for the absorbers equipped with base masses equal to 40% (a) and 70% (b) of the unit cell mass. In both cases the proof masses are equal to 20% of the unit cell mass

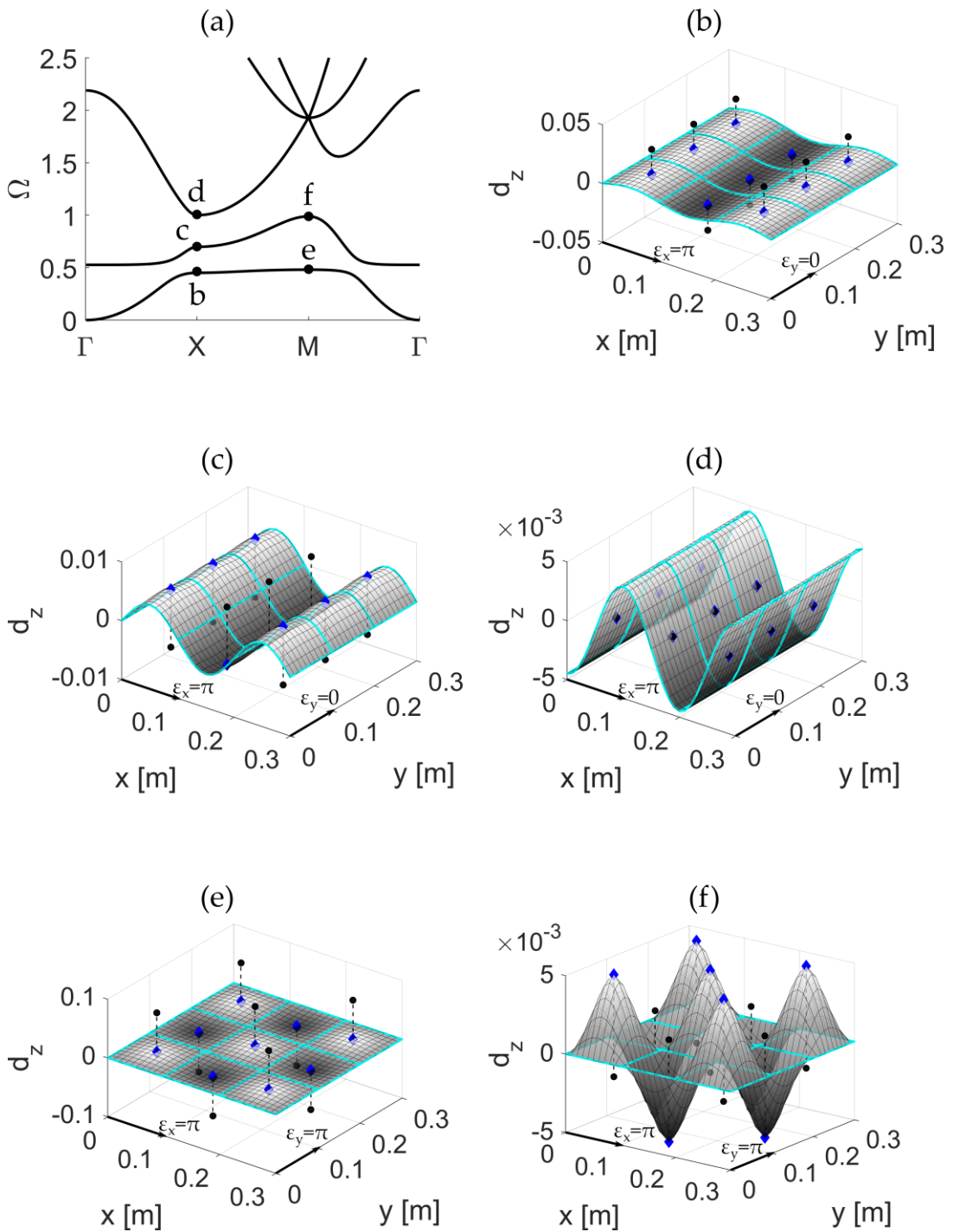


Figure 3.13 Displacement patterns for 9 unit cells of an infinite plate with periodic spring-mass vibration absorbers tuned to dimensionless frequency 0.5 and whose proof masses are equal to 20% and base masses to 70% of the mass of the unit cell. The visualized displacement patterns: (b), (c), (d), (e), (f) corresponds to the points indicated with black dots on dispersion diagram in plot (a).

### 3.3.5 Infinite plate with regular array of piezoelectric patch transducers connected to inductive shunts

Application of periodic arrays of piezoelectric patch transducers connected to shunt circuits can also lead to developments of the stop band phenomena. The concept of vibration absorber composed of a piezoelectric patch transducer connected to a shunt circuit is very similar to the tunable vibration absorber since as discussed in Section 1.2 it produces an electro-mechanical resonant vibration absorption effect. The principle of operation of these devices lies in the conversion of mechanical energy from vibrations into electrical energy dissipated in the components of electrical circuits. The shunt circuits are often chosen to maximise energy transfer from one domain to the other at resonance frequency, so that the vibration absorption of the mechanical vibrations can be optimised. An inductive shunt is used, which combined with the inherent capacitive effect of the piezoelectric transducers give rise to a resonant circuit.

The work here starts from the governing equations of the unit cell

$$(\mathbf{M}_p + \mathbf{M}_{pe})\ddot{\mathbf{d}}_k + (\mathbf{K}_p + \mathbf{K}_{pe})\mathbf{d}_k + \boldsymbol{\theta}_{pe}v_{pe} - \mathbf{f} = \mathbf{0} , \quad (3.136)$$

$$\boldsymbol{\theta}_{pe}^T \mathbf{d}_k + C_{pe}v_{pe} + q = 0 . \quad (3.137)$$

First it is assumed that piezoelectric patch is shunted by a single inductor L in which case

$$v_{pe} = L\dot{q} . \quad (3.138)$$

In this case the piezoelectric patch charge can be treated as additional degree of freedom, such that Eqs.(3.136) and (3.137) can be casted in such a way as

$$\mathbf{M}\ddot{\mathbf{u}} + \mathbf{K}\mathbf{u} = \mathbf{F} , \quad (3.139)$$

where the vectors are organized in following way  $\mathbf{u} = [\mathbf{d} \ q]^T$ ,  $\mathbf{F} = [\mathbf{f} \ 0]^T$  and the matrices defined as

$$\mathbf{M} = \begin{bmatrix} \mathbf{M}_t & \boldsymbol{\theta}_{pe}L \\ \mathbf{0} & C_{pe}L \end{bmatrix} , \quad (3.140)$$

$$\mathbf{K} = \begin{bmatrix} \mathbf{K}_t & \mathbf{0} \\ \boldsymbol{\theta}_{pe}^T & -1 \end{bmatrix} . \quad (3.141)$$

Assuming harmonic motion at frequency  $\omega$  Eq. 42 becomes

$$(\mathbf{K} - \omega^2 \mathbf{M})\mathbf{u} = \mathbf{F}, \quad (3.142)$$

where vectors  $\mathbf{u}$  and  $\mathbf{F}$  are arranged according to Figure 3.2,  $\mathbf{u} = [\mathbf{d}_i \mathbf{d}_b \mathbf{d}_t \mathbf{d}_l \mathbf{d}_r \mathbf{d}_{lb} \mathbf{d}_{rb} \mathbf{d}_{lt} \mathbf{d}_{rt} q]^T$ ,  $\mathbf{F} = [\mathbf{f}_i \mathbf{f}_b \mathbf{f}_t \mathbf{f}_l \mathbf{f}_r \mathbf{f}_{lb} \mathbf{f}_{rb} \mathbf{f}_{lt} \mathbf{f}_{rt} 0]^T$ . Application of the Blochs theorem leads to a transfer matrix

$$\tilde{\mathbf{T}} = \begin{bmatrix} \mathbf{T}^T & 0 \\ 0 & 1 \end{bmatrix}^T, \quad (3.143)$$

where the matrix  $\mathbf{T}$  is given by Eq. (3.114). From this point onwards, the procedure of obtaining dispersion curves does not vary from that described in the first subsection.

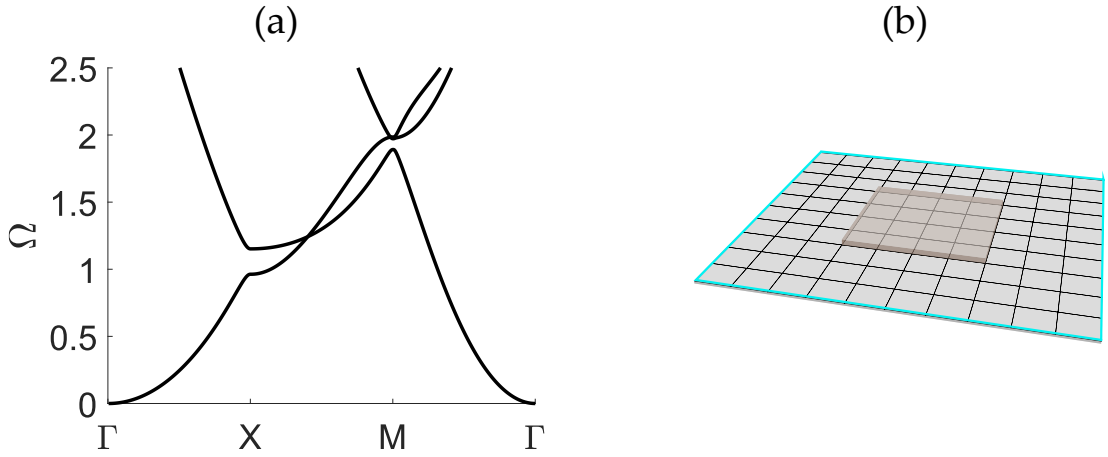


Figure 3.14 (a) Dispersion curves of an infinite plate with periodic piezoelectric patch transducers whose electrical terminals are open. (b) Depiction of a unit cell.

Figure 3.14(a) presents the dispersion curves for an infinite plate with periodic array of piezoelectric patch transducers whose electrical terminals remain open  $L = 0$ . The resultant dispersion curves do not vary much from the ones obtained for an ordinary plate with no inclusions. Every frequency on the band diagram can be associated with a point in the wave domain, thus there are no frequency zones where the wave propagation is stopped. Although there is no stop band phenomenon present, some interference effects occur for two directions of propagations  $[\pi, 0]$ ,  $[\pi, \pi]$  where the development of small openings can be spotted. The displacement pattern associated with edge frequencies of these effects are depicted in plots (b), (c), (e) and (f) of Figure 3.15.

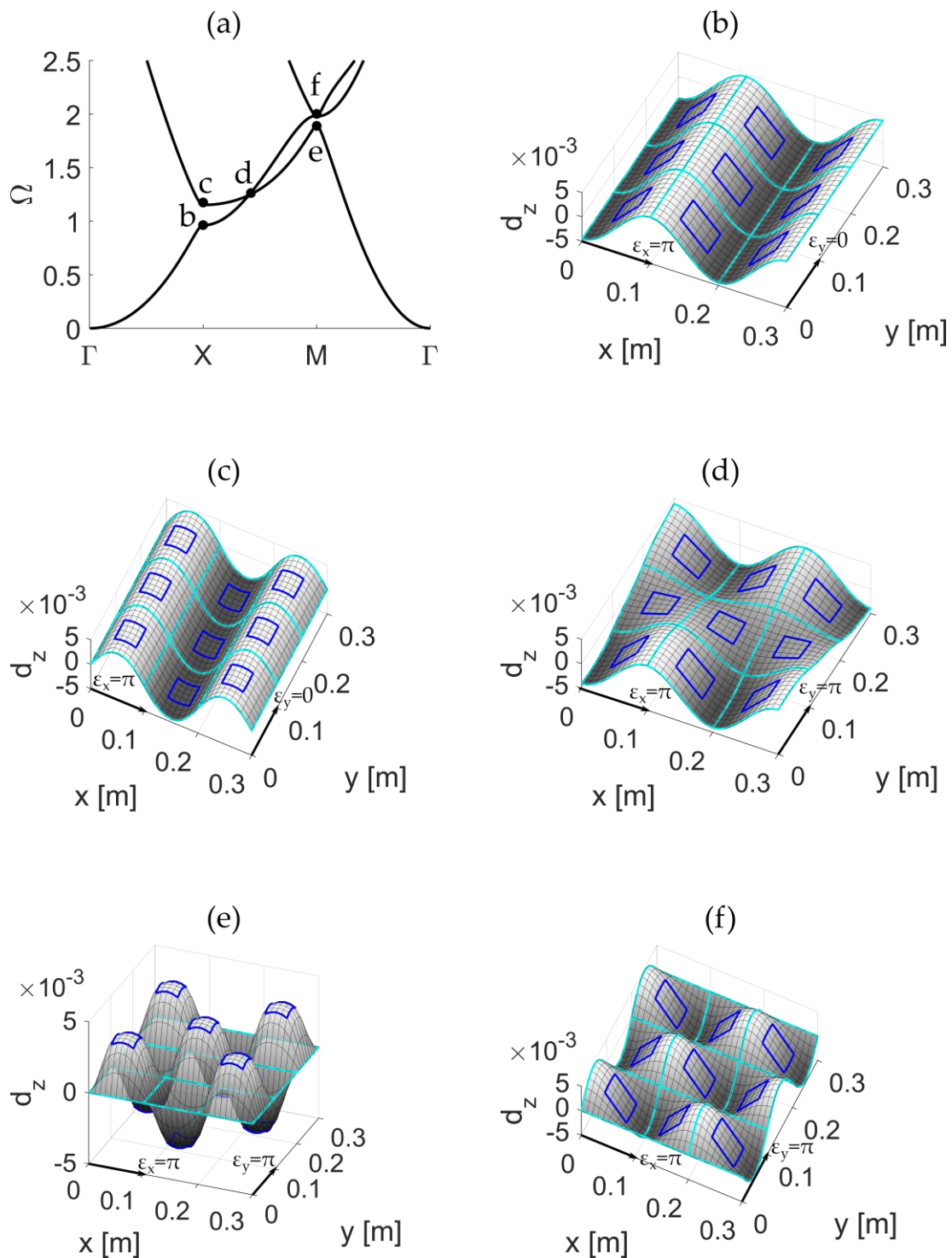


Figure 3.15 Displacement patterns for 9 unit cells of an infinite plate with piezoelectric patch transducers whose electrical terminals are open. The visualized displacement patterns: (b), (c), (d), (e), (f) correspond to the points indicated with black dots on dispersion diagram in plot (a).

When the shunt inductance is greater than zero, the shunted piezoelectric patch produces a vibration absorption effect such that separation of dispersion curves occurs, which leads to the formation of the narrow resonance stop band effect around the dimensionless frequency 0.5. Further analysis showed that a stop band distribution is indeed very narrow within investigated frequency span 0-1.5 and does not vary much. Due to this fact, the relation between resonance frequency and a distribution of the stop is only to small extend depicted in Figure 3.17.

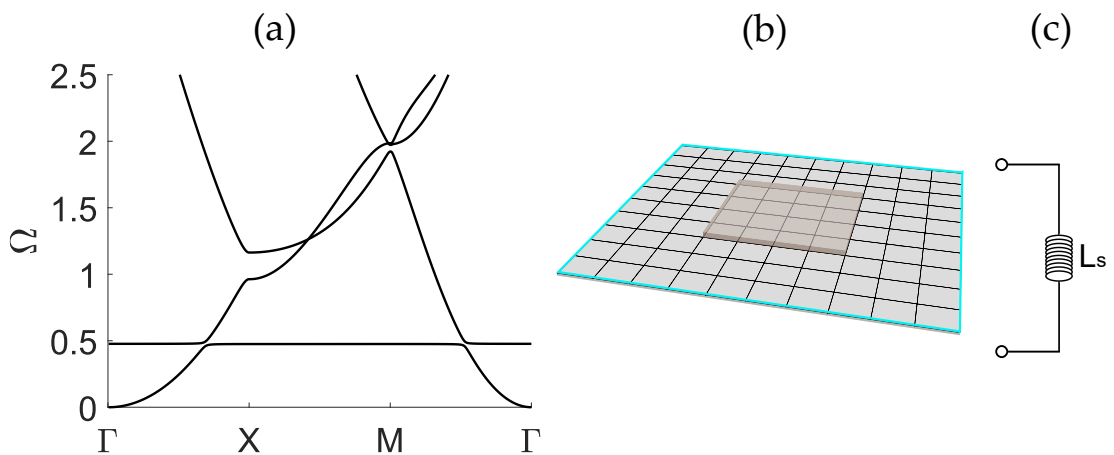


Figure 3.16 (a) Dispersion curves of an infinite plate with periodic piezoelectric patch transducers connected to single inductors tuned to dimensionless frequency 0.5 (b) Depiction of a unit cell. (c) Shunting inductor.

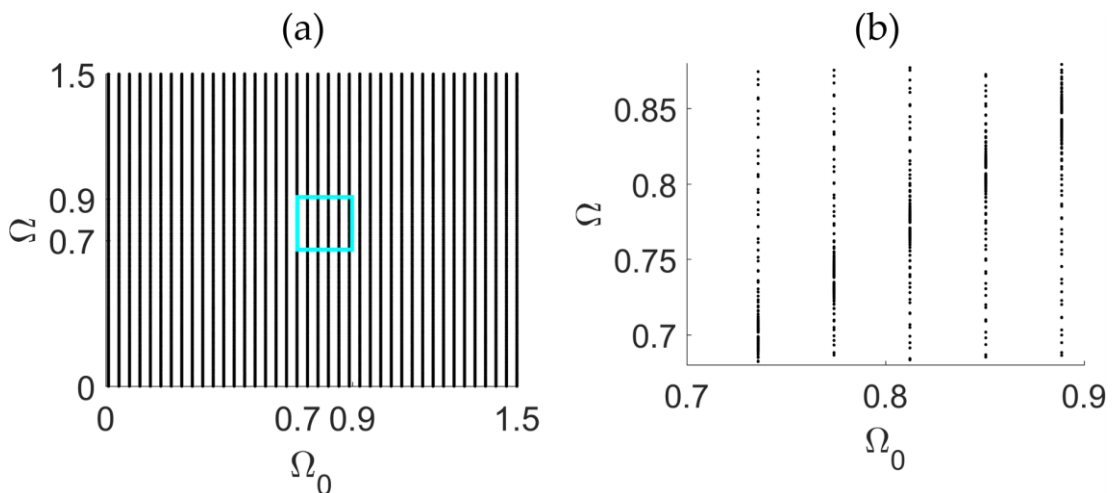


Figure 3.17 (a) Relation between resonance frequency of the piezoelectric patches connected to single inductors and distribution of the stop band effects. (b) Magnified part of the relation indicated in plot (a).

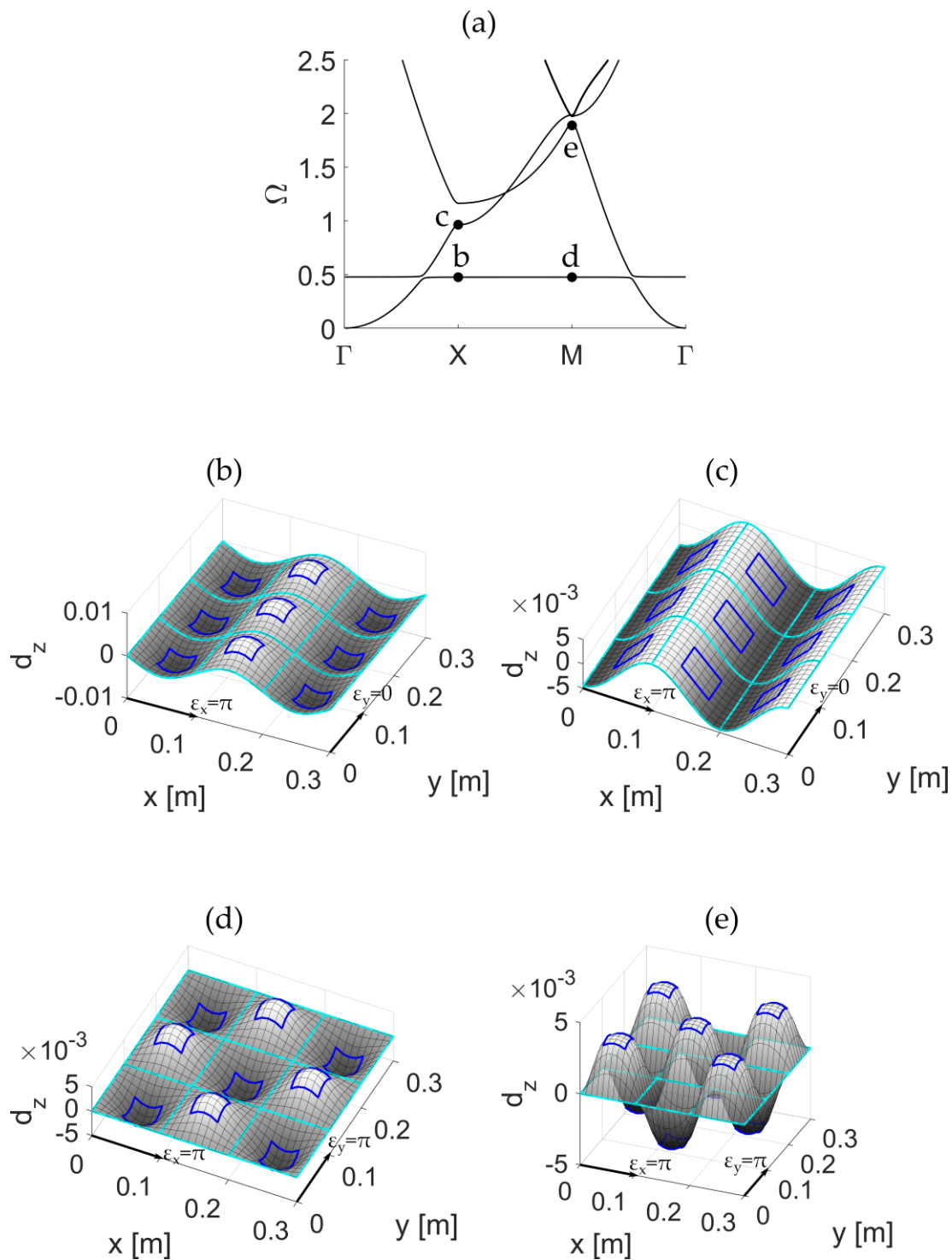


Figure 3.18 Displacement patterns for 9 unit cells of an infinite plate with piezoelectric patch transducers connected to single inductors and tuned to dimensionless frequency 0.5. The visualized displacement patterns: (b), (c), (d), (e), (f) correspond to the points indicated with black dots on dispersion diagram in (a).

### 3.3.6 Infinite plate with regular array of piezoelectric patch transducers connected to multi-resonant shunt circuits

In this section the effect produced by two-dimensional arrays of piezoelectric patches connected to multi-resonant shunts is analysed. Assuming the electrical functions are time-harmonic and given in the form  $f(t) = f(\omega)exp(j\omega t)$ , where  $f(\omega)$  is the complex amplitude,  $\omega$  is the circular frequency, the ratio of charge and potential difference across of the current flowing shunt circuit can be expressed as the sum of two second order terms:

$$\frac{q}{v_{pe}} = \frac{\frac{1}{L_{b1}}}{-\omega^2 + \frac{1}{C_{f1}L_{b1}}} + \frac{\frac{1}{L_{b2}}}{-\omega^2 + \frac{1}{C_{f2}L_{b2}}}, \quad (3.144)$$

Each second order term in Eq. (3.144) can be envisaged as the ratio between a generalized charge and potential difference. Thus, the charge can be expressed with the following matrix equation

$$q = \Psi \Lambda, \quad (3.145)$$

where  $\Psi = \left[ \frac{1}{\sqrt{L_{b1}}} \quad \frac{1}{\sqrt{L_{b2}}} \right]$ . And  $\Lambda = [\Lambda_1 \quad \Lambda_2]^T$  is the vectors with generalized charges, which can be given by the following matrix relation

$$\Lambda = \mathbf{G} \Psi^T v_{pe}, \quad (3.146)$$

that is

$$\begin{bmatrix} \Lambda_1 \\ \Lambda_2 \end{bmatrix} = \begin{bmatrix} \frac{1}{-\omega^2 + \frac{1}{C_{f1}L_{b1}}} & 0 \\ 0 & \frac{1}{-\omega^2 + \frac{1}{C_{f2}L_{b2}}} \end{bmatrix} \begin{bmatrix} \frac{1}{\sqrt{L_{b1}}} \\ \frac{1}{\sqrt{L_{b2}}} \end{bmatrix} v_{pe}. \quad (3.147)$$

Considering the expanded form of Eq. (3.147)

$$\mathbf{I} \ddot{\Lambda} + \mathbf{\Omega} \Lambda = \Psi^T v_{pe}. \quad (3.148)$$

Where

$$\mathbf{I} = \begin{bmatrix} 1 & 0 \\ 0 & 1 \end{bmatrix}, \quad (3.149)$$

$$\mathbf{\Omega} = \begin{bmatrix} \frac{1}{C_{f1}L_{b1}} & \\ & \frac{1}{C_{f2}L_{b2}} \end{bmatrix}. \quad (3.150)$$

With Eqs. (3.145)-(3.150) it is possible to express the governing Eqs. (3.136)-(3.137) in terms of vectors:  $\ddot{\mathbf{d}}$ ,  $\mathbf{d}$  and  $\ddot{\mathbf{\Lambda}}$ ,  $\mathbf{\Lambda}$ . First, substituting Eq. (3.145) to Eq. (3.137) yields

$$\boldsymbol{\theta}_{pe}^T \mathbf{d} + C_{pe} v_{pe} = \boldsymbol{\Psi} \mathbf{\Lambda}, \quad (3.151)$$

so that potential difference can be written as

$$v_{pe} = C_{pe}^{-1} \boldsymbol{\Psi} \mathbf{\Lambda} - C_{pe}^{-1} \boldsymbol{\theta}_{pe}^T \mathbf{d}. \quad (3.152)$$

This equation is in turn substituted to Eq. (3.136) to obtain the first set of the governing equations in terms of the vectors:  $\ddot{\mathbf{d}}$ ,  $\mathbf{d}$  and  $\ddot{\mathbf{\Lambda}}$ ,  $\mathbf{\Lambda}$ :

$$\mathbf{M}_t \ddot{\mathbf{d}} + (\mathbf{K}_t - \boldsymbol{\theta}_{pe} C_{pe}^{-1} \boldsymbol{\theta}_{pe}^T) \mathbf{d} + \boldsymbol{\theta}_{pe} C_{pe}^{-1} \boldsymbol{\Psi} \mathbf{\Lambda} = \mathbf{f}. \quad (3.153)$$

The second set of governing equations is derived from pre-multiplying of Eq. (3.152) by  $\boldsymbol{\Psi}^T$

$$\boldsymbol{\Psi}^T v_{pe} = \boldsymbol{\Psi}^T C_{pe}^{-1} \boldsymbol{\Psi} \mathbf{\Lambda} - \boldsymbol{\Psi}^T C_{pe}^{-1} \boldsymbol{\theta}_{pe}^T \mathbf{d}, \quad (3.154)$$

and from substitution of Eq. (3.148) into Eq. (3.154)

$$\mathbf{I} \ddot{\mathbf{\Lambda}} + \boldsymbol{\Omega} \mathbf{\Lambda} = \boldsymbol{\Psi}^T C_{pe}^{-1} \boldsymbol{\Psi} \mathbf{\Lambda} - \boldsymbol{\Psi}^T C_{pe}^{-1} \boldsymbol{\theta}_{pe}^T \mathbf{d}. \quad (3.155)$$

In this way the governing system equations are reformulated to account for multi-resonating shunt circuit, composed of two LC branches.

$$\mathbf{M}_t \ddot{\mathbf{d}} + (\mathbf{K}_t - \boldsymbol{\theta}_{pe} C_{pe}^{-1} \boldsymbol{\theta}_{pe}^T) \mathbf{d} + \boldsymbol{\theta}_{pe} C_{pe}^{-1} \boldsymbol{\Psi} \mathbf{\Lambda} = \mathbf{f}, \quad (3.156)$$

$$\mathbf{I} \ddot{\mathbf{\Lambda}} + \boldsymbol{\Psi}^T C_{pe}^{-1} \boldsymbol{\theta}_{pe}^T \mathbf{d} + (\boldsymbol{\Omega} - \boldsymbol{\Psi}^T C_{pe}^{-1} \boldsymbol{\Psi}) \mathbf{\Lambda} = \mathbf{0}. \quad (3.157)$$

The governing equations can now be casted in the form of

$$\mathbf{M} \ddot{\mathbf{u}} + \mathbf{K} \mathbf{u} = \mathbf{F}, \quad (3.158)$$

where,  $\mathbf{M}$  and  $\mathbf{K}$  matrices are organized as

$$\mathbf{M} = \begin{bmatrix} \mathbf{M}_t & \mathbf{0} \\ \mathbf{0} & \mathbf{I} \end{bmatrix}, \quad (3.159)$$

$$\mathbf{K} = \begin{bmatrix} \mathbf{K}_t - \boldsymbol{\theta}_{pe} C_{pe}^{-1} \boldsymbol{\theta}_{pe}^T & \boldsymbol{\theta}_{pe} C_{pe}^{-1} \boldsymbol{\Psi} \\ \boldsymbol{\Psi}^T C_{pe}^{-1} \boldsymbol{\theta}_{pe}^T & \boldsymbol{\Omega} - \boldsymbol{\Psi}^T C_{pe}^{-1} \boldsymbol{\Psi} \end{bmatrix}, \quad (3.160)$$

and the vectors arranged according to Figure 3.2(a)

$$\mathbf{u} = [\mathbf{d}_i \mathbf{d}_b \mathbf{d}_t \mathbf{d}_l \mathbf{d}_r \mathbf{d}_{lb} \mathbf{d}_{rb} \mathbf{d}_{lt} \mathbf{d}_{rt} \Lambda_1 \Lambda_2]^T, \quad \mathbf{F} = [\mathbf{f}_i \mathbf{f}_b \mathbf{f}_t \mathbf{f}_l \mathbf{f}_r \mathbf{f}_{lb} \mathbf{f}_{rb} \mathbf{f}_{lt} \mathbf{f}_{rt} 0 0]^T.$$

Application of the Bloch's theorem leads to the following transfer matrix

$$\tilde{\mathbf{T}} = \begin{bmatrix} \mathbf{T}^T & 0 & 0 \\ 0 & 1 & 0 \\ 0 & 0 & 1 \end{bmatrix}^T. \quad (3.161)$$

Where matrix  $\mathbf{T}$  is given by Eq. (3.114). From this point onwards, the procedure of obtaining dispersion relation is the same as seen above for uniform infinite plate.

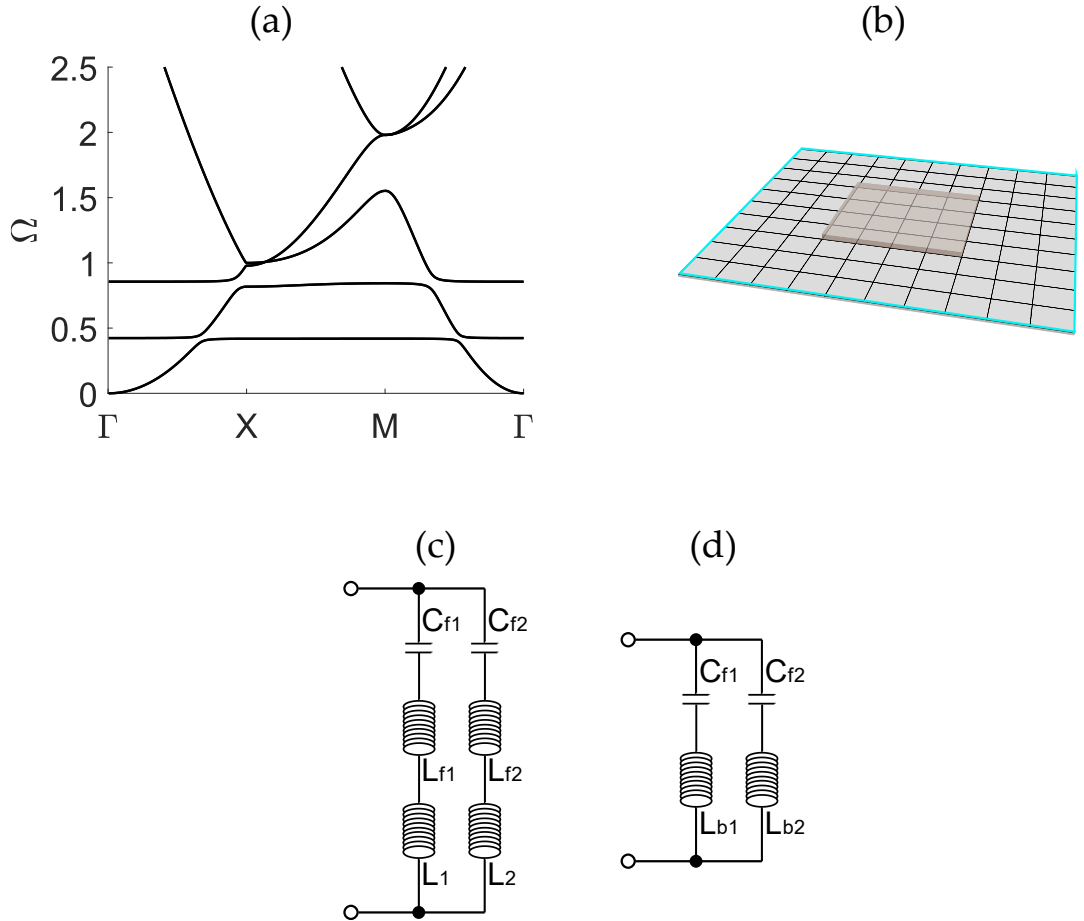


Figure 3.19 (a) Dispersion curves of an infinite plate with periodic piezoelectric patch transducers connected to multi-resonating shunt circuits and tuned to dimensionless frequencies 0.5 and 1. (b) Depiction of a unit cell. (c) Multi-resonating shunt circuit. (d) Simplification of the multi-resonating circuit.

Figure 3.19 (a) shows the dispersion curves for an infinite plate equipped with periodic piezoelectric patch transducers connected to multi-resonant electrical shunts. Inductances of the shunts were selected according to approximated formula provided by Berhens [43] and correspond to the two resonant frequencies: 0.5 and 1. The results demonstrate the benefits of using this type of solution to generate stop band effects for wave propagation control, without the need for excessive mass increase, as in the case of dynamic absorbers. As one can see in the Figure 3.19 (a), two resonant stop-band effects with relatively wide widths are generated in all directions of propagation. What is more important, the electrical shunt can be extended with additional branches, allowing for supplementary local resonance effects. The condition for an efficient use of this type of shunt is frequency tuning, which ensures a certain difference in resonant frequencies corresponding to individual branches. Small differences in individual resonant frequencies may lead to a coupling between branches and an efficiency drop.

#### 3.4 CONCLUDING REMARKS

The work presented in this chapter was focused on the characterization of stop band phenomena produced by two-dimensional arrays of inclusions distributed on an infinite plate. The studies first confirmed that the interference stop bands generated through the wave scattering from the arrays of discrete masses are linked to the standing wave behaviour and therefore related to the geometry of the unit cell. The obtained results indicate that the right-hand side edge frequency associated with the interference stop bands is limited by the Bragg's condition and thus, the effects can only be expanded towards lower frequencies by increasing the mass of the inclusions. As pointed out in this chapter, the broadband interference effects are possible in two-dimensional structures, but require significant mass addition which make them less suitable for practical applications.

The simulation studies then confirmed that the arrays of locally resonant inclusions can produce stop bands in two-dimensional mechanical structures, although certain frequency range limiting restrictions are present. In general, the resonance stop bands can be generated at the resonance frequency of the inclusions, however spring-mass vibration absorbers cannot develop the effect at dimensionless frequencies higher than 1. This is related to the implementation of idealised, point-like vibration absorbers, which are found to be in nodal positions above the dimensionless frequency 1. In contrary, shunted piezoelectric patch vibration absorbers can produce stop bands for certain directions of propagation at frequencies above dimensionless frequency 1. It is possible due to spatial organization of the piezoelectric patches on the surface of the plate, that allows for some degree of electro-mechanical coupling even with high frequency modes.

In addition, the simulation studies demonstrated that the phenomenon of widening of the resonance stop bands is also present in two-dimensional structure. The bandwidth of the resonance effects is expanding from very narrow along with increase of the resonance frequency until the maximum width is reached at dimensionless frequency 1. At this frequency, resonance and interference effects are fully coupled producing a cumulative stop band characterised by the widest bandwidth. Since the broadband resonance effects are only possible at frequencies not very distant from the Bragg's frequency, the structures determined by such dynamics carry some practical limitations regarding low frequency applications.

At the end of the chapter, the modal formulation of the multi-resonant shunt circuits to was implemented into the finite-element model. This formulation constitutes a major contribution in considered subject as it allows to derive dispersion relations of two-dimensional structures with periodic arrays of piezoelectric patch transducers characterised by a number of locally resonant effects. The formulation was then used to calculate the band structure of an infinite plate equipped with piezoelectric patches connected to double-resonance shunts. The formulation has proven to be valuable, because not only overcomes the common issue of the nonlinear eigenvalue problem, but also allows to obtain dispersion properties of two-dimensional electro-mechanical structures in a computationally nondemanding way.

The analysis of stop band effects is continued for two-dimensional finite plate in the next chapter.

---

## FINITE PLATE WITH PERIODIC INCLUSIONS

---

In this chapter two-dimensional arrays of inclusions are analysed as the means of passive vibration treatment in a finite rectangular thin plate. Again, a focus of this chapter is devoted to the generation and characterisation of the band gaps, occurring for point masses, spring-mass vibration absorbers and RLC shunted piezoelectric patch vibration absorbers. The chapter first considers a simplified model problem, which is composed of a finite plate with two-dimensional array of discrete masses and spring-mass vibration absorbers. The plate is exposed to a rain on the roof stochastic excitation and the system response is derived through a mobility-impedance based model. The inclusions are spaced in such a way as to produce a considerable reduction of the flexural response in a given frequency band. The stop band effects are obtained both via the spatial spacing of the discrete masses (Bragg gaps) and the physical properties of the vibration absorbers (locally resonant). The overall response of the plate is considered in terms of the Power Spectral Density (PSD) functions of the time averaged total kinetic energy of the plate structure.

The second part of the chapter introduces the formulation of the fully coupled modal model of the finite plate with regular arrays of piezoelectric patch transducers connected to RLC shunt circuits. In the following part, the transducers are connected to identical shunts and the evolution of the resonance stop bands are presented in terms of the time averaged total kinetic energy. In the final part of the chapter, multi-resonant shunt circuits are implemented to emphasize the possibility of obtaining multiple stop band effects also in finite structures.

The vibration attenuation properties of all plate systems are then analysed and interpreted in view of the physical effects enlighten in the previous chapter for an infinite plate structure.

## 4.1 DESCRIPTION OF THE SYSTEM

The vibration attenuation effects produced by two dimensional arrays of point masses and point spring-mass vibration absorbers on a thin panel is now investigated in view of the attenuation frequency stop band concepts introduced for infinite plates in the previous chapter. As shown in Figure 4.1, the plate material considered here comprises an array of 25 inclusions that is: point masses, spring-mass vibration absorbers and RLC shunted piezoelectric patch vibration absorbers which are arranged in a  $5 \times 5$  grid such that they are equally spaced in  $x$  and  $y$  directions by  $L = 5.7$  cm. The details of the dimensions and material properties of the plate is given in Table 4.1. As shown in Figure 4.1 (a), the plate is exposed to an  $4 \times 4$  array of uncorrelated white noise point forces, which resemble a rain on the roof excitation.

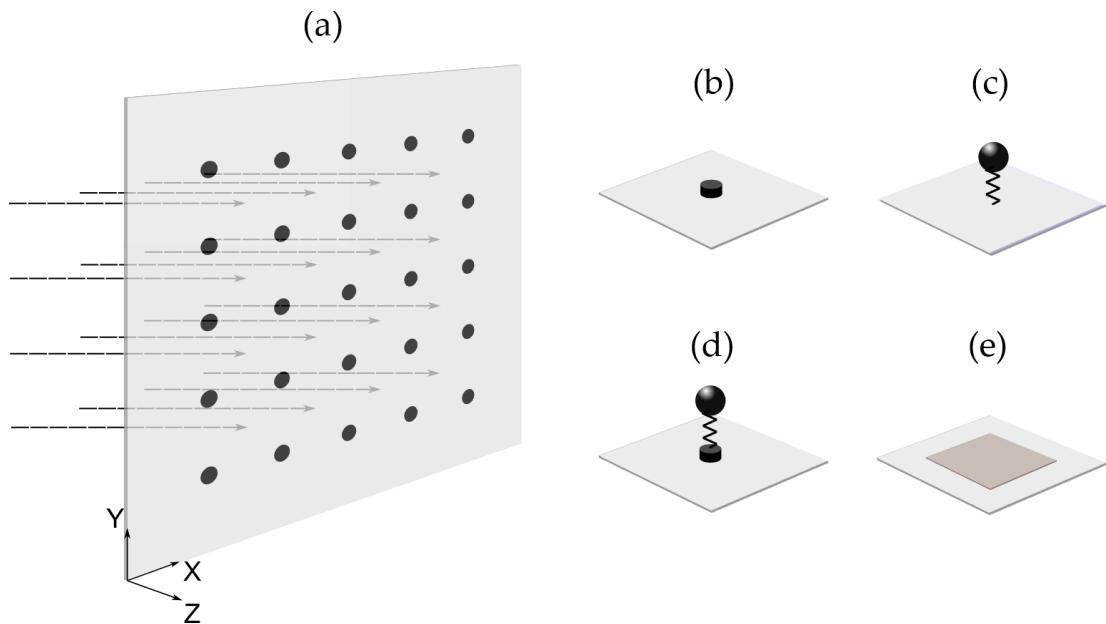


Figure 4.1 Finite plate material equipped with  $5 \times 5$  array of inclusions and excited by the rain-on-the-roof stochastic process, modelled as  $4 \times 4$  matrix of uncorrelated point forces. Four types of inclusions used in this framework point mass (b), vibration absorber (c), vibration absorber with base mass (d), piezoelectric patch transducer (e).

Table 4.1. Physical and geometrical parameters of the plate.

Parameter	Plate
Thickness	$h_p = 1 \text{ mm}$
Width	$l_x = 0.314 \text{ m}$
Length	$l_y = 0.314 \text{ m}$
Density	$\rho_p = 2700 \text{ kg/m}^3$
Young's modulus	$Y_p = 7 \times 10^{10} \text{ N/m}^2$
Poisson's ratio	$\nu_p = 0.33$
Plate loss factor	$\eta = 2\%$
Resonators damping ratio	$\zeta = 3\%$
Lattice constant	$L = 5.7 \text{ cm}$

## 4.2 STOP BAND PHENOMENA IN FINITE PLATES

### 4.2.1 Finite plate with regular array of point masses / spring-mass vibration absorbers

The flexural response of the panel is derived from a mobility-impedance model. Assuming harmonic time dependence in complex form of  $\exp(j\omega t)$  at circular frequency  $\omega$ , the complex transverse velocities at the bases of the point masses / spring-mass vibration absorbers were grouped into the column vector:

$\dot{\mathbf{w}}_m(\omega) = [\dot{w}(x_{m_1}, y_{m_1}, \omega) \dots \dot{w}(x_{m_{24}}, y_{m_{24}}, \omega)]^T$ . The flexural vibration at these positions can be expressed with a mobility matrix expression in terms of the vector with the complex primary forces  $\mathbf{f}_p(\omega) = [f(x_{p_1}, y_{p_1}, \omega) \dots f_m(x_{p_{16}}, y_{p_{16}}, \omega)]^T$  and the complex secondary excitations  $\mathbf{f}_m(\omega) = [f(x_{m_1}, y_{m_1}, \omega) \dots f(x_{m_{25}}, y_{m_{25}}, \omega)]^T$  generated by the inclusions:

$$\dot{\mathbf{w}}_m = \mathbf{Y}_{mp}\mathbf{f}_p + \mathbf{Y}_{mm}\mathbf{f}_m. \quad (4.1)$$

The mobility elements in the matrices  $\mathbf{Y}_{pm}$  and  $\mathbf{Y}_{mm}$  are derived from the following matrix expressions

$$\mathbf{Y}_{mp} = \boldsymbol{\Phi}_m^T \boldsymbol{\Omega} \boldsymbol{\Phi}_p, \quad (4.2)$$

$$\mathbf{Y}_{mm} = \boldsymbol{\Phi}_m^T \boldsymbol{\Omega} \boldsymbol{\Phi}_m, \quad (4.3)$$

where  $\Phi_m$  and  $\Phi_p$  are the matrices with the following amplitudes of the plate flexural natural modes

$$\Phi_m = \begin{bmatrix} \phi_1(x_{m_1}, y_{m_1}) & \cdots & \phi_1(x_{m_{25}}, y_{m_{25}}) \\ \vdots & \ddots & \vdots \\ \phi_N(x_{m_1}, y_{m_1}) & \cdots & \phi_N(x_{m_{25}}, y_{m_{25}}) \end{bmatrix}, \quad (4.4)$$

$$\Phi_p = \begin{bmatrix} \phi_1(x_{p_1}, y_{p_1}) & \cdots & \phi_1(x_{p_{16}}, y_{p_{16}}) \\ \vdots & \ddots & \vdots \\ \phi_N(x_{p_1}, y_{p_1}) & \cdots & \phi_N(x_{p_{16}}, y_{p_{16}}) \end{bmatrix}, \quad (4.5)$$

and  $\Omega$  is the following diagonal matrix

$$\Omega = \begin{bmatrix} \frac{j\omega}{M_p[\omega_{n_1}^2(1+j\eta)-\omega^2]} & & \\ & \ddots & \\ & & \frac{j\omega}{M_p[\omega_{n_N}^2(1+j\eta)-\omega^2]} \end{bmatrix}. \quad (4.6)$$

Here,  $M_p = \rho h l^2$  is the mass of the plate,  $\rho$  is the density of the material of the plate,  $l$ , and  $h$  are the dimensions and thickness of the plate, and  $\eta$  is the plate loss factor. The  $i$ -th natural frequency  $\omega_{ni}$  and  $i$ -th natural mode  $\phi_{ni}(x, y)$  for the simply supported plate are given by

$$\omega_{ni} = \sqrt{\frac{D}{\rho h} \left[ \left( \frac{n_1 \pi}{l} \right)^2 + \left( \frac{n_2 \pi}{l} \right)^2 \right]}, \quad (4.7)$$

$$\phi_{ni}(x, y) = 2 \sin\left(\frac{n_1 \pi x}{l}\right) \sin\left(\frac{n_2 \pi y}{l}\right), \quad (4.8)$$

where  $n_1, n_2$  are the indices of the  $i$ -th natural mode.

The arrays of point masses and point absorbers are characterised by the following impedance relation:

$$\mathbf{f}_m = -\mathbf{Z}_m \dot{\mathbf{w}}_m, \quad (4.9)$$

where  $\mathbf{Z}_m$  is a diagonal  $25 \times 25$  matrix with the point impedances either of the point masses,  $Z_i(\omega) = j\omega m$ , or the spring-mass point vibration absorbers:  $Z_i(\omega) = \frac{(-m_b \omega^2 + j\omega c + k)(-m \omega^2 + j\omega c + k) - (j\omega c + k)^2}{j\omega(-m \omega^2 + j\omega c + k)}$ . The negative sign in Eq. (4.9) is because the forces in the vector  $\mathbf{f}_m$  act on the plate, thus the forces acting on the point masses and the point absorbers are given by  $-\mathbf{f}_m$ . Substituting Eq. (4.9) into Eq. (4.1) yields

$$\dot{\mathbf{w}}_m = (\mathbf{I} + \mathbf{Y}_{mm} \mathbf{Z}_m)^{-1} \mathbf{Y}_{mp} \mathbf{f}_p. \quad (4.10)$$

The overall vibration of the plate produced by rain-on-the-roof disturbance, which is a stationary white noise process, can be assessed in terms of time-averaged total kinetic energy:

$$S_K(\omega) = \frac{1}{2} \int_{A_p} \rho_p h_p \mathcal{F}[\mathcal{R}_{\dot{w}\dot{w}}(\tau)] dA_p, \quad (4.11)$$

where  $\mathcal{F}[\ ]$  denotes the Fourier Transform. Also,  $\mathcal{R}_{\dot{w}\dot{w}}(\tau)$  is the autocorrelation function between plate velocities. Using the definition of Fourier Transform given in Ref. [86], the above PSD functions can be rewritten as follows:

$$S_k(\omega) = \frac{1}{2} \rho_p h_p \int_{A_p} \lim_{T \rightarrow \infty} E \left[ \frac{1}{T} \dot{w}(x, y, \omega)^* \dot{w}(x, y, \omega) \right] dA_p, \quad (4.12)$$

where the superscript  $*$  indicates the complex conjugate and  $\dot{w}(x, y, \omega)$  is the complex transverse velocity over the plate surface. The flexural vibration on a generic position of the panel due to primary and secondary force excitations can be then expressed as

$$\dot{w}(x, y, \omega) = \boldsymbol{\Phi}^T(x, y) \boldsymbol{\Omega} \boldsymbol{\Phi}_p \mathbf{f}_p + \boldsymbol{\Phi}^T(x, y) \boldsymbol{\Omega} \boldsymbol{\Phi}_m \mathbf{f}_m, \quad (4.13)$$

where  $\boldsymbol{\Phi}^T(x, y) = [\phi_1(x, y) \ \cdots \ \phi_N(x, y)]$  is a row vector with the modal amplitudes at position  $(x, y)$  of the plate. Also, according to Eqs. (4.9) and (4.10),

$$\mathbf{f}_m = -\mathbf{Z}_m (\mathbf{I} + \mathbf{Y}_{mm} \mathbf{Z}_m)^{-1} \mathbf{Y}_{mp} \mathbf{f}_p. \quad (4.14)$$

Substituting Eq. (4.13) into Eq. (4.12) yields

$$S_k(\omega) = \frac{1}{2} \rho_p h_p \int_{A_p} \lim_{T \rightarrow \infty} E \left[ \frac{1}{T} \mathbf{f}_p^H \mathbf{Y}^H \boldsymbol{\Phi} \boldsymbol{\Phi}^T \mathbf{Y} \mathbf{f}_p \right] dA_p, \quad (4.15)$$

where

$$\mathbf{Y} = \boldsymbol{\Omega} \boldsymbol{\Phi}_p - \boldsymbol{\Omega} \boldsymbol{\Phi}_m \mathbf{Z}_m (\mathbf{I} + \mathbf{Y}_{mm} \mathbf{Z}_m)^{-1} \mathbf{Y}_{mp}. \quad (4.16)$$

The plate natural modes are orthogonal and normalised such that

$$\int_{A_p} \boldsymbol{\Phi}(x, y) \boldsymbol{\Phi}^T(x, y) dA_p = A_p, \quad (4.17)$$

where  $A_p = l^2$  is the area of the plate. Thus, after a few mathematical manipulations, Eq. (4.17) results

$$S_k(\omega) = \frac{1}{2} \mathbf{M}_p \text{Tr} \left[ \mathbf{Y} \mathbf{S}_{\mathbf{f}_p \mathbf{f}_p}(\omega) \mathbf{Y}^H \right], \quad (4.18)$$

where  $\text{Tr}[\dots]$  is the trace matrix function and  $\mathbf{S}_{f_p f_p}(\omega)$  is a matrix with PDSs of the excitations, which, for the uncorrelated rain-on-the-roof forces of unit amplitudes is given by

$$\mathbf{S}_{f_p f_p}(\omega) = \mathbf{I}. \quad (4.19)$$

Plot (a) in Figure 4.2 presents the evolution of the flexural kinetic energy of the plate with an array of 25-point masses against the dimensionless weight ratio of the point masses with reference to the weight of the plate:

$$\gamma = \frac{\sum_{i=1}^{25} m_i}{m_p}. \quad (4.20)$$

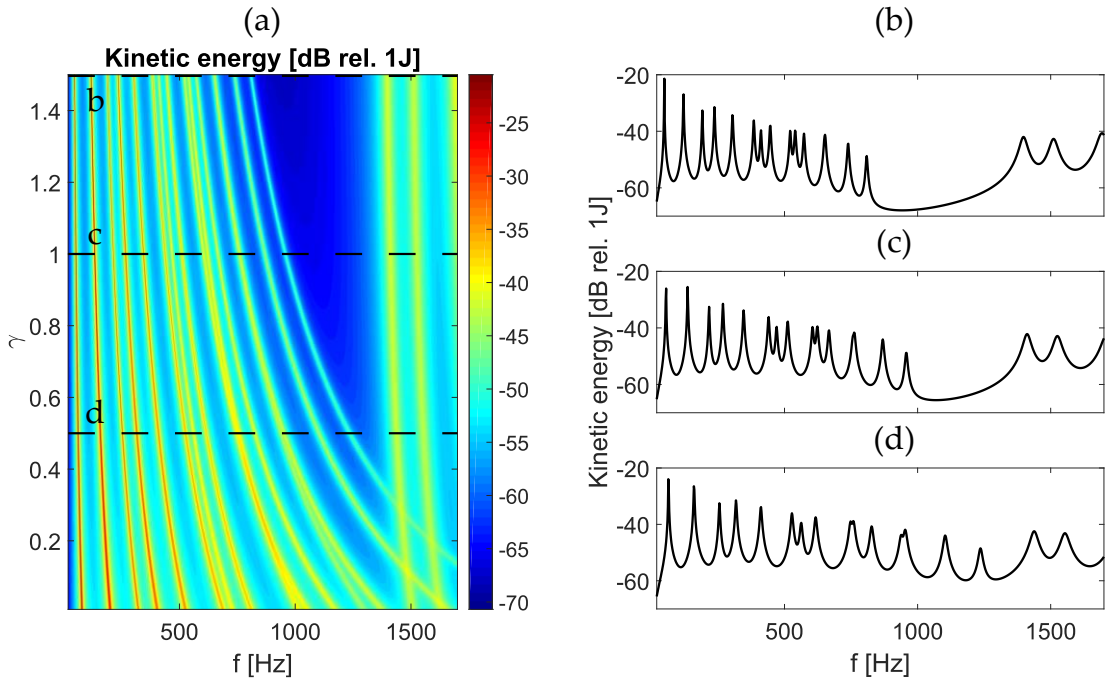


Figure 4.2 (a) Evolution of the flexural kinetic energy of the finite plate equipped with periodic masses against their dimensionless ratio. Power spectral density functions of the kinetic energy when dimensionless mass is equal to 0.5 (d), 1 (c) and 1.5 (b).

This graph effectively shows that, when the weight of point masses reaches about 40% of the weight of the plate, the band gap starts to develop at around 1350 Hz and expands with added mass towards lower frequencies. This result seems to confirm the findings of simulation studies performed for the infinite plate with periodic point

masses. Wherein, the distribution of the interference stop band produced by the scattering from the inclusions is unilaterally limited at dimensionless frequency 1. For the considered finite plate system this frequency corresponds to 1350 Hz. Plots (b), (c), and (d) show the spectra of the total kinetic energy of the plate when total weight of point masses is equal to 150%, 100% and 50% of the mass of the plate. Plot (d) does not differ from a typical spectrum of the total flexural response of a uniform plain plate, which is characterised by a sharp resonance peak due to the fundamental natural mode of the plate, followed by well separated resonance peaks due to the lower order natural modes of the panel. Above about 500 Hz, the plate modal overlap exceeds unity and thus the response of the panel at each frequency is characterised by the superposition of an increasing number of higher order natural modes, which generate sequences of wide band crests and wide band lows. In contrast, plots (b) and (c) show that, when the total weight of the point masses is relevant compared to the weight of the plate, the plate dynamics is characterised by a wide band gap.

Figure 4.3 (a) presents the evolution of the flexural kinetic energy of the plate equipped with vibration absorbers whose total mass is equal to 20% of the mass of the plate. The distribution of the stop band effect with reference to resonance frequency of the absorbers is depicted by the blue shadow elongating diagonally through the surface plot. When resonance frequency of the absorbers is increased towards 1350 Hz, a tendency of widening of the stop band effect can be noticed. The effect reaches its maximal width at around 1300 Hz and vanishes at around 1350 Hz. When the weight of the proof masses is increased to 40% of the mass of the plate, the interference effect linked to the proof masses is enhanced. As a consequence, the vertical elongation of the blue shadow is visible above resonance frequency of 1350 Hz, as illustrated in Figure 4.4 (a).

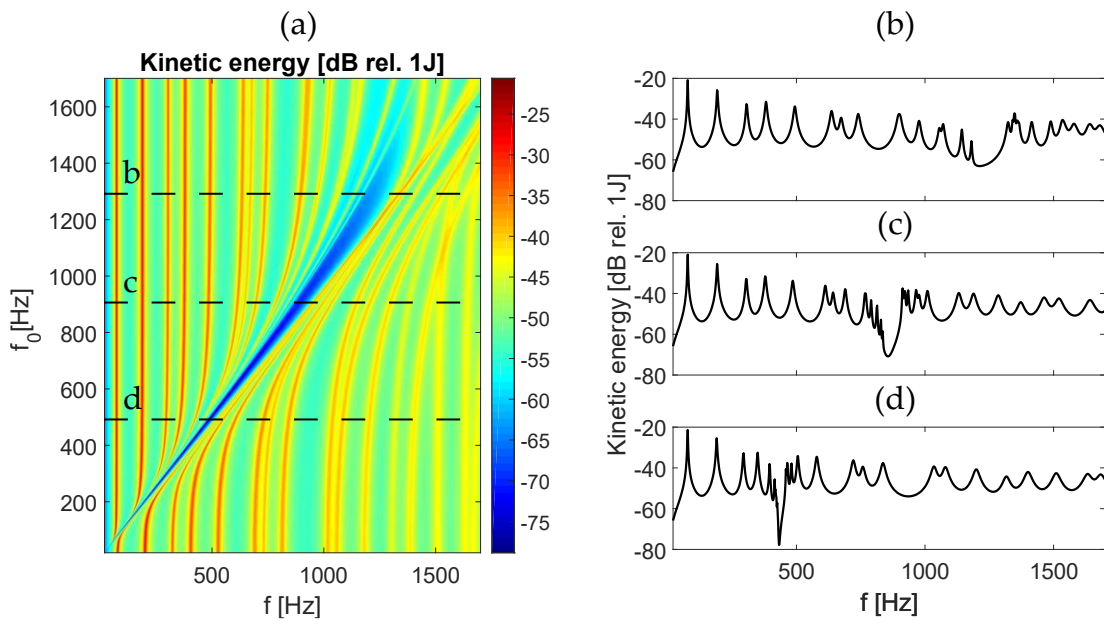


Figure 4.3 (a) Evolution of flexural kinetic energy of the finite plate equipped with a  $5 \times 5$  array of vibration absorbers whose masses are equal to 20% of the plate mass with respect to their resonance frequency (A). Power spectral density functions of the kinetic energy when absorbers are tuned to 1300 Hz (b), 900 Hz (c) and 460 Hz (d).

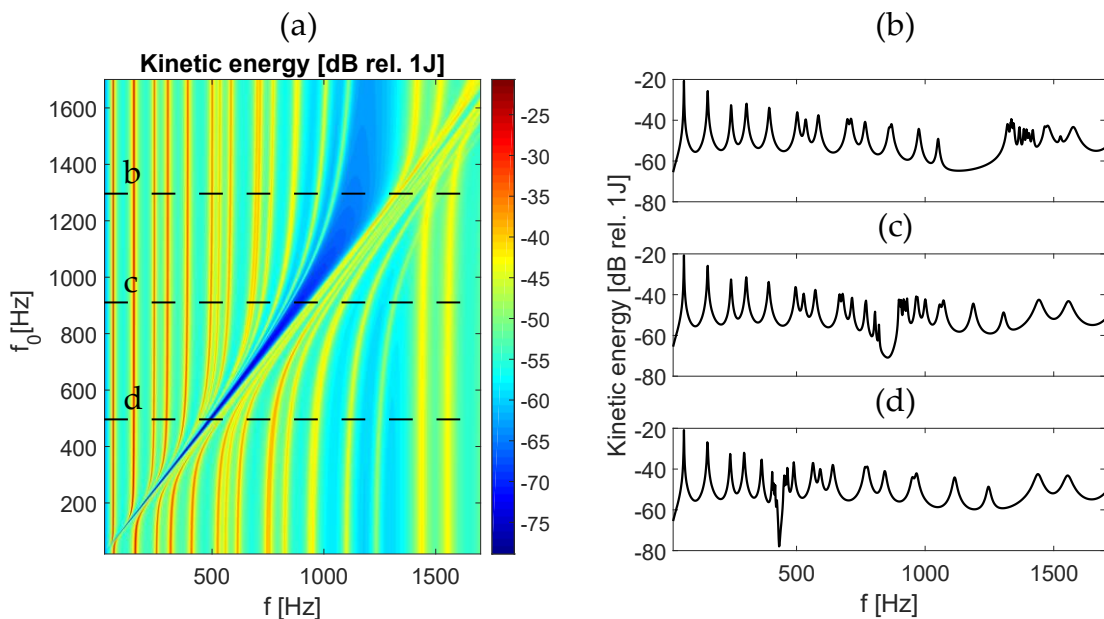


Figure 4.4 (a) Evolution of the flexural kinetic energy of the finite plate equipped with a  $5 \times 5$  array of vibration absorbers whose masses are equal to 40% of the plate mass with respect to their resonance frequency. Power spectral density functions of the kinetic energy when absorbers are tuned to 1300 Hz (b), 900 Hz (c) and 460 Hz (d).

The influence of the weight of the proof masses on the distribution of the resonance stop band effect is presented in Figure 4.5(a). The resonance frequency of the absorbers was kept constant at 650 Hz by adjusting the stiffness of the springs as a function of added mass. The results of this simulations indicate that the distribution of the stop band effect at frequencies below 1350 Hz can be modified to great extent by the suspended mass weight.

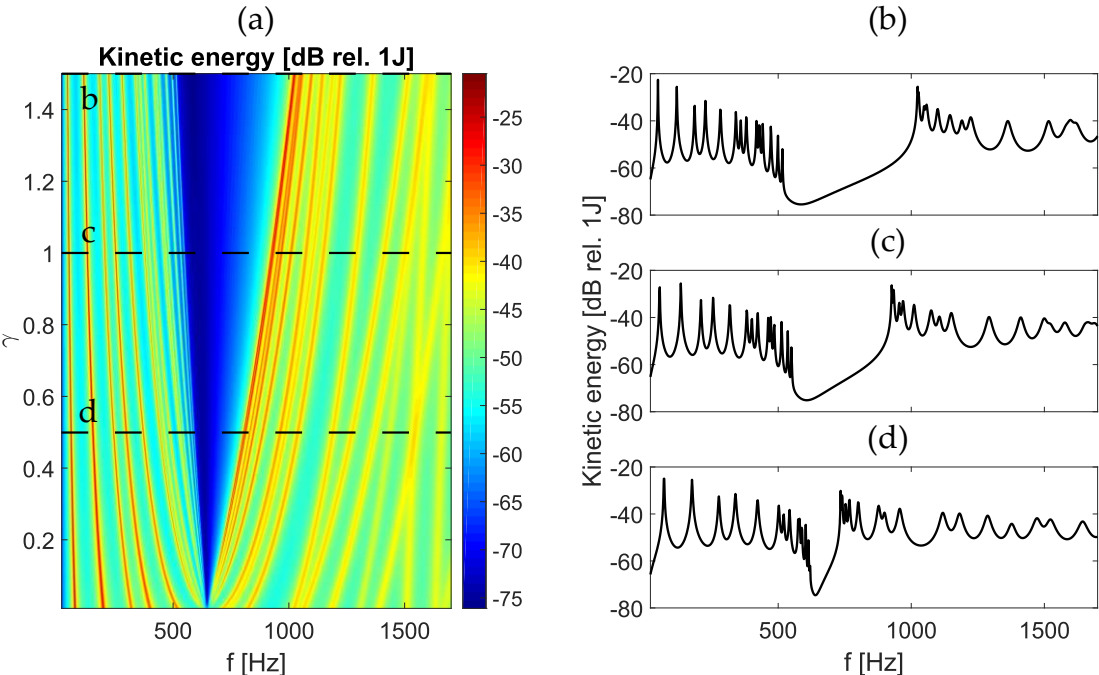


Figure 4.5 (a) Evolution of the flexural kinetic energy of the finite plate equipped with a  $5 \times 5$  array of vibration absorbers tuned to 650 Hz against the dimensionless mass ratio of the absorbers. The power spectral density functions of the kinetic energy when the mass ratios are equal to 0.2 (b), 1 (c) and 0.5 (d).

Equipping the resonators with base masses introduces additional scattering processes that lead to the interference band gap. When the weight of the base masses is significant in relation to the weight of the plate, the interference becomes relevant and influences the evolution of the resonance stop band effect. Figure 4.6 (a) highlights how, a noticeable resonance stop band effect can be affected by the presence of the additional scatterers. In this plot, the wide blue shadow centred at around 1200Hz indicates a strong interference effect that elongates vertically with the resonance frequency of the absorbers. The resonance effect of vibrating absorbers and the interference effect due to the point masses coexist up to the resonance frequency of

800Hz. Between 800 Hz and 1200 Hz the interference effect becomes increasingly smaller and finally vanishes leaving a narrow separation gap, between the two effects. The gap itself is a strong manifestation of the physics of the Fano scattering, where the resonance peak of the hosting structure is modified into a pair of peaks of the same amplitude by the oscillating vibration absorbers. From the other hand, the resonance stop band effect becomes wider with the resonance frequency until it reaches its maximum width due to the coupling with interference effect occurring for proof masses. As one can note, further increase of the resonance frequency has no impact on the evolution of the resonance stop band effects, thus the remaining effect is driven mostly by the interference.

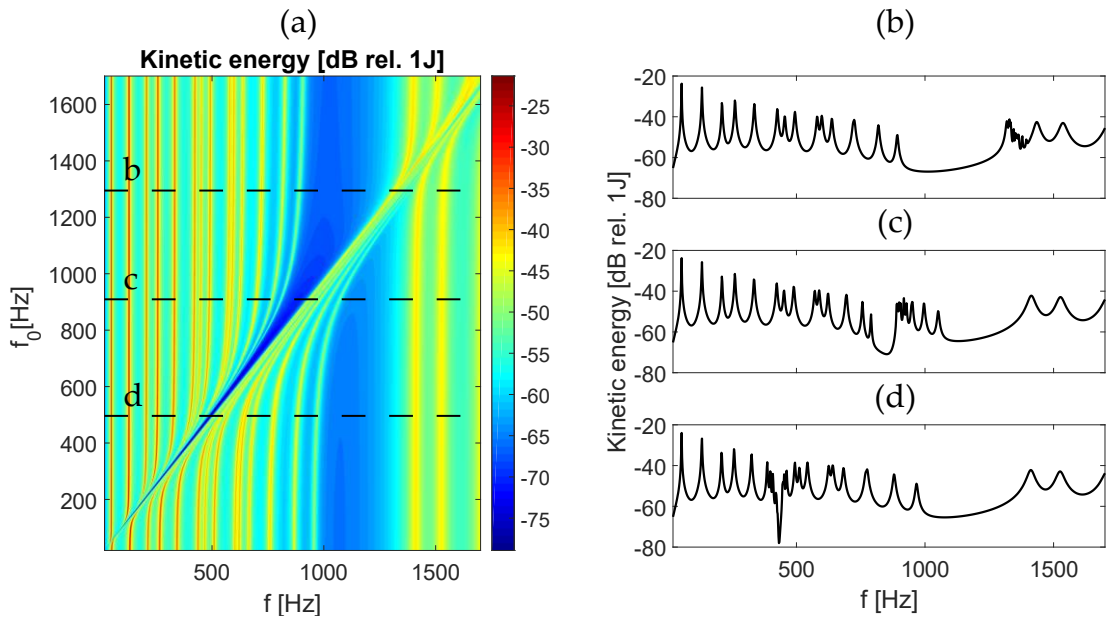


Figure 4.6 (a) Evolution of flexural kinetic energy of the finite plate equipped with a  $5 \times 5$  array of vibration absorbers with base masses equal to 0.7 and proof masses to 0.2 of the plates mass, with reference to resonance frequency of the absorbers. Power spectral density functions of the kinetic energy when absorbers are tuned to 460 Hz (d), 900 Hz (c) and 1350 Hz (b).

#### 4.2.2 Finite plate with regular array of piezoelectric patch transducers connected to resistive-inductive shunts

The mathematical formulation used to study the flexural response when the plate is equipped with shunted piezoelectric patches is based on Kirchhoff hypothesis

[17,85,87]. In-plane vibrations are not taken into account, which is a reasonable assumption within the considered frequency range, that is 50 – 1.5 kHz. Also, the fluid loading effect of air is simply modelled as a damping effect on the flexural response of the plate. The response of the smart plate is derived from the generalised form of Hamilton's principle for electromechanical systems [17,73,88,89]:

$$\int_{t_1}^{t_2} [\delta(K^* - V + W_e^*) + \delta W_{nc}] dt = 0, \quad (4.21)$$

where  $\delta(\ )$  is the variation operator,  $K^*$ ,  $V$ ,  $W_e^*$  are the kinetic coenergy, the elastic potential energy and the electrical coenergy for the flexural vibrations of the plate with the piezoelectric patches and  $\delta W_{nc}$  is the virtual work done by non-conservative actions, that is the virtual work done by the external uncorrelated transverse forces exciting the panel, the virtual work done by the damping forces exerted by the interaction between the panel flexural vibration and the air and the virtual work done by the shunts currents flowing into the piezoelectric patches. The expressions presented in Ref. [17] for these energy functions have been used in Eq. (4.21) assuming the transverse displacement of the plate is given by the following modal summation [90]:

$$w(x, y, t) = \boldsymbol{\phi}(x, y) \mathbf{d}(t), \quad (4.22)$$

where  $\boldsymbol{\phi}(x, y) = [\phi_1(x, y) \ \cdots \ \phi_R(x, y)]$  is a row vector with the first  $R$  natural modes of the plain plate (i.e. with no piezoelectric patches bonded on it),  $\phi_1(x, y), \dots, \phi_R(x, y)$ , and  $\mathbf{d}(t) = [d_1(t) \ \cdots \ d_R(t)]^T$  is a column vector with the first  $R$  generalized coordinates for the transverse vibrations of the plain plate,  $d_1(t), \dots, d_R(t)$ . The natural frequencies and natural modes of the simply supported plain plate have been derived from the following expressions

$$\omega_{nr} = \sqrt{\frac{B_p}{m_p} \left[ \left( \frac{r_1 \pi}{l_{xp}} \right)^2 + \left( \frac{r_2 \pi}{l_{yp}} \right)^2 \right]}, \quad \phi_r(x, y) = 2 \sin \left( \frac{r_1 \pi x}{l_{xp}} \right) \sin \left( \frac{r_2 \pi y}{l_{yp}} \right), \quad \text{where,}$$

$B_p = Y_p h_p^3 / (12(1 - \nu_p^2))$  and  $m_p = \rho_p h_p$  are the bending stiffness and mass per unit surface of the plate assuming  $Y_p$ ,  $\nu_p$ ,  $\rho_p$  are the Young's modulus, Poisson ratio and density of the plate material,  $l_{xp}$ ,  $l_{yp}$  are the plate dimensions and  $r_1$ ,  $r_2$  are the modal indices of the  $r$ -th mode. After implementing the lengthy sequence of mathematical manipulations described in Refs. [17,91], the integral equation of Hamilton's principle is transformed into a set of mechanical and a set of electrical ordinary differential equations, which are casted in the following two matrix equations

$$\mathbf{M}_t \ddot{\mathbf{d}}(t) + \mathbf{C}_p \dot{\mathbf{d}}(t) + \mathbf{K}_t \mathbf{d}(t) + \mathbf{\Theta}_{pe} \mathbf{v}_s(t) = \mathbf{\Phi}_p \mathbf{f}_p(t), \quad (4.23)$$

$$-\mathbf{\Theta}_{pe}^T \mathbf{d}(t) + \mathbf{C}_{pe} \mathbf{v}_s(t) = \mathbf{q}_s(t), \quad (4.24)$$

In Eq. (4.25),  $\mathbf{M}_t = \mathbf{M}_p + \mathbf{M}_{pe}$  and  $\mathbf{K}_t = \mathbf{K}_p + \mathbf{K}_{pe}$  are the  $R \times R$  modal mass and stiffness matrices, which are given by the sum of a diagonal matrix for the plain plate modal responses, respectively  $\mathbf{M}_p$  and  $\mathbf{K}_p$ , and a fully populated matrix for the coupled modal responses due to the piezoelectric patches effects, respectively  $\mathbf{M}_{pe}$  and  $\mathbf{K}_{pe}$ . Also,  $\mathbf{C}_p$  is the  $R \times R$  modal damping matrix of the plate.

$$\mathbf{M}_p = m_p \int_{A_p} \boldsymbol{\varphi}^T \boldsymbol{\varphi} dA_p = m_p \mathbf{I}, \quad (4.25)$$

$$\mathbf{M}_{pe} = \sum_{i=1}^{25} m_{pe} \int_{A_{pe,i}} \boldsymbol{\varphi}^T(x, y) \boldsymbol{\varphi}(x, y) dA_{pe,i}, \quad (4.26)$$

$$\mathbf{C}_p = \int_{A_p} \mu \boldsymbol{\varphi}^T \boldsymbol{\varphi} dA_p = 2\zeta_p m_p \boldsymbol{\Omega}, \quad (4.27)$$

$$\mathbf{K}_p = I_p \int_{A_p} \boldsymbol{\Psi}^T \mathbf{c}_p \boldsymbol{\Psi} dA_p = m_p \boldsymbol{\Omega}^2, \quad (4.28)$$

$$\mathbf{K}_{pe} = \sum_{i=1}^{25} I_{pe} \int_{A_{pe,i}} \boldsymbol{\Psi}^T \mathbf{c}_{pe}^E \boldsymbol{\Psi} dA_{pe,i}, \quad (4.29)$$

Here  $\mathbf{I}$  is a  $R \times R$  identity matrix,  $I_p$ ,  $I_{pe}$  are the second moments of the plate and piezoelectric patch and

$$\boldsymbol{\Psi} = \begin{bmatrix} \boldsymbol{\varphi}_{,xx} \\ \boldsymbol{\varphi}_{,yy} \\ 2\boldsymbol{\varphi}_{,xy} \end{bmatrix}, \quad (4.30)$$

$$\boldsymbol{\Omega} = \begin{bmatrix} \omega_{n_1} & & \\ & \ddots & \\ & & \omega_{n_R} \end{bmatrix}. \quad (4.31)$$

In these expressions  $\boldsymbol{\Phi}_p$  is a  $R \times 16$  matrix with the modal amplitudes at the excitation points  $\boldsymbol{\Phi}_p = [\boldsymbol{\varphi}^T(x_1, y_1) \cdots \boldsymbol{\varphi}^T(x_{16}, y_{16})]$  and  $\mathbf{f}_p = [f_{p1} \cdots f_{p16}]^T$  is the vector with the amplitudes of the  $4 \times 4$  array of uncorrelated rain on the roof forces acting on the plate. In Eq. (4.26), the vector  $\mathbf{q} = [q_1 \cdots q_{25}]^T$  and  $\mathbf{v}_s = [v_{s1} \cdots v_{s25}]^T$  contain respectively the charges and voltages of the shunts. Also,  $\mathbf{C}_{pe}$  is a  $25 \times 25$  diagonal matrix with the capacitances of the piezoelectric

patches:  $C_{pe} = \varepsilon_{pe}^S A_{pe} / h_{pe}$ , where  $\varepsilon_{pe}^S$  is the permittivity for constant strain and  $A_{pe}$  and  $h_{pe}$  are respectively the area and thickness of the piezoelectric patches. Finally,  $\Theta_{pe} = [\Phi_{pe,1} \ \cdots \ \Phi_{pe,25}]$  is the  $R \times 25$  piezoelectric coupling matrix given by

$$\Phi_{pe,i} = z_{pe} \int_{A_{pe,i}} \Psi^T \mathbf{e}_{pe} dA_{pe,i} . \quad (4.32)$$

The details of all these matrices can be found in Refs. [17,91]. The modal summation formulation used to reconstruct the flexural vibration of the plate and piezoelectric patches refers to the flexural natural modes of the plain plate. Therefore, as discussed in Ref. [17] a rather large number of natural modes has been taken into account to form a mathematical basis that properly reconstructs the effective flexural deflection shapes of the plate and piezoelectric patches assembly in the low frequency range taken into consideration in this work. A convergence study indicated that, for the 20 – 250 Hz frequency range considered in the simulations, the modal summation should include at least 300 flexural natural modes of the plain plate with natural frequencies up to 7.7 kHz. This rather large number of modes is necessary to model the discontinuity effects occurring along the borders of the piezoelectric patches.

Assuming the time-harmonic motion given in the form  $g(\omega) = g(\omega) \exp(j\omega t)$ , where  $g(\omega)$  is the complex amplitude and  $\omega$  is the circular frequency, the two matrix expressions describing the system can be written in terms of the complex amplitudes  $\mathbf{d}(\omega)$ ,  $\mathbf{f}_p(\omega)$ ,  $\mathbf{v}_s(\omega)$ ,  $\mathbf{q}_s(\omega)$  as follows:

$$\mathbf{M}_t \ddot{\mathbf{d}}(\omega) + \mathbf{C}_p \dot{\mathbf{d}}(\omega) + \mathbf{K}_t \mathbf{d}(\omega) + \Theta_{pe} \mathbf{v}_s(\omega) = \Phi_p \mathbf{f}_p(\omega) , \quad (4.33)$$

$$-j\omega \Theta_{pe}^T \mathbf{d}(\omega) + j\omega \mathbf{C}_{pe} \mathbf{v}_s(\omega) = \mathbf{i}_s(\omega) . \quad (4.34)$$

Application of Ohm's law to the decentralized shunt circuits leads to the following matrix relation

$$\mathbf{v}_s(\omega) = -\mathbf{Z}_s(\omega) \mathbf{i}_s(\omega) , \quad (4.35)$$

where  $\mathbf{Z}_s(\omega)$  is a diagonal matrix with the impedances of the shunt. Substitution of Eq. (4.36) into Eq. (4.35) and then of the resulting equation into Eq. (4.34) gives

$$[-\omega^2 \mathbf{M}_t + j\omega(\mathbf{C}_p + \Theta_{pe} \bar{\mathbf{Z}}_s \Theta_{pe}^T) + \mathbf{K}_t] \mathbf{d}(\omega) = \Phi_p \mathbf{f}_p(\omega) , \quad (4.36)$$

where

$$\bar{\mathbf{Z}}_S = [\mathbf{I} + j\omega \mathbf{Z}_S \mathbf{C}_{pe}]^{-1} \mathbf{Z}_S . \quad (4.37)$$

The overall vibration of the plate produced by rain-on-the roof disturbance, which is a stationary white noise process, can be assessed in terms of the Power Spectral Density (PSD) of the time-averaged total kinetic energy, which, as shown in Refs. [17], is given by

$$\begin{aligned} S_K(\omega) &= \frac{1}{2} \rho_p h_p \int_{A_p} \lim_{T \rightarrow \infty} E \left[ \frac{1}{T} \dot{w}^*(x, y, \omega) \dot{w}(x, y, \omega) \right] dA_p + \\ &+ \sum_{i=1}^{25} \frac{1}{2} \rho_{pe} h_{pe} \int_{A_{pe,i}} \lim_{T \rightarrow \infty} E \left[ \frac{1}{T} \dot{w}^*(x, y, \omega) \dot{w}(x, y, \omega) \right] dA_{pe,i} , \end{aligned} \quad (4.38)$$

where  $E[\dots]$  denotes the expectation operator,  $\dot{w}(x, y, \omega)$  is the complex transverse velocity over the plate surface and the superscript \* indicates the complex conjugate operator. According to Eq. (4.22)  $\dot{w}(x, y, \omega) = \boldsymbol{\varphi}(x, y) \mathbf{d}(\omega)$ , thus the total kinetic energy PSD results in

$$\begin{aligned} S_K(\omega) &= \frac{1}{2} \rho_p h_p \int_{A_p} \lim_{T \rightarrow \infty} E \left[ \frac{1}{T} \mathbf{d}^H(\omega) \boldsymbol{\varphi}^T(x, y) \boldsymbol{\varphi}(x, y) \mathbf{d}(\omega) \right] dA_p + \\ &+ \sum_{i=1}^{25} \frac{1}{2} \rho_{pe} h_{pe} \int_{A_{pe,i}} \lim_{T \rightarrow \infty} E \left[ \frac{1}{T} \mathbf{d}^H(\omega) \boldsymbol{\varphi}^T(x, y) \boldsymbol{\varphi}(x, y) \mathbf{d}(\omega) \right] dA_{pe,i} = \\ &= \frac{1}{2} \text{Tr}[\mathbf{M}_t \mathbf{S}_{dd}(\omega)] . \end{aligned} \quad (4.39)$$

Here  $\text{Tr}[\mathbf{S}_{dd}(\omega)]$  is the trace matrix of the fully populated matrix  $\mathbf{S}_{dd}(\omega)$  containing the self and cross PSD terms of the plate modal velocities produced by the random excitation, and superscript  $^H$  denotes the Hermitian transpose.

$$\mathbf{S}_{dd}(\omega) = \lim_{T \rightarrow \infty} E \left[ \frac{1}{T} \mathbf{d}(\omega) \mathbf{d}^H(\omega) \right] . \quad (4.40)$$

According to Eq. (4.37) the complex modal velocities can be expressed in terms of the following equation

$$\mathbf{d}(\omega) = \mathbf{Y}(\omega) \mathbf{f}_p(\omega) , \quad (4.41)$$

where,  $\mathbf{Y}(\omega)$  is a modal mobility matrix, which is given by

$$\mathbf{Y}(\omega) = j\omega \left[ -\omega^2 \mathbf{M}_t + j\omega (\mathbf{C}_p + \boldsymbol{\Theta}_{pe} \bar{\mathbf{Z}}_S \boldsymbol{\Theta}_{pe}^T) + \mathbf{K}_t \right]^{-1} \boldsymbol{\Phi}_p . \quad (4.42)$$

Substitution of Eq. (41) into Eq. (40) yields

$$\mathbf{S}_{dd}(\omega) = \lim_{T \rightarrow \infty} E \left[ \frac{1}{T} \mathbf{Y}(\omega) \mathbf{f}_p(\omega) \mathbf{f}_p^T(\omega) \mathbf{Y}^H(\omega) \right] = \mathbf{Y}(\omega) \mathbf{S}_{\mathbf{f}_p \mathbf{f}_p}(\omega) \mathbf{Y}^H(\omega) , \quad (4.43)$$

where  $\mathbf{S}_{f_p f_p}(\omega)$  is the matrix with the PSD functions of the 16 uncorrelated white noise forces acting on the plate, which, assuming unit excitations, is given by a  $16 \times 16$  identity matrix. In summary, the kinetic energy PSD can be derived by substituting Eq. (4.44) into Eq. (4.40) so that

$$S_K(\omega) = \frac{1}{2} \text{Tr} \left[ \mathbf{M}_t \mathbf{Y}(\omega) \mathbf{S}_{f_p f_p}(\omega) \mathbf{Y}^H(\omega) \right]. \quad (4.44)$$

This paragraph presents simulation studies that show the plate vibration control effects that could be produced with the  $5 \times 5$  array of piezoelectric patches connected to identical, series RL shunts. As discussed in Ref. [17], when the resonance frequency  $\omega_0$  of a piezoelectric patch connected to an inductive shunt corresponds to a resonance of the hosting structure, the resonance peak that characterizes the PSD of the flexural response at  $\omega_0$  is modified in a pair of peaks of about the same amplitude. The amplitude of the two peaks can then be lowered by introducing a resistor in series with an inductor. Figure 4.7 (a) shows how the kinetic energy PSD varies as the inductance of the 25 shunts is tuned to a given frequency and the quality factor

$$Q_{RLC} \approx \frac{\omega_0 L_s}{R_s}, \quad (4.45)$$

that characterizes the losses produced by the resistors in the electrical shunts is set equal to 25 (i.e. damping ratio of 3%). In Eq. (4.45) the inductance of the shunt is set such that the shunt resonates at frequency  $\omega_0$ , thus it has been set equal to

$$L_s = \frac{1}{\omega_0^2 C_{pe}}. \quad (4.46)$$

The shunted piezoelectric patches produce rather smaller effects at the targeted frequencies compared to spring-mass vibration absorbers. Plots (b), (c) and (d) in figure Figure 4.7 show the kinetic energy PSD at three targeted frequencies, which are highlighted by the blue arrows in the spectra. Despite the poorer performance, the piezoelectric transducers can generate stop-band effects at frequencies above the edge frequency limiting the central effects produced by vibration absorbers. This is due to the spatial distribution of the patches on the surface of the plate, such that they can couple to flexural modes also when they are positioned across modal lines. This can also be seen in Figure 4.7 (a), where the transverse blue shadow indicating the resonance stop band effect generated by the transducers elongates through a

sequence of vertical yellow lines in correspondence to the resonance peaks of the plate. The blue shadow vanishes at around 1450 Hz, which corresponds to the resonance crest of the higher order natural modes and reappear when the resonance frequency of the shunts is further increased to around 1470 Hz. This example shows that the spatial distribution of the patches can immunize the resonance stop band effect to a certain extent from a standing wave behaviour. Other advantages of the piezoelectric patch transducers could be their low weight and ability to generate many locally resonant effects when combined with multi-resonating shunt circuits.

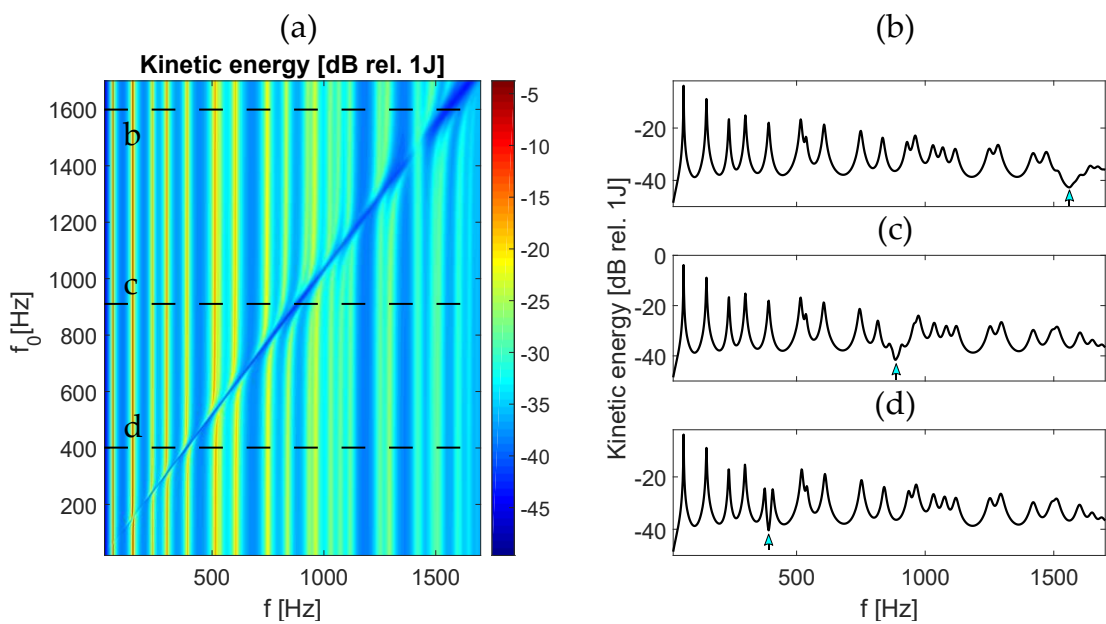


Figure 4.7 (a) Evolution of flexural kinetic energy of the finite plate equipped with a  $5 \times 5$  array of piezoelectric patch transducers connected to series RL shunts. Power spectral density function of the kinetic energy when the shunts are tuned to 400 Hz (b), 900 Hz (c) and 1600 Hz (d).

#### 4.2.3 Finite plate with arrays of shunted piezoelectric patch transducers connected to multi-resonating shunts

In this short section, the multi-resonating shunt circuits, are implemented to demonstrate the concept of double stop-band generation in a finite simply supported plate with a  $5 \times 5$  array of piezoelectric patch transducers. The piezoelectric patches are organized on the plate as depicted in plot (b) of Figure 4.8 and connected to identical shunts illustrated in plot (c) of this figure.

The application of multi-resonant shunts to the model is simple and requires only substitution of the electric impedance of the circuits into Eq. (4.37). Since all the shunts are identical and composed of two parallel LC branches, the total electrical impedance is given by the following formula:

$$Z_S(\omega) = - \left[ \frac{j\omega \frac{1}{L_{b1}}}{-\omega^2 + j\omega \frac{R_{s1}}{L_{b1}} + \frac{1}{C_{f1}L_{b1}}} - \frac{j\omega \frac{1}{L_{b2}}}{-\omega^2 + j\omega \frac{R_{s2}}{L_{b2}} + \frac{1}{C_{f2}L_{b2}}} \right]^{-1}. \quad (4.47)$$

The two target frequencies, as well as two resistances were arbitrarily chosen, and set to  $f_1 = 780\text{Hz}$ ,  $R_{s1} = 5\text{k}\Omega$  and  $f_2 = 1200$ ,  $R_{s2} = 7\text{k}\Omega$ . Figure 4.8(a) illustrates the power spectral density function of the kinetic energy of the plate. The graph clearly shows double peak resonance effects characterised by rather significant attenuation amplitudes.

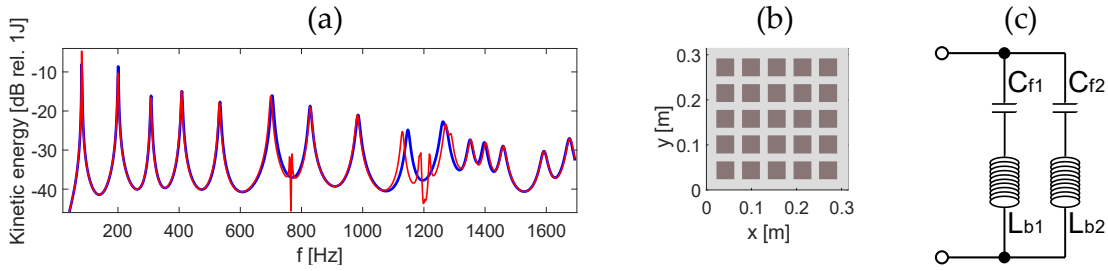


Figure 4.8 (a) Power spectral density function of the kinetic energy of the plate with a  $5 \times 5$  array of piezoelectric patches connected to multi-resonating shunts in open circuit configuration (blue line) and tuned to  $f_1 = 780\text{Hz}$  and  $f_2 = 1200\text{Hz}$  (red line). (b) Spatial configuration of piezoelectric patches. (c) Depiction of the multi-resonating shunt circuit.

#### 4.3 CONCLUDING REMARKS

This chapter was focused on the generation and characterization of stop band phenomena in a finite plate equipped with two-dimensional arrays of inclusions. Most of all the studies confirmed that both interference and resonance stop bands can be effectively produced in finite plates and their general characteristics do not differ from ones obtained for infinite plates. In line with the previous findings the study showed, that relevant interference effects generated by arrays of point masses arise only at frequency associated with standing wave whose spatial period matches twice the spacing between scatterers. Due to this limitation the interference effects can only be extended towards lower frequencies by increasing the mass of inclusions. Indeed, a significant low-frequency band coverage is possible, but requires substantial mass addition, which makes this type of solution far less practical. Then, the studies

demonstrated that significant stop band effects can be produced in finite plates by relatively small number of resonating inclusions. It was showed that an  $5 \times 5$  array of spring-mass vibration absorbers can be effectively tuned to produce stop bands up to certain edge frequency. Above this limiting frequency the stop bands cannot be generated due to the coupling limitations of the point-like absorbers with high frequency plate natural modes. Piezoelectric patches can partly overcome this difficulty and deliver some effects at higher frequencies due their spatial organization, which allows them to avoid nodal positions. The simulation studies also confirmed that a phenomenon of widening of resonance stop bands is maintained in finite plates. The stop band distribution maps assembled from the power spectral density functions of the plates flexural kinetic energy illustrate widening of the resonance bands along with resonance frequency of the inclusions. The results therefore indicate that the periodicity of the structure significantly influences the tuning range of the inclusions, in which broadband resonance effects are achievable at frequencies not very distant from the edge frequency. This represent a considerable practical limitation for low-frequency broadband applications, since a decrease of the edge frequency comes with an increase of the spacing between resonators. For this reason, the presented solutions can be rather valuable in mid to high-frequency applications.

---

## FINITE PLATE WITH ARRAYS OF SHUNTED PIEZOELECTRIC PATCHES FOR LOW FREQUENCIES VIBRATION CONTROL

---

In this chapter a practical algorithm is proposed for the on-line tuning of multi-resonant shunts connected to piezoelectric patches that are bonded on thin structures to reduce the effects of flexural vibrations over a wide frequency band. Unlike the previous chapters, where investigations were associated with rather mid to high frequency regimes, this chapter focuses on the low frequencies range where the response of the plate at each frequency is characterised by the superposition of one or few modes. In the following studies the multi-resonant shunts are formed by multiple resistance-inductance-capacitance (RLC) branches connected in parallel. A tuning algorithm is proposed which sequentially tunes the RL elements of the branches in each shunt in such a way as to maximise the vibration energy absorption from a progressively larger number of resonant flexural modes of the hosting structure. The algorithm can be used also to tune the RL elements of classical, single branch, shunts. In practice the vibration energy absorption is estimated from the measured electric power absorbed by each shunt so that the on-line tuning algorithm can be conveniently implemented locally. To prove the validity of the proposed algorithm, first a simulation study is presented considering the flexural response of a thin plate structure, which is equipped with piezoelectric patches connected to multi-resonant shunts and is excited by a rain on the roof space and time stochastic disturbance. The study shows that the proposed approach allows the online tuning of the RLC branches in each shunt to control the resonant response of low order flexural modes so that the flexural response of the smart plate is effectively reduced over a wide low frequencies band. The proposed algorithm is then validated experimentally with a test rig composed of a clamed aluminium plate equipped with five piezoelectric patches connected to identical shunts. The multi-resonant shunts are synthesized digitally in a multi-channel dSPACE platform and tuned with the proposed method

such that piezoelectric patches exhibit multi-resonance vibration control effect on three flexural modes of the plate in the low-frequency range 40-150Hz.

## 5.1 INTRODUCTION

This chapter proposes a novel practical algorithm for the on-line tuning of multi-resonant current-flowing shunts connected to piezoelectric patches that are bonded on thin structures to reduce the effects of flexural vibrations in a wide frequency band. The multi-resonant shunts are formed by multiple RLC branches connected in parallel. The proposed algorithm sequentially sets the RLC elements of the branches in each shunt in such a way as to maximise the vibration energy absorption from a progressively larger number of resonant flexural modes of the hosting structure. In practical applications, the vibration energy absorption will be estimated from the measured electric power absorbed by each shunt. In this way, the on-line tuning algorithm can be conveniently implemented in the electronic board of the shunt. To make the proposed tuning approach more readily comprehensible, a simple problem is considered in this chapter, which, as detailed in Section 5.2, is composed of a thin rectangular plate equipped with two piezoelectric patches connected to multi-resonant current-flowing shunts and excited by a rain on the roof space and time stochastic disturbance. As mentioned in Section 5.3, the flexural response of the smart plate is derived by combining the classical modal formulation for the coupled electromechanical response of the plate and piezoelectric patches used in Chapter 4 with an original modal formulation for the electric response of the multi-resonant shunts, which is described in Section 5.3.2. The proposed on-line tuning algorithm of the RLC components in the branches of the shunts is then introduced and discussed in Section 5.4. A parametric study is presented in Section 5.5 to show the flexural vibration reduction effects that can be obtained when the plate is equipped with increasingly larger arrays of shunted piezoelectric patch transducers connected to multi-resonant current-flowing shunts tuned on line. Finally, the experimental evaluation of the proposed method of sequential multi-resonant shunt tuning is presented in Section 5.6.

## 5.2 DESCRIPTION OF THE SYSTEM

Figure 5.1 shows the system considered in this study, which is composed of a simply supported rectangular thin aluminium plate immersed in air, whose geometry and physical properties are summarised in Table 5.1 As depicted in Figure 5.1, the plate

is exposed to a white noise rain-on-the-roof time and space stochastic excitation, which is modelled in terms of a  $4 \times 4 = 16$  array of uncorrelated random point forces uniformly distributed over the surface of the plate. To start with, two square piezoelectric patches are arranged on the plate as shown in Figure 5.1 (a). The geometry and physical properties of the two patches are also summarised in Table 5.1. Each patch is connected to a multi-resonant shunt, which, as described in Figure 5.1 (b) is composed of a cascade of parallel RLC branches. Each branch is formed by an inductor  $L_{fij}$  and a capacitor  $C_{fij}$  that produce the so called current flowing effect, that is a band pass filtering effect with centre frequency  $\omega_{fi} = 1/\sqrt{L_{fij}C_{fij}}$ . Also it encompasses an inductor  $L_{sij}$ , which, coupled with the piezoelectric patch capacitor  $C_{pej}$ , produces the shunt vibration absorption effect at the tuning frequency  $\omega_{si} = 1/\sqrt{L_{sij}C_{pej}}$ . Finally, it incorporates a resistor  $R_{sij}$  which is set to maximise the vibration absorption via the piezoelectric patch at frequencies close to the tuning frequency  $\omega_{si}$ . In practice, as shown in Figure 5.1 (c), since the two inductors are connected in series, they are implemented with a single inductor  $L_{bij} = L_{fij} + L_{sij}$ . The response of the smart plate with the two piezoelectric patches connected to multi-resonant shunts is used initially to describe the physics of the proposed tuning approach and to introduce the proposed on-line tuning algorithm. The vibration control effects produced by an increasingly denser array of piezoelectric patches that implement multi-resonant shunts with an increasingly larger number of RLC branches are then examined.

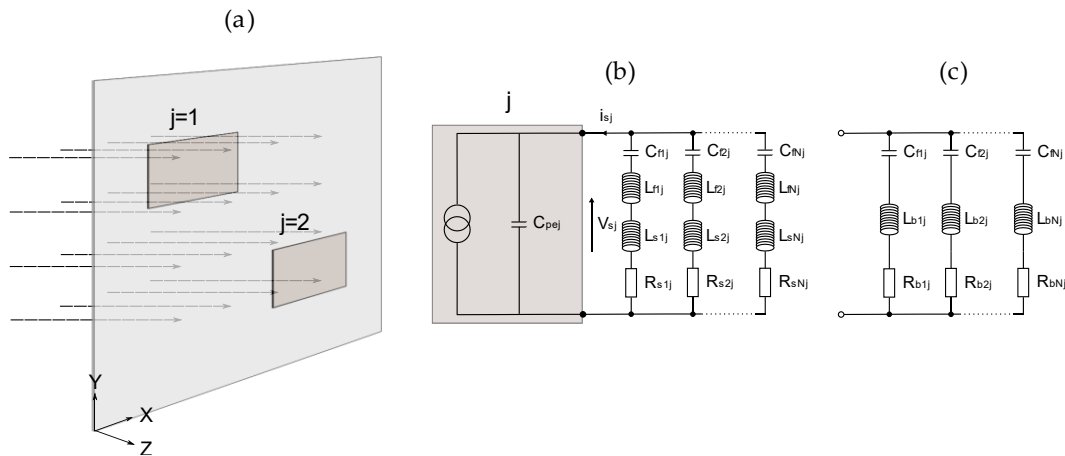


Figure 5.1 (a) Plate equipped with two piezoelectric patches subject to a rain on the roof excitation modelled as a  $4 \times 4$  array of uncorrelated point forces. (b) Electrical model of a piezoelectric patch connected to the current-flowing shunt composed of multiple RLC branches. (c) Simplified electrical model of the shunt.

Table 5.1. Physical and geometrical parameters of the plate.

Parameter	Plate	Piezoelectric patches
Dimensions	$l_{xp} \times l_{yp} = 414 \times 314 \text{ mm}$	$l_{xpe} \times l_{ype} = 85 \times 85 \text{ mm}$
Thickness	$h_p = 1 \text{ mm}$	$h_{pe} = 1 \text{ mm}$
Density	$\rho_p = 2700 \text{ kg/m}^3$	$\rho_{pe} = 7600 \text{ kg/m}^3$
Young's modulus	$E_p = 7 \times 10^{10} \text{ N/m}^2$	$E_{pe} = 2.7 \times 10^{10} \text{ N/m}^2$
Poisson ratio	$\nu_p = 0.33$	$\nu_{pe} = 0.275$
Modal damping ratio	$\zeta_p = 0.02$	$\zeta_{pe} = 0.02$
Strain / charge constants		$d_{31}^0 = 150 \times 10^{-12} \text{ m/V}$ $d_{32}^0 = 150 \times 10^{-12} \text{ m/V}$ $d_{36}^0 = 0$
Permittivity for constant stress		$\epsilon_{pe}^T = 84 \times 10^{-9} \text{ F/m}$
Capacitance		$C_{pe} = 2.113 \times 10^{-7} \text{ F}$
Centre position patch 1		$x_{pe1} = 166 \text{ mm}, y_{pe1} = 266 \text{ mm}$
Centre position patch 2		$x_{pe2} = 333 \text{ mm}, y_{pe2} = 133 \text{ mm}$

### 5.3 MATHEMATICAL MODEL

The mathematical model used in this chapter is the same as presented in Section 4.2.2 of Chapter 4. The following Section 5.3.1 briefly recalls the expressions for the coupled mechanical and electrical equations that characterise the flexural response of the smart plate with reference to modal coordinates. The formulation assumes the plate is equipped with two shunted piezoelectric patches. Section 5.3.2 introduces the formulation used to describe the electrical response of the  $j$ -th shunt, which is casted in an original form based on "electrical modal coordinates" for the  $i = 1, \dots, N$  branches. Then, Section 5.3.3 presents a state-space formulation with reference to mechanical and electrical modal state variables. Starting from this formulation, the time averaged electrical power absorbed by each shunt are then derived in Section 5.3.4 with simple matrix expressions based on Lyapunov equation [92,93]. The time averaged total flexural kinetic energy is used to assess the global flexural response of the smart plate whereas the time averaged electrical power absorbed by each shunt is used to estimate the flexural vibration energy absorbed by each shunted piezoelectric patch. This second parameter is therefore employed in the on-line local tuning of the electrical components in the multi-resonant shunts proposed in this

chapter. Finally, the Power Spectral Density (PSD) of the total flexural kinetic energy of the smart plate and the PSD of the electrical power absorbed by each shunt [92] are derived in Section 5.3.5 for the frequency analysis used to assess the effects produced by the shunted piezoelectric patches and to investigate the physics of the proposed tuning approach.

### 5.3.1 Mechanical and electrical equations

According to Section 4.2.2 the system governing equations are given by

$$\mathbf{M}_t \ddot{\mathbf{d}}(t) + \mathbf{C}_p \dot{\mathbf{d}}(t) + \mathbf{K}_t \mathbf{d}(t) + \mathbf{\Theta}_{pe} \mathbf{v}_s(t) = \mathbf{\Phi}_p \mathbf{f}_p(t), \quad (5.1)$$

$$-\mathbf{\Theta}_{pe}^T \mathbf{d}(t) + \mathbf{C}_{pe} \mathbf{v}_s(t) = \mathbf{q}_s(t). \quad (5.2)$$

In Eq. (5.1),  $\mathbf{M}_t = \mathbf{M}_p + \mathbf{M}_{pe}$  and  $\mathbf{K}_t = \mathbf{K}_p + \mathbf{K}_{pe}$  are the  $R \times R$  total modal mass and stiffness matrices. Also,  $\mathbf{C}_p$  is the  $R \times R$  modal damping matrix of the plain plate and  $\mathbf{d} = [d_1 \ \cdots \ d_R]^T$  is the vector with the generalized coordinates. Next,  $\mathbf{\Theta}_{pe}$  is the  $R \times 2$  piezoelectric coupling matrix and  $\mathbf{v}_s = [v_{s,1} \ \cdots \ v_{s,2}]^T$  contain the voltages of the shunts. Finally,  $\mathbf{\Phi}_p$  is a  $R \times 16$  matrix with the modal amplitudes at the excitation positions and  $\mathbf{f}_p = [f_{p,1} \ \cdots \ f_{p,16}]^T$  is the vector with the amplitudes of the  $4 \times 4$  array of the rain on the roof process. In Eq. (5.2),  $\mathbf{q}_s = [q_{s1} \ q_{s2}]^T$  contain charges of the shunts and  $\mathbf{C}_{pe}$  is the  $2 \times 2$  diagonal matrix with capacitances of the piezoelectric patches, which are assumed equal and thus given by:  $C_{pe} = \varepsilon_{pe}^S A_{pe} / h_{pe}$ , where  $\varepsilon_{pe}^S$  is the permittivity for constant strain and  $A_{pe}$  and  $h_{pe}$  are respectively the area and thickness of the piezoelectric patches.

The modal summation formulation used to reconstruct the flexural vibration of the plate and piezoelectric patches refers to the flexural natural modes of the plain plate. Therefore, as discussed in Ref. [17] a rather large number of natural modes has been taken into account to form a mathematical basis that can be used to properly reconstruct the effective flexural deflection shapes of the plate and piezoelectric patches assembly in the low frequency range taken into consideration in this work. A convergence study indicated that, for the 20 – 250 Hz frequency range considered in the simulations, the modal summation should include at least 300 flexural natural modes of the plain plate with natural frequencies up to 7.7 kHz. This rather large number of modes is necessary to model the discontinuity effects occurring along the borders of the piezoelectric patches.

### 5.3.2 Multi-resonant shunt equations

To derive a state space model for the coupled response of the structure and piezoelectric patches connected to multi-resonant shunts, a modal formulation is proposed for the multiple RLC branches shunt circuits, which considers “modal currents” or “modal charges” and “modal voltage” variables. The new formulation allows to express the systems governing equations in the form of the continuous Lyapunow equation, which can be conveniently solved. The derivation starts from the complex impedance of multiple RLC branches of the shunt. Assuming time-harmonic functions to have the form  $f(t) = Re\{f(\omega)exp(j\omega t)\}$ , where  $f(\omega)$  is the complex amplitude,  $\omega$  is the circular frequency. The admittance of the shunt circuit can be recalled from Section 1.2.1 as the following series of  $N$  second order terms:

$$\frac{i_{sj}(\omega)}{v_{sj}(\omega)} = \frac{\dot{q}_{sj}(\omega)}{v_{sj}(\omega)} = -Y_{sj}(\omega) = -\sum_{i=1}^N \frac{1}{L_{bij}} \frac{j\omega}{-\omega^2 + j\omega \left( \frac{R_{bij}}{L_{bij}} \right) + \frac{1}{c_{fij}L_{bij}}} . \quad (5.3)$$

As it was already shown in the previous chapters, each second order term in the summation of Eq. (5.3), can be envisaged as the weighted sum of the ratio between a modal current  $I_{ij}$ , i.e. modal charge rate  $\dot{Q}_{sij}$ , and modal voltage  $V_{sij}$ , that is  $\frac{I_{sij}}{V_{sij}} = \frac{\dot{Q}_{sij}}{V_{sij}} = -\frac{j\omega}{-\omega^2 + j\omega \left( \frac{R_{sij}}{L_{bij}} \right) + \frac{1}{c_{fij}L_{bij}}}$ . The charge flowing in the  $j$ -th shunt can thus be expressed in terms of the modal charges with the following matrix equation

$$q_{sj} = \mathbf{\Psi}_{sj} \mathbf{Q}_{sj} , \quad (5.4)$$

where  $\mathbf{\Psi}_{sj} = \left[ \frac{1}{\sqrt{L_{b1j}}} \quad \cdots \quad \frac{1}{\sqrt{L_{bNj}}} \right]$  contains modal weighting factors and  $\mathbf{Q}_{sj} = [Q_{s1j} \quad \cdots \quad Q_{sNj}]^T$  is the vector with the modal charges, which can be written in terms of the modal voltages by the following matrix relation

$$\mathbf{Q}_{sj}(\omega) = \mathbf{G}_{sj}(\omega) \mathbf{V}_{sj}(\omega) , \quad (5.5)$$

that is

$$\begin{bmatrix} Q_{s1j}(\omega) \\ \vdots \\ Q_{sNj}(\omega) \end{bmatrix} = - \begin{bmatrix} \frac{1}{-\omega^2 + j\omega \left( \frac{R_{s1j}}{L_{b1j}} \right) + \frac{1}{c_{f1j}L_{b1j}}} \\ \vdots \\ \frac{1}{-\omega^2 + j\omega \left( \frac{R_{sNj}}{L_{bNj}} \right) + \frac{1}{c_{fNj}L_{bNj}}} \end{bmatrix} \begin{bmatrix} V_{s1j}(\omega) \\ \vdots \\ V_{sNj}(\omega) \end{bmatrix} \quad (5.6)$$

Here  $\mathbf{V}_{sj}(\omega) = [V_{s1j} \quad \cdots \quad V_{sNj}]^T$  is the vector with the modal voltages, which in turn is given by

$$\mathbf{V}_{sj} = \mathbf{\Psi}_{sj}^T v_{sj}, \quad (5.7)$$

where  $v_{sj}$  is the voltage at the terminals of the  $j$ -th shunt. Considering the expanded matrix (5.6), the frequency domain Eq. (5.5) can be straightforwardly transformed into the following time domain expression:

$$\mathbf{I}\ddot{\mathbf{Q}}_{sj}(t) + \mathbf{\Delta}_{sj}\dot{\mathbf{Q}}_{sj}(t) + \mathbf{\Omega}_{sj}\mathbf{Q}_{sj}(t) = -\mathbf{V}_{sj}(t), \quad (5.8)$$

where  $\mathbf{I}$ ,  $\mathbf{\Delta}_{sj}$ ,  $\mathbf{\Omega}_{sj}$  are  $N \times N$  diagonal matrices given by:

$$\mathbf{I} = \begin{bmatrix} 1 & & \\ & \ddots & \\ & & 1 \end{bmatrix}, \quad (5.9)$$

$$\mathbf{\Delta}_{sj} = \begin{bmatrix} \frac{R_{s1j}}{L_{b1j}} & & \\ & \ddots & \\ & & \frac{R_{sNj}}{L_{bNj}} \end{bmatrix}, \quad (5.10)$$

$$\mathbf{\Omega}_{sj} = \begin{bmatrix} \frac{1}{C_{f1j}L_{b1j}} & & \\ & \ddots & \\ & & \frac{1}{C_{fNj}L_{bNj}} \end{bmatrix}. \quad (5.11)$$

Now, considering two independent shunt circuits, Eq. (5.8) becomes

$$\ddot{\hat{\mathbf{Q}}}_s(t) + \hat{\mathbf{\Delta}}_s\dot{\hat{\mathbf{Q}}}_s(t) + \hat{\mathbf{\Omega}}_s\hat{\mathbf{Q}}_s(t) = -\hat{\mathbf{V}}_s(t), \quad (5.12)$$

where  $\hat{\mathbf{Q}}_s = [\mathbf{Q}_{s1}^T \quad \mathbf{Q}_{s2}^T]^T$ ,  $\hat{\mathbf{V}}_s = [\mathbf{V}_{s1}^T \quad \mathbf{V}_{s2}^T]^T$ , and matrices are given by

$$\hat{\mathbf{I}} = \begin{bmatrix} \mathbf{I} & \mathbf{0} \\ \mathbf{0} & \mathbf{I} \end{bmatrix}, \quad (5.13)$$

$$\hat{\mathbf{\Delta}}_s = \begin{bmatrix} \mathbf{\Delta}_{s1} & \mathbf{0} \\ \mathbf{0} & \mathbf{\Delta}_{s2} \end{bmatrix}, \quad (5.14)$$

$$\hat{\mathbf{\Omega}}_s = \begin{bmatrix} \mathbf{\Omega}_{s1} & \mathbf{0} \\ \mathbf{0} & \mathbf{\Omega}_{s2} \end{bmatrix}, \quad (5.15)$$

where  $\mathbf{0}$  are square matrices of zeros. Also Eqs. (5.4) and (5.10) become

$$\mathbf{q}_s(t) = \hat{\mathbf{\Psi}}_s\hat{\mathbf{Q}}_s(t), \quad (5.16)$$

$$\hat{\mathbf{V}}_s(t) = \hat{\mathbf{\Psi}}_s^T \mathbf{v}_s(t), \quad (5.17)$$

where

$$\widehat{\Psi}_s = \begin{bmatrix} \Psi_{s1} & \mathbf{0} \\ \mathbf{0} & \Psi_{s2} \end{bmatrix} \quad (5.18)$$

is a rectangular matrix and  $\mathbf{q}_s = [q_{s1} \quad q_{s2}]^T$ ,  $\mathbf{v}_s = [v_{s1} \quad v_{s2}]^T$ . Here  $\mathbf{0}$  are vectors of zeros. This formulation for 2 shunts can be straightforwardly expanded to systems with several shunts.

### 5.3.3 State-space formulation

The time domain Eqs. (5.1), (5.2) are now used to generate a State Space formulation [91,93,94] for the response of the plate with the shunted piezoelectric patches. First, Eq. (5.16) is employed to rewrite Eq. (5.2) as follows:

$$-\boldsymbol{\theta}_{pe}^T \mathbf{y}(t) + \mathbf{C}_{pe} \mathbf{v}_s(t) = \widehat{\Psi}_s \widehat{\mathbf{Q}}_s(t), \quad (5.19)$$

such that the vector with the shunt voltages results:

$$\mathbf{v}_s(t) = \mathbf{C}_{pe}^{-1} \widehat{\Psi}_s \widehat{\mathbf{Q}}_s(t) + \mathbf{C}_{pe}^{-1} \boldsymbol{\theta}_{pe}^T \mathbf{d}(t). \quad (5.20)$$

This expression is then substituted into Eq. (5.1) to derive the following matrix expression for the vector  $\dot{\mathbf{d}}(t)$ :

$$\begin{aligned} \dot{\mathbf{d}}(t) = & -\mathbf{M}_t^{-1} [\mathbf{K}_t + \boldsymbol{\theta}_{pe} \mathbf{C}_{pe}^{-1} \boldsymbol{\theta}_{pe}^T] \mathbf{d}(t) - \mathbf{M}_t^{-1} \mathbf{C}_p \dot{\mathbf{d}}(t) - \\ & -\mathbf{M}_t^{-1} \boldsymbol{\theta}_{pe} \mathbf{C}_{pe}^{-1} \widehat{\Psi}_s \widehat{\mathbf{Q}}_s(t) + \mathbf{M}_t^{-1} \boldsymbol{\Phi}_p \mathbf{f}_p(t). \end{aligned} \quad (5.21)$$

Also, Eq. (5.12) is used to rewrite the electric Eq. (5.20) in terms of the modal charges. This is done by pre-multiplying the left and right hand side of Eq. (5.20) by  $\widehat{\Psi}_s^T$  such that, the following equation is obtained:

$$\widehat{\Psi}_s^T \mathbf{v}_s(t) = \widehat{\Psi}_s^T \mathbf{C}_{pe}^{-1} \widehat{\Psi}_s \widehat{\mathbf{Q}}_s(t) + \widehat{\Psi}_s^T \mathbf{C}_{pe}^{-1} \boldsymbol{\theta}_{pe}^T \mathbf{y}(t). \quad (5.22)$$

Recalling Eqs. (5.12) and (5.17), the equation derived above is then rewritten as follows

$$-\ddot{\widehat{\mathbf{Q}}}_s(t) - \widehat{\Delta}_s \dot{\widehat{\mathbf{Q}}}_s(t) - \widehat{\Omega}_s \widehat{\mathbf{Q}}_s(t) = \widehat{\Psi}_s^T \mathbf{C}_{pe}^{-1} \widehat{\Psi}_s \widehat{\mathbf{Q}}_s(t) + \widehat{\Psi}_s^T \mathbf{C}_{pe}^{-1} \boldsymbol{\theta}_{pe}^T \mathbf{d}(t), \quad (5.23)$$

such that the following matrix expression is derived for the vector  $\ddot{\widehat{\mathbf{Q}}}_s(t)$ :

$$\ddot{\widehat{\mathbf{Q}}}_s(t) = -\widehat{\Psi}_s^T \mathbf{C}_{pe}^{-1} \boldsymbol{\theta}_{pe}^T \mathbf{y}(t) - [\widehat{\Psi}_s^T \mathbf{C}_{pe}^{-1} \widehat{\Psi}_s + \widehat{\Omega}_s] \widehat{\mathbf{Q}}_s(t) - \widehat{\Delta}_s \dot{\widehat{\mathbf{Q}}}_s(t). \quad (5.24)$$

At this point, Eqs. (5.21) and (5.24) are used to construct the state space formulation with respect to the following modal state vector

$$\mathbf{x}(t) = [\mathbf{d}^T \quad \dot{\mathbf{d}}^T \quad \hat{\mathbf{Q}}_s^T \quad \dot{\hat{\mathbf{Q}}}_s^T]^T. \quad (5.25)$$

A classical state space formulation is thus derived with two output equations, one for the modal velocities of the structural response, and one for the modal charges of the  $j$ -th shunt:

$$\dot{\mathbf{x}}(t) = \mathbf{A}\mathbf{x}(t) + \mathbf{B}\mathbf{f}_p(t), \quad (5.26)$$

$$\dot{\mathbf{d}}(t) = \mathbf{C}_y\mathbf{x}(t), \quad (5.27)$$

$$\dot{\hat{\mathbf{Q}}}_{sj}(t) = \mathbf{C}_{\hat{\mathbf{Q}}_j}\mathbf{x}(t). \quad (5.28)$$

Here, the state and the input matrices are given by the following expressions

$$\mathbf{A} = \begin{bmatrix} \mathbf{0} & \mathbf{I} & \mathbf{0} & \mathbf{0} \\ -\mathbf{M}_t^{-1}[\mathbf{K}_t + \boldsymbol{\Theta}_{pe}\mathbf{C}_{pe}^{-1}\boldsymbol{\Theta}_{pe}^T] & -\mathbf{M}_t^{-1}\mathbf{C}_p & -\mathbf{M}_t^{-1}\boldsymbol{\Theta}_{pe}\mathbf{C}_{pe}^{-1}\hat{\boldsymbol{\Psi}}_s & \mathbf{0} \\ \mathbf{0} & \mathbf{0} & \mathbf{0} & \mathbf{I} \\ -\hat{\boldsymbol{\Psi}}_s^T\mathbf{C}_{pe}^{-1}\boldsymbol{\Theta}_{pe}^T & \mathbf{0} & -[\hat{\boldsymbol{\Psi}}_s^T\mathbf{C}_{pe}^{-1}\hat{\boldsymbol{\Psi}}_s + \hat{\boldsymbol{\Omega}}_s] & -\hat{\boldsymbol{\Delta}}_s \end{bmatrix}, \quad (5.29)$$

$$\mathbf{x}(t) = [\mathbf{d}^T \quad \dot{\mathbf{d}}^T \quad \hat{\mathbf{Q}}_s^T \quad \dot{\hat{\mathbf{Q}}}_s^T]^T. \quad (5.30)$$

Also, the two output matrices are given by

$$\mathbf{C}_y = [\mathbf{0} \quad \mathbf{I} \quad \mathbf{0} \quad \mathbf{0}]^T, \quad (5.31)$$

$$\mathbf{C}_{\hat{\mathbf{Q}}_j} = [\mathbf{0} \quad \mathbf{0} \quad \mathbf{0} \quad \mathbf{I}_j]^T, \quad (5.32)$$

where, for example,  $\mathbf{I}_1$  is a diagonal matrix with the first  $N$  terms equal to 1 and the remaining terms equal to 0.

#### 5.3.4 Time averaged energy functions

As anticipated above, this study considers two energy functions: the total flexural kinetic energy of the smart plate and the electric power absorbed by the  $j$ -th shunt, which are given by the following expressions [17,91,92,95].

$$K(t) = \frac{1}{2} \int_{A_p} \rho_p h_p \dot{w}(x, y, t)^2 dA_p + \frac{1}{2} \sum_{j=1}^2 \int_{A_{pej}} \rho_{pe} h_{pe} \dot{w}(x, y, t)^2 dA_{pej}, \quad (5.33)$$

$$P_j(t) = v_{sj}(t)i_{sj}(t). \quad (5.34)$$

In Eq. (36),  $\rho_p, h_p$  and  $\rho_{pe}, h_{pe}$  represent the material density and thickness of the plate and piezoelectric patches respectively. Also,  $A_p, A_{pej}$  are the surface area of the plate and piezoelectric patches. Finally,  $\dot{w}(x, y, t)$  is the plate transverse velocity, whereas, in Eq. (37),  $v_{sj}$  and  $i_{sj}(t)$  are the voltage and current at the terminals of the  $j$ -th shunt. Considering the formulations presented in Refs. [92], the time averaged total flexural kinetic energy of the smart plate,  $\bar{K}$ , and the time averaged total power absorbed by the the  $j$ -th shunt,  $\bar{P}_j$ , can be expressed as follows:

$$\bar{K} = E[K(t)] = E \left[ \frac{1}{2} \dot{\mathbf{d}}^T \mathbf{M}_t \dot{\mathbf{d}} \right] = \frac{1}{2} \text{Tr} \left[ \mathbf{C}_{\dot{\mathbf{y}}}^T \mathbf{M}_t \mathbf{C}_{\dot{\mathbf{y}}} \mathbf{X} \right], \quad (5.35)$$

$$\bar{P}_j = E[P_j(t)] = E \left[ \dot{\mathbf{Q}}_{sj}^T \mathbf{L}_{sj}^{-1} \mathbf{R}_{sj} \dot{\mathbf{Q}}_{sj} \right] = \text{Tr} \left[ \mathbf{C}_{\dot{\mathbf{Q}}_j}^T \mathbf{L}_{sj}^{-1} \mathbf{R}_{sj} \mathbf{C}_{\dot{\mathbf{Q}}_j} \mathbf{X} \right], \quad (5.36)$$

where  $E[\ ]$  is the expectation operator and

$$\mathbf{L}_{sj} = \begin{bmatrix} L_{b1j} & & \\ & \ddots & \\ & & L_{bNj} \end{bmatrix}, \quad (5.37)$$

$$\mathbf{R}_{sj} = \begin{bmatrix} R_{s1j} & & \\ & \ddots & \\ & & R_{sNj} \end{bmatrix}, \quad (5.38)$$

are diagonal matrices with the inductance and resistance in the branches of the  $j$ -th shunt. Finally, the covariance matrix  $\mathbf{X}$  satisfies the Lyapunov equation [92,93]

$$\mathbf{A}\mathbf{X} + \mathbf{X}\mathbf{A}^H + \mathbf{B}\mathbf{F}\mathbf{B}^T = \mathbf{0}, \quad (5.39)$$

where  $\mathbf{F} = E[\mathbf{f}_p \mathbf{f}_p^T]$  is the covariance matrix of the rain on the roof excitation, which, in this study, is assumed as an identity matrix.

### 5.3.5 Power spectral density of the time average energy functions

The physics of the proposed tuning approach is studied with reference to the PSD of the plate total flexural kinetic energy and the PSD of the power absorbed by the  $j$ -th shunt, which, considering the formulations presented in Refs. [17,91,92], are given by the following expressions:

$$S_K(\omega) = \frac{1}{2} \int_{A_p} \rho_p h_p \mathcal{F}[\mathcal{R}_{\dot{w}\dot{w}}(\tau)] dA_p + \frac{1}{2} \sum_{j=1}^2 \int_{A_{pej}} \rho_{pe} h_{pe} \mathcal{F}[\mathcal{R}_{\dot{w}\dot{w}}(\tau)] dA_{pej}, \quad (5.40)$$

$$S_{p_j}(\omega) = Re \left\{ \mathcal{F} \left[ \mathcal{R}_{v_{sj}i_{sj}}(\tau) \right] \right\}. \quad (5.41)$$

Here,  $\mathcal{F}[\ ]$  and  $Re\{ \ }$  are respectively the Fourier Transform and real part operators. Also,  $\mathcal{R}_{\dot{w}\dot{w}}(\tau)$  is the autocorrelation function between plate velocities and  $\mathcal{R}_{v_{sj}i_{sj}}(\tau)$  is the cross-correlation function between the voltage and current at the terminals of the  $j$ -th shunt [92]. By using the mathematical procedure presented in Section 4.2.2. Eq. (5.40) can be expressed as

$$S_K(\omega) = \frac{1}{2} \text{Tr}[\mathbf{M}_t \mathbf{Y}(\omega) \mathbf{S}_{ff}(\omega) \mathbf{Y}^H(\omega)], \quad (5.42)$$

where,  $^H$  is the Hermitian transpose matrix operator,  $\text{Tr}[\ ]$  is a trace matrix operator,  $\mathbf{Y}$  is the global mobility matrix and  $\mathbf{S}_{ff}$  is a diagonal matrix with the PSD of the 16 uncorrelated white noise rain on the roof forces acting on the plate, which is therefore equal to a  $16 \times 16$  identity matrix.

By using the definition of Fourier Transform given in Ref. [86], Eq. (5.41) can be rewritten as

$$S_{p_j}(\omega) = Re \left\{ \lim_{T \rightarrow \infty} E \left[ \frac{1}{T} v_{sj}(\omega) i_{sj}^*(\omega) \right] \right\}, \quad (5.43)$$

where the superscript  $*$  indicates the complex conjugate and  $\dot{w}(x,y,\omega)$  is the complex amplitude of the plate time-harmonic transverse velocity whereas  $v_{sj}(\omega)$  and  $i_{sj}(\omega)$  are the complex amplitudes of the time-harmonic voltage and current at the terminals of the  $j$ -th shunt. Assuming time-harmonic functions, Eqs. (5.1) and (5.2) can be rewritten as follows:

$$[-\omega^2 \mathbf{M}_t + j\omega \mathbf{C}_p + \mathbf{K}_t] \mathbf{d}(\omega) + \mathbf{\Theta}_{pe} \mathbf{v}_s(\omega) = \mathbf{\Phi}_p \mathbf{f}_p(\omega), \quad (5.44)$$

$$-j\omega \mathbf{\Theta}_{pe}^T \mathbf{d}(\omega) + j\omega \mathbf{C}_{pe} \mathbf{v}_s(\omega) = \mathbf{i}_s(\omega). \quad (5.45)$$

Moreover, considering the notation shown in Figure 5.1, the voltages and currents at the terminals of the shunt can be linked via the following impedance expression:

$$\mathbf{v}_s(\omega) = -\mathbf{Z}_s \mathbf{i}_s(\omega). \quad (5.46)$$

In these three equations,  $(\omega)$ ,  $\mathbf{f}_p(\omega)$ ,  $\mathbf{v}_s(\omega)$ ,  $\mathbf{i}_s(\omega)$  are the vectors with the complex amplitudes of the time-harmonic plate modal displacements, plate excitation forces, shunts voltages and shunts currents. Also the diagonal matrix  $\mathbf{Z}_s$  contains the impedances of the multi-branches shunts. Eqs. (5.44), (5.45) and (5.46) can be combined to give:

$$\mathbf{d}(\omega) = \mathbf{Y}(\omega)\mathbf{f}_p(\omega), \quad (5.47)$$

$$\mathbf{i}_s(\omega) = \mathbf{H}(\omega)\mathbf{f}_p(\omega), \quad (5.48)$$

where:

$$\mathbf{Y}(\omega) = j\omega[-\omega^2\mathbf{M}_t + j\omega(\mathbf{C}_p + \boldsymbol{\Theta}_{pe}\mathbf{Z}_{spe}\boldsymbol{\Theta}_{pe}^T) + \mathbf{K}_t]^{-1}\boldsymbol{\Phi}_p, \quad (5.49)$$

$$\mathbf{Z}_{spe}(\omega) = [\mathbf{I} + j\omega\mathbf{Z}_s\mathbf{C}_{pe}]^{-1}\mathbf{Z}_s, \quad (5.50)$$

$$\mathbf{H}(\omega) = [\mathbf{I} + j\omega\mathbf{Z}_s\mathbf{C}_{pe}]^{-1}\boldsymbol{\Theta}_{pe}^T\mathbf{Y}(\omega). \quad (5.51)$$

At this point, recalling the modal summation  $w(x, y, \omega) = \boldsymbol{\Phi}(x, y)\mathbf{d}(\omega)$  and using Eqs. (5.44), (5.45), (5.46) the expression is derived for the PSD of the power absorbed by the  $j$ -th shunt [92]:

$$\begin{aligned} S_{P_j}(\omega) &= Re \left\{ \lim_{T \rightarrow \infty} E \left[ \frac{1}{T} v_{sj}(\omega) i_{sj}(\omega) \right] \right\} = \\ &= -Re \left\{ \lim_{T \rightarrow \infty} E \left[ \frac{1}{T} \mathbf{i}_s^H(\omega) \mathbf{Z}_{sj}^H(\omega) \mathbf{i}_s(\omega) \right] \right\} = \\ &= -Re \left\{ \lim_{T \rightarrow \infty} E \left[ \frac{1}{T} \mathbf{f}_p(\omega)^H \mathbf{H}^H(\omega) \mathbf{Z}_{sj}^H(\omega) \mathbf{H}(\omega) \mathbf{f}_p(\omega) \right] \right\}, \end{aligned} \quad (5.52)$$

where  $^H$  is the Hermitian transpose matrix operator and  $\mathbf{Z}_{sj}(\omega)$  contains the impedances of the  $N$  branches relative to the  $j$ -th shunt only. These two equations can be further simplified using the trace matrix operator  $\text{Tr}[\ ]$ , which is invariant under cyclic product operations, such that Eq. (5.52) can be rewritten as

$$S_{P_j}(\omega) = -\text{Tr} \left[ Re \left\{ \mathbf{Z}_{sj}^H(\omega) \right\} \mathbf{H}(\omega) \mathbf{S}_{ff}(\omega) \mathbf{H}^H(\omega) \right], \quad (5.53)$$

where

$$\mathbf{S}_{ff}(\omega) = \lim_{T \rightarrow \infty} E \left[ \frac{1}{T} \mathbf{f}_p(\omega)^H \mathbf{f}_p(\omega) \right] \quad (5.54)$$

is a diagonal matrix with the PSD of the 16 uncorrelated white noise rain on the roof forces and assumed equal to a  $16 \times 16$  identity matrix.

#### 5.4 TUNING OF MULTI-RESONANT SHUNTS

This section describes the proposed novel algorithm to locally tune the RL components in the RLC branches of multi-resonant shunts. Before entering into the details of the algorithm, the physical effects produced by the RLC branches in the shunts are first examined. For the sake of clarity, the effects produced by a single classical RL branch and a single RLC branch connected to a piezoelectric path are first analysed in Section 5.4.1. Then, the incremental effects of multi-resonant RLC branches connected to two piezoelectric patches are discussed in Section 5.4.2. Finally, the proposed algorithm for the on-line tuning of the RL components in multiple RLC branches of multi-resonant shunts is presented and discussed in Section 5.4.3.

##### 5.4.1 Effects produced by RL and RLC single branches

To start with, this section assumes the piezoelectric patch  $N.1$  is connected to a classical RL shunt whereas the second patch is left in open circuit. Figure 5.2 shows (a) the time averaged total flexural kinetic energy of the plate,  $\bar{K}$ , and (b) the time averaged total power absorbed by the first shunt,  $\bar{P}_1$ , when the shunt inductance is varied in the range  $L_{s11} = 2 - 300H$  and the shunt resistance is varying in the range  $R_{s11} = 0.1 - 2k\Omega$ . As highlighted in the bottom axis of the two surface graphs, the combined effect of the varied shunt inductance ( $L_{s11} = 2 - 300H$ ) and fixed piezoelectric patch capacitance ( $C_{pe1} = 2.113 \times 10^{-7}F$ ) produces a tuning resonance frequency of the shunt comprised between 20 and 250Hz. The left hand side plots (a) show that, when the shunt resistance is set to low values, the time averaged total flexural kinetic energy of the plate is characterised by a sequence of troughs aligned in parallel direction to the inductance axis and centred at four resonance frequencies of the smart plate structure, that is at  $f_{r1} = 44Hz$ ,  $f_{r2} = 92Hz$ ,  $f_{r3} = 135Hz$ ,  $f_{r4} = 190Hz$ , that coincide with the resonance frequencies of the low order flexural natural modes of the smart plate, i.e.  $f_{s1} = f_{r1}$ ,  $f_{s2} = f_{r2}$ , etc. and the shunt resistance is suitably tuned. The companion right hand side plots (b) show symmetrical graphs, which in this case are characterised by a sequence of crests aligned in parallel direction to the inductance axis and centred at the first four resonance frequencies of the smart plate structure. An accurate analysis and comparison of plots (b) with the equivalent plots (a) shows that the maxima of the power crests occurs for the same

shunt inductance and resistance as those for the minima of the kinetic energy troughs. This indicates that, when the shunt is optimally tuned to minimise the response of a resonant flexural mode of the smart plate, the power absorbed by the shunt is actually maximised. This is quite an important observation since it suggests that the RL components of the shunt can be locally tuned to minimise the response of a flexural resonant mode of the smart plate simply by maximising the total power absorbed by the shunt band-filtered in correspondence to the resonance frequency of the targeted flexural mode of the smart plate.

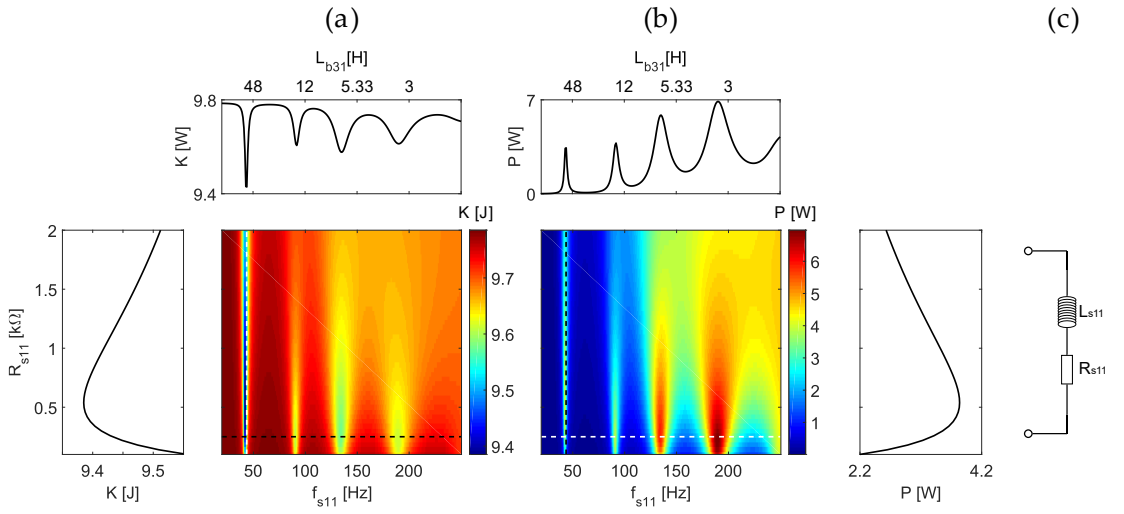


Figure 5.2 Time averaged total flexural kinetic energy of the smart plate structure (a) and time averaged electrical power absorbed (b) by the RL shunt circuit connected to the piezoelectric patch  $N.1$  (c).

The effects produced by a band pass filtered classical RL shunt are therefore now considered. As anticipated in Section 1.2.1 of Chapter 1, the band filtering effect is generated by adding in series to the classical  $R_{s11}, L_{s11}$  shunt components two additional  $L_{f11}, C_{f11}$  filtering components that create the current-flowing effect, which narrows the band of the current signal passed to the  $R_{s11}, L_{s11}$  elements at a centre frequency given by  $\omega_{f1} = \frac{1}{\sqrt{L_{f11}C_{f11}}}$ . The series of plots in Figure 5.3 show (a) the time averaged total flexural kinetic energy of the smart plate  $\bar{K}$  and (b) the time averaged total power absorbed by the first shunt  $\bar{P}_1$ , with reference to the combined shunt and current flow inductances  $L_{b11} = L_{s11} + L_{f11}$  and with reference to the shunt resistance  $R_{s1}$  when the current flow capacitance is set to three values: first row,  $C_{f11} = 10C_{pe1}$ ,

second row  $C_{f11} = C_{pe1}$ , third row  $C_{f11} = 0.1C_{pe1}$ . Assuming the inductance of the shunt  $L_{s11}$  and the inductance of the current-flowing filter  $L_{f11}$  are set such that both the shunt and the filter are tuned to the same target frequency, such that  $\omega_{s1} = \omega_{f1} = \omega_{b1}$ , according to

$$L_{bij} = L_{fij} + L_{sij} = \frac{1}{\omega_{ri}^2 C_{fij}} + \frac{1}{\omega_{ri}^2 C_{pej}} = \frac{C_{fij} + C_{pej}}{\omega_{ri}^2 C_{fij} C_{pej}}. \quad (5.55)$$

The combined effect of piezoelectric patch capacitance  $C_{pe1}$  with the shunt  $R_{s11}, L_{s11}$  and current-flowing  $L_{f1}, C_{f1}$  elements connected in series produces a sharp resonance effect at frequency:

$$\omega_{b1} = \sqrt{\frac{C_{pe1} + C_{f11}}{L_{b11} C_{pe1}}}. \quad (5.56)$$

The sequence plots in Figure 5.3 show that, as the combined inductance effect  $L_{b11} = L_{s11} + L_{f11}$  is varied between given ranges such that the resonance frequency of the shunt is swept between 20 and 250Hz, the kinetic energy troughs and the electrical power crests that occur in correspondence of four resonance frequencies of the smart plate become progressively sharper as the value of the capacitance  $C_{f11}$  is reduced with respect to the capacitance of the piezoelectric patch  $C_{pe1}$ . Therefore, to have a sharp filtering effect, the capacitance in the shunt branch should be fixed to a value comparatively smaller than the capacitance of the piezoelectric patch, although this may then require rather large shunt inductances to produce the filtering and shunt effects. The forthcoming simulation results were derived assuming the capacitances in the shunt branches are equal to  $C_{fij} = 0.2C_{pe1}$ .

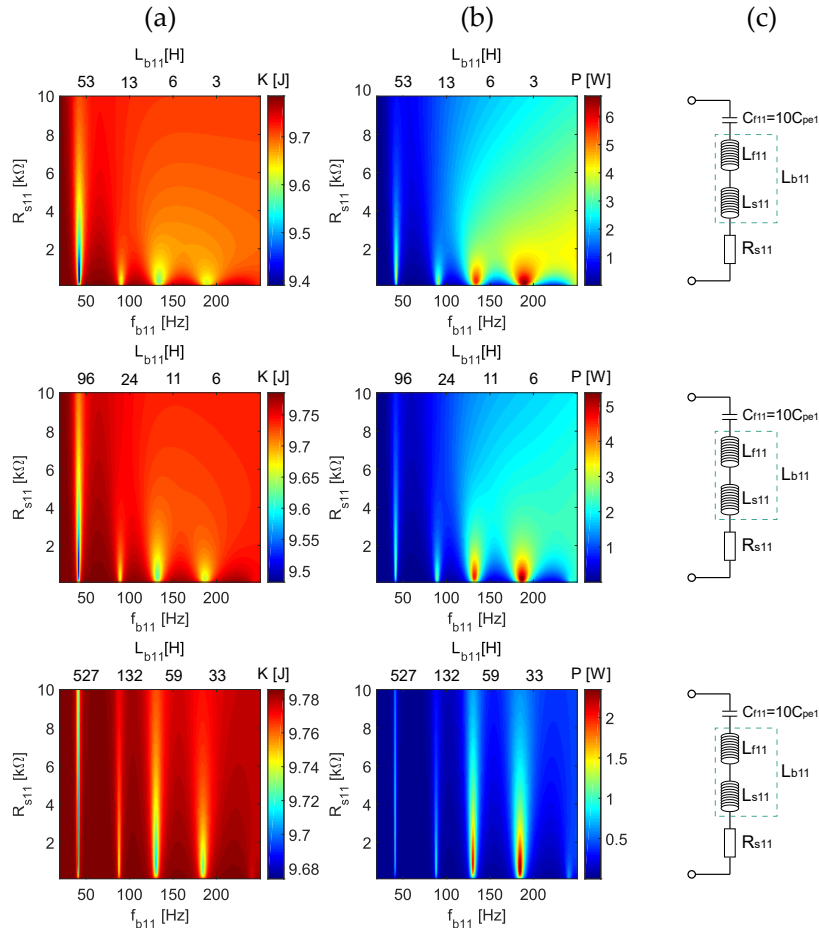


Figure 5.3 Time averaged total flexural kinetic energy of the smart plate structure (a) and time averaged electrical power absorbed (b) by the RLC shunt circuits connected to the piezoelectric patch  $N.1$  (c) having  $C_{f11} = 10C_{pe1}$  (first row),  $C_{f11} = C_{pe1}$  (second row),  $C_{f11} = 0.1C_{pe1}$  (third row).

It is important to highlight that, as the capacitance in the shunt is lowered, the aggregate inductance  $L_{b11} = L_{s11} + L_{f11}$  necessary to obtain the band pass filtering effect and the shunt resonant effect becomes increasingly larger and reaches values that would require a rather bulky inductor element. This is a critical practical problem, which, however, could be overcome by synthesising the shunt inductance electronically with an active circuit involving operational amplifiers [96]. In this case, a negative capacitance could also be synthesised in the active circuit to lower the capacitive effect of the piezoelectric patch and thus increase the vibration energy absorption from the target flexural mode so that its flexural response is significantly reduced [17,24-42]. This study is focussed on the tuning of single and multi-branch shunts, therefore, to keep the formulation and discussion simple, classical shunts

composed of passive electrical elements will be considered, which do not produce the negative capacitance necessary to magnify the vibration control effect of the target resonant modes of the hosting structure. Thus, it is important to anticipate that the vibration reductions predicted in the following part of the chapter could be significantly increased in practice with multi-resonant shunts formed by active circuits that synthesise negative capacitors, large inductors and, indeed, also the tuning algorithm proposed in this study.

#### 5.4.2 Incremental effect produced by multiple RLC branches

The vibration control effects produced by multi-resonant RLC branches connected to the two piezoelectric patches are now investigated. To start with, the piezoelectric patch  $N.1$  is connected to a shunt with 1, 2, 3, 4 RLC branches whereas the piezoelectric patch  $N.2$  is left open circuit. The simulation results for the incremental effects produced by the four branches are summarised in Figure 5.4, which is organised in four rows, each with three plots that show (a) the smart plate time averaged flexural kinetic energy, (b) the shunt time-averaged absorbed electric power and (c) the PSD of the plate flexural kinetic energy (solid blue line – no shunt; dashed red line – with shunt) and electric power absorbed by the shunt (dotted black line) when the piezoelectric patch  $N.1$  is connected to shunts with respectively 1, 2, 3, 4 RLC branches (d). Let's consider first the case where the piezoelectric patch is connected to the first RLC branch. In this case plots (a) and (b) replicate those already discussed above in Section 5.4.1. The two graphs are characterised respectively by a sequence of troughs and crests that occur for values of the shunt inductance  $L_{b11}$  such that the branch resonates in correspondence of four resonances of the low order flexural modes of the smart plate. As observed above, the RL values for the minima of the four troughs correspond to the RL values for the maxima of the four crests. Hence, if, for example, the inductance  $L_{b11}$  and resistance  $R_{s11}$  components of this first branch are fixed to the optimal values that would maximise the absorbed electric power in correspondence to the fourth crest and thus would minimise the flexural response in correspondence of the fourth trough, i.e.  $L_{b11} = L_{opt1}$  and  $R_{s11} = R_{opt1}$ , as shown by the solid blue and dashed red lines in plot (c), the PSD of the flexural kinetic energy would be effectively minimised in correspondence of the fifth resonance frequency of the smart plate whereas the PSD of the absorbed electric power (dotted black line) would be characterised by a dominant peak at the fifth resonance frequency of the smart plate.

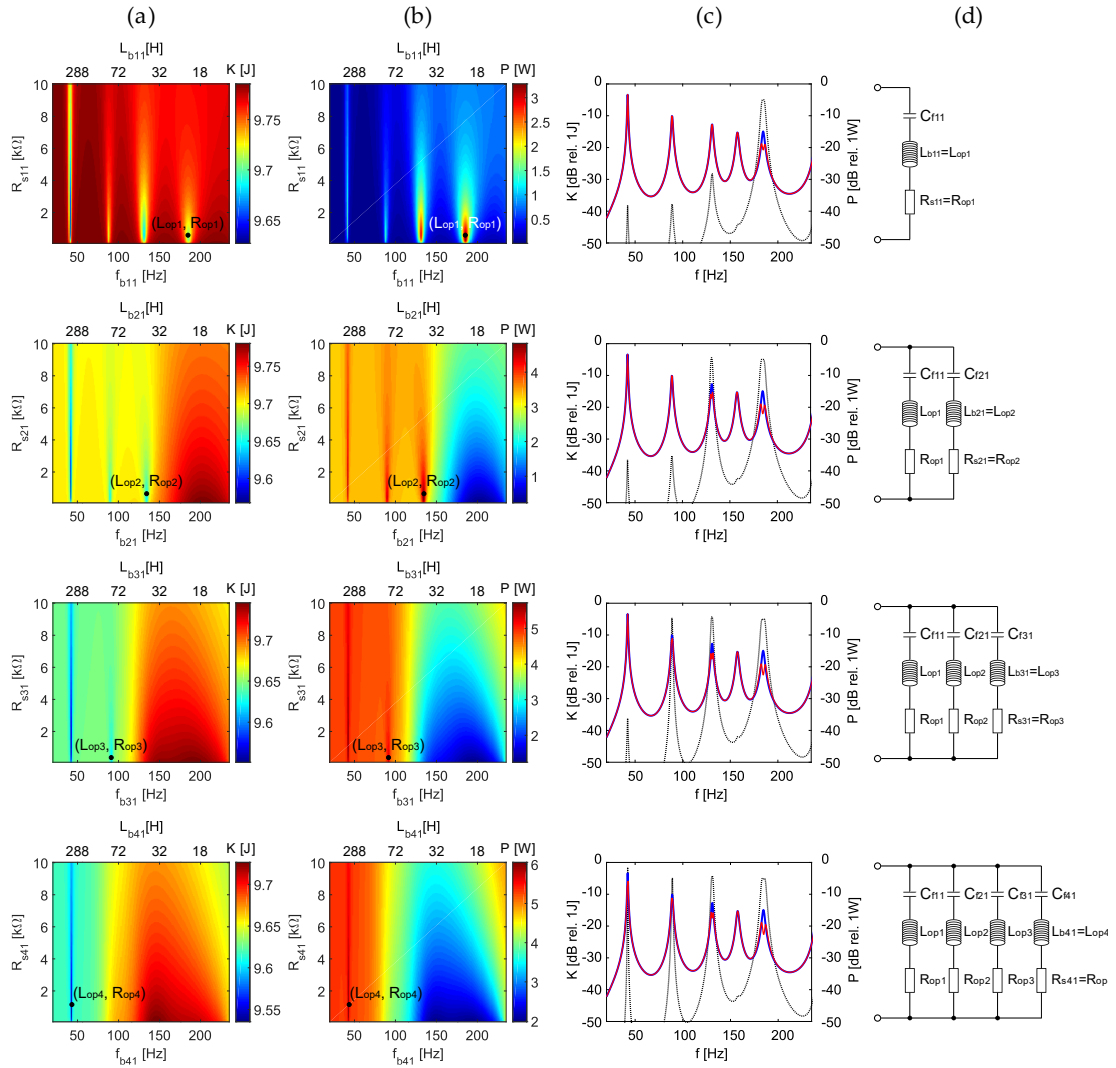


Figure 5.4 (a) Time averaged total flexural kinetic energy of the smart plate structure, (b) time averaged electrical power absorbed and (c) PSD of the plate flexural kinetic energy (solid blue line no shunt; dashed red line with shunt) and electric power absorbed by the shunt (dotted black line) by the RLC multi-resonant shunt circuits connected to the piezoelectric patch  $N.1$  (d) while the piezoelectric patch  $N.2$  is in open circuit.

Plots (a) and (b) are characterised respectively by four troughs and four crests whereas plot (c) is characterised by five resonance peaks. Indeed, plots (a), (b) are missing respectively a trough and a crest in correspondence to the fourth resonance frequency of the smart plate. This is due to the fact that the piezoelectric patch  $N.1$  is positioned in the vicinity of a nodal line of the fourth flexural mode of the smart plate

so that the patch is weakly coupled with this mode. As a result, the shunt cannot extract vibration energy and thus minimise the flexural response of this resonant mode. If now a second RLC branch is added to the shunt, plots (a) and (b) in the second row of Figure 5.4 show only three troughs and three crests that occur for values of the shunt inductance  $L_{b21}$  such that the branch resonates in correspondence of the first three resonances of the smart plate. There is no a fourth trough and a fourth crest since the first branch in the shunt is already optimally tuned to maximise the vibration energy absorption, and thus minimise the flexural vibration energy, due to the fifth resonant mode of the smart plate. If now the inductance  $L_{b21}$  and resistance  $R_{s21}$  components of this second branch are fixed to the optimal values that would maximise the absorbed electric power and minimise the flexural response in correspondence of the third crest and trough respectively, i.e.  $L_{b21} = L_{opt2}$  and  $R_{s21} = R_{opt2}$ , as shown by the solid blue and dashed red lines in plot (c), the PSD of the flexural kinetic energy would be effectively minimised in correspondence of the third and fifth resonance frequencies of the smart plate whereas the PSD of the absorbed electric power (dotted black line) would be characterised by two dominant peaks at these two resonance frequencies. A third branch can now be added to the shunt, such that plots (a) and (b) in the third row of Figure 5.4 show only two troughs and two crests. The inductance  $L_{b31}$  and resistance  $R_{s31}$  components of this third branch can thus be fixed to maximise the absorbed electric power and minimise the flexural response in correspondence to the second crest and second trough respectively, i.e.  $L_{b31} = L_{opt3}$  and  $R_{s31} = R_{opt3}$ . In this case, plot (c) shows that the PSD of the flexural kinetic energy (solid blue line and dashed red line) is brought down in correspondence of the second, third and fifth resonance frequencies of the smart plate whereas the PSD of the absorbed electric power (dotted black line) is characterised by three peaks at these resonance frequencies. inductance  $L_{b41}$  and resistance  $R_{s41}$  can be fixed to maximise the absorbed electric power and minimise the flexural response of this crest and trough respectively, i.e.  $L_{b41} = L_{opt4}$  and  $R_{s41} = R_{opt4}$ , such that, as shown in plot (c), the PSD of the flexural kinetic energy (blue solid line and red dashed line) is brought down in correspondence of the first, second, third and fifth resonance frequencies of the smart plate whereas the PSD of the absorbed electric power (dotted black line) is characterised by four peaks at the first, second, third and fifth resonance frequencies of the smart plate.

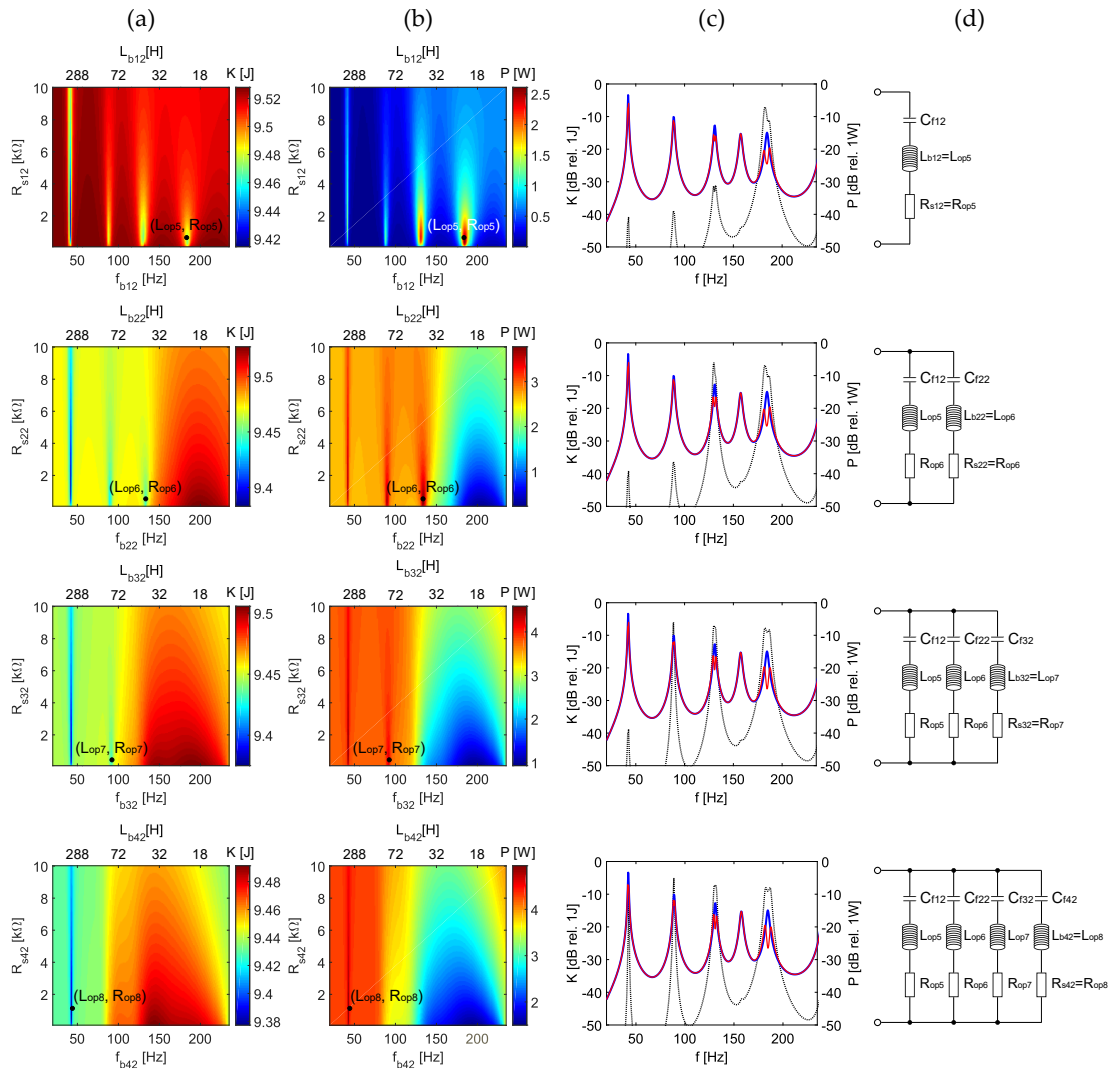


Figure 5.5 (a) Time averaged total flexural kinetic energy of the smart plate structure, (b) time averaged electrical power absorbed and (c) PSD of the plate flexural kinetic energy (solid blue line no shunt; dashed red line with shunt) and electric power absorbed by the shunt (dotted black line) by the RLC multi-resonant shunt circuits connected to the piezoelectric patch  $N.2$  (d) while the piezoelectric patch  $N.1$  implements a four branches multi-resonant shunt.

The same analysis can now be repeated for the piezoelectric patch  $N.2$  assuming the piezoelectric patch  $N.1$  is connected to the four branches multi-resonant shunt set to control the flexural response of the first, second, third and fifth resonances of the smart plate as described just above. Figure 5.5 shows the same sequence of plots than Figure 5.4, which are once more organised in four rows, each with three plots that show (a) the plate time averaged flexural kinetic energy, (b) the shunt time-averaged absorbed electric power and (c) the PSD of the plate flexural kinetic energy (solid blue

line – no shunt; dashed red line – with shunt) and electric power absorbed by the shunt (dotted black line) when the piezoelectric patch  $N.2$  is connected to shunts with respectively 1, 2, 3, 4 RLC branches (d). The four rows of plots present a very similar story to that depicted in Figure 5.4 for the piezoelectric patch  $N.1$  connected to a four multi-resonant branches shunt. Therefore, the four RLC branches can be iteratively tuned to maximise the electric power absorption by the shunt filtered in correspondence to the fifth, third, second and first resonance frequency of the smart plate such that, the flexural response of the smart plate is then minimised at these resonance frequencies. The same procedure proposed above can thus be implemented to find the optimal values of the inductance and resistance elements in the four branches such that: first,  $L_{b12} = L_{opt5}$  and  $R_{s12} = R_{opt5}$ ; second,  $L_{b22} = L_{opt6}$  and  $R_{s22} = R_{opt6}$ ; third,  $L_{b32} = L_{opt7}$  and  $R_{s32} = R_{opt7}$ ; fourth  $L_{b42} = L_{opt8}$  and  $R_{s42} = R_{opt8}$ .

The results presented in this section naturally lead to the conception of a practical approach for the tuning of the RL components in the branches of multi-resonant shunts connected to piezoelectric patches that are bonded on thin structures to control the flexural response due to resonance effects of low order flexural modes. Indeed an algorithm can be devised, which iteratively search for the maximum power absorption in the vicinity of a resonance frequency of the smart plate to set the optimal values of the inductance and resistance elements in a first branch of a shunt and then move forward to search for the maximum power absorption in the vicinity of a neighbour resonance frequency of the smart plate to set the optimal values of the inductance and resistance elements in a second branch of a shunt and so on. This process can be repeated sequentially in the shunts of all piezoelectric patches bonded on the hosting structure. In principle, every time a branch is added to each shunt the existing branches could become mistuned and thus the tuning sequence described above should be repeated indefinitely. For instance, for the system at hand, after the branches in the shunts  $N.1$  and  $N.2$  have been tuned, the algorithm should restart from the shunt  $N.1$  and then move again to the shunt  $N.2$  and so on to upgrade the optimal values of the RL components in the four branches of the two shunts. However, further simulations have shown that a second iteration would slightly modify the optimal values of the RL components in the branches of the shunts  $N.1$  and  $N.2$  and, thus, marginally modify the electric power absorbed by the multi-resonant shunts as well as the flexural response of the smart plate. Nevertheless, in many practical applications it may be essential to run the tuning sequence

continuously to track changes in the dynamic response of the hosting structure due for example to temperature changes or tensioning effects generated by operation conditions.

#### 5.4.3 *Tuning algorithm based on the maximisation of electric power absorbed by a multi resonant shunt*

The previous section has shown that the time-averaged electric power absorbed by a shunt varies with respect to the inductance and resistance components in a branch of the shunt so as to form a surface characterised by a series of crests. For instance, if a single RLC branch is connected to the piezoelectric patch  $N.1$ , as shown in Figure 5.6, the electric power absorbed by the shunt is characterised by a surface with four crests. The crests have stretched bell shapes with principal axes parallel to the inductance, which is the stretching direction, and resistance axes. Therefore, the inductance and resistance values of the crests maxima can be found independently with a two stages search: the first stage finds the optimal inductance by setting a fixed tentative value of the shunt resistance (normally a low value) whereas the second stage finds the optimal resistance with reference to the optimal inductance identified in the first stage. These searches are therefore carried out on slices of the absorbed electric power surface that resemble the curves in the top and left-hand side plots of Figure 5.6. The RL components in the branches of the multi-resonant shunts considered in this study can therefore be found with an iterative procedure, which, as proposed in Section 5.4.2, scrolls the RL components of the first branch until the optimal values that maximise the absorbed electric power filtered in correspondence of the fourth crest are found, then scrolls the RL components of the second branch until the optimal values that maximise the absorbed electric power filtered in correspondence of the third crest are found, and so on. As discussed in Section 5.4.2 and depicted in the second column of the plots presented in Figure 5.4 and Figure 5.5 for the shunts  $N.1$  and  $N.2$  respectively, this scrolling procedure will work on absorbed power surfaces that change every time a new branch is added to the shunt. For the first branch the search starts by setting the resistance to a relatively low value and the inductance to a value such that the branch resonates at a given upper frequency that defines the operation band of the multi-resonant shunt. For instance, for the model problem considered in this study, the initial resistance and inductance of the first branch were chosen equal to  $R_{s11} = 200 \Omega$   $L_{b11} = 12.5$  H. The searches for the successive branches then start by setting the branch resistance to a relatively low value and the branch

inductance to a value equal to the optimal inductance found in the previous search. In other words, the searching algorithm restart for each branch from the resonance frequency of the previous branch.

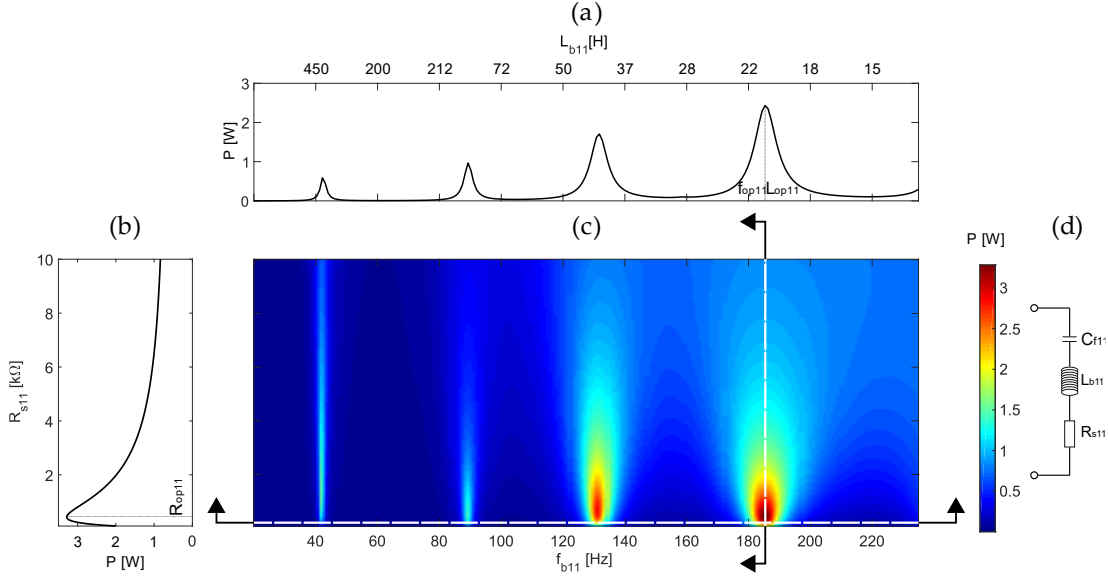


Figure 5.6 (c) Time averaged electrical power absorbed by the shunt circuit shown in (d). Plots (a) and (b) present slices of the surface plot (c) cut along a constant resistance  $R_{s11} = 200 \Omega$  (a) and constant inductance  $L_{b11} = 21.1$  H (b), that is a plate and shunt resonance frequency  $f_{b11} = 184.5$ Hz.

Several algorithms can be employed for the two stages search of the optimal inductance and resistance components that maximise the electric power absorbed by a branch of the shunt. For instance, in this study, a coarse and fast initial search was implemented with a simple algorithm based on the following finite difference expressions of the first and second derivatives of the electric power absorbed by the shunt with reference to either fixed steps increments of the inductance, Eqs. (5.57-5.58), or fixed steps increments of the resistance, Eqs. (5.59-5.60), in the branch of the shunt:

$$\left. \frac{\partial \bar{P}}{\partial L_b} \right|_m \cong \frac{\bar{P}_{m+1} - \bar{P}_{m-1}}{2\Delta L_b}, \quad \left. \frac{\partial^2 \bar{P}}{\partial L_b^2} \right|_m \cong \frac{\bar{P}_{m+1} - 2\bar{P}_m + \bar{P}_{m-1}}{\Delta L_b^2}, \quad (5.57-5.58)$$

$$\left. \frac{\partial \bar{P}}{\partial R_s} \right|_n \cong \frac{\bar{P}_{n+1} - \bar{P}_{n-1}}{2\Delta R_s}, \quad \left. \frac{\partial^2 \bar{P}}{\partial R_s^2} \right|_n \cong \frac{\bar{P}_{n+1} - 2\bar{P}_n + \bar{P}_{n-1}}{\Delta R_s^2}. \quad (5.59-5.60)$$

Here the indices  $m, n$  identify the  $m$ -th iteration for the optimal inductance search and the  $n$ -th iteration for the optimal resistance search, which are implemented considering fixed steps of the inductance and resistance equal to  $\Delta L_b$  and  $\Delta R_s$  respectively. Thus, at each iteration the optimal values of the branch inductance and resistance are updated by simply summing the fixed step intervals, that is:  $L_{b_{m+1}} = L_{b_m} + \Delta L_b$  and  $R_{s_{n+1}} = R_{s_n} + \Delta R_s$ . The maxima of the two stages search occur when the first derivative changes sign from negative to positive and the second derivative is negative.

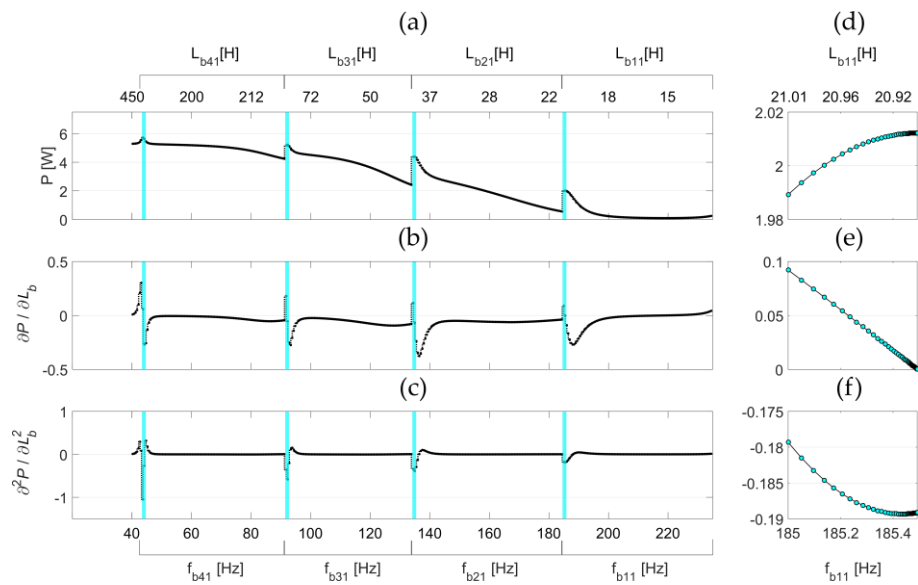


Figure 5.7 First stage coarse (a, b, c) and fine (d, e, f) inductance (frequency) tuning based on the maximisation of the electrical power absorbed by the shunt branches. (a, d) Amplitude, (b, e) first derivative, (c, f) second derivatives of the absorbed power with respect to the inductances implemented in the four branches. Thick vertical bands indicate the inductances (frequencies) where the fine frequency tuning is performed as shown in plots (d, e, f).

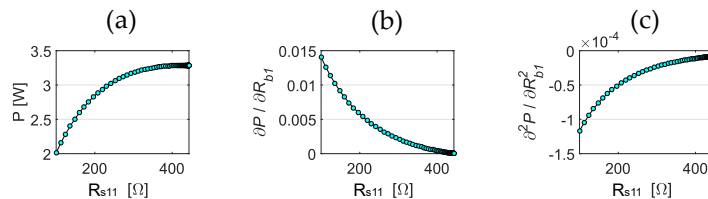


Figure 5.8 Second stage fine (a, b, c) resistance tuning based on the maximisation of the electrical power absorbed by the shunt branches. (a) Amplitude, (b) first derivative, (c) second derivative of the absorbed electric power with respect to the resistances implemented in the four branches.

Plots (a), (b), (c) in Figure 5.7 show the details of the first stage search for the inductances in the four branches of the multi-resonant shunt connected to the piezoelectric patch  $N.1$ . In this case, the search is carried out assuming the branches implement small resistances equal to  $100 \Omega$ . Plots (a), (b), (c) respectively show the amplitude, the first derivative and the second derivative of the electric power absorbed by the shunt with reference to constant increments of the inductances implemented sequentially in the four branches of the multi-resonant shunt connected to the piezoelectric patch  $N.1$ . It is interesting to note how, once the optimal inductance in a given branch is identified and then the search for the optimal inductance in the following branch starts the amplitude, first derivative and second derivative plots of the electric power function undergo an abrupt change, which, as discussed in Section 5.4.2 is due in fact to the action of the new branch assuming the initial value of its inductance element is equal to the optimal inductance found for the previous branch. Therefore, there is now a new branch absorbing power even though it doesn't yet implement the optimal inductance necessary to maximise the power absorption from the neighbour resonant flexural mode of the smart plate. Unless very small steps are implemented, though at the expenses of convergence speed, this simple search procedure is not sufficiently accurate, particularly for the search of the optimal inductance which, as can be deduced from the top plot in Figure 5.6, is carried out along sharp bell-shaped curves. Thus, the two stages search was refined by implementing either Eqs. (5.57-5.58) or Eqs. (5.59-5.60) with variable step iterations, where the amplitudes of the inductance and resistance steps is given by Newton's algorithm [97], so that at each iteration

$$\Delta L_{b_{m+1}} = -\left. \frac{\partial \bar{P}}{\partial L_b} \right|_m / \left. \frac{\partial^2 \bar{P}}{\partial L_b^2} \right|_m, \quad \Delta R_{s_{n+1}} = -\left. \frac{\partial \bar{P}}{\partial R_s} \right|_n / \left. \frac{\partial^2 \bar{P}}{\partial R_s^2} \right|_n \quad (5.61-5.62)$$

and thus at each iteration the optimal values of the branch inductance and resistance are updated with the following formulae:  $L_{b_{m+1}} = L_{b_m} - \left. \frac{\partial \bar{P}}{\partial L_b} \right|_m / \left. \frac{\partial^2 \bar{P}}{\partial L_b^2} \right|_m$  and  $R_{s_{n+1}} = R_{s_n} - \left. \frac{\partial \bar{P}}{\partial R_s} \right|_n / \left. \frac{\partial^2 \bar{P}}{\partial R_s^2} \right|_n$ . In this case, as can be noticed in plots d, e, f of Figure 5.7 this refined iterative procedure is characterised by increasingly smaller steps as the inductance and resistance values progressively converge toward the optimal values. Plots (a), (b), (c) in Figure 5.8 show respectively the amplitude, first derivative and second derivative of the electric power absorbed by the shunt with reference to increasingly smaller increments of the resistance implemented sequentially in the first

branch of the multi-resonant shunt connected to the piezoelectric patch  $N.1$  after the optimal inductance crest has been found in the first stage search.

#### 5.5 SMART PLATE EQUIPPED WITH INCREASINGLY DENSER ARRAYS OF PIEZOELECTRIC PATCHES CONNECTED TO MULTI-RESONANT SHUNTS TUNED TO MAXIMISE POWER ABSORPTION

To conclude this study, Figure 5.9 shows the effects produced by 1, 6, 12, 20, 35, 48 piezoelectric patches connected respectively to 4, 7, 8, 8, 8, 8 branches multi-resonant RLC shunts whose optimal RL components are derived with the two-stage search tuning sequence proposed in this chapter. The overall surface of the piezoelectric patches is kept constant and equal to 30% of that of the plate. The plots show that the PSD of the smart plate total flexural kinetic energy between 20 and 500 Hz (solid blue lines) is progressively reduced in correspondence of 8 resonance frequencies (dashed red lines) thanks to the shunted piezoelectric patches that effectively absorb vibration energy at these frequencies as can be seen from the dashed black lines, which show the total electric power absorbed by the shunts. Reductions up to 10 dB are obtained for most resonance peaks, although, as highlighted above, the results shown here consider classical shunts. Thus, it is expected that the reductions shown in this chapter can be significantly increased by implementing a negative capacitance in the shunts that reduces the capacitive effect of the piezoelectric patches. Nevertheless, as shown in Figure 5.10, when for example the setup with 48 piezoelectric patches is connected to 12 branches resonant shunts, rather large reductions of the plate flexural kinetic energy PSD comprised between 5 and 10 dB are produced up to 1300 Hz.

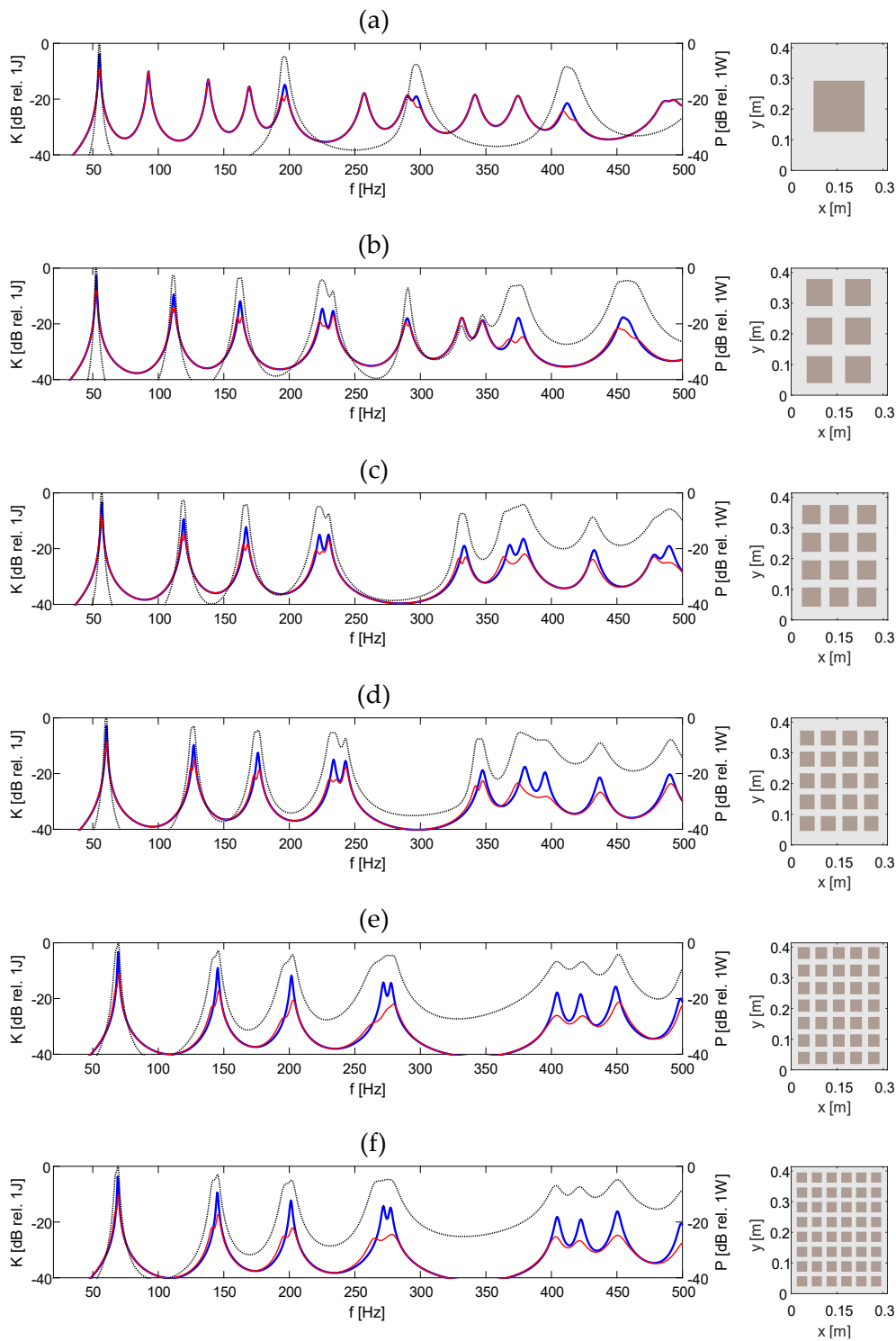


Figure 5.9 Power spectral densities of the total flexural kinetic energy of the plate equipped with 1, 6, 12, 20, 35, 48 piezoelectric patches in open loop (solid blue lines) and connected to shunts with respectively 4, 7, 8, 8, 8, 8 branches (dashed red lines) whose RL elements are set in such a way as to maximize the electric power absorbed by the shunts (dotted black lines).

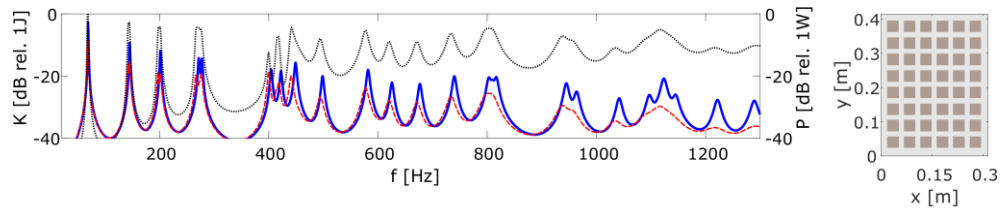


Figure 5.10 Power spectral densities of the total flexural kinetic energy of the plate equipped with 48 piezoelectric patches in open loop (solid blue lines) and connected to shunts with 12 branches (dashed red lines) whose RL elements are set in such a way as to maximize the electric power absorbed by the shunts (dotted black lines).

## 5.6 EXPERIMENTAL VALIDATION OF THE PROPOSED TUNING METHOD OF MULTI RESONANT SHUNTS

This section presents experimental validation tests on the feasibility of the tuning approach proposed in the previous sections for multi-resonant RLC shunts connected to piezoelectric patches to form electromechanical vibration absorbers, that can be used to control the flexural vibrations of thin structures. A test rig is used, which is composed of a clamped aluminium plate equipped with five piezoelectric hexagonal patches connected to identical shunts, synthesised digitally in a multi-channel dSPACE platform. The tuning approach presented in the previous section has been applied to find optimal RL branch parameters such that the shunted piezoelectric patches form multi-resonant vibration absorbers that control three flexural modes of the plate in the low frequency regime 40-150Hz. Two set of measurements were carried out in order to evaluate the proposed method. In the first, the total kinetic energy of the vibrating plate was estimated with reference to the inductance and resistance values of the branches of the shunts. In the second, voltage drops across the piezoelectric patches and current flows through the shunt circuits were measured with respect to the inductance and the resistance values of the branches. With the help of these measurements, the evolution of both total flexural kinetic energy and absorbed electrical power with respect to the inductance and resistance implemented in the branches of the shunts was visualized on surface plots as in the previous section. In this way the flexural kinetic energy minimisation and shunt electric power maximisation was demonstrated experimentally. The optimal RLC parameters for the

branches of the shunts were then derived using the algorithm proposed in the previous section.

### 5.7 EXPERIMENTAL SETUP

Figure 5.11 (a) shows the experimental setup used in this study, which is composed of a thin rectangular panel clamped on Perspex box. The panel is made of aluminium and has thickness of 1 mm and dimensions of 414 × 314 mm. Five hexagonal piezoelectric patches are bonded on the bottom side of the panel as depicted in Figure 5.11 (b). The dimensions, positions and physical properties of the panel and piezoelectric patches are summarised in Table 5.2 panel is excited at position  $x_p = 85 \text{ mm}$ ,  $y_p = 110 \text{ mm}$  by a point random disturbance generated by the shaker located in the Perspex box. The flexural response of the panel was measured with a scanning laser vibrometer, while the electrical response of the shunt circuits was acquired with the ABACUS Data Physics acquisition system.

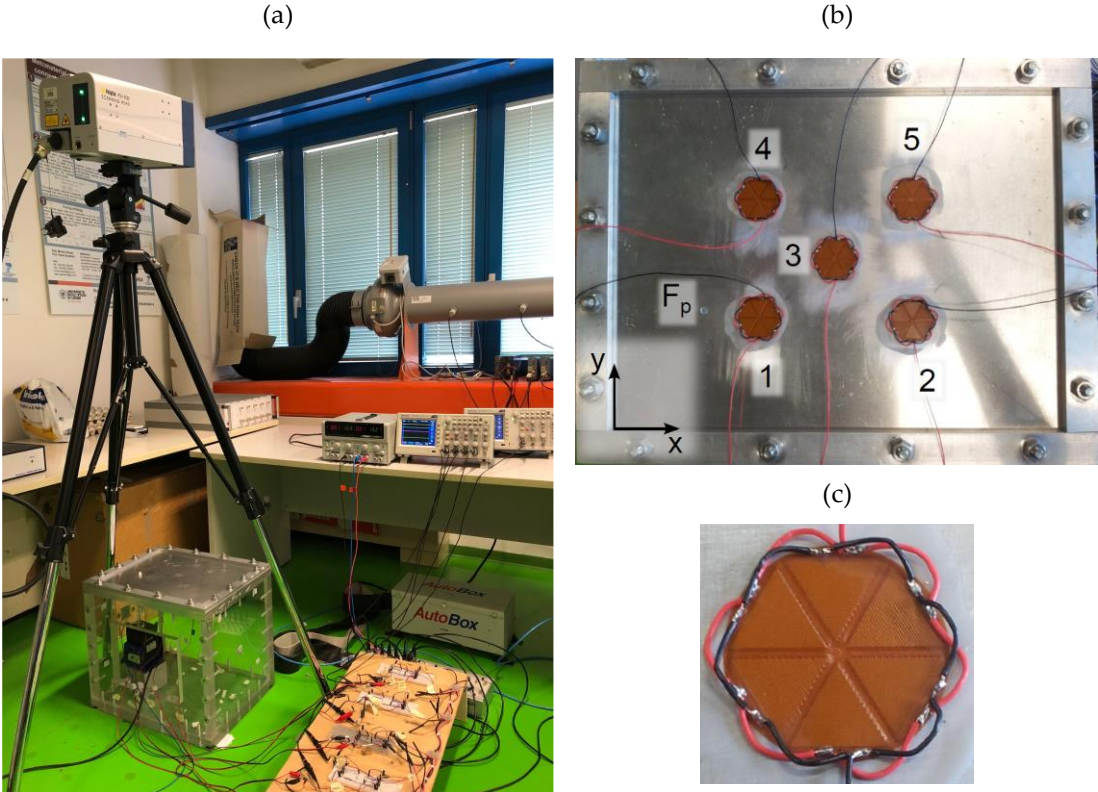


Figure 5.11 (a) Experimental setup. (b) Perspex box showing the five patches. (c) Hexagonal piezoelectric patch.

Table 5.2. Dimensions and physical properties of the panel and piezoelectric patches.

Parameter	Plate	Piezoelectric patches
Dimensions	$l_{xp} \times l_{yp} = 414 \times 314 \text{ mm}$	$l_{xpe} \times l_{ype} = 80 \times 80 \text{ mm}$
Thickness	$h_p = 1 \text{ mm}$	$h_{pe} = 1 \text{ mm}$
Density	$\rho_p = 2700 \text{ kg/m}^3$	$\rho_{pe} = 7600 \text{ kg/m}^3$
Young's modulus	$Y_p = 7 \times 10^{10} \text{ N/m}^2$	$Y_{pe} = 5 \times 10^{10} \text{ N/m}^2$
Poisson ratio	$\nu_p = 0.33$	$\nu_{pe} = 0.275$
Modal damping ratio	$\zeta_p = 0.02$	$\zeta_{pe} = 0.02$
Strain / charge constants		$d_{31}^0 = -190 \times 10^{-12} \text{ m/V}$ $d_{32}^0 = -190 \times 10^{-12} \text{ m/V}$
Capacitance		$C_{pe} = 5.3 \times 10^{-8} \text{ F}$
Centre position patch 1		$x_{pe1} = l_{xp}/2, y_{pe1} = l_{yp}/2$
Centre position patch $j=2-5$		$x_{pej} = \frac{l_{xp}}{2} \pm 60 \text{ mm},$ $y_{pej} = \frac{l_{yp}}{2} \pm 60 \text{ mm}$
Shaker, excitation force position	$x_f = y_f = 85.11 \text{ mm}$	

To facilitate the implementation of the multi-resonant shunts and thus to overcome a possible issue due to excessive values of RLC branch components, the multi-resonant shunts were synthesised digitally in a multi-channel dSPACE digital platform. To obtain the designed analogue multi-resonant shunt effect, the dSPACE platform was connected to the piezoelectric patches via ad hoc interface circuits specifically designed to produce the multi-resonant impedance load digitally programmed in the platform. Considering a single piezoelectric patch, the circuitry used to implement the desired shunt impedance load is illustrated in Figure 5.12 (a). In this figure, a piezoelectric transducer is connected to the dSPACE platform through an operational amplifier characterised by high input impedance. This amplifier is used to deliver a voltage signal from the piezo to the platform, without affecting the current flow. Also, the output signal from dSPACE platform is connected to an operational amplifier such that there is no current flow in the in dSPACE platform. In this way the ratio between the voltage and current at the patch terminals is indeed the desired impedance load.

The synthesis of the multi-resonating shunt circuits is carried out digitally in the dSPACE system according to the following formulation for the electric response of the interface circuit.

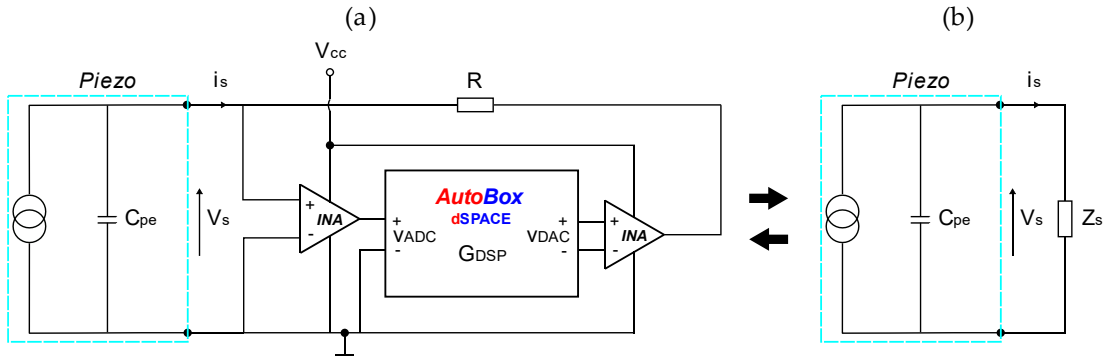


Figure 5.12 (a) Electrical implementation of the synthetic shunt impedances in dSPACE platform. (b) An equivalent electrical circuit.



Figure 5.13 (a) Multi-resonant, current flowing shunt circuit. (b) Simplified current flowing shunt circuit.

Considering the electrical scheme depicted in Figure 5.12 (a), the following relations can be written:

$$v_{ADC} = v_s, \quad (5.63)$$

$$v_{DAC} = G_{DSP} v_{ADC}, \quad (5.64)$$

$$v_s - v_{DAC} = R i_s. \quad (5.65)$$

In Eqs. (5.4)-(5.66),  $v_{ADC}$  is the potential difference at the terminals of the piezoelectric patch,  $v_{DAC}$  is the voltage at the output of the control system,  $G_{DSP}$  is the transfer function to be implemented in the dSPACE platform,  $R$  is the reference resistor and  $i_s$  is the current flowing through the piezoelectric patch terminal. Also, according to the electrical scheme in Figure 5.12 (b).

$$v_s = Z_s i_s, \quad (5.66)$$

where  $Z_s$  is the desired shunt impedance. Combining Eqs (5.4)-(5.66) gives the following expressions for the impedance and the digital platform transfer function

$$Z_s = \frac{v_s}{i_s} = \frac{R}{1-G_{DSP}}, \quad (5.67)$$

$$G_{DSP} = \frac{v_{DAC}}{v_{ADC}} = 1 - Z_s R. \quad (5.68)$$

As discussed in Section 5.3.1, the complex admittance of the simplified multi-resonant shunt depicted in Figure 5.13 (b) is given by the following summation of second order terms:

$$Y_s = \sum_{i=1}^N \frac{1}{L_{bi}} \frac{j\omega}{-\omega^2 + j\omega \left( \frac{R_{bi}}{L_{bi}} \right) + \frac{1}{C_{fi} L_{bi}}}. \quad (5.69)$$

Substituting Eq. (5.70)(5.69) to Eq. (5.68) gives the transfer function, that should be implemented in the dSPACE platform to generate the desired multi-resonance impedance load.

$$G_{DSP} = \frac{v_{DAC}}{v_{ADC}} = 1 - Y_s^{-1} R. \quad (5.70)$$

Indeed, implementing this transfer function in the digital platform connected to the piezoelectric patch via the interface circuit shown in Figure 6.2(a) produces indirectly the desired multi-resonant shunt load presented in Figure 6.3 on the piezoelectric patch.

## 5.8 KINETIC ENERGY AND POWER ABSORPTION MEASUREMENTS

This section discusses the effects produced when the incremental method of multi-resonant shunt tuning presented in the above simulation study is applied in practice. First of all, it is important to note, that in this practical investigation all the patches are tuned jointly, i.e. at every step of the incremental procedure all transducers are connected to identical RLC shunts. Although this approach differs from the one described in Section 5.4.2, which considers individual tuning of each piezoelectric patch, it constitutes a reasonable way to simplify the optimization process and shorten the otherwise lengthy measurements of the kinetic energy and electrical power cost functions. Second, the branch capacitances were chosen to be  $C_{fi} = 0.1C_{pe}$  and the investigated frequency range was set between 40 and 150Hz. For the purpose of this study, the inductances of the shunts were varied using the formula  $L_{bi} = \frac{C_{fi} + C_{pe}}{\omega_b^2 C_{fi} C_{pe}}$  to provide incremental changers of the branches resonance frequencies

of 5 Hz starting from 40Hz up to 150Hz. Also, the shunt resistances were progressively raised in the range of  $3.5k\Omega - 8k\Omega$  with increments of  $500\Omega$  for each combination of branch parameters i.e.  $(f_{bi}, R_{bi})$ , and for the given three branches, a set of measurements was taken including:

- velocity-excitation force transfer functions measurements at a  $3 \times 3$  grid points located on the surface of the plate, performed by the laser scanning vibrometer.
- current-excitation force and voltage-excitation force transfer functions measurements of at the terminals of the five piezoelectric patches.

The total flexural kinetic energy per unit force and total electrical power absorbed by five shunts per unit force were obtained from the measurements for each combination of branch parameters  $(f_{bi}, R_{bi})$ . Based on these results, two-dimensional maps with the evolution of the flexural kinetic energy and electric power absorption with reference to the shunt inductance and resistance parameters were created to experimentally validate the method proposed in Section 5.4.2. The experimental results for the incremental effects produced by the three branches in the five shunts are summarized in Figure 5.14 and Figure 5.15. Considering first Figure 5.14, when all five piezoelectric patches are connected to the first branches of the shunts, plots (a) and (b) in the first row are characterised by a sequence of four local troughs and four local crests respectively. In line with the findings presented in Section 5.4.2. the minima of the kinetic energy troughs and the maxima of the electric power crests of the measured cost functions occur for very similar values of the inductances and resistances:  $L_{b1}, R_{s1}$ . Thus, by setting the first branches such that  $L_{b1} = L_{opt1}$  and  $R_{s1} = R_{opt1}$ , where  $L_{opt1}, R_{opt1}$  are the optimal shunt parameters for the maximum of the third crest of the electric power measured cost function, the shunts resonate in correspondence to third resonance of the plate. When the second RLC branch is added to the shunts, plot (a) in the second row of Figure 5.14 shows only two troughs of the kinetic energy cost function, which can be used to tune inductances  $L_{b2}$  and resistances  $R_{s2}$  of the second branches of the shunts to minimise the kinetic energy of the plate with respect to the first and second resonance of the plate. There is no third trough, since the first branches of the shunts are indeed tuned at the third resonance and thus the kinetic energy of the plate in correspondence to the third resonance mode is already minimised. In contrary, plot (b) shows four crests of the measured

electrical power cost function, which can be utilised to tune inductances  $L_{b2}$  and resistances  $R_{s2}$  of the second branches of the shunts to maximise the electric power absorption of the shunts due to the first, second, third and fourth resonances of the plate. The presence of the third crest at around  $f_{b2} = 120$  Hz;  $L_{b2} = 365$  is indicating that the tuning of the first branches can be improved, since the previously adopted values  $L_{b1} = L_{opt1}$ ,  $R_{s1} = R_{opt1}$  are now slightly offset. Now, by setting inductances and resistances of the second branches such as  $L_{b2} = L_{opt2}$  and  $R_{s2} = R_{opt2}$ , where  $L_{opt2}$  and  $R_{opt2}$  are the optimal shunt parameters for the maximum of the second crest of the electric power measured cost function, the shunts resonate in correspondence to the second and third resonances of the plate. When the third RLC branch is implemented to the shunts, plots (a) and (b) in the third row of Figure 5.14 show only

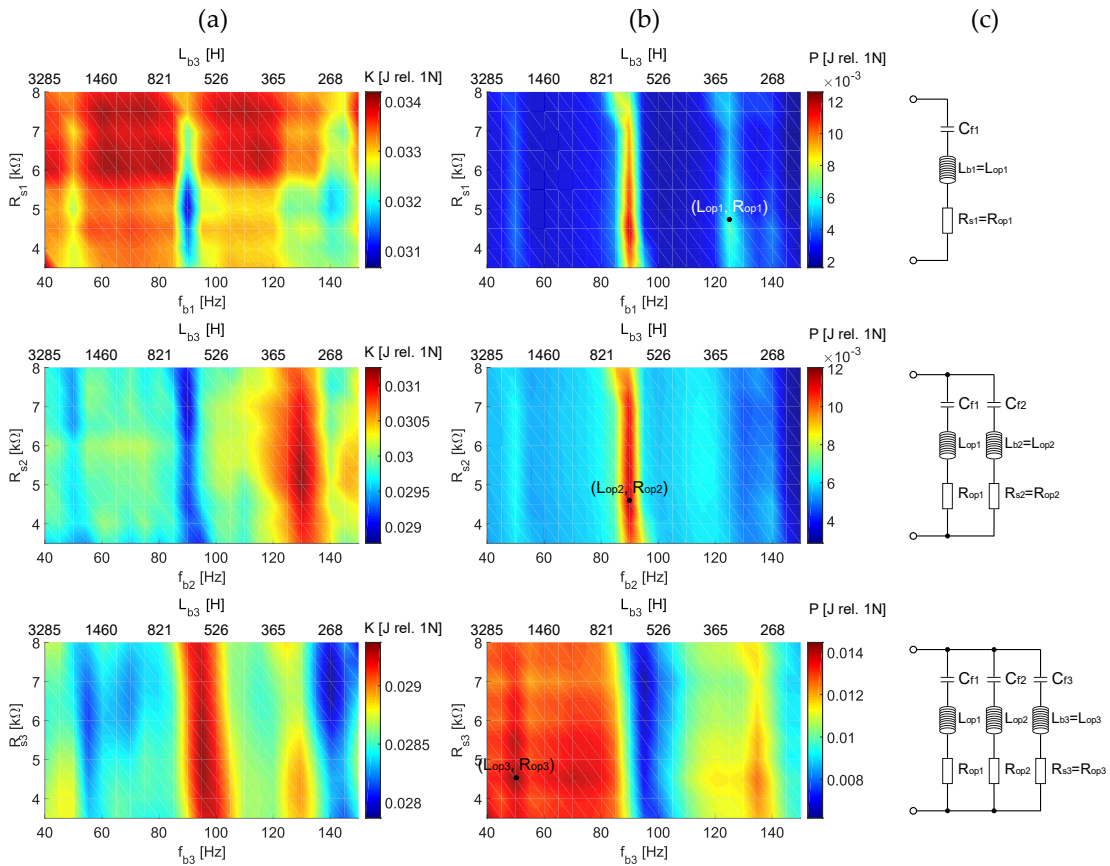


Figure 5.14 (a) The flexural kinetic energy per unit force of the smart plate structure. (b) The electrical power absorbed by five identical shunts illustrated in plot (c).

two troughs and two crests, respectively which are in correspondence to the first and fourth resonances of the plate. As for the previous cases the inductances  $L_{b3}$  and resistances  $R_{s3}$  of the third branches can now be set to maximise the electric power absorption associated with the first resonance mode of the plate, i.e.  $L_{b3} = L_{opt3}$  and  $R_{s3} = R_{opt3}$ . As a result of this iterative procedure, the spectra in column (a) of Figure 5.15 show, that every time the optimal branch is introduced, the flexural kinetic energy (solid blue and red lines) of the plate is brought down at the targeted resonance frequencies. Meanwhile, the absorbed electric power by the shunt circuits (dotted black lines) is maximised at these frequencies.

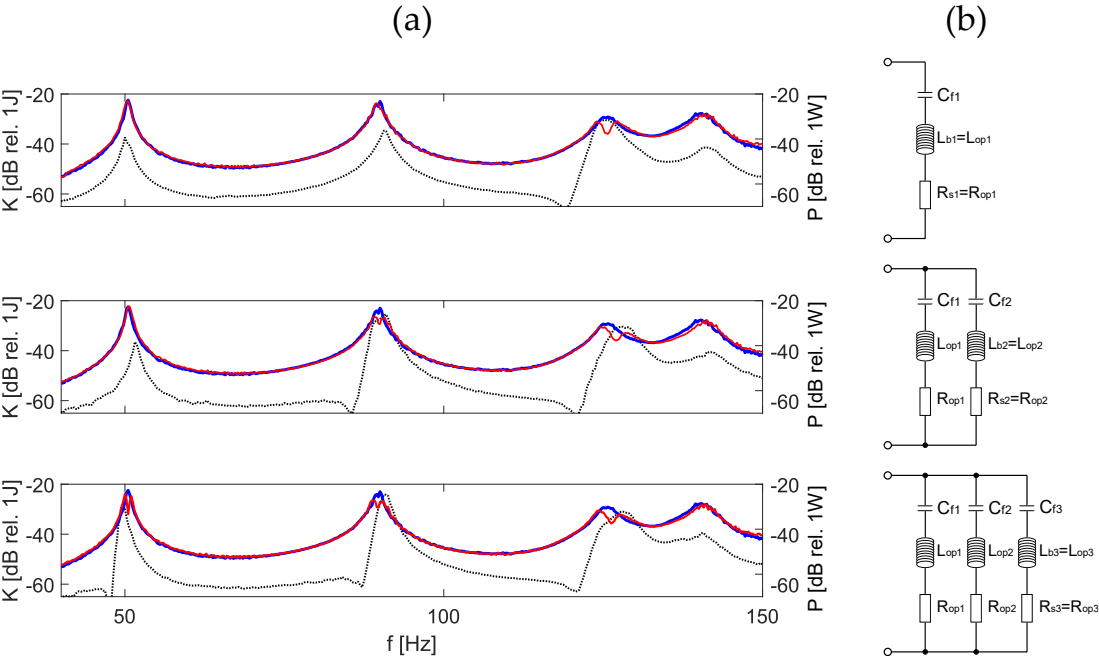


Figure 5.15 (a) The flexural kinetic energy per unit force (solid blue line - shunts in open loop; solid red line - optimal shunts) and power absorbed per unit force by five optimal shunts (dotted black line). (b) Configurations of the optimal multi-resonant shunt circuits.

Plot (a) in the second row of Figure 5.15 confirms also that indeed, the values associated with the third mode of the plate:  $L_{b1} = L_{opt1}$ ,  $R_{s1} = R_{opt1}$  are not optimal due to the small shift of the vibration absorption effect towards higher frequencies. This is rather caused by environmental factors affecting the system over very long measurement sequences lasting several days.

Although the mistuning of existing branches of the shunt circuits can indeed be caused by the addition of a next one, it applies more to branches whose resonance frequencies are not very apart, which is not the case here

## 5.9 CONCLUDING REMARKS

This chapter has first presented a simulation study on the implementation of multi-resonant shunts connected to piezoelectric patches bonded on a plate, which produce multi-resonant vibration absorption effects. The study has shown that the RLC branches that form the shunts can be tuned to globally minimise the resonant response of given modes of the structure by locally maximising the electric power absorbed by each shunt. A simple tuning algorithm based on Newton's method has therefore been proposed to tune on-line the branches in each shunt. The multi-resonant shunts composed of three RLC current flowing branches on five piezoelectric patches was then studied experimentally by utilising shunt impedances synthesized in a dSPACE platform. The experimental study confirmed simulation predictions, that is the reduction of the total flexural kinetic energy of the plate and electrical power absorbed by the multi-resonant shunts with reference to the resistance and inductance parameters in a branch of the shunt is characterised by a sequence of minima and sequence of maxima. The corresponding minima and maxima respectively coincide, which indicates that the branch RL components that would minimise the resonant response of low order flexural modes of the smart plate also maximise the electric power absorbed by the shunts. This effect of the RLC branch gives the opportunity to sequentially tune three branches in such a way as to maximise the electric power absorbed by five shunts, and thus to minimise the smart plate flexural kinetic energy in correspondence to given first resonance frequencies. Although the simulation studies have shown that there is no need for a tuning update every time a branch is added to a shunt, the practical implementation showed that small adjustments may be required to track changes in the dynamic response due to the environmental changes during the long periods of operation.

---

## CONCLUSIONS

---

The research presented in this dissertation is focused on the theoretical and experimental investigations concerning the control of flexural vibrations in beams and plates equipped with arrays of periodic inclusions. Considering that this type of systems can be implemented in a wide variety of applications, the dissertation investigated not only the physical phenomena of vibration absorption effects generated by the arrays of inclusions, but also proposed a practical method of vibration suppression through multi-resonant shunts connected to piezoelectric patch vibration absorbers.

Chapter 2 of the thesis investigated the wave propagation in an infinite one-dimensional Euler-Bernoulli beam equipped with periodic grids formed by point masses, spring-mass vibration absorbers and piezoelectric patch transducers connected to single and multi-resonant shunt circuits in such a way to constitute single and multi-resonant vibration absorbers. The main purpose of this chapter was to characterize the stop band phenomena resulting from each type of the inclusions. The study has shown the existence of two types of stop band effects occurring for the beam with aforementioned inclusions. The first type, also known as the interference stop band effect, can be observed in beams equipped with periodic grid of masses when the spatial period of the traveling wave is equal twice the distance between masses. This type of effect is characterised by rather small attenuation, and its frequency is closely related to the distance between masses. The effect can be extended only towards lower frequencies by increasing the weight of the point masses, in which case, the stop band effects can achieve significant bandwidth. In contrast, the resonance stop band effects generated by spring-mass vibration absorbers and shunted piezoelectric patch transducers are characterised by the high attenuation amplitude and rather narrow frequency band. These effects do not depend upon the spatial organization of the unit cells, on the contrary they depend on the cell resonance frequency, and thus can be tuned by changing the physical properties of the resonant inclusions. It has also been shown that the bandwidth of

resonance stop band effect can be broadened when an energy dissipation mechanism is introduced into resonant inclusions (i.e. mechanical damping in the spring-mass system and electrical resistance in a shunt circuit connected to piezoelectric patch).

The studies on the beam structure with a one-dimensional grid of inclusions in Chapter 2 were continued in Chapter 3, which considers the wave propagation in an infinite plate equipped with two-dimensional arrays of point masses, spring-mass vibration absorbers, and shunted piezoelectric patch vibration absorbers. The focus in this chapter was devoted to the characterisation of the interference and resonance stop band phenomena for two-dimensional arrays of inclusions. This study confirmed that the interference effect associated with the periodic point masses is related to the standing wave behaviour and therefore related to the geometry of the array. As in the case of an infinite beam, the interference stop band generated by the arrays of point masses can be widened only towards lower frequencies by increasing the weight of point masses. Again, large mass inclusions are required to achieve the effect in a wide frequency range. Resonant stop band effects have been achieved both with spring-mass vibration absorbers and the shunted piezoelectric patch vibration absorbers. In the case of vibration absorbers, the effect is generated at the resonance frequency of the absorbers but cannot be maintained above dimensionless frequency 1. This is related to the point-like modelling of vibration absorbers, which occur to be in modal positions at the dimensionless frequencies higher than 1. The use of shunted piezoelectric patch transducers partially overcome this issue and creates resonance effects for certain propagation directions above the dimensionless frequencies above 1. This is possible due to the spatial distribution of the piezoelectric patches on the surface of the plate, which allows them to avoid nodal positions.

In Chapter 4 the stop band effects generated by point masses, spring-mass vibration absorbers and shunted piezoelectric patch vibration absorbers were investigated for a finite rectangular plate. For the purpose of this work, two mathematical models were introduced for the response of the finite plate with arrays of periodic inclusions. The mobility-impedance model was used to simulate stop band effects generated by point masses and spring-mass vibration absorbers, whereas a fully coupled modal model based on Hamilton's principle was employed to simulate stop band effects of shunted piezoelectric patch vibration absorbers. In these studies evolutions of the power spectral density functions of the total kinetic energy of the plate was utilised to characterize the stop band phenomena. Simulation results confirmed that both

interference and resonance stop band effects can be effectively generated in finite thin plates. The obtained evolutions of the power spectral density functions of the total kinetic energy of the plate equipped with arrays of inclusions revealed two-dimensional patterns of the stop band distributions as found in Chapter 3, and confirmed the observations made for infinite plates are valid also for finite plates. To conclude this chapter a multi-resonant shunt was implemented to demonstrate multiple resonance stop band effect in a finite structure.

Chapter 5 has proposed a practical algorithm for the on-line tuning of multi-resonant shunts connected to piezoelectric patches that are bonded on thin structures to reduce the effects of flexural vibrations over a wide frequency band. The study first considered the implementation of a classical single branch RL shunt on a single piezoelectric patch and analysed how the time averaged total flexural kinetic energy of the smart plate and the time averaged total electrical power absorbed by the shunt vary with reference to the shunt RL components. Simulation results showed that the function of the total flexural kinetic energy is characterised by a sequence of troughs whereas the function of the total electrical power absorbed by the shunt is characterised by a mirror surface with a sequence of crests, whose respective minima and maxima coincide and occurs for optimal values of the shunt RL components that would minimise the resonant response of low order flexural modes of the smart plate. This is a rather important result since it shows that the shunt RL components can be conveniently tuned with reference to the total electrical power absorbed by the shunt, which is a local quantity that can be easily measured in the shunt circuit. The implementation of a RLC current-flowing shunt on a single piezoelectric patch was then considered. This shunt produces two effects, which can be described by seeing the inductance as the sum of two components in series. The first component couples with the capacitance in the shunt to produce a resonance and thus a filtering effect at a specific frequency. The second component couples with the shunt capacitance to generate the vibration absorption effect via the piezoelectric patch. The filtering effect narrows the troughs and crests respectively of the flexural kinetic energy and electric power functions so that they assume stretched two-dimensional reverse and conventional bell shapes with principal axes parallel to the inductance (which is the stretching direction) and resistance components. In this way the maxima of the power crests can be conveniently found with a two-stage search, which first finds the optimal shunt inductance with reference to a fixed small shunt resistance and then finds the optimal resistance with reference to the optimal shunt inductance.

The implementation of multi-resonant shunts composed of multiple RLC current flowing branches on multiple piezoelectric patches was finally investigated. In this case the filtering effects of the multiple RLC branches give the opportunity to tune sequentially each branch in such a way as to maximise the electric power absorbed by the shunt, and thus to minimise the smart plate flexural kinetic energy, relative to a sequence of resonant flexural modes of the smart plate. The chapter therefore proposed a simple procedure that sequentially find the optimal values of the RL components in each branch of a shunt with a two-stage search algorithm, which is based on finite difference approximation of the electric power absorbed by the shunt amplitude, first derivative and second derivative with reference to either branch inductance and branch resistance incremental variations. This procedure is carried out sequentially in each shunted patch. The simulation results have shown that there is no need for a tuning updating every time a branch is added to a shunt. However, in many practical applications it may be preferable to keep on-line the iterative tuning such that the RL components in each branch may be continuously updated to track changes in the dynamic response of the smart plate due, for example, to temperature variations or tensioning effects during operation conditions. The work was concluded with an overview simulation study of the smart plate total flexural kinetic PSD when the plate is equipped with an increasingly larger number of piezoelectric patches connected to the multi-resonant shunts whose RL components are tuned with the procedure proposed in this chapter. The study showed that, as the number of shunts and the number of branches is augmented, increasingly greater reductions of the smart plate flexural response are obtained with reductions comprised between 5 and 10 dB over a wider frequency band. These results are obtained considering shunts composed of classical branches with passive RLC components. Thus, it is likely that, if active circuits are used to synthesise the shunts, and thus they can be equipped with negative capacitors that reduce the inherent capacitance of the piezoelectric patches, the vibration control effects can be significantly increased.

It is worth mentioning that, alongside to a classical modal formulation of the coupled flexural response of the plate and piezoelectric patches, this chapter introduced an original modal formulation for the electrical response of the multiple RLC branches in the shunts, which allowed the derivation of the time averaged total flexural kinetic energy and time averaged total electric power with a simple matrix expression.

The experimental validation of the sequential multi-resonant shunt tuning was also presented. In these investigations, the multi-resonant shunt circuits composed of three RLC current flowing branches were synthesized in dSPACE system and

connected with five piezoelectric patches bonded to a thin rectangular panel. The shunts were then tuned, according to the proposed incremental method. The experimental studies confirmed simulation predictions, that is the flexural response of the vibrating plate at the target resonant modes can be minimised, by maximising the electrical power absorption of the shunts. Indeed, the experimentally obtained the two-dimensional patterns of the total flexural kinetic energy of the plate and the total electric power absorbed by the shunt circuits indicate sequences of local minima and maxima, respectively. These local extrema occur for very similar values of the shunt circuit components and thus, gave confirmed the practicality of the proposed control method.

Bearing in mind future work in this topic, the following activities are suggested:

- Experimental evaluation of the ability of the shunted piezoelectric patches to generate multiple stop band effects in the mid and high-frequency range.
- Experimental validation of the proposed method of sequential tuning of multi-resonant shunts in the mid and high-frequency range.
- Implementation of the synthetic negative capacitances into multi-resonant shunt circuits to reduce the inherent capacitances of the piezoelectric patches and thus to enhance the vibration absorption effects of the shunted piezoelectric patches.

In addition, following ideas emerged as a natural extension of the current research

- Substitution of the resistance components in the shunts with energy-harvesting circuits and implementation of the power maximisation algorithm.
- Further investigation on self-powered autonomous platform, where harvested energy by certain shunted piezoelectric patches is redistributed to power up the semi-active vibration control of the other units.



---

## LIST OF PUBLICATIONS

---

### INTERNATIONAL PEER REVIEWED JOURNAL PUBLICATIONS

P. Gardonio, M. Zientek, On-line tuning of multi-resonant shunts connected to piezoelectric patches, submitted to Journal of Sound and Vibration (in review), 2018.

### PROCEEDINGS OF INTERNATIONAL CONFERENCES

M. Zientek, P. Gardonio, *Piezoelectric patches with multi-resonant shunts for multiple frequency band vibration control*, Proceedings of the International Conference on Noise and Vibration Engineering (ISMA), 2018, Leuven, Belgium.

M. Zientek, P. Gardonio, Panel with piezoelectric patches connected to multi resonant shunts set to maximize power absorption, Proceedings of the International Congress and Exposition on Noise Control Engineering (INTERNOISE), 2017, Hong-Kong, China.

M. Zientek, P. Gardonio, Metamaterial panel with arrays of piezoelectric patches connected to multi-resonant electrical shunts, Proceedings of the International Congress on Sound and Vibration (ICSV), 2017, London, UK.

M. Zientek, P. Gardonio, D. Casagrande, *Smart metamaterials for noise and vibration control*. Proceedings of the International Conference on Noise and Vibration Engineering (ISMA), 2016, Leuven, Belgium.

M. Zientek, P. Gardonio, *Plate Metamaterial for broadband vibration control*. Proceedings of the International Conference on Motion and Vibration control and International Conference on Recent Advances in Structural Dynamics (MoViC/RASD), 2016, Southampton, UK.

---

## BIBLIOGRAPHY

---

- [1] M. Griffin, *Handbook of human vibration*, London, Academic Press, (2000).
- [2] N. Mansfield, *Human response to vibration*, Boca Raton, Florida, CRC Press (2005).
- [3] D. Mead, *Passive vibration control*, Chichester, John Wiley & Sons, (2000).
- [4] C. Fuller, S. Elliot, P. Nelson, *Active Control of Vibration*, London, Academic Press (2000).
- [5] N. W. Hagood, A. von Flotow, *Damping of structural vibrations with piezoelectric materials and passive electrical network*, Journal of Sound and Vibration 146 (2) (1991).
- [6] L. Airoldi, M. Ruzzene, *Design of tunable acoustic metamaterials through periodic arrays of resonant shunted piezos*, New Journal of Physics 13 (2011).
- [7] R. L. Forward, *Electronic damping of vibrations in optical structures*, Applied Optics 18 (5) (1979).
- [8] K. Uchino, T. Ishii, *Mechanical damper using piezoelectric ceramics*, Journal of the Ceramic Society of Japan 96 (8) (1988).
- [9] N. W. Hagood, E. F. Crawley, *Experimental investigations of passive enhancement of damping space structures*, Journal of Guidance, Control and Dynamics 14 (6) (1991).
- [10] C. D. Johnson, *Design of passive damping systems*, Journal of Mechanical Design 117 (B) (1995).
- [11] H. H. Law, P. L. Rossiter, G. P. Simon, L. L. Koss, *Characterization of mechanical vibration damping by piezoelectric materials*, Journal of Sound and Vibration 197 (4) (1996).
- [12] G. A. Lesieutre, *Vibration damping and control using shunted piezoelectric materials*, The Shock and Vibration Digest 30 (3).
- [13] M. Ahmadian, P. DeGuilio, *Recent advances in the use of piezoceramics for vibration suppression*, The shock and Vibration Digest 33 (1) (2001).
- [14] S. O. R. Moheimani, *A survey of recent innovations in vibration damping and control using shunted piezoelectric transducers*, IEEE Transactions on Control Systems Technology 11 (4) (2003).
- [15] S. O. R. Moheimani, A. J. Fleming, *Piezoelectric transducers for vibration control and damping*, London, Springer-Verlag (2006).
- [16] J. P. Den Hartog, *Mechanical Vibrations*, New York Reprinted in Dover (1985).

- [17] P. Gardonio, D. Casagrande, *Shunted piezoelectric patch vibration absorber on two-dimensional thin structures: Tuning considerations*, *Journal of Sound and Vibration* 395 (2017).
- [18] K. Yamada, H. Matsuhisa, H. Utsuno, K. Sawada, *Optimum tuning of series and parallel LR circuits for passive vibration suppression using piezoelectric elements*, *Journal of Sound and Vibration* 329 (2010).
- [19] J. Høgsberg, S. Krenk, *Balanced calibration of resonant shunt circuits for piezoelectric vibration control*, *Journal of Intelligent Materials Systems and Structures* 23 (2012).
- [20] P. Soltani, G. Kerschen, G. Tondreau, A. Deraemaeker, *Piezoelectric vibration damping using resonant shunt circuits: an exact solution*, *Smart Materials and Structures* 23 (2014).
- [21] O. Thomas, J. Ducarne, J.-F. Deü, *Performance of piezoelectric shunts for vibration reduction*, *Smart Materials and Structures* 21 (1) (2011).
- [22] M. Berardengo, A. Cigada, S. Manzoni, M. Vanali, *Vibration control by means of piezoelectric actuators shunted with LR impedances: Performance and robustness analysis*, *Shock and Vibration* (2015).
- [23] S. Y. Wu, *Piezoelectric shunts with parallel RL circuits for structural damping and vibration control*, *Proceedings of the SPIE* (1996).
- [24] R.L. Forward, *Electromechanical transducer-coupled mechanical structure with negative capacitance compensation circuit*, United States patent 4,158,787, (1979).
- [25] M.S. Tsai, K.W. Wang, *On the structural damping characteristics of active piezoelectric actuators with passive shunt*, *Journal of Sound and Vibration* 221 (1999).
- [26] J.J. Tang, K.W. Wang, *Active-passive hybrid piezoelectric networks for vibration control: comparison and improvement*, *Smart Materials and Structures* 10 (2001).
- [27] S.Y. Wu, *Broadband piezoelectric shunts for passive structural vibration control*, *Proceedings of SPIE* (2001).
- [28] M.S. Tsai, K.W. Wang, *A coupled robust control/optimization approach for active-passive hybrid piezoelectric networks*, *Smart Materials and Structures* 11 (2002).
- [29] R.A. Morgan, K.W. Wang, *An active-passive piezoelectric absorber for structural vibration control under harmonic excitations with time-varying frequency, part 2: algorithm development and analysis*, *Transactions of the ASME Journal of Vibration and Acoustic* 124 (2002).
- [30] J. Kim, *Smart panel technology for broadband noise reduction*, *Noise & Vibration Worldwide* 34 (2003).

- [31] C.H. Park, A. Baz, *Vibration control of beams with negative capacitive shunting of interdigitated electrode piezoceramics*, Journal of Vibration and Control 11 (2005).
- [32] S.O.R. Moheimani, A.J. Fleming, S. Behrens, *Highly resonant controller for multimode piezoelectric shunt damping*, Electronics letters 37 (2001).
- [33] S.O.R. Moheimani, S. Behrens, *Multimode piezoelectric shunt damping with a highly resonant impedance*, IEEE Transactions on Control Systems Technology 12 (2004).
- [34] S. Behrens, A.J. Fleming, S.O.R. Moheimani, *A broadband controller for shunt piezoelectric damping of structural vibration*, Smart materials and Structures 12 (2003).
- [35] S.O.R. Moheimani, A.J. Fleming, S. Behrens, *On the feedback structure of wideband piezoelectric shunt damping systems*, Smart materials and Structures 12 (2003).
- [36] A.J. Fleming, S.O.R. Moheimani, *Control orientated synthesis of high-performance piezoelectric shunt impedances for structural vibration control*, IEEE Transactions on control systems Technology 13 (2005).
- [37] E. Fukada, M. Date, K. Kimura, T. Okubo, H. Kodama, P. Mokry, Y. Yamamoto, *Sound isolation by piezoelectric polymer films connected to negative capacitance circuits*, IEEE transactions on dielectrics and electrical insulation 11 (2004).
- [38] K.W. Wang, J.S. Lai, K. Yu, *An energy based parametric control approach for structural vibration suppression via semi-active piezoelectric networks*, Transactions of the ASME Journal of vibration and acoustics 118 (1996).
- [39] M. Neubauer, R. Oleskiewicz, K. Popp, T. Krzyzynski, *Optimization of damping and absorbing performance of shunted piezo elements utilizing negative capacitance*, Journal of Sound and Vibration 298 (2006).
- [40] G. Zhao, N. Alujevic, B. Depraetere, P. Sas, *Dynamic analysis and optimization of a piezo-based tuned vibration absorber*, Journal of Intelligent Material Systems and Structures 26 (15) (2014).
- [41] R. Zhu, Y.Y. Chen, M.V. Barnhart, G.K. Hu, C.T. Sun, G.L. Huang, *Experimental study of an adaptive elastic metamaterial controlled by electric circuits*, Applied Physics Letters 108 (1) (2016).
- [42] Y.Y. Chen, G.K. Hu, G.L. Huang, *An adaptive metamaterial beam with hybrid shunting circuits for extremely broadband control of flexural waves*, Smart Materials and Structures 25 (10) (2016).

- [43] S. Behrens, S. O. R. Moheimani, A. J. Fleming, *Multiple mode current flowing passive piezoelectric shunt controller*, *Journal of Sound and Vibration*, 266 (5) (2003).
- [44] J. J. Hollkamp, *Multimodal passive vibration suppression with piezoelectric materials and resonant shunts*, *Journal of Intelligent Material Systems and Structures* 5 (1) (1994).
- [45] D. Niederberger, A. Fleming, S.O.R. Moheimani, M. Morari, *Adaptive multimode resonant piezoelectric shunt damping*, *Smart Materials and Structures* 13 (5) (2004).
- [46] S.-Y. Wu., *Method for multiple mode piezoelectric shunting with single PZT transducer for vibration control*, *Journal of Intelligent Material Systems and Structures* 9 (1998).
- [47] D. A. Saravanos, *Damped vibration of composite plates with passive piezoelectric-resistor elements*, *Journal of Sound and Vibration* 221 (1999).
- [48] S. O. R. Moheimani, A. J. Fleming, S. Behrens, *Highly resonant controller for multimode piezoelectric shunt damping*, *Electronics Letters* 37 (2001).
- [49] A. J. Fleming, S. Behrens, S. O. R. Moheimani, *Optimization and implementation of multimode piezoelectric shunt damping systems*, *IEEE/ASME Transactions on Mechatronics* 7 (2002).
- [50] S. O. R. Moheimani, S. Behrens, *Multimode Piezoelectric Shunt Damping With a Highly Resonant Impedance*, *IEEE Transactions on Control Systems Technology* 12 (2004).
- [51] L. Brillouin, *Wave propagation in periodic structures*, McGraw-Hill Book Company (1946).
- [52] K.O. Hill, G. Meltz, *Fiber Bragg grating technology fundamentals and overview*, *Journal of Lightwave Technology* 15 (8) (1997).
- [53] P. Fuchs, J. Friedl, S. Hofling, J. Koeth, A. Forchel, L. Worschech, M. Kamp, *Single mode quantum cascade lasers with shallow-etched distributed Bragg reflector*, *Optics Express* 20 (4) (2012).
- [54] Z. Liu, X. Zhang, Y. Mao, Y. Y. Zhu, Z. Yang, C. T. Chan, P. Sheng, *Locally resonant sonic materials*, *Science* 289 (2000).
- [55] R.V. Craster, S. Guenneau (Eds.), *Acoustic Metamaterials: Negative Refraction, Imaging, Lensing and Cloaking*, Springer (2013).
- [56] U. Fano, *Effects of configuration interaction on intensities and phase shifts*, *Physical Review* 124 (6) (1961).
- [57] Y. S. Joe, A. M. Satanin, C. S. Kim, *Classical analogy of Fano resonances*, *Physica Scripta* 74 (259) (2006).

- [58] Y. Xiao, J. Wen, D. Yu, X. Wen, *Flexural wave propagation in beams with periodically attached vibration absorbers: Band-gap behavior and band formation mechanisms*, Journal of Sound and Vibration (2012).
- [59] Y. Xiao, J. Wen, X. Wen, *Longitudinal wave band gaps in metamaterial-based elastic rods containing multi-degree-of-freedom resonators*, New Journal of Physics 14 (2012).
- [60] Y. Xiao, J. Wen, X. Wen, *Flexural wave band gaps in locally resonant thin plates with periodically attached spring-mass resonators*, Journal of Physics, Applied Physics 45.
- [61] D. Yu, Y. Liu, G. Wang, H. Zhao, J. Qiu, *Flexural vibration band gaps in Timoshenko beams with locally resonant structures*, Journal of Applied Physics 100 (2006).
- [62] D. Yu, J. Wen, H. Zhao, Y. Liu, X. Wen, *Vibration reduction by using the idea of phononic crystals in a pipe-conveying fluid*, Journal of Sound and Vibration 318 (2008).
- [63] C. Claeys, K. Vergote, P. Sas, W. Desmet, *On the potential of tuned resonators to obtain low-frequency vibrational stop bands in periodic panels*, Journal of Sound and Vibration 332 (2013).
- [64] E. J. P. de Miranda Jr., J. M. C. Dos Santos, *Flexural band gaps in phononic crystal Euler-Bernoulli beams using wave finite element and plane wave expansion methods*, Materials Research, DOI: <http://dx.doi.org/10.1590/1980-5373-MR-2016-0877>.
- [65] D. Duhamel, B.R. Mace, M.J. Brennan, *Finite element analysis of the vibrations of waveguides and periodic structures*, Journal of Sound and Vibration 294 (2006).
- [66] B. R. Mace, D. Duhamel, M.J. Brennan, L. Hinke, *Finite element prediction of wave motion in structural waveguides*, The Journal of the Acoustical Society of America 117 (6) (2005).
- [67] L.Y. Wu, M.L. Wu, L.W. Chen, *The narrow pass band filter of tunable 1D phononic crystal with a dielectric elastomer layer*, Smart Materials and Structures 18 (1) (2009).
- [68] Y.P. Zhao, P.J. Wei, *The band gap of 1D viscoelastic phononic crystal*. Computational Materials Science 46(3) (2009).
- [69] Y.Z. Xie, H.F. Qi, M. Zhao, H. Fang, J. Gao, X.G. Zhang. *Thickness-modulated one-dimensional periodic phononic crystal*, Advanced Materials Research 750-752 (2013).
- [70] Z.Q. Ni, Y. Zhang, L.H. Jiang, L. Han. *Bending vibration band structure of phononic crystal beam by modified transfer matrix method*, International Journal of Modern Physics B. 28 (15) (2014).

- [71] M. Sigalis, M. Kushwaha, E. Economou, M. Kafesaki, I.E. Psarobas, W. Steurer. *Classical vibrational modes in phononic lattices: theory and experiment*, Zeitschrift für Kristallographie 220 (2005).
- [72] R. Szilard, *Theories and applications of plate analysis: classical, numerical and engineering methods*, Hoboken, New Jersey, John Wiley & Sons (2004).
- [73] A. Preumont, *Mechatronics*, Dordrecht: Springer (2006).
- [74] V. Lopes Jr., J.A. Pereira, D.J. Inman, *Structural FRF acquisition via impedance measurement applied to damage location*, XVII IMAC, San Antonio, USA.
- [75] W.X. Zhong, F.W. Williams, *On the direct solution of wave propagation for repetitive structures*, Journal of Sound and Vibration 181 (3) (1995).
- [76] K.C. Chuang, Z.Q. Zhang, H.X. Wang, *Experimental study on slow flexural waves around the defect modes in a phononic crystal beam using fiber Bragg gratings*, Physical Letters A 380 (2016).
- [77] Y. Xiao, B.R. Mace, J. Wen, X. Wen, *Formation and coupling of band gaps in a locally resonant elastic system comprising a string with attached resonators*, Physics Letters A 375 (12).
- [78] C. Claeys, P. Sas, W. Desmet, *On acoustic radiation efficiency of local resonance based stop band materials*, Journal of Sound and Vibration
- [79] C. Sheng-Bing, W. Ji-Hong, W. Gang, W. Xi-Sen, *Tunable band gaps in acoustic metamaterials with periodic arrays of resonant shunted piezos*, Chinese Physics B 22 (7) (2013).
- [80] A. Spadoni, M. Ruzzene, K. Cunefare, *Vibration and wave propagation control of plates with periodic arrays of shunted piezoelectric patches*, Journal of Intelligent Material Systems and Structures 20 (8) (2009).
- [81] G.L.C.M. de Abreu, J.F. Ribeiro, V. Steffen Jr., *Finite element modelling of a plate with localized piezoelectric sensors and actuators*, Journal of the Brazilian Society of Mechanical Sciences and Engineering 26 (2) (2004).
- [82] C. Kittel, *Introduction to Solid State Physics*, Wiley, (2005).
- [83] A. Diaz, A. Haddow, L. Ma, *Design of band-gap grid structures*, Structural and Multidisciplinary Optimization 29 (6) (2005).
- [84] O. Sigmund, J.S. Jensen, *Systematic design of phononic band-gap materials and structures by topology optimization*, Philosophical Transactions of The Royal Society 361 (2003).
- [85] J.N. Reddy, *Mechanics of Laminated Composite Plates and Shells: Theory and Analysis*, CRC Press, Boca Raton (2004).

- [86] J.S. Bendat, A.G. Piersol, *Random Data Analysis and Measurement Procedures*, John Wiley & Sons, Chichester (1990).
- [87] H.T. Banks, R.C. Smith, Y. Wang, *Smart Material Structures, Modeling, Estimation and Control*, Wiley & Sons, Chichester (1996).
- [88] N.W. Hagood, W.H. Chung, A. von Flotow, *Modelling of piezoelectric actuator dynamics for active structural control*, *Journal of Intelligent Material Systems and Structures* 1 (1990).
- [89] H. Crandall, D.C. Karnopp, A.F. Kurtz, D.C. Pridmore-Brown, *Dynamics of Mechanical and Electromechanical Systems*, R. E. Krieger Pub. Co., Malabar, Florida (1982).
- [90] L. Meirovitch, *Principles and Techniques of Vibration*, Prentice Hall, Upper Saddle River, NJ (1997).
- [91] D. Casagrande, P. Gardonio and M. Zilletti, *Smart panel with time-varying shunted piezoelectric patch absorbers for broadband vibration control*, *Journal of Sound and Vibration* 400 (2017).
- [92] P. Gardonio, S. Miani, F. Blanchini, D. Casagrande and S.J. Elliott, *Plate with decentralised velocity feedback loops: Power absorption and kinetic energy considerations*, *Journal of Sound and Vibration* 331 (2012).
- [93] A. Preumont, *Vibration Control of Active Structures*, 2<sup>nd</sup> ed., Kluwer Academic Publishers Group, London (2002).
- [94] R.L. Clark, W.R. Saunders, G.P. Gibbs, *Adaptive Structures*, 1<sup>st</sup> ed., John Wiley & Sons, New York (1998).
- [95] P. Gardonio, M. Zilletti, *Vibration Energy harvesting from an array of flexible stalks exposed to airflow*, *Journal of Smart Materials and Structures* 25 (2016).
- [96] D. Mayer, C. Linz, V. Krajenski, 2001, *Synthetic inductor for passive damping of structural vibrations*, ADAMES Abschlusskolloquium.
- [97] A. Galantai, *The theory of Newton's method*, *Journal of Computational and Applied Mathematics* 124 (1-2) (2000).
- [98] O. Thorp, M. Ruzzene, A. Baz, *Attenuation and localization of wave propagation in rods with periodic shunted piezoelectric patches*, *Smart Materials and Structures* 10 (5) (2001).
- [99] O. Thorp, M. Ruzzene, A. Baz, *Attenuation and wave propagation in fluid-loaded shells with periodic shunted piezoelectric rings*, *Smart Materials and Structures* 14 (4) (2005).

- [100] F. Casadei, M. Ruzzene, L. Dozio, K.A. Cunefare, *Broadband vibration control through periodic arrays of resonant shunts: experimental investigation on plates*, *Smart Materials and Structures* 19 (1) (2009).
- [101] F. Casadei, L. Dozio, M. Ruzzene, K.A. Cunefare, *Periodic shunted arrays for the control of noise radiation in an enclosure*, *Journal of Sound and Vibration* 329 (18) (2010).
- [102] S. Chen, G. Wang, J. Wen, X. Wen, *Wave propagation and attenuation in plates with periodic arrays of shunted piezo-patches*, *Journal of Sound and Vibration* 332 (6) (2013).
- [103] A.J. Fleming, S. Behrens, S.O.R. Moheimani, *Reducing the inductance requirements of piezoelectric shunt damping systems*, *Smart Materials and Structures* 12 (1) (2003).
- [104] S.Y. Wu, *Method for multiple mode piezoelectric shunting with single PZT transducer for vibration control*, *Journal of Intelligent Material Systems and Structures* 9 (12) (1998).